

THE H α GALAXY SURVEY AND STAR
FORMATION IN THE LOCAL UNIVERSE

Neville S. Shane

Astrophysics Research Institute

A thesis submitted in partial fulfilment of the requirements of

Liverpool John Moores University

for the degree of

Doctor of Philosophy.

October 2002

Declaration

The work presented in this thesis was carried out in the Astrophysics Research Institute, Liverpool John Moores University. Unless otherwise stated, it is the original work of the author.

While registered as a candidate for the degree of Doctor of Philosophy, for which submission is now made, the author has not been registered as a candidate for any other award. This thesis has not been submitted in whole, or in part, for any other degree.

Neville Shane
Astrophysics Research Institute
Liverpool John Moores University
Twelve Quays House
Egerton Wharf
Birkenhead
CH41 1LD
UK
October 2002

Abstract

This thesis presents the H α Galaxy Survey, the largest and most representative optical sample of nearby star-forming galaxies to date. In total, 334 spiral and irregular galaxies have been imaged in the H α line as part of a survey of galaxies in the local Universe. H α fluxes, equivalent widths and surface brightnesses are used to measure the on-going star formation activity in the galaxies. The distribution of star formation within galaxies, the relation between star formation and the properties and surrounding environment of a galaxy, and the total current star formation density of the local Universe are all investigated.

Sources of uncertainty, due to both astrophysical and non-astrophysical effects are also examined. The largest, non-astrophysical, source of error in the H α fluxes comes from the subtraction of the continuum emission from the galaxies. A new method, employing photometric separation of the [NII] and H α emission, is proposed to correct for uncertainties due to [NII] contamination. The method shows that [NII]/H α varies widely within each galaxy and that the current standard corrections need to be updated. Internal extinction effects are investigated and found to vary within individual galaxies. Data from the Universidad Complutense de Madrid H α survey collaboration is used to show that the quantity of extinction is related to galaxy type.

Star formation rates calculated from the H α fluxes are compared to those derived from far-infrared data. There is a strong, but non-linear correlation between the two.

The comparisons of H α to continuum concentration indices show that the major-

ity of massive-star formation is occurring in the outer regions of the galaxies. The distribution of star formation within galaxies is found to vary amongst galaxies with the same Hubble type and is strongly affected by tidal interactions. The profile of a nuclear bar is found to correlate with the circumnuclear distribution of HII regions.

Star formation activity is found to correlate with Hubble type, although there is a large amount of scatter. Once normalisations for size or mass have been applied, Sm-Im galaxies are found to be the most active, on average. With the exception of S0/a-Sa galaxies, no correlation between H α equivalent width or surface brightness and galaxy luminosity is found. Star formation rates and equivalent widths are not found to significantly differ between field and group populations. Both the H α and continuum surface brightnesses are found to be enhanced in group galaxies compared to the field.

The total star formation rate density for $z=0$ is found, by integrating under the H α luminosity function, to be $0.027 \pm 0.006 \text{ M}_{\odot} \text{ yr}^{-1} \text{ Mpc}^{-3}$, with the largest contributions coming from galaxies with M_B between -19 and -20 , but with a larger share coming from faint galaxies than previously predicted. The dominant star-forming Hubble types are Sbc-Sc galaxies, but a significant contribution is found from the, previously undersampled, Sm-Im population. Comparing with higher-redshift studies shows that there has been little evolution in the total star formation rate since $z=0.3$.

Acknowledgements

I would like to thank my supervisor, Phil James, for his help and encouragement throughout the course of my PhD.

I am also grateful to the Astrophysics Research Institute and Liverpool John Moores University for allowing me the opportunity to undertake this course of study. I acknowledge funding from the UK Particle Physics and Astronomy Research Council.

This research has made use of the NASA/IPAC Extragalactic Database (NED) which is operated by the Jet Propulsion Laboratory, California Institute of Technology, under contract with the National Aeronautics and Space Administration.

Contents

Declaration	ii
Abstract	iii
Acknowledgements	v
Contents	vi
List of Tables	xiii
List of Figures	xv
1 Introduction	1
1.1 Why study local star formation?	1
1.2 Using $H\alpha$ to study star formation	2
1.3 Previous $H\alpha$ studies	3
1.3.1 Kennicutt & Kent (1983)	3
1.3.2 The Universidad Complutense de Madrid Survey	5
1.3.3 Young et al. (1996)	6
1.4 Other methods of calculating star formation rates	7
1.4.1 Integrated colours and spectra; synthesis modeling	8

1.4.2	Ultraviolet continuum	9
1.4.3	Far-infrared continuum	10
1.4.4	Recombination lines	11
1.4.5	Radio-continuum measurements	12
1.4.6	Comparisons of different methods of measuring SFR	13
1.5	Aims and layout of the thesis	15
2	The Hα Galaxy Survey	18
2.1	Sample selection criteria	18
2.2	Statistics on the main observing time	20
2.3	The final observed sample	21
3	Observations and Data Reduction	27
3.1	The telescope, instrumentation and filters	27
3.2	The observations	28
3.3	Data reduction	29
3.4	Photometric calibration using standard stars	31
3.5	Photometric calibration of galaxy images taken on non-photometric nights	32
3.6	Calculating galaxy fluxes	33
3.7	Calculating star formation rates	37
3.8	Calculating equivalent widths	37
3.9	Calculating surface brightnesses	38
3.10	Elliptical apertures	38

3.11	Calculating galaxy distances	39
4	Non-astrophysical sources of error in photometric parameters	43
4.1	Internal comparison tests on repeat measurements	43
4.2	External comparison tests with published results in the literature	44
4.3	The sky background	47
4.3.1	The effect of the sky background variation on concentration indices	50
4.4	Continuum scaling factors	51
4.5	Errors due to surface fitting and source removal	53
4.6	Errors in the flux calibration	54
4.7	Distance errors	56
4.8	Summary	57
5	Astrophysical sources of error: extinction and [NII] corrections	59
5.1	[NII] Contamination	60
5.1.1	Photometric separation of [NII] and H α	61
5.1.2	[NII] contamination - summary and conclusions	69
5.2	Atmospheric extinction	70
5.3	Galactic extinction	71
5.4	Internal extinction	71
5.4.1	UKIRT observations and data reduction	73
5.4.2	Br γ detections	75
5.4.3	Putting limits on Br γ detections	80

5.4.4	Br γ fluxes in the literature	81
5.4.5	The dependence of internal extinction on inclination and morphology	82
5.4.6	Internal extinction - summary and conclusions	85
6	Comparison of Hα and IR SFRs	88
6.1	IRAS flux densities, FIR luminosities and converting to SFR . . .	89
6.2	Comparing H α GS and IRAS star formation rates	90
6.3	The dependence of the FIR luminosity on galaxy morphology . .	92
7	Star formation within galaxies	96
7.1	Calculating concentration indices	97
7.1.1	Effective radii	97
7.1.2	The log C_{31} index	97
7.1.3	The Petrosian index	98
7.1.4	Comparing concentration indices	100
7.1.5	The relationship between concentration index and galaxy type	103
7.1.6	Concentration indices - summary	109
7.2	H α concentration and galaxy environment	111
7.3	The distribution of star formation in normal galaxies	113
7.4	The distribution of star formation in interacting and highly disturbed galaxies	114
7.4.1	UGC3740 and UGC3798	116

7.4.2	UGC3847 and UGC3851	116
7.4.3	UGC12699 and UGC12700	118
7.4.4	UGC3429	120
7.4.5	UGC5637	121
7.4.6	UGC12048	121
7.5	The effects of bars on circumnuclear star formation	122
8	Investigating global star formation dependencies	126
8.1	Morphology dependencies	127
8.1.1	Hubble types	127
8.1.2	Concentration Indices	135
8.2	Luminosity dependencies	137
8.3	Environmental dependencies	139
8.3.1	SFR dependence on environment	142
8.3.2	EW dependence on environment	145
8.3.3	H α surface brightness dependence on environment	148
8.4	Interactions	151
8.5	Summary	153
9	Star formation in the local Universe	156
9.1	The local luminosity function	157
9.2	The local SFR density as a function of galaxy luminosity	164
9.3	The H α luminosity function	168

9.4	The SFR density of the local Universe	172
9.5	The local morphology function	173
9.6	The local SFR density as a function of galaxy morphology	174
9.7	Evolution of SFR density	177
10	Summary, conclusions and further work	180
10.1	The H α Galaxy Survey	180
10.1.1	Non-astrophysical errors	181
10.1.2	Astrophysical errors	182
10.2	Results and conclusions	183
10.2.1	Comparison of H α and FIR as a measure of star formation	183
10.2.2	Star formation within galaxies	183
10.2.3	Global star formation dependencies	185
10.2.4	Star formation in the local Universe	186
10.3	Further work	187
10.3.1	Further investigation into [NII] contamination	187
10.3.2	Star formation in the Virgo Cluster	188
10.3.3	Star formation in interacting galaxies	188
10.3.4	Disk and circumnuclear star formation	188
10.3.5	Arm-induced star formation in spiral galaxies	189
10.3.6	HII luminosity functions	190
	Bibliography	191

List of Tables

3.1	29
4.1	44
4.2	45
4.3	49
4.4	51
5.1	68
5.2	69
5.3	70
5.4	79
5.5	81
5.6	82
5.7	83
6.1	93
8.1	153
9.1	164

9.2 170

List of Figures

1.1	From Cram et al. (1998). Comparison of SFRs deduced from 1.4 GHz luminosities (horizontal axis) with the rates deduced using the other luminosities indicated. Symbols are coded by the initials of the authors' last names and the year of publication (see Cram et al. 1998).	14
2.1	The morphological make up of the original sample (empty histograms) and the observed sample (filled histograms).	22
2.2	The distribution of galaxy diameters in the original sample (empty histograms) and the observed sample (filled histograms).	24
2.3	The distribution of total R-band absolute magnitude for the observed galaxies.	26
3.1	28
4.1	Comparison of literature values for the total galaxy H α fluxes with values from the present study.	46
4.2	Comparison of literature values for the total galaxy EW with values from the present study.	46
4.3	The image of UGC5672 taken through the h6570 filter. The 'creased' background effect was found on several other images taken through the narrow-band filters, but has not been explained.	48

4.4	The percentage uncertainty in the transmission value due to the uncertainties in the galaxy's recession velocity.	55
4.5	A comparison of galaxy distances as calculated using the model of Schechter (1980) and the catalogue of Tully (1988). The solid line represents a one-to-one correlation.	56
5.1	UGC2141	64
5.2	UGC2210	64
5.3	UGC2855	66
5.4	UGC3580	66
5.5	UGC8403	67
5.6	UGC11872	67
5.7	B γ image of UGC5786. Regions investigated in Table 5.4 are labeled.	76
5.8	H α image of UGC5786. Regions investigated in Table 5.4 are labeled.	76
5.9	The H α extinction coefficient plotted against the cosine of the inclination for 109 UCM galaxies.	84
5.10	The H α extinction coefficient plotted against Hubble type. The plot on the left shows the mean values for each type, with the error bars representing the standard deviation divided by the square root of the number of galaxies of that type. The plot on the right shows each of the 120 UCM galaxies for which both extinction and morphology data are available.	85

5.11	The $H\alpha$ extinction coefficients and upper limits calculated using $Br\gamma$ fluxes, plotted against Hubble T-type. Error bars have been omitted for clarity, but uncertainties can be found in Tables 5.4, 5.5 and 5.7. The solid line is positioned at $A(H\alpha)=1.1$ mag, and the dashed lines at 0.5 and 1.8 mag.	86
6.1	The SFRs derived using infrared compared to those found from the $H\alpha$ data. The dashed line is the one-to-one relation and the solid line is the best-fit line to the data. The axis on the right displays the FIR luminosity of the galaxies in Solar units.	91
6.2	Histograms of the ratio of IRAS SFRs to $H\alpha$ GS SFRs as a function of morphological type. $H\alpha$ fluxes have been corrected using a uniform extinction correction of 1.1 mag.	94
6.3	As in figure 6.2, but with the morphologically-dependent extinction corrections derived from the UCM data (see text) applied to the $H\alpha$ fluxes.	94
7.1	The galaxy UGC5589 in R-band light (left) and in $H\alpha$ (right) . . .	101
7.2	The variation of η with semi-major axis in the R-band image (left) and in $H\alpha$ (right). The vertical line indicates the first value where $\eta = 0.2$ for the galaxy image, and hence is located at a Petrosian radius. The $H\alpha$ profile crosses the $\eta = 0.2$ line several times, and hence there is clearly some ambiguity as to the location of the Petrosian radius to be used.	101
7.3	The horizontal line indicates the Petrosian flux (in $Wm^{-2}nm^{-1}$ for the continuum image (left) and in Wm^{-2} for the $H\alpha$ (right)) and the vertical line shows the Petrosian radius. From this example, it is clear that this method is not the most suitable for use with $H\alpha$ images.	101

7.4	Comparing the two forms of the concentration index for continuum light.	102
7.5	Comparing the two forms of the concentration index for H α light.	102
7.6	Comparing the two forms of the relative concentration index. . . .	103
7.7	Comparing the relative concentration index to the ratio of effective radii.	104
7.8	The continuum concentration index CI plotted against Hubble type T. The plot on the left shows the mean value of CI for each type, with the error bars representing the standard deviation divided by the square root of the number of galaxies of that type. The plot on the right shows each of the galaxies for which CI has been calculated.	105
7.9	The H α concentration index CI plotted against Hubble type T. The plot on the left shows the mean value of CI for each type, with the error bars representing the standard deviation divided by the square root of the number of galaxies of that type. The plot on the right shows each of the galaxies for which CI has been calculated.	106
7.10	The relative concentrations $CI(R)-CI(H\alpha)$ plotted against Hubble type T. The plot on the left shows the mean values for each type, with the error bars representing the standard deviation divided by the square root of the number of galaxies of that type. The plot on the right shows each of the galaxies for which concentration indices have been calculated.	106

7.11	The continuum concentration index CI_p plotted against Hubble type T. The plot on the left shows the mean value of CI_p for each type, with the error bars representing the standard deviation divided by the square root of the number of galaxies of that type. The plot on the right shows each of the galaxies for which CI_p has been calculated. This plot can be compared to Figure 10 in Shimasaku et al. (2001).	107
7.12	The $H\alpha$ concentration index CI_p plotted against Hubble type T. The plot on the left shows the mean value of CI_p for each type, with the error bars representing the standard deviation divided by the square root of the number of galaxies of that type. The plot on the right shows each of the galaxies for which CI_p has been calculated.	108
7.13	The relative concentrations $CI_p(R)/CI_p(H\alpha)$ plotted against Hubble type T. The plot on the left shows the mean values for each type, with the error bars representing the standard deviation divided by the square root of the number of galaxies of that type. The plot on the right shows each of the galaxies for which Petrosian concentration indices have been calculated.	109
7.14	The relative effective radii $r_e(H\alpha)/r_e(R)$ plotted against Hubble type T. The plot on the left shows the mean values for each type, with the error bars representing the standard deviation divided by the square root of the number of galaxies of that type. The plot on the right shows each of the galaxies for which effective radii have been calculated.	110
7.15	The distribution of $H\alpha$ concentration indices as a function of Hubble T-type. Different galaxy environments are coded with different colours and symbols.	112

7.16	Mean $H\alpha$ concentration indices for field and group+pair galaxies as a function of Hubble T-type.	113
7.17	A Hubble tuning fork diagram composed of R-band (upper image of each pair) and $H\alpha$ (lower image) observed galaxies.	115
7.18	UGC3740 and UGC3798. The left-hand image contains the continuum R-band emission. The right-hand image displays the continuum-subtracted $H\alpha$ emission. North is the top of the images and east is to the left.	116
7.19	UGC3847 and UGC3851. The left-hand image contains the continuum R-band emission. The regions identified by different labels, as used in this study, are marked. The three parts of NGC2363 are as labeled in Drissen et al. (2000). The right-hand image displays the continuum-subtracted $H\alpha$ emission. North is the top of the images and east is to the left.	117
7.20	The main star forming regions of UGC3847 and UGC3851 in $H\alpha$ light. North is to the top of the image, and east is to the left . . .	118
7.21	UGC12699 and UGC12700. The left-hand image contains the continuum R-band emission. The right-hand image displays the continuum-subtracted $H\alpha$ emission. North is the top of the images and east is to the left. A very bright star is situated below the south-eastern corner of the image, which has saturated the CCD and is the cause of the vertical line.	119
7.22	UGC3429. The left-hand image contains the continuum R-band emission. The right-hand image displays the continuum-subtracted $H\alpha$ emission. North is the top of the images and east is to the left.	120
7.23	UGC5637. The left-hand image contains the continuum R-band emission. The right-hand image displays the continuum-subtracted $H\alpha$ emission. North is the top of the images and east is to the left.	121

7.24	UGC12048. The left-hand image contains the continuum R-band emission. The right-hand image displays the continuum-subtracted H α emission. North is the top of the images and east is to the left.	122
7.25	UGC4705 (SBb): R-band (left) and H α (right) images.	123
7.26	UGC8116 (SBc).	123
7.27	UGC12343 (SBc).	123
7.28	UGC4444 (SBcd): R-band (left) and H α (right) images.	124
7.29	UGC4469 (SBcd).	124
7.30	UGC6797 (SBd).	124
7.31	UGC4273 (SBb): R-band (left) and H α (right) images.	125
7.32	UGC9824 (SBbc).	125
7.33	UGC10470 (SBbc).	125
8.1	The distribution of SFRs as a function of T-type.	127
8.2	Mean SFRs for barred and unbarred galaxies as a function of T-type.	129
8.3	Median SFRs for barred and unbarred galaxies as a function of T-type.	129
8.4	Median SFRs for barred and unbarred galaxies as a function of T-type, with the extinction corrections derived from the UCM data applied to the H α fluxes.	130
8.5	The distribution of EWs as a function of T-type.	131
8.6	Mean EWs for barred and unbarred galaxies as a function of T-type.	133
8.7	Median EWs for barred and unbarred galaxies as a function of T-type.	133

8.8	The distribution of $H\alpha$ surface brightnesses as a function of T-type. The surface brightness scale is in arbitrary units.	134
8.9	Mean $H\alpha$ surface brightnesses for barred and unbarred galaxies as a function of T-type.	135
8.10	SFR plotted against the $\log C_{31}$ concentration index.	136
8.11	SFR plotted against the Petrosian concentration index.	136
8.12	EW plotted against the $\log C_{31}$ concentration index.	137
8.13	EW plotted against the Petrosian concentration index.	137
8.14	$H\alpha$ surface brightness plotted against the $\log C_{31}$ concentration index.	138
8.15	$H\alpha$ surface brightness plotted against the Petrosian concentration index.	138
8.16	The relationship between the R band magnitude and the $H\alpha$ EW of $H\alpha$ GS galaxies, grouped into 3 bins of Hubble type, and for all types together.	139
8.17	$H\alpha$ surface brightness as a function of total R-band magnitude. . .	140
8.18	The distribution of SFRs as a function of T-type. Different galaxy environments are coded with different colours and symbols.	142
8.19	Mean SFRs for field and group+pair galaxies as a function of T-type.	143
8.20	Median SFRs for field and group+pair galaxies as a function of T-type.	143
8.21	SFR plotted against the $\log C_{31}$ concentration index. Different galaxy environments are coded with different colours.	145
8.22	The distribution of EWs as a function of T-type. Different galaxy environments are coded with different colours and symbols.	146
8.23	Mean EWs for field and group+pair galaxies as a function of T-type.	147

8.24	Median EWs for field and group+pair galaxies as a function of T-type.	147
8.25	EW plotted against the $\log C_{31}$ concentration index. Different galaxy environments are coded with different colours.	148
8.26	The distribution of $H\alpha$ surface brightnesses as a function of T-type. Different galaxy environments are coded with different colours and symbols.	149
8.27	Mean $H\alpha$ surface brightnesses for field and group+pair galaxies as a function of T-type.	150
8.28	Mean R-band surface brightnesses for field and group+pair galaxies as a function of T-type.	150
8.29	As for figures 8.27 and 8.28, but using the R-band effective radius as a measure of galaxy area instead of the R-band Petrosian radius.	151
8.30	$H\alpha$ surface brightness plotted against the $\log C_{31}$ concentration index. Different galaxy environments are coded with different colours.	152
9.1	The distribution of absolute blue magnitudes within the parent sample, with galaxies in the Virgo region removed, and highly inclined galaxies included. Each bin represents 0.5 mag.	158
9.2	The calculated parent luminosity functions for each distance shell. The error bars represent $\phi(M_B)/\sqrt{n}$, where n is the number of galaxies contributing to the point.	162
9.3	The luminosity function for the entire parent sample. The solid line shows the best-fit Schechter curve and the dashed line shows the Schechter fit from the AARS data.	163
9.4	The log of the star formation rate plotted against binned absolute blue magnitudes for the observed galaxies.	165

9.5	The distribution of absolute magnitudes amongst each galaxy T-type for both the parent (left) and the observed samples (right).	165
9.6	SFR density as a function of absolute blue magnitude found using the points in the luminosity function (Fig. 9.3).	166
9.7	SFR density as a function of absolute blue magnitude found using the Schechter fit to the luminosity function (Fig. 9.3).	167
9.8	SFR density as a function of absolute blue magnitude found using the Schechter fit to the AARS luminosity function (Fig. 9.3).	168
9.9	The $H\alpha$ luminosity function found using the points in the M_B luminosity function (Fig. 9.3). The solid line represents the best-fit Schechter function, and the dashed line is the fit found by Gallego et al. (1995) for the UCM data. The scale at the top of the diagram indicates the log of the SFR corresponding to the $H\alpha$ luminosity.	169
9.10	The $H\alpha$ luminosity function found using the Schechter fit to the M_B luminosity function (Fig. 9.3). The solid line represents the best-fit Schechter function, and the dashed line is the fit found by Gallego et al. (1995) for the UCM data. The scale at the top of the diagram indicates the log of the SFR corresponding to the $H\alpha$ luminosity.	171
9.11	The $H\alpha$ luminosity function found using the Schechter fit to the AARS M_B luminosity function (Fig. 9.3). The solid line represents the best-fit Schechter function, and the dashed line is the fit found by Gallego et al. (1995) for the UCM data. The scale at the top of the diagram indicates the log of the SFR corresponding to the $H\alpha$ luminosity.	171
9.12	The calculated parent morphology functions for each distance shell. The error bars represent $\phi(T)/\sqrt{n}$, where n is the number of galaxies contributing to the point, and T is the T-type of the galaxy.	175

9.13	The morphology function for the entire parent sample.	176
9.14	SFR density as a function of galaxy morphology with the standard 1.1 mag extinction correction applied to all galaxies.	178
9.15	SFR density as a function of galaxy morphology with the type- dependent extinction corrections from the UCM data applied. . .	178
9.16	SFR density as a function of redshift - taken from Hopkins et al. (2000), with the addition of the H α GS point at z=0. This diagram is a compilation of SFR densities derived from emission-line and UV continuum measurements taken from the literature. The UV- based points are shown here with extinction corrections from Stei- del et al. (1999). References are as follows, along with the origin of the SFR density estimate: (Hop00) Hopkins et al. (2000) (H α); (Ste99) Steidel et al. (1999) (UV); (Gla99) Glazebrook et al. (1999) (H α); (Yan99) Yan et al. (1999) (H α); (Tre98) Treyer et al. (1998) (UV); (TM98) Tresse & Maddox (1998) (H α); (Con97) Connolly et al. (1997) (UV); (Mad96) Madau et al. (1996) (UV); (Lil96) Lilly et al. (1996) (UV); (Gal95) Gallego et al. (1995) (H α). . . .	179

Chapter 1

Introduction

1.1 Why study local star formation?

Two of the biggest topics in extragalactic astronomy today are the formation of galaxies and their evolution over the age of the Universe. The star formation histories of galaxies are fundamental in our understanding of both.

The current star formation rate (SFR) of a galaxy not only measures the birth of new stars, but, since stars are formed through gravitational instabilities in the inter-stellar medium (ISM), they can also be used to trace the gas and dust that make up this medium (Schmidt, 1959; Kennicutt, 1989).

Current models can combine cosmology, dark matter, gas and stars to make definite predictions for galaxies throughout the evolutionary timescale. These include predictions of current star formation rates (e.g. Kauffmann et al. 1993). The majority of previous observations of extragalactic star formation have been devoted to high-redshift galaxies and the evolution in the total star formation rate of the Universe as a function of cosmological look-back time (e.g. Madau et al. 1996, 1998; Glazebrook et al. 1999; Steidel et al. 1999; Hopkins et al. 2000; Lanzetta et al. 2002). The reason for this is due, at least partly, to the relative ease with which large, representative volumes of the Universe can be observed at

high redshift, whilst only a small area of sky is actually being investigated.

There are, therefore, still many gaps in our understanding of star formation in the local Universe and, for example, both the total rate of star formation and the types of galaxy which dominate are still poorly understood.

1.2 Using $H\alpha$ to study star formation

The $H\alpha$ luminosity observed in spiral and irregular galaxies is believed to be a consequence of the ionisation of the ISM by the ultraviolet (UV) radiation which is produced by young high-mass OB stars. When a free electron recombines with an ionised hydrogen atom and moves down through the different orbits, photons of specific wavelengths are emitted. An $H\alpha$ photon with a wavelength of 656.3 nm is emitted when an electron falls from the $n=3$ shell to the $n=2$ shell.

Evolutionary synthesis models are used to compute the conversion factor between the ionising flux and the SFR. Since only high mass ($>10 M_{\odot}$) and, therefore, short-lived (<20 Myr) stars contribute significantly to the integrated ionising flux (Kennicutt, 1998), the $H\alpha$ emission line thus provides a nearly instantaneous measure of the SFR, independent of the previous star formation history.

The two main advantages of using $H\alpha$ to detect star formation are the direct relationship between the nebular line emission and the massive SFR, and also the high sensitivity. A small telescope can map star formation down to low levels at high angular resolution, even in faint, low surface-brightness galaxies. Only relatively modest integration times (of order 1 hour per galaxy) are needed on a 1 m telescope, and this is an important consideration when trying to individually image a large sample of galaxies.

$H\alpha$ imaging of galaxies also has several limitations. $H\alpha$ emission is subject to large extinction effects, both within the host galaxy and our own. Whilst there are now well developed maps for use in correcting for Galactic extinction (Schlegel

et al., 1998), the corrections for internal extinction are still largely uncertain. A second drawback is the need to assume a stellar initial mass function (IMF) to extrapolate the total star-forming population from the measurements of the high-mass star formation rates. A further complication comes from the presence of the two [NII] emission lines at 654.8 nm and 658.4 nm either side of the $H\alpha$ line. In most cases, these will be included in observations through $H\alpha$ filters and will add a random scatter about the true $H\alpha$ flux. Again, the corrections for this contamination contain large uncertainties.

A final disadvantage is that the use of narrow-band $H\alpha$ filters prohibits the possibility of a large-area, comprehensive survey such as those of Sloan and the Infrared Astronomy Satellite (IRAS). The small recession velocity coverage of the filters means that a pre-existing galaxy catalogue is required to provide a target list for specific pointed observations of galaxies with measured redshifts through the appropriate $H\alpha$ filter.

1.3 Previous $H\alpha$ studies

Several large $H\alpha$ surveys of normal galaxies have already been completed. Three of the most relevant to this thesis - those of Kennicutt & Kent (1983), the Universidad Complutense de Madrid (UCM), and Young et al. (1996) - will be outlined here.

1.3.1 Kennicutt & Kent (1983)

Kennicutt and Kent combine the results of photometric and spectrophotometric surveys of ~ 200 nearby field and Virgo Cluster galaxies.

Long-slit spectrophotometric observations were made of 57 field galaxies selected from the Second Reference Catalogue of Bright Galaxies (RC2; de Vaucouleurs et al. 1976) with total blue-band apparent magnitudes $B_T < 12.5$, and covering a

range of morphological types. The high spectral resolution of this method enables the $H\alpha$ and [NII] lines to be resolved and, if desired, corrected for. The use of a long slit means that the spatial distribution of $H\alpha$ across the galaxy can be examined. The major disadvantage of spectrophotometric measurements is that the small entrance apertures only admit a fraction of the galactic light for all but the smallest galaxies. The slit was generally centred on the nucleus, and thus the fraction of light detected may not necessarily be representative of the integrated disk emission. Whilst equivalent widths (EWs) can be measured by this method, total line fluxes cannot.

The large-aperture photometric $H\alpha$ survey observed 175 field and Virgo Cluster galaxies, mostly spirals, selected from the Shapley-Ames catalogue (Sandage & Tammann, 1981) with UBV photometry available in RC2. This results in an effectively magnitude-limited sample, and hence intrinsically faint galaxies are undersampled. There is a 25 galaxy overlap between the two samples. The photometry is contaminated by the inclusion of [NII] in the bandpass of the filters used, but, unlike the spectrophotometric study, the aperture size is large enough to contain the entire galaxy disk.

Whilst the aperture photometry provides absolute line fluxes and equivalent widths, the spectrometer is better at detecting very low levels of star formation in early-type galaxies, and has the wavelength resolution to separate the $H\alpha$ emission, [NII], and $H\alpha$ absorption contribution to the total flux. Neither method is able to map the two-dimensional distribution of emission such that individual star formation regions can be identified across the galaxy disk.

The authors find that the integrated emission of a galaxy is strongly correlated with its Hubble type and colour. Later-type galaxies have larger $H\alpha + [\text{NII}]$ equivalent widths than early types, and bluer galaxies have higher emission values than redder galaxies. They also find that emission among galaxies of a given type varies greatly, and in most cases is due to real dispersion in star formation activity. This activity is only weakly correlated with galaxy luminosity.

Kennicutt (1983) uses the photometric data to investigate the SFR in normal disk galaxies. He finds total SFRs ranging from 0 to $20 M_{\odot}/\text{yr}$,

This work was subsequently built on to investigate the effects of interactions (Kennicutt et al., 1987) and to look at star formation histories (Kennicutt et al., 1994).

1.3.2 The Universidad Complutense de Madrid Survey

Large surveys using spectrometers or charge-coupled device (CCD) cameras can be very time consuming due to the small field of view that can be investigated at any one time. The Universidad Complutense de Madrid survey (Zamorano et al., 1994, 1996), however, uses a Schmidt telescope, a low-dispersion objective prism and photographic emulsion to search a wide field of sky for low-redshift emission-line galaxies (ELGs).

The UCM instrument set-up limits the survey to $z \lesssim 0.045$. Gallego et al. (1995) report the detection of 264 ELGs in an area covering 471.4 square degrees. More than half of the sample (138 objects) do not appear in any published catalogue.

Follow up imaging has been published in Vitores et al. (1996a) and Vitores et al. (1996b). In Vitores et al. (1996a), a Hubble type was attributed to each UCM galaxy. In Vitores et al. (1996b), the statistical properties of the sample were analysed. The UCM survey is shown to select objects fainter (in apparent magnitudes) than those of colour surveys, and in terms of absolute magnitudes, it also detects objects intrinsically fainter than those found by other selection techniques. The morphological distribution of the sample is dominated by late-type galaxies (66% being Sb or later) with $\sim 10\%$ presenting typical parameters of E-S0 types, and a further $\sim 10\%$ being irregulars. This result is a consequence of the UCM survey-selection technique - galaxies were selected by the presence of emission features. Nine blue compact-dwarf galaxy candidates were also detected.

Gallego et al. (1996) present follow up spectroscopy. This provides redshift in-

formation, plus optical reddening estimates, line fluxes and equivalent widths. Gallego et al. (1997) use these data to find that, in the Coma field, $H\alpha$ ELGs are considerably less clustered than the normal population. This indicates an environmental dependence of SFR on galaxy density.

Gil de Paz et al. (2000) use near-infrared J and K imaging of 67 UCM galaxies to identify two separate classes of star-forming galaxies in the sample. The first are low-luminosity, high-excitation galaxies (HII-like). The second are relatively luminous spiral galaxies (starburst disk-like). The HII-like galaxies show higher star formation rates per unit mass and lower stellar masses than the second class.

Since the sample was $H\alpha$ selected, Gallego et al. (1995) were able to use the UCM results to plot an estimated $H\alpha$ luminosity function for the local Universe. Integrating over all $H\alpha$ luminosities they determine the current SFR density of the local Universe to be $0.013 \pm 0.001 \text{ M}_{\odot} \text{ yr}^{-1} \text{ Mpc}^{-3}$ in star-forming galaxies with $\text{EW}(H\alpha + [\text{NII}]) > 1.0 \text{ nm}$ (for $H_0 = 50 \text{ kms}^{-1} \text{ Mpc}^{-1}$ and a Scalo IMF).

1.3.3 Young et al. (1996)

Young et al. carried out a major CCD imaging survey using a small (0.9 m) telescope. One hundred and twenty spiral galaxies were observed in $H\alpha$ and R in order to determine the distribution of star formation within the galaxies and the total continuum-subtracted $H\alpha$ flux of each one.

The galaxies were chosen from a sample of 300 observed as part of the Five College Radio Astronomy Observatory (FCRAO) Extragalactic CO Survey (Young et al., 1995). The parent sample covers a wide range of Hubble types (S0-Im), optical diameters (4-100 kpc), environment (pairs-clusters), and isolated and merging systems. It is neither complete in a flux-limited sense nor in a volume-limited sense, but was chosen to span a wide range of parameter space.

The 120 galaxies imaged in $H\alpha$ are weighted towards large, early-type spirals, with just 18 Scd-Sdm galaxies, and only 8 irregulars. A full range of environments is

covered, including 43 Virgo cluster members and 6 close pairs. Merger remnants and peculiar galaxies are also investigated.

The authors find a small, but significant, variation in the mean $H\alpha$ surface brightness for spiral galaxies along the Hubble sequence; the Sd-Irr galaxies exhibit a mean $H\alpha$ surface brightness 1.4 times higher than the Sbc-Scd galaxies, and 2-3 times higher than the Sa-Sb galaxies. They find that the mean efficiency of high-mass star formation (i.e. the rate of star formation per unit mass of molecular gas) in this sample of spiral galaxies shows little dependence on morphology for galaxies of types Sa to Scd, although there is a wide range in star formation efficiencies within each type. Galaxies in disturbed environments (i.e. strongly interacting systems) are found to have a mean star formation efficiency ~ 4 times higher than isolated spiral galaxies, uncorrected for extinction.

Koopmann et al. (2001) add to the Virgo observations to produce an atlas of $H\alpha$ and R images and radial profiles for 63 bright spiral galaxies in the cluster. They discover a population of Virgo galaxies with active star formation in circumnuclear regions, but no other disk star formation. They label these truncated star-forming disks ‘St’ galaxies. These will be discussed further in Section 7.2.

1.4 Other methods of calculating star formation rates

Early SFR measures were based on synthesis modeling of broadband colours. This method is still applied to multicolour observations of faint galaxies, though nowadays, most information on the star formation properties of galaxies comes from the integrated light measurements in the ultraviolet, far-infrared (FIR), nebular recombination lines (including $H\alpha$), or from radio-continuum measurements.

1.4.1 Integrated colours and spectra; synthesis modeling

Very faint or high-redshift galaxies cannot always be resolved from the ground. Virtually the only source of information on the stellar populations of these galaxies comes from their integrated spectra or colours. Kennicutt (1992) has compiled a reference library of spectra for galaxies of different types and shown that the integrated galaxy spectra for different Hubble types show different features (see Figure 2 of Kennicutt 1992).

Whilst the spectra contain contributions from a full range of stellar types, the visible wavelengths are dominated by the intermediate main-sequence stars (A to early F) and G-K giants. The integrated colours and spectra of normal galaxies will, therefore, provide information on the ratio of young (<1 Gyr) to old (3-15 Gyr) stars in the galaxy. The observed colours can hence be used to estimate the mean SFR over the past 10^8 - 10^9 years.

To relate the observed quantities in any of the measurement techniques described here to the SFR of a galaxy, a synthesis model is required. This uses stellar-evolution tracks, combined with stellar-atmosphere models or spectral libraries to derive the broadband luminosities or spectra for various stellar masses as a function of time. The individual templates are weighted using the IMF and combined to synthesise the spectrum or colours of a galaxy with an arbitrary star formation history. The most commonly used models for star-forming galaxies include those of Bruzual & Charlot (1993), Bertelli et al. (1994), and Fioc & Rocca-Volmerange (1997).

The synthesis model provides a relation between the SFR per unit mass or luminosity and the integrated colour of the population.

The disadvantages of using integrated colours to derive SFRs are that they are relatively imprecise and prone to systematic errors. The main sources of these errors are due to reddening, or an incorrect IMF, age or metallicity assumed for the star formation region (Larson & Tinsley, 1978). The method is still useful

for comparing the average star-forming properties of a large sample of galaxies where absolute accuracy is not required.

1.4.2 Ultraviolet continuum

At UV wavelengths, the integrated spectrum is dominated by hot, young stars. Thus, SFR will scale approximately linearly with luminosity between 125 and 250 nm. This wavelength range falls longward of the Ly α forest, but short of the wavelengths where contamination from older stellar populations becomes significant (Kennicutt, 1998). This region can only be observed from the ground in the redshifted spectra of distant galaxies at $z \sim 1-5$ (see e.g. Steidel et al. 1999).

Local galaxies can be studied using balloon, rocket, and space experiments (see e.g. Bell & Kennicutt 2001). The GALaxy Evolution EXplorer (GALEX) satellite, due to be launched shortly, is a NASA UV imaging and spectroscopic survey mission designed to map the global history and probe the causes of star formation and its evolution over the redshift range $0 < z < 2$ (Bianchi & the GALEX Team, 1999).

Synthesis models are again used to convert UV flux over a given wavelength interval into SFR (see e.g. Madau et al. 1998).

The primary advantage of using UV is the direct relationship with the photospheric emission of the young stellar population. This method can also be applied to star-forming galaxies over a wide range of redshifts, and thus used to investigate the cosmological evolution of SFR with lookback time (Madau et al., 1996, 1998).

The main disadvantage is that UV is very sensitive to extinction, with typical corrections between 0 and 3 magnitudes (mag) (Buat, 1992; Buat & Xu, 1996). This method is also sensitive to the form of the IMF used since the integrated spectrum in the 150-250 nm range is dominated by stars with masses above $5 M_{\odot}$. To determine the total SFR of the galaxy therefore requires a large extrapolation

to lower stellar masses.

1.4.3 Far-infrared continuum

Inter-stellar dust within galaxies is heated by the absorption of a large fraction of the bolometric luminosity emitted by the stars, particularly the UV emission from the hot, young population. The absorbed radiation is re-emitted in the thermal infrared (IR) at wavelengths of roughly 10-300 μm . Thus, the FIR emission from a galaxy can be used to trace star formation. IRAS was launched in 1983 and has provided FIR fluxes for over 30,000 galaxies (Moshir et al., 1992).

The optical depth of the dust in the galaxy and the exact contribution of the young stars to its heating both determine the extent to which the FIR can be used to detect star formation. The situation is complicated and can vary, not just between galaxies, but also between the disk and the circumnuclear regions of a normal spiral galaxy. The relation between global FIR emission and the SFR of a galaxy has caused much controversy. This topic will be explored in Chapter 6.

A good correlation has been found, however, between the FIR luminosity of late-type star-forming galaxies (where young stars are expected to dominate the dust heating) and other star formation tracers such as the UV continuum and the $\text{H}\alpha$ emission (see e.g. Sauvage & Thuan 1992; Buat & Xu 1996). For early-type galaxies, the UV and $\text{H}\alpha$ emissions are found to be low compared to the FIR luminosity.

As well as the ambiguities surrounding the calibration of FIR luminosity to SFR, another problem is, again, the sensitivity to the IMF. On the other hand, FIR observations suffer very little from extinction effects and are also considered the ultimate SFR tracer in dense, dusty circumnuclear starbursts where the young stars dominate the radiation field throughout the UV-visible and the dust opacity is high.

1.4.4 Recombination lines

As well as measurements of the $H\alpha$ line, other recombination lines, including $H\beta$, $P\alpha$, $P\beta$, $Br\alpha$, and $Br\gamma$ have been used to probe the young, massive stellar population. These nebular lines are produced in a similar way to the $H\alpha$ line, and thus provide a direct probe of the young stellar population.

The choice of stellar evolution and atmospheric models used to find the relationship between the ionising flux and the SFR results in a variation of $\sim 30\%$ in the published calibrations (see e.g. Kennicutt 1983; Gallagher et al. 1984; Kennicutt et al. 1994; Leitherer & Heckman 1995; Madau et al. 1998).

The most important source of systematic error in $H\alpha$ derived fluxes is extinction. This is particularly strong in the dense HII regions in circumnuclear starbursts. The near-IR Paschen or Brackett recombination lines can be used to reliably measure the SFR in these regions (see e.g. Puxley et al. 1990; Ho et al. 1990; Calzetti et al. 1996). However, these lines are typically 1-2 orders of magnitude weaker than $H\alpha$, and can be very hard to detect for all but the highest surface-brightness HII regions.

Higher-order recombination lines, such as the $n = 54 \rightarrow 53$ transition of atomic hydrogen ($H53\alpha$) (Puxley et al., 1989) can also be used to investigate star formation by following the same method.

Forbidden lines

For distances beyond $z \sim 0.5$, the $H\alpha$ emission line is redshifted out of the visible window. A bluer emission line is therefore desirable to trace star formation in more distant galaxies. The $H\beta$ and the higher-order Balmer emission lines are strongly influenced by stellar absorption and too weak to be used to quantify SFR.

The $[OII]\lambda 3727$ forbidden-line doublet is the strongest feature in the blue. Forbidden-line luminosities are not directly correlated to the ionising UV flux from the young

stars and are also sensitive to the abundance and ionisation state of the gas. Since the excitation of [OII] is sufficiently well behaved, however, it can be calibrated empirically using $H\alpha$ and used as a quantitative measure of the SFR of a galaxy. [OII] emission has been used to investigate several large samples of faint galaxies out to redshifts of ~ 1.6 (Kennicutt, 1992; Cowie et al., 1996; Ellis, 1997).

The [OII] fluxes must be corrected for extinction, remembering that the $H\alpha$ measurements used for calibration will also be affected. The variation of the mean [OII]/ $H\alpha$ ratios in individual galaxies will lessen the precision of the derived SFRs. The forbidden line fluxes, however, are useful for looking at the large-scale, star-forming properties in samples of distant galaxies and can also be used as a consistency check on SFRs derived in other ways.

1.4.5 Radio-continuum measurements

Condon (1992) has shown that there is a tight correlation between the FIR luminosity of a galaxy and the 1.4 GHz radio power. The 1.4 GHz radio-continuum emission is believed to be mainly due to synchrotron radiation produced by relativistic electrons accelerated by supernovae (Biermann, 1976; Kirk et al., 1994). The implication is that both the FIR and the radio-continuum emission from a galaxy are consequences of ongoing massive-star formation.

Decimetric radiation does not suffer significant extinction. It does, however, rely on the hypothesis that the radio luminosity is directly proportional to the supernova rate. The correlation with FIR supports this, though comparisons with $H\alpha$ and U-band predictions (see below) might be seen as evidence against it (Cram et al., 1998).

Radio selection of candidate galaxies will preferentially reveal objects with high rates of current star formation. There is a potential problem that the 1.4 GHz luminosities might be contaminated by radio emission arising from a nuclear 'engine', rather than star formation. These are generally found in bright elliptical

galaxies, often with red colours, however, whereas star formation investigations generally tend to focus on spiral or blue-peculiar galaxies. Optical observations can be used to confirm that the galaxy is not host to one of these nuclear ‘monsters’.

1.4.6 Comparisons of different methods of measuring SFR

Cram et al. (1998) have made an empirical check of the utility of several different measures of current SFRs in galaxies using a sample of nearby galaxies for which the radio-flux density and several other indicators were available. They plot values of SFR from radio power against SFR from $60\ \mu\text{m}$ FIR luminosities, $\text{H}\alpha$ luminosities and U-band ultraviolet magnitude (see Figure 1.1). They have adopted consistent initial mass functions, models for the time-dependence of the SFR, and models of stellar-population evolution.

The plots indicate that there is a broad agreement between the various SFR indicators. The tightness of the radio/FIR correlation over more than 4 orders of magnitude is well demonstrated here.

The radio versus $\text{H}\alpha$ plot shows substantially more scatter. Estimates of the SFR from $\text{H}\alpha$ data tend to lie about a factor of 10 above the trend defined by the $1.4\ \text{GHz}/60\ \mu\text{m}$ estimates when $\text{SFR} \lesssim 0.1\ \text{M}_{\odot}\text{yr}^{-1}$, and about a factor of 10 below the trend when $\text{SFR} \gtrsim 20\ \text{M}_{\odot}\text{yr}^{-1}$. This can also be seen in Figure 8 of Young et al. (1996) and Figure 1 of Devereux & Young (1990). The deviation at low values of SFR is related, in part, to the difficulty in determining the zero-point level for $\text{H}\alpha$ emission from HII regions in the presence of stellar $\text{H}\alpha$ absorption. The escape of cosmic rays from galaxies with weak star formation (Condon et al., 1991) could also cause an underestimate of the SFRs based on the radio luminosities.

At high luminosities, the offset and the scatter could be caused by the large amount of extinction in those objects undergoing the most vigorous star forma-

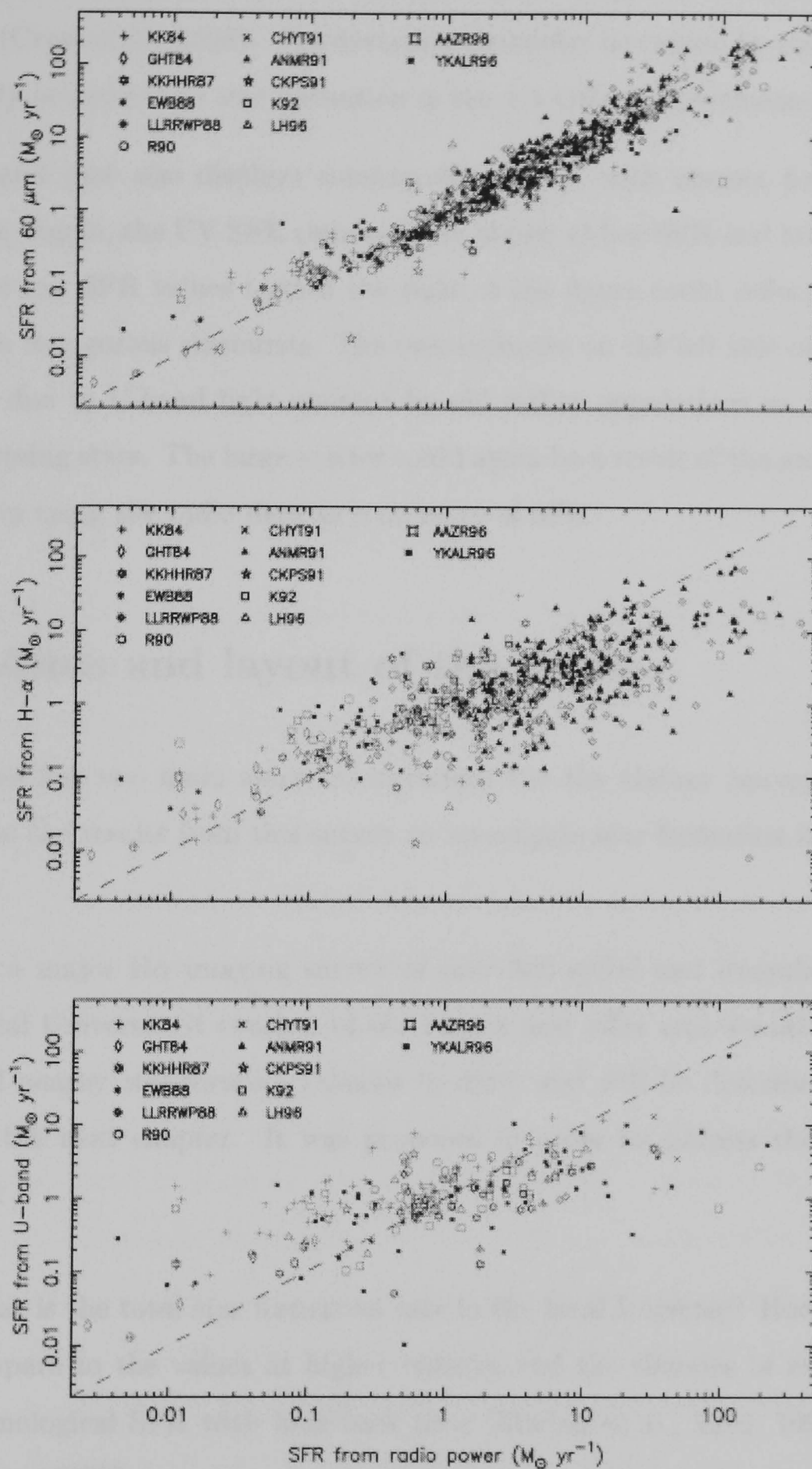


Figure 1.1: From Cram et al. (1998). Comparison of SFRs deduced from 1.4 GHz luminosities (horizontal axis) with the rates deduced using the other luminosities indicated. Symbols are coded by the initials of the authors' last names and the year of publication (see Cram et al. 1998).

tion, from the absorption of the Lyman photons by dust, or from uncertainties in the IMF (Cram et al., 1998). The deviation could also be caused by contributions incorrectly accredited to star formation in the 1.4 GHz measurements.

The U-band plot also displays considerable scatter with respect to the radio estimates. Again, the UV SFR estimates are higher at low SFR and lower at high SFR. The low SFR values toward the right of the figure could reflect enhanced extinction in vigorous starbursts. The over-estimate on the left side of the figure could be due to U-band light emitted by old stellar populations as well as the newly-forming stars. The large scatter could again be a result of the uncertainties inherent in using the radio data as a measure of SFR.

1.5 Aims and layout of the thesis

This thesis has two main aims: to introduce the H α Galaxy Survey (H α GS), and to use the results from this survey to investigate star formation in the local Universe.

H α GS is a major H α imaging survey of over 300 spiral and irregular galaxies in the local Universe. It consists of the largest and most representative optical sample of nearby star-forming galaxies to date, and will be described in more detail in the next chapter. It was proposed in order to address the following questions:

- What is the total star formation rate in the local Universe? How does this compare to the values at higher redshift and the theories of evolution of cosmological SFR with look-back time (Madau et al., 1996, 1998; Steidel et al., 1999)?
- Which galaxy types and morphologies dominate? What fraction of the total star formation locally can be found in faint, dwarf galaxies, compared to large, bright spirals?

- Does nuclear activity (star formation or active galactic nuclei (AGN)) depend on galaxy properties and environment?
- What is the star formation distribution within galaxies? Can density wave theory explain the distribution? Where does star formation occur with respect to the bulge, bar and disk, spiral arms and rings?
- How does environment (groups, clusters, interacting pairs, mergers, etc.) affect star formation rate and distribution?

The following chapters will attempt to answer many, but not all, of these questions. The remainder will be left as further work.

In this chapter we have looked at some of the motivation for studying local star formation, discussed the different techniques by which this may be done, and summarised three of the main previous studies. In Chapter 2, the H α Galaxy Survey will be presented in detail, along with the selection criteria and details of the resulting observed sample. Chapter 3 will outline the observational technique and the data-reduction process. In Chapter 4, some of the main non-astrophysical sources of error involved in calculating H α SFRs will be investigated. Chapter 5 will focus on the two main astrophysical sources of uncertainty which have already been mentioned in this chapter: extinction and [NII] contamination. FIR SFRs will be calculated using IRAS fluxes in Chapter 6. These will be compared with the overlapping results from our H α study. In Chapter 7, some of the questions concerning star formation distribution will be tackled. Concentration indices will be used to look at large-scale distributions of young and old stellar populations. An examination of the distribution of star formation in strongly-interacting and highly-disturbed galaxies will be included, as will an investigation into the relation between nuclear bars and the star formation associated with them. Chapter 8 will deal with star formation dependencies, in particular, on morphology, environment and galaxy luminosity. In Chapter 9, the total SFR of the local Universe will be calculated and compared to higher-redshift results. The contributions from different types of galaxy to this value will be derived. Chapter 10 will summarise

the findings and conclusions of this thesis, as well as describing related studies currently in progress, and providing suggestions for future work.

In the remainder of this work, unless otherwise specified, $H\alpha$ fluxes, EWs and surface brightnesses are taken to include the [NII] doublet contribution. A Hubble constant of $75 \text{ kms}^{-1}\text{Mpc}^{-1}$ is used throughout.

Chapter 2

The H α Galaxy Survey

The H α Galaxy Survey is the largest and most comprehensive optical study of star formation in the local Universe to date. The 1.0 m Jacobus Kapteyn Telescope (JKT), part of the Isaac Newton Group (ING) of telescopes situated on La Palma in the Canary Islands, was used in conjunction with redshifted H α filters and the Harris R-band filter to determine the quantity and spatial distribution of ionised gas in 334 spiral and irregular galaxies within $30 h^{-1}$ Mpc.

2.1 Sample selection criteria

The H α GS sample was selected using the Uppsala Galaxy Catalogue (UGC; Nilsson 1973) as the parent catalogue. The UGC contains essentially all galaxies to a limiting diameter of 1.0' and/or to a limiting apparent magnitude of 14.5 on the blue prints of the Palomar Observatory Sky Survey (POSS). It was chosen for its inclusion of all Hubble types (including relatively low-surface-brightness dwarf galaxies) and because it provides full northern-sky coverage (all declinations $> -2.5^\circ$). The galaxies are ordered by 1950 Right Ascension.

85% of all UGC galaxies now have measured recession velocities, which are essential for calculating the redshifted wavelength of the H α line. The remaining 15%.

therefore, cannot be selected for our study. This represents a possible source of bias which should be kept in mind when interpreting the results.

Selection from the UGC was performed using the NASA/IPAC Extragalactic Database (NED)¹ ‘Advanced All-Sky Search For Objects By Parameters’ facility. The galaxies were grouped into 5 recession velocity shells: 0-1000 kms^{-1} , 1000-1500 kms^{-1} , 1500-2000 kms^{-1} , 2000-2500 kms^{-1} , and 2500-3000 kms^{-1} . Only galaxies with D_{25} diameters in the range 1.7-6.0' were selected. The upper limit ensured that all galaxies would fit on the JKT CCD field. The different shells effectively sample different parts of the galaxy diameter function. The central shell is dominated by the low-luminosity dwarf Im and Sm galaxies, but excludes the intrinsically-larger galaxies that exceed the upper- D_{25} limit at the lowest redshifts. These, rarer, S0/a-Sc galaxies are sampled more thoroughly in the outer shells, whilst the faint, dwarf galaxies fall below the observational detection threshold at larger distances.

Only spiral and irregular galaxies, with Hubble types from S0/a to Im inclusive, were chosen. Early-type galaxies (E-S0) were demonstrated by Kennicutt & Kent (1983) to show virtually no detectable star formation at all. The spectra for these galaxies, shown in Figure 2 of Kennicutt (1992) are dominated by absorption features, with no sign of $\text{H}\alpha$ emission. Given this evidence, and the fact that early type galaxies are known to be gas poor and, therefore, unable to generate new stars, there is little point in trying to observe star formation through $\text{H}\alpha$ observations of ellipticals and S0 galaxies.

If a dust-filled disk galaxy is viewed in an edge-on orientation, the flux emitted from stars and HII regions typically has to pass through a longer column of the galaxy's dusty ISM to reach us (Binney & Merrifield, 1998). The light is then more likely to be absorbed or scattered out of the line of sight before reaching the telescope, and we are likely to drastically underestimate the SFR of the galaxy. To prevent observations of highly-inclined galaxies, a selection criterion

¹<http://nedwww.ipac.caltech.edu/>

was, therefore, added to ensure that the major-to-minor axis ratio of all spiral galaxies was less than, or equal to 4.0.

The final selection criterion was to only select galaxies situated more than 20° in Galactic latitude away from the plane of the Galaxy. This was to avoid contamination of the observations by large numbers of foreground stars, and excessive Galactic extinction.

The result of these selection criteria was a pre-observation sample containing 233 galaxies in the first redshift bin ($0-1000 \text{ km s}^{-1}$), 203 in the 2nd, 169 in the third, 128 in the 4th and 102 in the final bin ($2500-3000 \text{ km s}^{-1}$), giving a total sample size of 835 galaxies.

Whilst the parent catalogue was the UGC, it should be noted that all galaxy details (classification, recession velocity, major- and minor-axis diameters) used in the selection are those quoted by NED. The majority of these values come from the Third Reference Catalogue of Bright Galaxies (RC3; de Vaucouleurs et al. 1991).

2.2 Statistics on the main observing time

The H α Galaxy Survey was originally awarded 98 nights of observing time on the JKT. This was rounded up to 100 after 2 extra nights were added as ‘payback’ for overrides by other projects. This time was distributed in approximately 7-12 night blocks between February 2000 and January 2002. No less than 10 members of the H α GS consortium assisted with the observations.

Of these 100 nights, 78 produced usable data for the project. The remaining 22 were weathered out completely. Fifty-two of the nights were considered photometric after examination of standard stars and comments logged by the observer on the night.

2.3 The final observed sample

A total of 313 galaxies were observed which strictly obeyed the selection criteria in Section 2.1. In addition 5 extra UGC galaxies were observed below the D_{25} limit. Two of these were ‘bonus’ galaxies which happened to be in the field of view of a sample galaxy and the other 3 were observed as a result of an earlier lower limit of $1.5'$. Two galaxies with $D_{25} > 6.0'$ were observed - one as a bonus galaxy. The other exceeded the size limit only after an update on NED. Three galaxies which exceeded the inclination limit were also observed, 1 bonus and 2 due to human error in the preparation of the selection sample. The latter was also responsible for the observations of 4 galaxies situated too close to the Galactic plane. Finally, a further 7 non-UGC galaxies were all observed as bonuses in the fields of other galaxies. Six of these fell below the $D_{25} > 1.7'$ criterion.

The grand total of observed galaxies is 334. All 334 galaxies were fully reduced to produce SFRs and $H\alpha$ equivalent widths (see Chapter 3).

In Figure 2.1 the morphological makeup of both the parent sample (empty histograms) and the observed sample (filled histograms) is shown. The x-axes display the galaxies’ T-types (where T is as defined in RC3, Volume I, de Vaucouleurs et al. 1991, such that T=0 represents an S0/a galaxy, T=1 is an Sa galaxy, and so on up to T=10 for Im classifications). The first 5 plots show the breakdown for each redshift shell. The final plot combines the data for the entire sample. The predominance of the Sm (T=9) and Im galaxies at low redshift can clearly be seen, as can the emergence of the Sc (T=5) class as the dominant detectable galaxy type at higher redshifts. The final plot in Figure 2.1 shows that these Sc galaxies have been undersampled in the observations. Account of this bias will be taken when the total star formation rate of the local Universe is calculated in Chapter 9.

Figure 2.2 shows the distribution of galaxy diameters in the original sample (empty histograms) and the observed sample (filled histograms). These diameters represent the intrinsic sizes of the galaxies in kpc. They are converted from

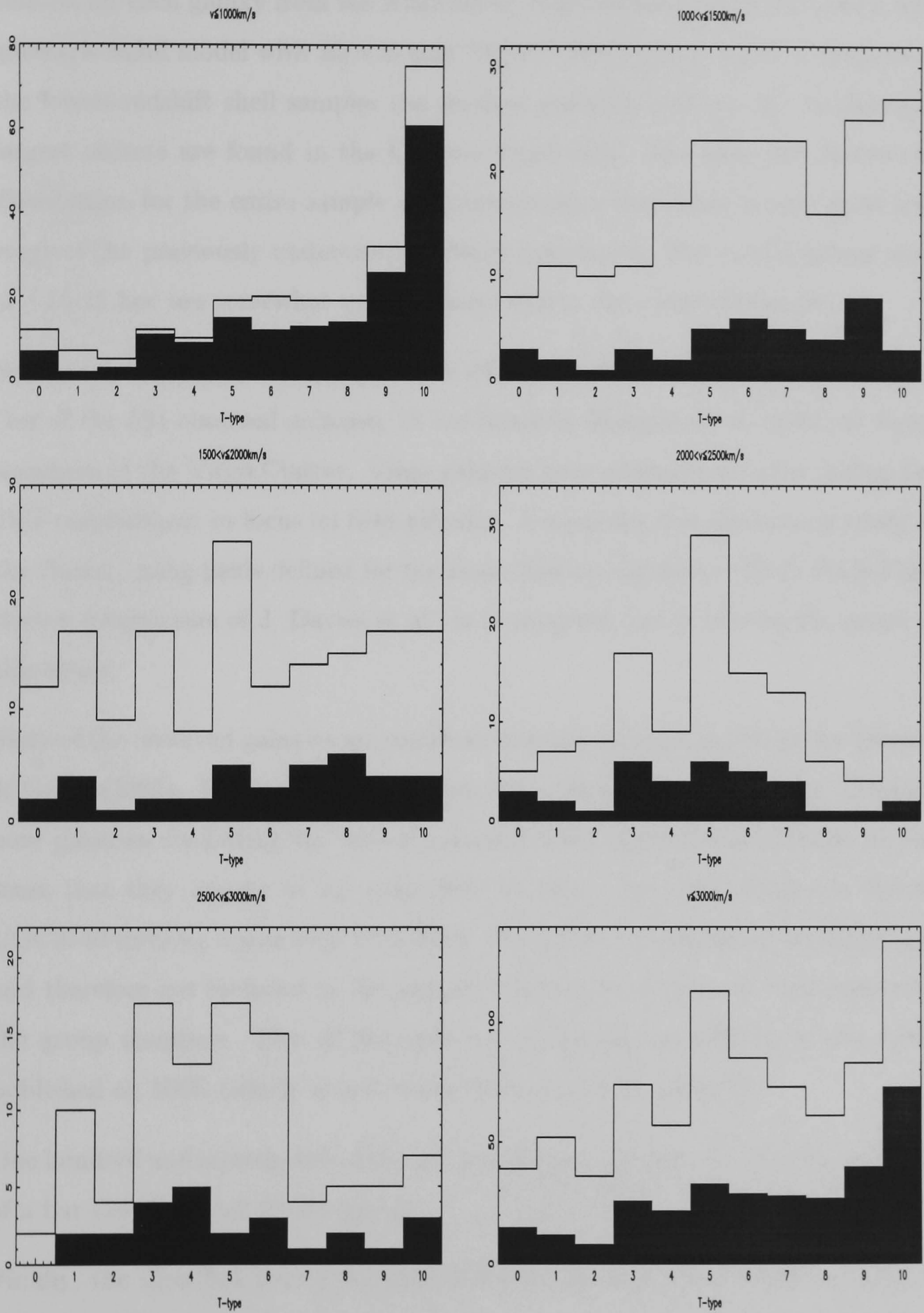


Figure 2.1: The morphological make up of the original sample (empty histograms) and the observed sample (filled histograms).

the D_{25} major axis values quoted on NED (in arcminutes), using distances calculated for each galaxy from the NED heliocentric recession velocities and a Virgo-centric infall model with $H_0=75 \text{ kms}^{-1}\text{Mpc}^{-1}$ (see Section 3.11). As expected, the lowest-redshift shell samples the smallest galaxies, whereas the intrinsically largest objects are found in the higher-redshift bins. The final plot shows the distribution for the entire sample and demonstrates that there is very good coverage of the previously undersampled dwarf population. The modal galaxy sizes of $\sim 15\text{-}25 \text{ kpc}$ are somewhat under-represented in the observed sample.

Sections 7.2 and 8.3 will investigate the effects of environment on star formation. Out of the 334 observed galaxies, 15 are listed by Binggeli et al. (1985) as being members of the Virgo Cluster. Virgo galaxies were generally avoided during the JKT observations to focus on field galaxies. A separate, complementary study of the cluster, using fields defined for the Isaac Newton Telescope (INT) Wide Field Survey programme of J. Davies et al., is in progress, but is beyond the scope of this thesis.

Sixty of the observed galaxies are members of galaxy groups, as defined by Huchra & Geller (1982). This includes an overlap of 7 with the Virgo members. Twenty-nine galaxies (including the bonus galaxies) form optically-close pairs, in the sense that they appear in the same field of view. The odd number is due to UGC3740 forming a pair with UGC3798. The latter is classified as an S0 galaxy, and therefore not included in the sample. There is an overlap of 7 galaxies with the group members. Five of the pairs are interacting as defined by the notes published on NED (which in turn come from the UGC and RC2).

One hundred and seventy-five of the 334 galaxies are classified as showing evidence of a bar (76 SAB and 99 SB types).

Finally, the distributions of absolute R-band magnitudes are shown in Figure 2.3 for the observed galaxy sample. These magnitudes are calculated from the measured R-band fluxes (see Section 3.6) and using the distances calculated for each galaxy in Section 3.11. As expected, only intrinsically-bright galaxies are

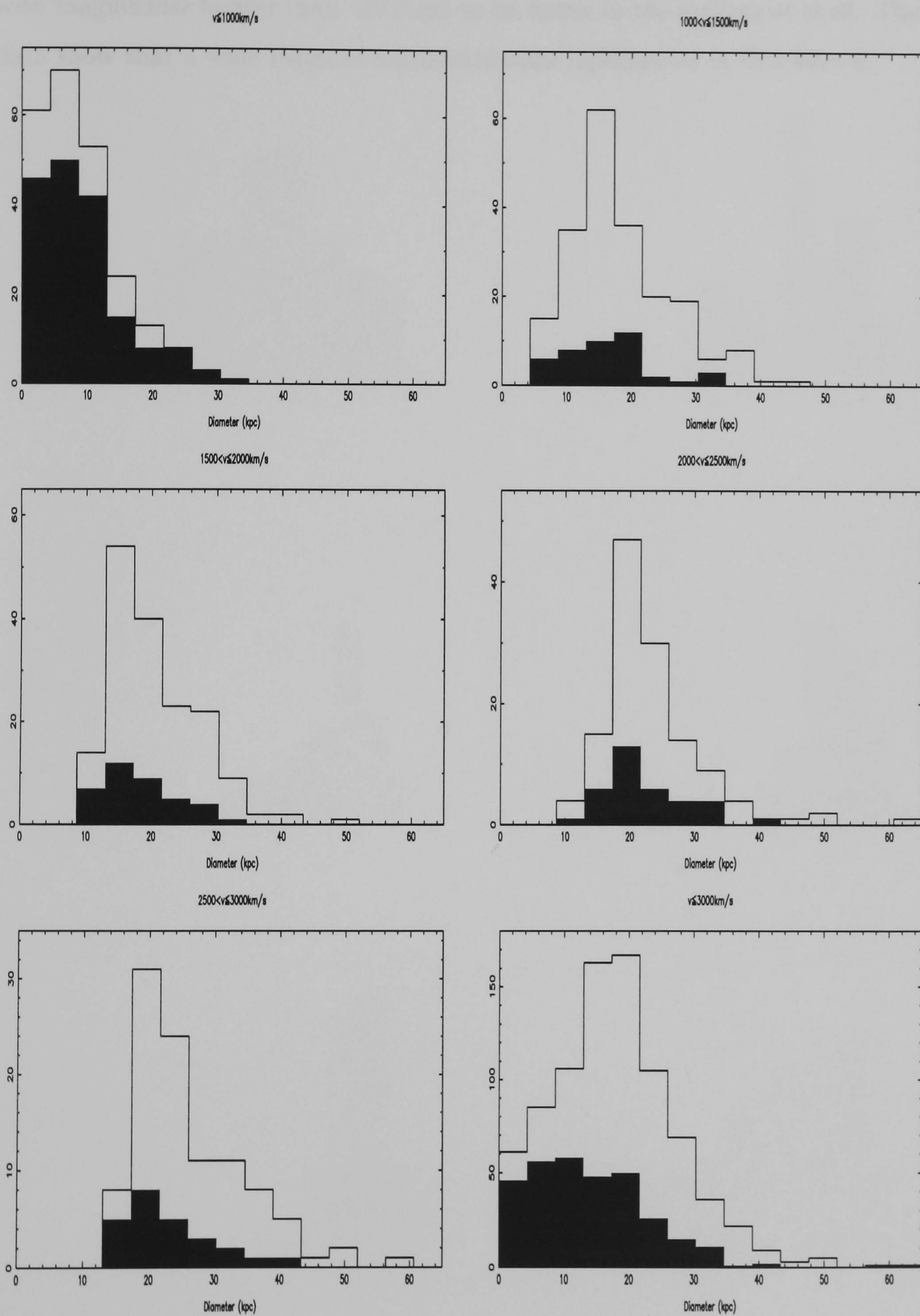


Figure 2.2: The distribution of galaxy diameters in the original sample (empty histograms) and the observed sample (filled histograms).

detected in the high-redshift bins. The vast majority of the observed galaxies with magnitudes fainter than -17.5 are to be found in the innermost shell. These data show that a wide range of luminosities are represented in this survey.

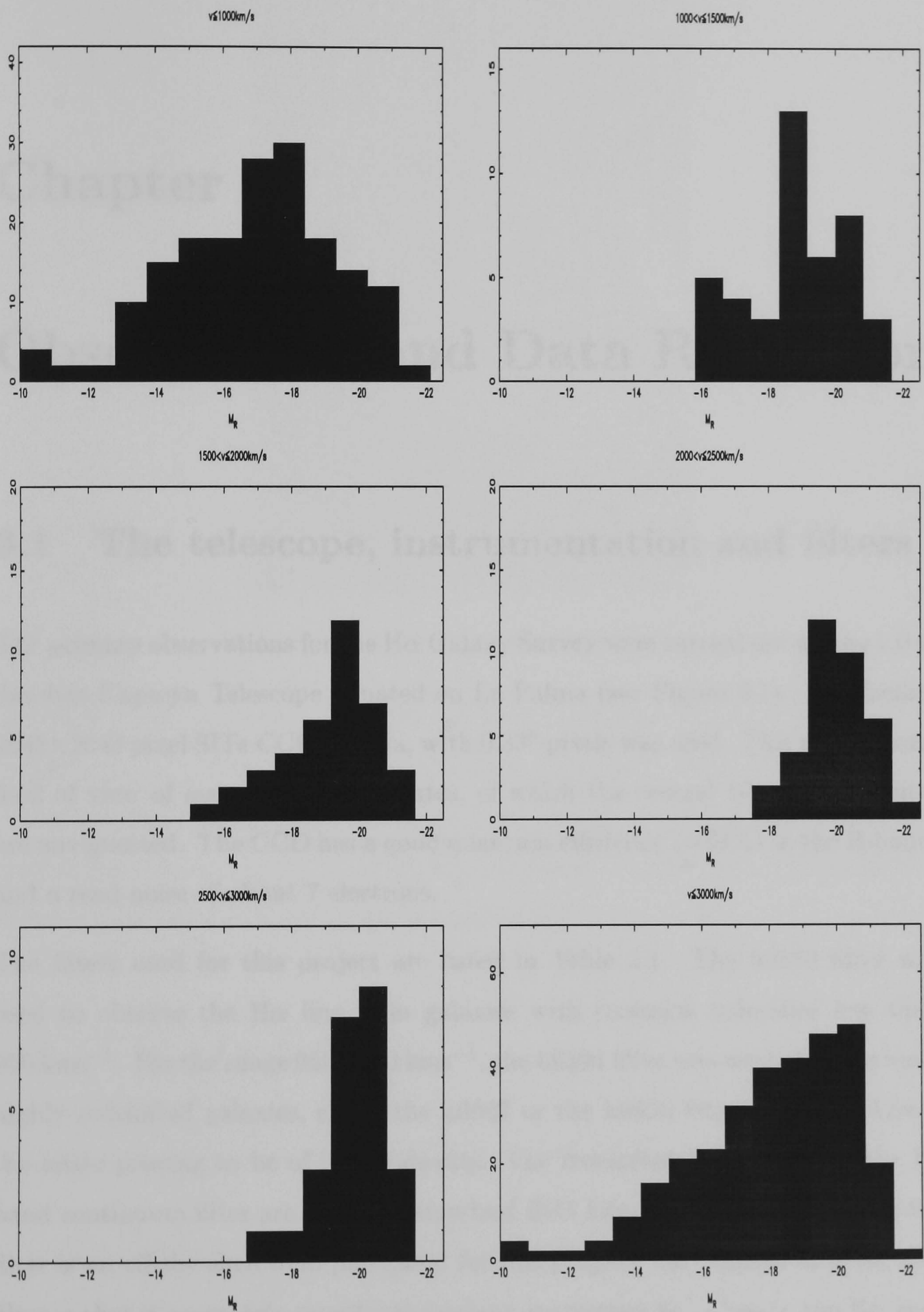


Figure 2.3: The distribution of total R-band absolute magnitude for the observed galaxies.

Chapter 3

Observations and Data Reduction

3.1 The telescope, instrumentation and filters

The primary observations for the H α Galaxy Survey were carried out on the 1.0 m Jacobus Kapteyn Telescope situated on La Palma (see Figure 3.1). The facility 2048 \times 2048 pixel SITe CCD camera, with 0.33'' pixels was used. This gives a total field of view of over 11 \times 11 arcminutes, of which the central 10 \times 10 arcminutes are unvignetted. The CCD has a good quantum efficiency (>60%) in the R-band, and a read noise of about 7 electrons.

The filters used for this project are listed in Table 3.1. The h6570 filter was used to observe the H α line from galaxies with recession velocities less than 950 kms $^{-1}$. For the range 950-2150 kms $^{-1}$, the h6594 filter was used. For the most highly redshifted galaxies, either the h6607 or the h6626 filters were employed, the latter proving to be of better quality. The redshifted H α filters and the R-band continuum filter are from the standard ING filter set, whereas the H α Cont filter is an off-the-shelf item purchased for this project. The benefit of using this filter is that it accurately samples the galaxy continuum flux close to the H α line, but has a broader bandpass than the narrow H α filters, thus reducing the time overhead in taking continuum observations compared with using ‘off-line’ narrow



Figure 3.1: The Jacobus Kapteyn Telescope

H α filters. The bandpass of the H α Cont filter is narrower than the R-band filter, giving it an advantage when observing during bright-sky conditions (moonlight or dark twilight). For fully-dark skies, however, the R filter provides excellent continuum subtraction for much shorter exposure times. The H α Cont filter is, therefore, not necessary under these conditions.

3.2 The observations

The raw data returned from the telescope comprised of:

- **Bias frames** - ideally taken at the start and end of every night.
- **Sky flats** - ideally taken during astronomical twilight at the start and end of every night. A minimum of three non-saturated exposures of blank fields in each filter used were required.

Filter name	Central wavelength (nm)	Passband width (nm)
Harris R (R)	637.3	149.1
H α 6570 (h6570)	657.0	5.5
H α 6594 (h6594)	659.4	4.4
H α 6607 (h6607)	660.7	5.0
H α 6626 (h6626)	662.6	4.4
H α Cont (C)	647.1	11.5

Table 3.1: The H α and continuum filters used during the H α Galaxy Survey. The name in brackets indicates the abbreviation by which each filter will be referred to throughout the rest of this work.

- **Photometric standards** - ideally taken throughout the night in the R-band filter to monitor the photometric conditions.
- **Spectrophotometric standards** - ideally taken at the start and end of each night.
- **Galaxy images** - one 300 s exposure through the broadband Harris R-continuum filter, three 1200 s exposures through the appropriate redshifted H α filter and, during bright-sky conditions, three 600s exposures through the H α Cont filter.

3.3 Data reduction

The majority of the data reduction was performed using the *Starlink* package *CCDPACK* with the rest making use of the *Starlink* *KAPPA* and *FIGARO* packages. The relevant commands were assembled in a set of executable scripts. This enabled the time spent on data reduction to be reduced as well as ensuring that the data were treated in an objective and reproducible way.

For each night's data, a master bias frame was created from a weighted median of all the bias frames taken on that night. This master bias was created with a mean value of zero, and was then used, in conjunction with the bias strips on each frame, to debias these frames. In some cases, objects had been observed

with the CCD windowed to improve readout time. These images mostly did not include bias strips. In these instances, a subset was produced of each of the individual bias frames so as to include the same region of the chip readout as found in the object images. These were combined without setting the mean to zero and subtracted directly from the object images.

Flatfield frames were created by taking a weighted median of all the sky-flat frames taken through each filter in a night. The gamma factor (the number of standard deviations by which a value has to deviate from the local mean before it is considered to be in error) was set to a value of 10. Aberrant pixels were removed. For images observed with a windowed CCD, separate flatfield frames were produced from the appropriate subsets of the sky-flat frames.

Each galaxy and standard star image was flatfielded using the appropriate flatfield frame. In cases where usable sky flat frames had not been obtained on a particular night, most often due to poor weather conditions at twilight, the flatfield frames from the nearest available night were used.

The debiased, flatfielded frames for each galaxy were then registered through an object-detection algorithm in *CCDPACK*. A linear transformation was performed on the frames to improve alignment. The multiple galaxy exposures taken through the redshifted H α filters and the H α Cont filter were mosaiced into one image. This improves signal-to-noise and also removes contamination by cosmic rays.

The galaxy and standard star images were all normalised to 1 s. The galaxy continuum images were also scaled relative to the appropriate H α -filter widths. The scaling factors were calculated from the comparisons of either unsaturated foreground stars, or standard stars through the different filters. The values were compared with those found by integrating under the filter profiles supplied by the ING (see Section 4.4).

The scaled continuum images were subtracted from the H α -filter images to yield the continuum-free H α emission. Slight adjustments to the alignments of the continuum and H α -filter images were made by hand to obtain the best results.

3.4 Photometric calibration using standard stars

Aperture photometry for photometric standard stars was performed using the *Starlink GAIA* package. A circular aperture with a radius of 20 pixels was placed around each photometric R-band standard. The sky background was subtracted using values, either from an annular region around the star, or from a circular region nearby if the former was not practical. The instrumental magnitude, m_i , for a star with k sky-subtracted counts per second is given by:

$$m_i = -2.5 \log k \quad (3.1)$$

For each star, this instrumental magnitude was then compared, either with the catalogued magnitude, m_c from Landolt (1992), or, for stars not included in the catalogue, with a value derived from a night that included Landolt standards and/or previously calibrated stars. The zeropoint, Z , for a given star is calculated using the equation:

$$Z = m_c - m_i - 0.08(AM - 1.0) \quad (3.2)$$

The last part of this equation corrects for the airmass, AM , of the star (see Section 5.2). An attempt was made to calculate the airmass coefficient using the data provided by the standard stars observed during the Survey. Plots of $(m_c - m_i)$ against airmass failed, however, to provide a clear correlation due to the narrow range of airmasses investigated. The plots were consistent, though, with the value of 0.08 mag/airmass that is quoted by the ING website ¹ for the central wavelength of our R-band filter.

The mean value of Z for all the photometric standards on a given night is taken as the zeropoint for that night.

¹<http://www.ing.iac.es/>

3.5 Photometric calibration of galaxy images taken on non-photometric nights

For observations taken on non-photometric nights, a further R-band image was subsequently taken for each galaxy during a night in which the conditions were considered to be photometric. These R-band images were reduced and scaled to the relevant H α -filter width.

Ten stars were selected from the vicinity of the galaxy. Aperture photometry was performed on these stars to yield the number of counts detected per second from each star in both the photometric and non-photometric observations. Employing Equations 3.1 and 3.2, and using the fact that the stars' catalogued magnitudes remain the same for both the photometric and non-photometric measurements, we calculated a zeropoint, Z_{np} , for each non-photometric image:

$$Z_{np} = 2.5 \log(k_{np}/k_p) + Z_p + 0.08(AM_p - AM_{np}). \quad (3.3)$$

Z_p is the zeropoint for the night on which the photometric image was observed, AM_p and AM_{np} are the airmasses for the photometric and non-photometric observations respectively, and k_{np}/k_p is the mean ratio of the counts per second for the 10 stars in the two frames.

This equation was applied to the images taken through both the continuum filters, and the narrow-band H α filters. As the conditions were not photometric, the zeropoints often varied between the observations taken with different filters. The difference between the zeropoints was used to scale up the continuum image so that it matched the image taken through the H α filter. This scaled continuum was then subtracted from the H α -filter image to give a calibrated image with the zeropoint of the latter.

3.6 Calculating galaxy fluxes

For each reduced galaxy image we used the Object Detection function in *GAIA* to find all the stars and galaxies in the frame. These were then removed and a surface fit was made to the remaining background using the *surfit* command in *KAPPA*. This surface fit was subtracted from the original image, removing any gradients and smoothing out the background. An eleventh-order polynomial surface fit was found to produce the best results. Lower-order polynomials do not fit to the corners of the images as effectively, whereas spline fits do not give the same overall flatness, often generating an oscillating pattern.

The stars in the resulting frame were then removed. In the first attempt, a series of concentric, circular apertures were placed around the galaxy centre. Circular apertures were chosen first due to their simplicity over ellipse fitting, whilst still measuring the radial distribution of a galaxy's flux. They are also more appropriate for irregular and peculiar galaxies which do not have an elliptical shape. Locating the centre of a galaxy was performed using the R-band image. For an undisturbed spiral galaxy this was usually a simple case of centroiding on the nucleus. For irregular and disturbed galaxies where there was no obvious nucleus, a degree of personal discretion was often required as to the location of the centre.

Typically 30-60 apertures were taken so as to cover the entire galaxy and reach well out into the background. The flux in counts/s was calculated in each aperture with sky subtraction determined by the mean values from the outer 10 annuli. The zeropoints derived from the standard stars, or from the processes described in Section 3.5, were used for calibration.

The formula for the conversion of flux in counts/s to flux in Wm^{-2} for $\text{H}\alpha$ emission was derived as follows:

$$\frac{k_{gal}}{k_0} = \frac{f_{gal}}{f_0} \quad (3.4)$$

where k_{gal} equals the counts/s measured from the galaxy in H α , k_0 is equal to the counts/s from a 0 mag star, f_{gal} is the flux detected from the galaxy in Wm $^{-2}$ and f_0 is the flux detected from a 0 mag star through a given narrow-band filter. So,

$$k_{gal} = k_0 \int_{H\alpha \text{ line profile}} F_{gal,\nu} T_{H\alpha} d\nu \bigg/ \int_{\text{filter profile}} F_0 T(\nu) d\nu \quad (3.5)$$

where $T_{H\alpha}$ is the transmission value through the filter at the redshifted H α frequency and $T(\nu)$ is the transmission at a frequency ν . F is the emitted flux of a source in Wm $^{-2}$ Hz $^{-1}$. For the narrow H α line from a galaxy, $T_{H\alpha}$ is constant. For the 0 mag star, F_0 is taken as a constant over the filter profile. The integral of the H α flux over the line profile gives the total flux F_{gal} emitted from the galaxy in H α in Wm $^{-2}$.

If we integrate the denominator over wavelength, rather than frequency, we find

$$T(\nu) d\nu \rightarrow \frac{c}{\lambda^2} T(\lambda) d\lambda \quad (3.6)$$

where c is the speed of light in vacuum.

The filter-profile data files can then be used to approximate this integral. Equation 3.5 can be rewritten:

$$k_{gal} = \frac{k_0 F_{gal} T_{H\alpha}}{c F_0} \times \frac{1}{\sum_{\lambda} \frac{T(\lambda)}{\lambda^2} \Delta\lambda}. \quad (3.7)$$

Both denominators are functions of the narrow-band filter used. F_0 can be interpolated from a plot of flux against wavelength for a A0V star (Colina et al., 1996), where the wavelength taken is the effective peak wavelength of the appropriate narrow band filter.

The magnitude of a star observed on a night with zeropoint Z is given by:

$$m_* = -2.5 \log k_* + Z + 0.08(AM - 1). \quad (3.8)$$

So, for a star with $m = 0$,

$$k_0 = 10^{0.4Z + 0.032(AM - 1)}. \quad (3.9)$$

The zeropoints were calculated from standard stars observed through the R-filter, so Equation 3.9 gives the number of counts/s expected in the broadband-continuum filter. This value needs to be scaled by the measured ratio of the widths, γ , of the R and $H\alpha$ filters (see Section 4.4) to give the number of counts expected from a 0 mag star in the narrow-band filters.

The total $H\alpha$ flux of a galaxy is thus given by:

$$F_{gal}(H\alpha) = \frac{\left[F_0 \gamma \sum_{\lambda} \frac{T(\lambda)}{\lambda^2} \Delta\lambda \right]_{filter}}{T_{H\alpha}(filter, redshift)} \times 10^{-[0.4Z(night) + 0.032(AM - 1)]} \times c \times k_{gal}. \quad (3.10)$$

A small correction needs to be included for galaxies where the R-band image has

been used for continuum subtraction, as the broad filter profile includes the $H\alpha$ line. At 656.3 nm, the transmission through the R filter is about 67%. When the R-band image is scaled to match the $H\alpha$ filter width, the effective throughput of the line will become $0.67/\gamma$. Subtraction of this continuum flux will therefore also subtract a small amount of the $H\alpha$ flux detected through the narrow-band filters. The effective transmission of the $H\alpha$ line through the narrow-band filters is therefore not $T_{H\alpha}$, but $T_{H\alpha} - 0.67/\gamma$. This change should be substituted into Equation 3.10.

The $H\alpha$ Cont filter does not include the $H\alpha$ line in its profile. Thus, there will be no $H\alpha$ contamination in the images taken through it. Equation 3.10 can be left unchanged for galaxies where the $H\alpha$ Cont filter has been used for continuum subtraction.

The continuum flux density of the galaxy (in $\text{Wm}^{-2}\text{nm}^{-1}$) can be derived by a similar method and is found to relate to the measured counts/s in the following way:

$$F_{gal}(R) = C \times \gamma \times 10^{-[0.4Z(\text{night})+0.032(AM-1)]} \times k_{gal}, \quad (3.11)$$

where $C = 2.175 \times 10^{-11}$ for the broad R-band filter and 2.218×10^{-11} for the $H\alpha$ Cont filter. These constants take into account the flux of the 0 mag star integrated under the filter profile and the effective area of the profile, as well as the factor c . The γ factor comes in again as the photometry is carried out on continuum images which have been scaled to match the narrow band images.

The measured fluxes in each aperture were used to plot growth curves. The total flux was taken as the value at which the curve flattened off at large distances from the centre of the galaxy. The curve was said to be flat when, at distances well away from the centre of the galaxy, three consecutive points varied by less than 0.5%. If this criterion was not met, then visual inspection was employed to

determine whether the curve flattened, and if so, at what point.

3.7 Calculating star formation rates

The $H\alpha$ fluxes were converted into luminosities using distances calculated with a Virgocentric inflow model. The model used was based on that of Schechter (1980) (see Section 3.11). The $H\alpha$ luminosities were converted to star formation rates using the relationship found by Kennicutt et al. (1994):

$$\text{SFR} (M_{\odot}\text{yr}^{-1}) = 7.94 \times 10^{-35} L_{H\alpha} (W) \quad (3.12)$$

This assumes a Salpeter IMF (Salpeter, 1955) with mass limits 0.1 and 100 M_{\odot} . The $H\alpha$ luminosities were corrected for internal extinction assuming a constant value of 1.1 mag for each galaxy (Kennicutt, 1983) and the Galactic extinction value given by NED. This is calculated using the all-sky maps of Schlegel et al. (1998) and the extinction law of Cardelli et al. (1989) (see Section 5.3). Corrections for contamination by the [NII] doublet lines which lie either side of the $H\alpha$ line were applied using the $H\alpha/(H\alpha+[NII])$ ratios derived spectrophotometrically by Kennicutt (1983): 0.75 ± 0.12 for spirals and 0.93 ± 0.05 for irregulars.

3.8 Calculating equivalent widths

Star formation rates are biased by galaxy size. Larger galaxies are more likely to have more star-forming regions and emit more $H\alpha$ flux. One way to remove this size bias is to calculate equivalent widths. The equivalent width (in nm) of a galaxy can be found by dividing the $H\alpha$ flux (in Wm^{-2}) by the continuum flux density (in $Wm^{-2}nm^{-1}$) at each point in the growth curve. EW therefore gives a measure of SFR per unit (red) luminosity, and thus helps to remove size biases.

Since the red continuum light is dominated by the old stellar populations, EWs also normalise the star formation activity by the number of older stars in the galaxy. Equivalent widths are also distance independent.

The total EW for a galaxy is taken as the asymptotic value at large radii from the centre of the galaxy. The EW for individual regions of interest can be calculated by taking the ratio of the $H\alpha$ flux and the continuum flux density in an aperture encompassing the region.

3.9 Calculating surface brightnesses

An alternative, and more direct way of removing the size bias is to normalise by the galaxy surface area. For each galaxy a hybrid $H\alpha$ surface brightness (with arbitrary units) is calculated by dividing the total detected $H\alpha$ flux of the galaxy by the square of the R-band Petrosian radius of the galaxy.

The Petrosian radius is defined by Petrosian (1976) and Shimasaku et al. (2001), and discussed further in Section 7.1.3 of this thesis. In short, it is defined to be independent of galaxy distance and photometric errors, and is the radius at which the local surface brightness is a given factor lower than the mean surface brightness within that radius. The R-band Petrosian radius is chosen over that found from the $H\alpha$ image as the smooth profiles in the continuum light prove a better definition of this radius than the discontinuous profiles found from the discrete HII regions (see Section 7.1.3).

3.10 Elliptical apertures

After the initial measurements made with circular apertures, the process was repeated for the inclined-spiral galaxies in the sample using elliptical apertures. The growth curves were derived by assuming fixed values of the ellipticity and position angle of each galaxy. The position angle was taken to be that quoted

in the UGC catalogue as stored on NED. The ellipticity was calculated from the major- and minor-axis lengths quoted under RED_SIZE in the same catalogue. The position of the galaxy centre was taken to be the same as that which was used for the circular apertures. The same ellipse parameters were used to measure both the continuum and the H α growth curves.

It was found that a larger number of apertures was required than had been applied in the circular case. This was in order for the sky background to be reached, particularly along the minor axis.

Elliptical apertures are more favourable than circular apertures when it comes to measuring the growth curves of inclined-spiral galaxies as they trace the radial profiles more accurately. This is important for the calculation of concentration indices.

The total fluxes and equivalent widths for the galaxies should be found to be the same, whether measured with circular or elliptical apertures. A comparison of the values calculated for the 181 inclined spiral galaxies showed that the mean H α flux ratio (elliptical aperture values / circular aperture values) is 0.969 and the mean ratio of equivalent widths is 1.042. This is consistent with the errors associated with measuring the flux (see Chapter 4).

3.11 Calculating galaxy distances

Calculating the distances to galaxies at low redshift is a complicated task. A galaxy's peculiar velocity can dominate over the velocity due to the Hubble expansion of the Universe, thus ruling out a simple application of the Hubble Law (Hubble, 1929):

$$D = v/H_0. \quad (3.13)$$

Here D is the line-of-sight distance to the galaxy, v is its recession velocity and H_0 in the present day Hubble Constant.

The greatest large-scale departure from the Hubble flow experienced by many of our galaxies is due to a gravitational infall motion towards the Virgo Cluster. This **Virgocentric flow** must be modeled before distances can be calculated from a galaxy's recession velocity.

The average galaxy density in a sphere centred on Virgo, reaching out to our Galaxy, is found to be a factor of 4 times higher than the mean universal galaxy density (Yahil et al., 1980). This implies nonlinear growth interior to the Galaxy, thus the nonlinear Virgocentric flow model of Schechter (1980) was applied to the H α GS galaxies to determine their distances. The model assumes that the Virgo Supercluster is a sphere with an inverse squared density profile (Silk, 1974, 1977). Each radial shell centred on the Virgo cluster can be treated as its own universe, with its own average density, $\rho(\eta)$, and its own Hubble constant, $h(\eta)$ (Schechter, 1980):

$$h(\eta) = \frac{\sinh \eta (\sinh \eta - \eta)}{(\cosh \eta - 1)^2}; \quad (3.14)$$

$$\rho(\eta) = \frac{(\sinh \eta - \eta)^2}{(\cosh \eta - 1)^3}. \quad (3.15)$$

The variable η (the 'arc parameter') comes from the parametric form of the open-Universe solution to the Friedmann equation (Weinberg, 1972):

$$t = \frac{q_0}{H_0(1 - 2q_0)^{3/2}} [\sinh \eta - \eta]; \quad (3.16)$$

$$R(t) = \frac{R_0 q_0}{1 - 2q_0} [\cosh \eta - 1]. \quad (3.17)$$

R describes the radius of a shell at time t , where R_0 is the value of $R(t)$ at

the present instant. q_0 is the deceleration parameter. For the closed-Universe solution, $\eta \rightarrow i\eta$.

If η_u is the present universal value of the arc parameter and η_g is the present value for the shell defined by the observed galaxy, then $h(\eta_g)/h(\eta_u)$ is the ratio of the local Hubble constant to the universal Hubble constant and $\rho(\eta_g)/\rho(\eta_u)$ is the ratio of the average interior density to the average density of the Universe. Schechter (1980) quotes the observed, line-of-sight, velocity of a galaxy as being:

$$v_{obs} = v_{Virgo} \left(\frac{h_u x - (h_u - h_l) \cos \theta - (x - \cos \theta)(h_u - h_g)}{h_g} \right). \quad (3.18)$$

where v_{Virgo} is the observed recession velocity of Virgo, corrected for the peculiar velocity of the Sun and our Galaxy, x is the distance to the observed galaxy in units of the distance to the Virgo Cluster, and θ is the angular separation between the galaxy and the cluster. The subscript l indicates the values of the various parameters which are appropriate to the Local Group. Schechter determines the amplitude of the peculiar velocity field at the position of our Galaxy to be given by $(h_u/h_l - 1)v_{Virgo}$. In accordance with the Nearby Galaxies Catalog, (Tully, 1988), a value of 300 kms^{-1} is taken for this study. v_{Virgo} is found by Tully & Shaya (1984) to be $1004 \pm 53 \text{ kms}^{-1}$. If $\rho(\eta_l)/\rho(\eta_u)$ is taken to be 4 (Yahil et al., 1980), then the universal value of η_u which satisfies all these observations is found to be 3.27.

If ρ_u is treated as a free parameter, the value of η_u can be used to define the global parameters h_u , h_l , and ρ_l . θ is calculated from the equatorial coordinates of the galaxy in question and of M87, taken to be the centre of the Virgo Cluster. For all possible line-of-sight distances, the corresponding distance between the galaxy and M87 is calculated using basic geometry, and the value of ρ_g for that separation is computed. A look-up table compiled using Equations 3.14 and 3.15 for varying values of η is used to find a value of h_g . When the right hand side of Equation 3.18 is equal to the galaxy's recession velocity, as cited on NED, then the corresponding distance is taken to be that of the galaxy.

For lines-of-sight sufficiently close to the Virgo Cluster (within $\sim 28^\circ$ of M87, Tully & Shaya 1984), Equation 3.18 produces three separate distances associated with the same observed velocity. This triple-value ambiguity refers to two possible distances associated with infall (one between us and M87, and one beyond M87), and one distance where there is no contribution to the line-of-sight velocity from the Virgocentric infall. For galaxies suffering from this triple-value problem, the distance in closest agreement to that listed in Tully (1988) was taken. Tully (1988) used independent distance estimators or association with galaxies with independently determined distances to resolve the problem. For galaxies not listed in Tully (1988), but defined by Binggeli et al. (1985) to be Virgo members, the distance closest to that of M87 was chosen. Since the majority of triple valued galaxies listed in Tully (1988) were found to be located within the Virgo Cluster, the remaining ambiguous galaxy distances were also assigned to be that closest to M87.

Galaxies with blueshifts, or very small redshifts ($v < 30\text{kms}^{-1}$), were set to the distances quoted by Tully (1988).

The correlation of the distances found here with those published in the Nearby Galaxies Catalog, together with a discussion of the effects of the uncertainties on the derived star formation rates, can be found in Section 4.7.

Chapter 4

Non-astrophysical sources of error in photometric parameters

4.1 Internal comparison tests on repeat measurements

During the course of the survey, several repeat observations of galaxies were made. These can be used as a test of the internal reliability of the photometry in this study. Table 4.1 gives $H\alpha$ fluxes and equivalent widths for the 12 galaxies which were observed twice. The asterisk next to the date indicates the data which were used in the final analysis. The decision was generally based on the comparative photometric and seeing conditions of the two nights.

The mean variations shown by the 12 pairs of observations are 29% in the $H\alpha$ flux and 38% in equivalent widths. These errors are on the pessimistic side, however, as many of the measurements in the table are subject to doubts over the observing conditions or the quality of the images. UGC2023 (18/12/00 observation) and UGC7232 (03/07/01) both suffer from an unexplained 'creased' pattern in the narrow-band filter images (see Section 4.3). The observations of UGC8188 (28/03/01), UGC11331 (18/05/01) and UGC11332 (18/05/01) for various rea-

Name			Name		
Obs. date	F(H α)	EW(H α)	Obs. date	F(H α)	EW(H α)
UGC2023			UGC4115		
22/11/00*	3.440×10^{-16}	3.7	19/11/00*	2.450×10^{-16}	3.4
18/12/00	2.610×10^{-16}	2.4	20/11/00	2.299×10^{-16}	3.4
UGC4173			UGC4469		
22/11/00*	2.041×10^{-16}	5.8	17/02/01	8.948×10^{-16}	2.7
17/12/00	1.339×10^{-16}	4.0	20/10/01*	9.771×10^{-16}	4.5
UGC4484			UGC6251		
17/02/01	8.781×10^{-16}	2.0	28/03/01*	1.795×10^{-16}	4.7
22/10/01*	6.057×10^{-16}	1.7	11/05/01	1.391×10^{-16}	4.6
UGC7232			UGC8188		
19/01/01*	4.685×10^{-16}	2.0	09/05/00*	8.479×10^{-16}	4.0
03/04/01	7.004×10^{-16}	3.2	28/03/01	5.657×10^{-16}	2.0
UGC11331			UGC11332		
18/05/01	1.013×10^{-16}	2.7	18/05/01	1.034×10^{-15}	6.2
22/10/01*	9.265×10^{-17}	2.9	22/10/01*	1.057×10^{-15}	5.0
UGC12294			NGC2604b		
04/08/01	2.577×10^{-15}	4.2	17/02/01	4.903×10^{-17}	1.4
23/10/01*	3.163×10^{-15}	4.4	20/10/01*	6.819×10^{-17}	2.4

Table 4.1: Repeat observations. H α fluxes are in Wm^{-2} , EWs are in nm.

sons only resulted in two usable H α integrations, instead of the three needed to achieve a good signal-to-noise ratio and to remove cosmic-ray contamination. For the three galaxies which were observed on two photometric nights with no major problems (UGC4115, UGC6251 and UGC12294), the agreements between the two sets of measurements are much better (a 17% error in the H α flux, and a 2% uncertainty in the EWs).

4.2 External comparison tests with published results in the literature

H α fluxes and/or EWs of several of the galaxies in the H α GS sample can be found in the literature as part of other studies. In Figures 4.1 and 4.2 a comparison is made between the 106 H α fluxes and 89 EWs published and those calculated from this study. The symbols in the plots are coded by the initials of the authors'

Authors	Code	Fluxes	EWs
Kennicutt & Kent (1983)	KK83	31	35
Gallagher et al. (1984)	GHT84	3	0
Kennicutt et al. (1987)	KKHHR87	9	10
Romanishin (1990)	R90	34	34
Kennicutt (1992)	K92	0	10
Young et al. (1996)	YAKLR96	26	0
Lehnert & Heckman (1996)	LH96	3	0

Table 4.2: Sources of published H α fluxes and EWs

last names and the year of publication and cross-referenced in Table 4.2.

The diagonal solid lines on the plot correspond to a one-to-one correlation. All of the measurements include the satellite [NII] lines (see Section 5.1) and most are uncorrected for extinction effects. Gallagher et al. (1984) calculate corrections for Galactic extinction, but find they are only significant for one galaxy in their sample (which is not in the H α GS sample). Lehnert & Heckman (1996) list H α luminosities, corrected for Galactic extinction. These were converted back to fluxes using the distances quoted in Lehnert & Heckman (1995) and de-corrected for extinction using the values quoted on NED (from Cardelli et al. 1989).

The data have not been corrected to account for the different aperture sizes used in each study. Some of the studies have measured line fluxes using apertures smaller than the software apertures used to calculate the fluxes in this survey. This will tend to move points below the solid line as the smaller apertures may not be detecting all the H α emission from the galaxies.

Figure 4.1 shows a good correlation between the H α GS fluxes and the literature values, with the deviation from the one-to-one line being in the direction expected. Figure 4.2 shows a reasonable correlation between the H α GS and the literature EWs, lying close to the one-to-one line. There is a significant scatter though, particularly for low-EW galaxies.

The scatter in these plots, and the deviation in the repeat measurements in Section 4.1 are the results of the various forms of non-astrophysical errors and uncer-

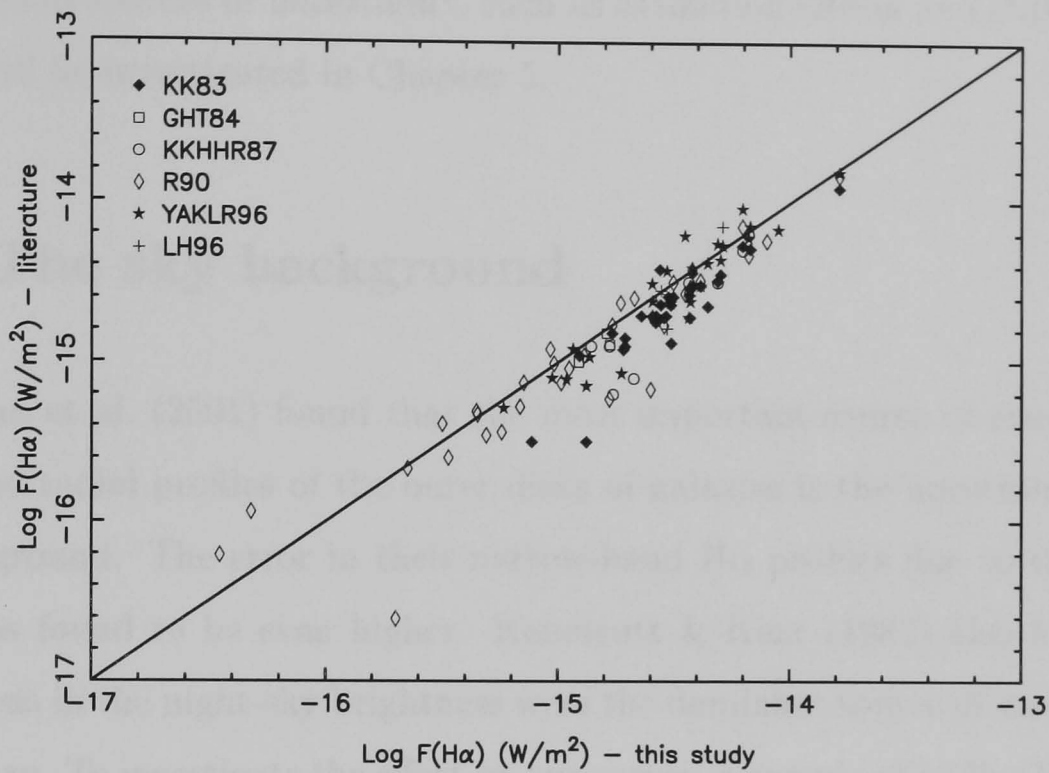


Figure 4.1: Comparison of literature values for the total galaxy H α fluxes with values from the present study.

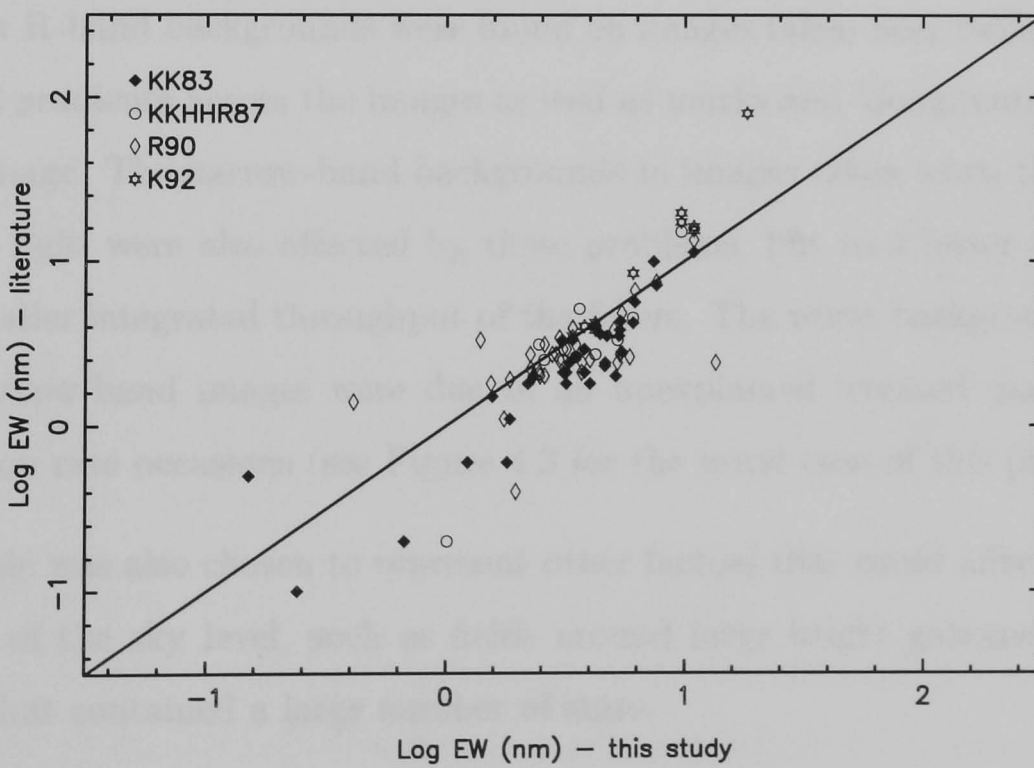


Figure 4.2: Comparison of literature values for the total galaxy EW with values from the present study.

tainties in the photometry. The remainder of this chapter will be an investigation into some of these errors.

Astrophysical sources of uncertainty, such as extinction effects and [NII] contamination will be investigated in Chapter 5.

4.3 The sky background

Koopmann et al. (2001) found that the most important source of error in their broadband radial profiles of the outer disks of galaxies is the uncertainty in the sky background. The error in their narrow-band H α profiles due to this uncertainty was found to be even higher. Kennicutt & Kent (1983) also found that fluctuations in the night-sky brightness were the dominant source of error in their photometry. To investigate the effect on our survey, a sample of 10 H α GS galaxies were selected so as to cover a broad range of background qualities.

The worst R-band backgrounds were found on images taken near twilight. These contained gradients across the images as well as marks and ‘doughnuts’ throughout the image. The narrow-band backgrounds in images taken when the sky was relatively light were also affected by these problems, but to a lesser extent due to the smaller integrated throughput of the filters. The worst backgrounds found in the narrow-band images were due to an unexplained ‘creased’ pattern that occurred on rare occasions (see Figure 4.3 for the worst case of this problem).

The sample was also chosen to represent other factors that could affect the measurement of the sky level, such as fields around large bright galaxies, or backgrounds that contained a large number of stars.

The standard deviation in the overall sky level for each galaxy was determined by measuring 8 blank regions of sky using aperture photometry. Circular apertures with radii of 100 pixels were used in most cases, though for smaller images or backgrounds with large numbers of stars, smaller apertures with radii of 50 pixels



Figure 4.3: The image of UGC5672 taken through the h6570 filter. The ‘creased’ background effect was found on several other images taken through the narrow-band filters, but has not been explained.

were used.

The mean number of counts per aperture was calculated and the standard deviation in the mean was divided by the area of the aperture to give the standard deviation per pixel. This was then converted into flux units. The total error in the galaxy flux was found by multiplying by the area of the aperture at which the total flux had been measured (see Section 3.6).

The sky levels were measured for both the R-band and the continuum-subtracted $H\alpha$ images. In the cases of 5 of the galaxies, there were also images taken through the $H\alpha$ Cont filter. The sky levels were also measured in these and the derived continuum-subtracted $H\alpha$ images. In Section 3.6, it was mentioned that a surface fit was applied to all images to remove gradients. The standard deviation in the sky levels were calculated both before and after the surface fit was subtracted from the galaxy images. It was found that removing the surface fit reduced the

UGC	Filter	Comment	σ/pix	$\sigma(r_{gal})$	r_{gal}	
1983	R	Good background, but quite a few stars.	3.61×10^{-24}	1.91×10^{-19} (0.03%)	130	
	H α -R		3.11×10^{-25}	1.65×10^{-20} (0.001%)	130	
	C		5.41×10^{-24}	2.87×10^{-19} (0.05%)	130	
	H α -C		4.29×10^{-25}	2.28×10^{-20} (0.001%)	130	
2684	R	Very faint galaxy. Poor background.	1.72×10^{-23}	7.80×10^{-19} (10.7%)	120	
	H α -R		Hardly any H α visible.	5.44×10^{-24}	2.46×10^{-19} (1.2%)	120
	C		Galaxy too faint for growth curve.	7.29×10^{-23}	3.30×10^{-18}	120
	H α -C		Galaxy too faint for growth curve.	4.56×10^{-24}	2.06×10^{-19}	120
3174	R	Faint galaxy. Very bad sky. No curve.	9.44×10^{-24}	1.19×10^{-18}	200	
	H α -R		No growth curve due to bad sky.	2.67×10^{-25}	3.36×10^{-20}	200
	C		Background better than R, but not great.	4.39×10^{-24}	5.52×10^{-19} (3.5%)	200
	H α -C			3.32×10^{-25}	4.17×10^{-20} (0.05%)	200
4426	R	Good background, but faint galaxy.	1.19×10^{-25}	1.99×10^{-20} (0.07%)	230	
	H α -R		Hardly any H α , but good background.	1.57×10^{-25}	2.61×10^{-20} (0.03%)	230
4645	R	Bad background with gradient.	1.50×10^{-22}	4.83×10^{-17} (2.4%)	320	
	H α -R			5.09×10^{-24}	1.64×10^{-18} (0.09%)	320
	C		Better than R, but slight gradient.	3.26×10^{-23}	9.81×10^{-18} (0.35%)	310
	H α -C			9.44×10^{-24}	2.85×10^{-18} (0.10%)	310
5672	R	Bright R background. Gradient.	2.20×10^{-23}	9.97×10^{-19} (0.81%)	120	
	H α -R		'Creased' background and gradient.	8.83×10^{-24}	3.99×10^{-19} (0.30%)	120
6272	R	Bright galaxy. Background not great.	2.42×10^{-23}	2.20×10^{-18} (0.14%)	170	
	H α -R		Sky looks ok.	2.61×10^{-24}	2.37×10^{-19} (0.008%)	170
6778	R	Large, bright galaxy. Good background.	2.35×10^{-23}	7.09×10^{-18} (0.45%)	310	
	H α -R			3.89×10^{-24}	1.18×10^{-18} (0.02%)	310
	C		Good background.	1.88×10^{-22}	5.67×10^{-17} (3.6%)	310
	H α -C			1.69×10^{-24}	5.11×10^{-19} (0.006%)	310
11300	R	Average galaxy and background.	8.47×10^{-24}	1.80×10^{-18} (0.53%)	260	
	H α -R			1.65×10^{-24}	3.51×10^{-19} (0.04%)	260
11604	R	Lots of foreground stars.	2.35×10^{-24}	7.08×10^{-19} (0.05%)	310	
	H α -R			2.11×10^{-25}	6.36×10^{-19} (0.003%)	310

Table 4.3: Results from the investigation into the effect of variations over the sky background. Column (1) gives the UGC number of the galaxy. Column (2) indicates the image investigated, where R is the broad R-band continuum filter, C is the H α Cont filter, H α -R and H α -C are the narrow-band H α images with the indicated broader-band filter used for continuum subtraction. Column (4) gives the standard deviation per pixel in the 8 sky regions in units of Wm^{-2} for the H α measurements, and $\text{Wm}^{-2}\text{nm}^{-1}$ for the continuum images. In Column (5), these values are multiplied by the area of the circular aperture at which the total galaxy flux was measured. The radii of these apertures are given in column (6). The effect of the variations in the sky background is compared to the total fluxes of the galaxies and given as a percentage in column (5).

standard deviation in the sky levels by typically a factor of ten. In the cases where there was a visible gradient across the sky, the background variation could be improved by 2 orders of magnitude by removing the fit.

The results from the images after the surface fits have been subtracted are presented in Table 4.3.

The table shows that the standard deviations in the sky background levels vary over two orders of magnitude. However, after gradients have been removed with a surface fit, there are no clear correlations between the apparent visual quality of the sky and the flatness of the background. In absolute flux terms, the brightness

of the galaxy or the presence of a large number of foreground stars also appear to have little effect.

The mean value of the standard deviation of the sky per pixel is 2.61×10^{-23} $\text{Wm}^{-2}\text{nm}^{-1}$ in the R-band images, 6.07×10^{-23} $\text{Wm}^{-2}\text{nm}^{-1}$ in the H α Cont-filter images, 2.85×10^{-24} Wm^{-2} for the H α images when the R-band image is used for continuum subtraction, and 3.29×10^{-24} Wm^{-2} if the H α Cont image is subtracted. Considering the 2 orders of magnitude in the variation of the individual values, it cannot be said here, or from examining Table 4.3, that there is any significant difference between the broad R-band filter and the H α Cont filter when it comes to the quality of the sky background.

Table 4.3 also shows that, in the majority of cases, the fluctuations in the sky background have an effect on the total measured flux of the galaxy of around 1% or less. The only case where there is a significant contribution of greater than 10% is for the R-band image of UGC2684, and this is one of the faintest galaxies in the entire sample.

4.3.1 The effect of the sky background variation on concentration indices

In Section 7.1.2, concentration indices will be introduced. In this chapter we will include an investigation into the effects of the index defined in Equation 7.1 as $\log[r_{75}/r_{25}]$, where r_{75} and r_{25} are the radii where the flux falls to 75% and 25% of the total flux respectively.

The effect of the sky background variation was investigated in the above 10 galaxies by replacing the total flux with the total flux plus or minus the error calculated for the galaxy at the radius at which the total flux was taken. In most cases the difference in the resulting concentration indices was less than 1%. The only cases where it was higher were for the R-band image of UGC2684 where it was 8.4% and the intermediate-band continuum image for UGC3174 (4.8%). These are

	n	observed scaling factor	σ	theoretical scaling factor
R/h6570	97	52.6	3.3	47.8
R/h6594	84	57.0	3.7	58.6
R/h6607	18	46.9	4.5	44.9
R/h6626	37	50.5	6.9	57.3
C/h6570	72	2.58	0.19	2.23
C/h6594	24	2.78	0.10	2.74
C/h6626	5	2.64	0.15	2.67

Table 4.4: Continuum scaling factors. Column (1) contains the two filters scaled, where R is the broadband-continuum filter and C is the H α Cont filter. No galaxies observed with the narrow band H α filter h6607 were observed through the C filter. Column (2) lists the number of stars used to determine the scaling factor in each case. Column (3) gives the mean value found for the scaling factor, and column (4) gives the standard deviation on that value. The theoretical scaling factors derived using the quoted filter profiles are shown in column (5).

both very faint galaxies.

4.4 Continuum scaling factors

A further source of error in the measurement of H α fluxes and concentration indices comes from the determination of the scaling factor when subtracting the continuum level from the H α -filter images. Due to the large number of galaxies in the H α GS sample, a single scaling factor was calculated between each of the H α filters used and both of the continuum filters.

These scaling factors were calculated from the comparisons of either unsaturated foreground stars, or standard stars through the different filters. The values are presented and compared with those found by integrating under the filter profiles supplied by the ING in Table 4.4.

These derived scaling factors were used in all photometric cases. For galaxies observed under non-photometric conditions, a separate scaling factor was calculated for that particular set of observations (see Section 3.5). A single scaling factor is not the ideal situation, especially when derived from stars which have different

spectral properties from galaxies, not to mention each other. However, for such a large data set, it is the most practical method.

Young et al. (1996) and Koopmann et al. (2001) find a $\pm 2-5\%$ error in the determination of their continuum levels. The errors listed in Table 4.4 show that the uncertainty in the scaling factors in this sample range from 3 to 14%, with the two most commonly used ratios (R/h6570 and R/h6594) having an error of around $\pm 6.5\%$.

Young et al. (1996) claim that their error in the determination of the continuum level can lead to an uncertainty of up to $\pm 20\%$ in the global H α flux for low-surface-brightness extended emission. Koopmann et al. (2001) find an error of 20-30%. An investigation into the effects of changing the scaling factor by 1σ on a small sample of H α GS galaxies was undertaken. For each of the R/H α scaling factors, 6 galaxies were investigated. For each of the C/H α scalings, 4 galaxies were looked at.

For galaxies observed through the h6570 or h6594 filters the uncertainty due to the scaling factor is around 10%, rising to 25% for low-EW galaxies where the continuum light overwhelms the H α . For those observed through the higher-redshift H α filters, a 1σ change in scaling factor will cause an uncertainty of around 15% in the flux, rising to 35% for galaxies with low-EWs.

As well as the effect of a 1σ change in scaling factors on H α flux, the effect on the concentration indices of the galaxies was also calculated. This turned out to be smaller with the average error through the h6570 and h6594 filter galaxies being around 4%. For images taken through the h6607 and h6626 filters the error was approximately 11%.

4.5 Errors due to surface fitting and source removal

In Section 4.3, subtracting a surface fit of an image was found to reduce significantly the error due to fluctuations in the sky background. Before a surface fit is made, however, the sources (both stars and galaxies) and any defects on the image need to be removed so that only the sky is left. In the cases of continuum-subtracted $H\alpha$ images, it is the residuals left by the brighter stars due to imperfect subtraction that need to be removed, rather than the stars themselves.

This process is partly automated using the Object Detection option in *GAI4*. The application, which is powered by the *Starlink* software *SExtractor*, finds the location and size of the sources on the image. This information is then converted to place circular apertures over the sources, which are then replaced by blank regions. These are ignored during the surface fit.

Occasionally extra apertures need to be added to cover image defects, or the size or shape of the current apertures need to be modified (for example in the case of a saturated star that has leaked along the CCD array). Diffuse galaxy light is also often not picked up completely by the automated part of the process. There is, therefore, some degree of manual input, which is not precisely reproduced if a repeat attempt is made. This causes slight differences in the surface fit before it is subtracted from the image.

A similar uncertainty is introduced when the stars/residuals and image defects are removed before the placing of the apertures to measure the growth curves. In the cases of removing stars that lie superimposed on the galaxy itself, the size and shape of the removal-aperture can be quite important to the measured flux.

For a representative sample of galaxies the process of removing sources and defects, fitting to the remaining background, subtracting the fit, removing the non-galaxy objects from the resulting image and finally measuring the $H\alpha$ flux was repeated five times. Each repeat was treated as a best attempt to remove the

objects, as opposed to taking extreme-case scenarios.

The standard deviation in the five measurements can be taken as some sort of repeatability uncertainty for this process. The results from the investigation suggest an uncertainty of around 1-4% in the total H α flux. The higher uncertainties were found for fainter galaxies, or for those with foreground stars superposed on the disk of the galaxy.

4.6 Errors in the flux calibration

Equation 3.10 gives the relationship between the number of counts/s measured in an H α image and the H α flux emitted from the galaxy (uncorrected for [NII] and extinction effects). Many of the factors in this equation contain uncertainties in their values which will contribute to the uncertainty in the overall flux.

The errors in the continuum scaling factor, γ , are the same as discussed in Section 4.4. These vary from 3-14%, depending on the filter (see Table 4.4). The most commonly used narrow-band filters were the h6570 and the h6594 filters. The error in R/h6570 and R/h6594 is around $\pm 6.5\%$ in both cases.

Table 4.4 also shows that there is a difference between the theoretical filter profiles and the actual profiles. The integrated area under the filter and the transmission value of the filter at the redshifted H α wavelength in Equation 3.10 assume the theoretical profile. These, therefore, introduce a further uncertainty of around 7% in the flux conversion.

The transmission value will also be affected by the uncertainty in the redshift of a galaxy. A galaxy's rotation gives an uncertainty in its recession velocity of around $\pm 100 \text{ km s}^{-1}$. Figure 4.4 shows the effect this has on the error in the transmission value as a function of redshift. The h6570 filter is used for galaxies with recession velocities below 950 km s^{-1} , the h6594 filter then takes over until velocities of greater than 2150 km s^{-1} . For the highest-redshift galaxies in our

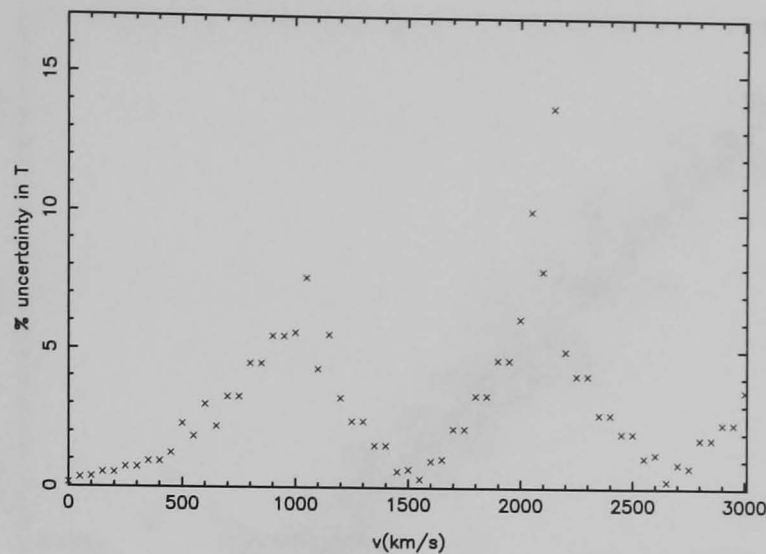


Figure 4.4: The percentage uncertainty in the transmission value due to the uncertainties in the galaxy's recession velocity.

sample, the uncertainty is plotted as calculated from the h6626 filter. The error in the transmission value due to its redshift dependence generally contributes around 5% to the total flux uncertainty.

One further source of uncertainty in Equation 3.10 comes from the photometric zeropoint. A separate zeropoint is used for each photometric night (see Section 3.4). Non-photometrically observed galaxies are calibrated with an R-band image of the same galaxy taken on a later photometric night. The appropriate zeropoint for that photometric night is then taken (see Section 3.5). Zeropoints are calculated from a number of standard stars observed on the same (photometric) night. The mean uncertainty in the adopted zeropoints over the entire survey is found to be:

$$\frac{\sum_{\text{photometric nights}} (\sigma_{\text{night}} / \sqrt{n_{\text{night}}})}{N} = 0.014 \text{ mag}, \quad (4.1)$$

where σ_{night} is the standard deviation in the value of the zeropoint for a given photometric night, n_{night} is the number of stars used to calculate that zeropoint, and N is the total number of photometric nights in the survey (52). This value corresponds to a contribution to the total flux uncertainty of around 1.3%.

Adding all these errors in quadrature gives an overall error in the H α flux due to the calibration from counts/s to Wm $^{-2}$ of 11%.

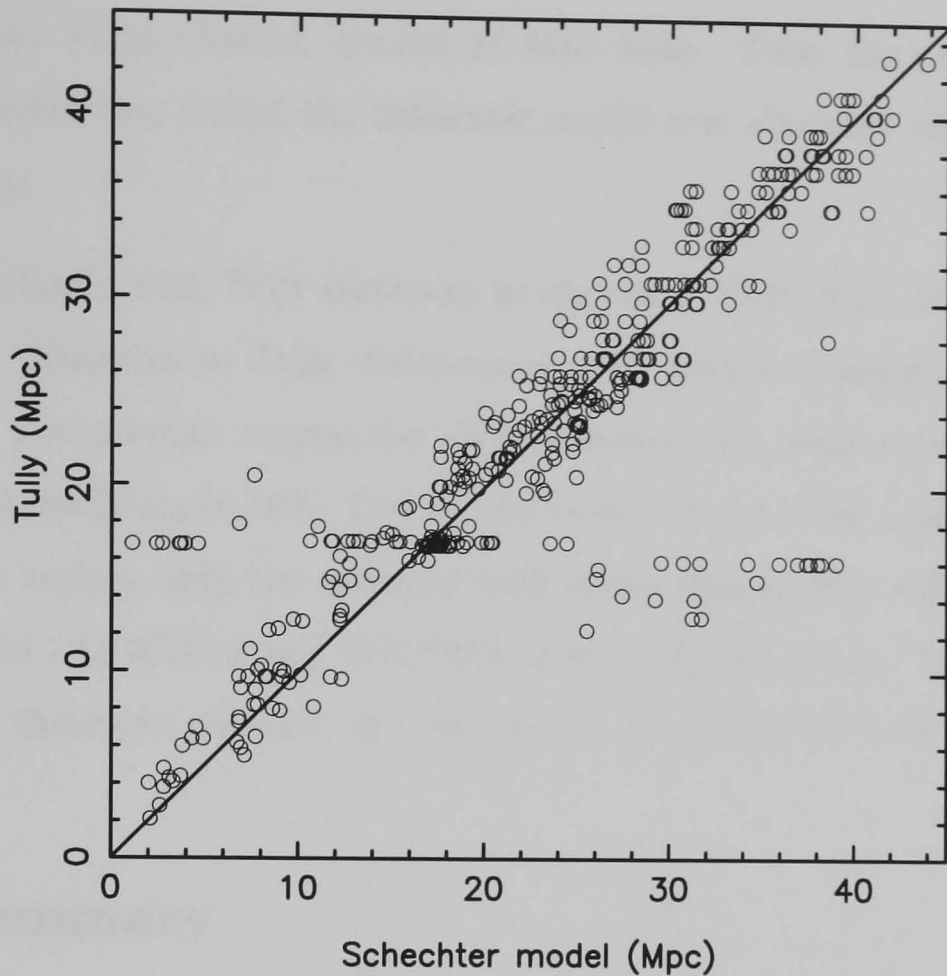


Figure 4.5: A comparison of galaxy distances as calculated using the model of Schechter (1980) and the catalogue of Tully (1988). The solid line represents a one-to-one correlation.

4.7 Distance errors

Equivalent widths, surface brightness and concentration indices are all independent of the galaxy distance to first order. Uncertainties in the distances allocated to galaxies do affect $H\alpha$ luminosity calculations, and hence the derived SFRs. They also affect the calculated R-band absolute magnitudes and intrinsic size estimates of the galaxies.

The method used to calculate distances, taking into account infall into the Virgo Cluster, was described in Section 3.11. Many of the $H\alpha$ GS galaxies are listed in the Normal Galaxies Catalog (Tully, 1988), where distances have been computed using a similar method. In Figure 4.5, the distances calculated using the model of Schechter (1980) are compared to those published by Tully (1988) for 398 galaxies. The solid line represents a one-to-one correlation. There is a small amount of scatter, but in general the agreement is good. The main exception

is close to the Virgo Cluster, around 17 Mpc away. Tully has classified some galaxies as members, whilst the Schechter model has allocated them distances outside Virgo.

Excluding galaxies with Tully distances in the range 12-18 Mpc, the mean ratio of Schechter distances to Tully distances is 0.97, with a standard deviation of 0.12 (12%). For galaxies around the Virgo distance, the mean ratio is 1.13, but the standard deviation is 50%. Due to the policy of generally avoiding galaxies in the Virgo region, only two galaxies with ratios significantly different from 1 were observed - UGC7215 and UGC7414, both with low ratios. Thus, with the exception of these two galaxies, the error in the derived SFRs is 24%.

4.8 Summary

Of the six non-astrophysical sources of error investigated, the uncertainty in the continuum scaling factor was found to be the most significant when calculating both $H\alpha$ fluxes and concentration indices. This is dependent on both the filters used and the surface brightness of the galaxy.

The process of subtracting a surface fit of the background from a galaxy image plays a large part in reducing the errors due to fluctuations in the sky. The measured errors are, therefore, not as significant as found in some previous studies, such as those by Koopmann et al. (2001) and Kennicutt & Kent (1983).

The application of a surface fit, combined with the removal of sources and defects, does introduce a further source of error, but this is found to be relatively small.

The conversion of the flux into units of Wm^{-2} introduces several sources of error, which, when combined, contribute a total of $\sim 11\%$. The conversion to $H\alpha$ luminosities introduces a further error of 24% due to uncertainties in the galaxy distance.

So, for a typical galaxy, the uncertainty in the $H\alpha$ flux will be $\sim 15-19\%$. The error

in the derived SFR will be $\sim 30\%$. The uncertainty in the concentration index will be $\sim 3-10\%$. For a low-EW galaxy the errors in the flux and concentration index will be $\sim 27-37\%$ and $\sim 5-12\%$ respectively. The error in the SFR will be $\sim 40\%$. Errors in derived values of EWs will be dominated by the uncertainties in the $H\alpha$ fluxes.

Chapter 5

Astrophysical sources of error: extinction and [NII] corrections

In Chapter 4, the effects of the non-astrophysical photometry errors and uncertainties on the $H\alpha$ flux were investigated. In this chapter, the two main astrophysical sources of error in the calculations of star formation rates and equivalent widths are discussed. Other sources of uncertainty, such as the choice of IMF and the precise value of the Hubble constant, will not be dealt with here.

[NII] corrections

One major problem with narrow-band $H\alpha$ imaging, is contamination by the [NII] doublet. These two lines are located either side of the 656.3 nm $H\alpha$ line, at 654.8 nm and 658.4 nm. The widths of the narrow-band $H\alpha$ filters range from 4.4 nm to 5.5 nm, thus including both [NII] lines. The first of these is the [NII]-short line and is much weaker than the second, [NII]-long, line ([NII]-long/[NII]-short $\sim 3:1$). The contribution to the total flux causes a scatter when using $H\alpha$ measurements to infer star formation rates. In order to improve calculations of SFRs it is therefore important to be able to correct for the [NII] contamination.

Extinction corrections

Extinction is caused by the scattering or absorption of light from the observed galaxy, thus reducing the detected flux. There are three sources of extinction that need to be corrected for when calculating luminosities and SFRs (EWs are calculated from the ratios of the $H\alpha$ and continuum fluxes and are thus relatively unaffected by extinction). These are the Earth's atmosphere, dust in our own Galaxy, and dust in the observed galaxy.

5.1 [NII] Contamination

For the majority of this thesis, reference to $H\alpha$ flux of a galaxy actually refers to the combined $H\alpha + [NII]$ flux. In this section, however, the two contributions are treated separately.

Whilst the ratio of [NII] to $H\alpha$ in the nuclei of spiral galaxies has been well studied (e.g. Keel 1983; Rubin & Ford 1986) and found to be high, Kennicutt & Kent (1983) find that nuclear [NII] emission rarely dominates the integrated photometry of galaxies. The most commonly used corrections for [NII] contamination for entire galaxies are those derived by Kennicutt (1983) and Kennicutt & Kent (1983). Spectrophotometric [NII]/ $H\alpha$ ratios of individual extragalactic HII regions from the literature (see Kennicutt & Kent 1983 for references) were compiled from 14 spiral galaxies (mostly Sc's) and 7 irregular galaxies. The average $H\alpha/(H\alpha + [NII])$ ratio was found to be fairly constant, spanning the ranges 0.75 ± 0.12 for the spirals, and 0.93 ± 0.05 for the irregulars. In terms of the ratio [NII]/ $H\alpha$ this corresponds to a median value of 0.33 for spirals and 0.08 for irregulars.

However, these values were calculated by finding the [NII]/ $H\alpha$ ratio of just a few regions, averaging for each galaxy and then finding the mean value for spiral and irregular types. This assumes that all HII regions have roughly the same proportion of [NII] to $H\alpha$ as those regions measured.

In this work, a new method of investigating the relative strengths of $H\alpha$ and [NII] is introduced and explored. This method will enable both the integrated ratio over the whole galaxy and the ratios of individual regions to be calculated. The relationship with galaxy morphology can also be investigated.

5.1.1 Photometric separation of [NII] and $H\alpha$

Theory

The [NII] 658.4 nm filter (n6584) at the JKT has a very narrow passband (2.1 nm). Galaxies with recession velocities close to 960 km s^{-1} will have their $H\alpha$ line redshifted to around 658.4 nm. If these galaxies are observed through the n6584 filter, the narrow passband is able to virtually exclude ($< 10\%$ transmission) the [NII] doublet. The observations taken through the wider 659.4 nm $H\alpha$ filter (h6594) will include both the [NII] and the $H\alpha$ emission. Using the transmission values quoted for both filters, the continuum subtracted images can be scaled and subtracted so as to produce images with only $H\alpha$ photons and with only [NII]-long light (the effects of the [NII]-short emission are less significant due to its relative weakness). The relative strengths of the two fluxes can be investigated using aperture photometry.

By applying this method to a range of galaxies of different types, it is possible to look at variations in the ratio of $H\alpha$ to [NII] both amongst different galaxy types, and within each galaxy itself. In the latter case the effects resulting from radial metallicity gradients, for example, can be investigated.

Observations

Five hours of service time were granted on the JKT for this project. The observing took place in December 2000 and January 2001. Three galaxies were observed through the n6584 ($3 \times 1200\text{s}$ integrations) and R-band continuum filters. $H\alpha$ data were taken as part of the main survey. Three further galaxies were observed

through the n6584 filter during the main H α GS observing time.

The galaxies range from spiral types S0/a to Scd. Further observations are required to include galaxies with irregular morphologies.

Photometric calibration was obtained through the use of standard stars.

Producing the separated images

The R-band continuum images were scaled and subtracted from the n6584 filter images. The scaling factor was found to be $R/n6584 = 118.5$ from photometry of 41 foreground and standard stars. This compares very well to the value of 118.4 from the quoted filter profiles.

The continuum-subtracted images taken through the h6594 filter were scaled so as to match the photometric zeropoint of the n6584 filter images. In the cases where there were large differences in the seeing conditions in the two images, *SExtractor* in *GAIA* was used to find the full width half maxima (FWHM) of around 10 foreground stars in each image. A Gaussian smoothing was applied to the image with the better seeing using the *KAPPA* command *gausmooth*. The correction was approximated as the root of the difference of the squares of the mean FWHM. The two images were also aligned.

The detected flux in each of the two images can be written as a sum of the transmitted H α flux and the transmitted [NII] flux:

$$\begin{aligned} (h6594 - R) &= T_{H\alpha, h6594} F(H\alpha) + T_{[NII], h6594} F([NII]) \\ (n6584 - R) &= T_{H\alpha, n6584} F(H\alpha) + T_{[NII], n6584} F([NII]) \end{aligned} \quad (5.1)$$

where $T_{x,y}$ is the transmission of the line x in filter y . Thus, solving these simultaneous equations gives:

$$\begin{aligned}
 F([NII]) &= \frac{\left[(h6594 - R) \frac{T_{H\alpha, n6584}}{T_{H\alpha, h6594}} - (n6584 - R) \right] \times T_{H\alpha, h6594}}{T_{[NII], h6594} T_{H\alpha, n6584} - T_{H\alpha, h6594} T_{[NII], n6584}} \\
 F(H\alpha) &= \frac{\left[(h6594 - R) \frac{T_{[NII], n6584}}{T_{[NII], h6594}} - (n6584 - R) \right] \times T_{[NII], h6594}}{T_{H\alpha, h6594} T_{[NII], n6584} - T_{[NII], h6594} T_{H\alpha, n6584}}. \quad (5.2)
 \end{aligned}$$

The various transmission values for the redshifted H α and [NII] lines were found from the supplied filter profiles. The above arithmetic operations were applied to the two continuum-subtracted images to produce one image mapping the [NII] content of the galaxy and one image containing only the H α light. Gradients in the sky background were removed using the surface-fitting method described in Section 3.6.

Findings

For each of the 6 galaxies, the ratio of the [NII] to the H α flux and the distribution of each was investigated for the whole galaxy. This was done by plotting growth curves in a similar way to that described in Section 3.6, using the same centre value and aperture shape. The growth curve from the separated [NII] image was divided by that obtained from the separated H α image to obtain the ratio [NII]/H α as a function of distance from the galaxy centre.

Figures 5.1 to 5.6 show this ratio and the two growth curves, normalised to the maximum [NII]/H α ratio, all displayed on the same plot. The middle image is the uncontaminated H α and the bottom image shows the distribution of the [NII] emission.

UGC2141 Figure 5.1 shows that in this galaxy, the [NII] and H α do not separate into distinct regions as found in some of the other galaxies. The [NII]-only image shows a diffuse mix of positive and negative readings, showing that the

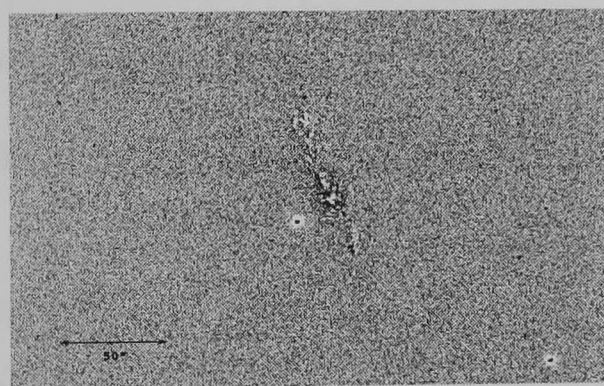
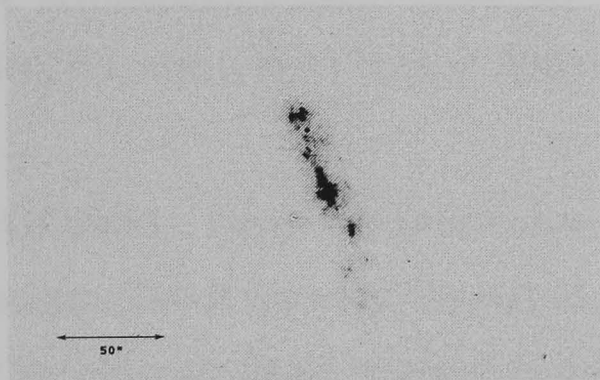
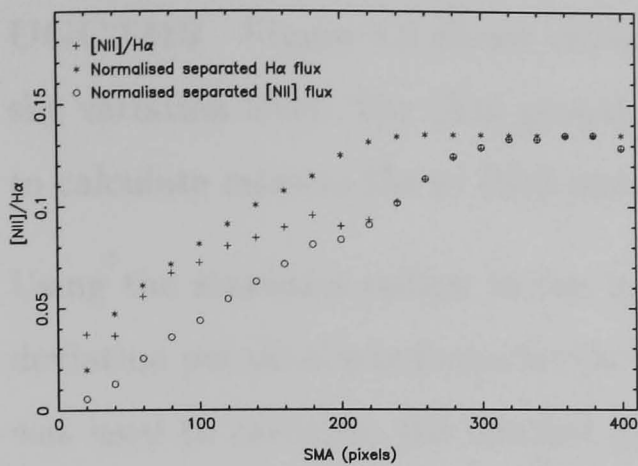


Figure 5.1: UGC2141

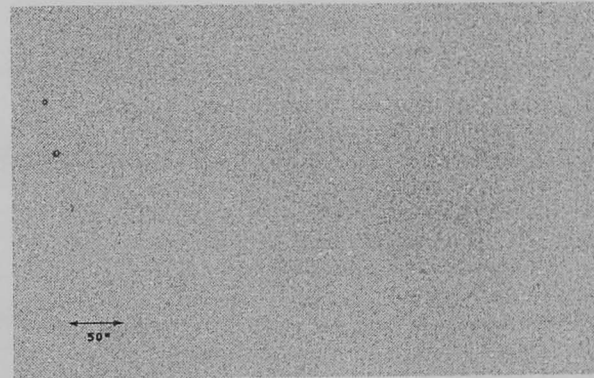
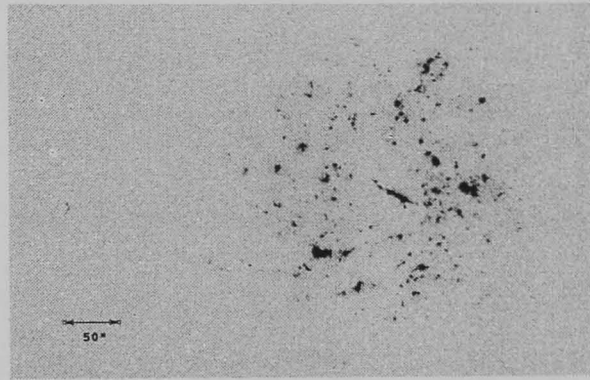
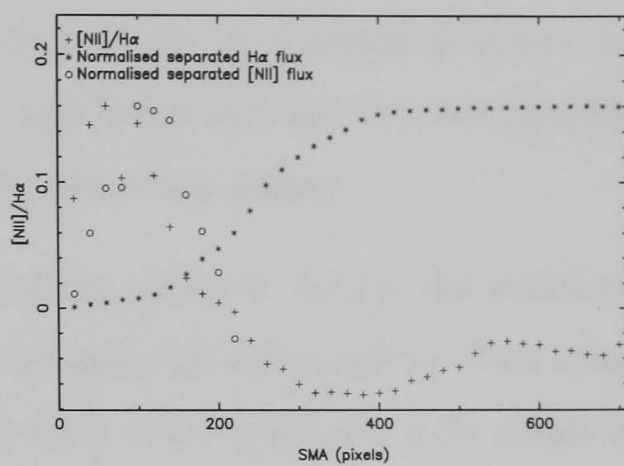


Figure 5.2: UGC2210

method has not worked particularly well in this case. This will be, in part, due to the large seeing differences between the nights in which the galaxy was observed through the h6594 filter (2.0'') and the n6584 filter (1.0''). The Gaussian smoothing correction is not perfect. However, this should not affect the large-scale trends or overall ratios shown in Figure 5.1.

The ratio of [NII] to H α increases in the outer regions of the galaxy and levels off at a value of 0.13. Thus, the value of $H\alpha/(H\alpha + [NII])$ is 0.88, which is higher than the mean value suggested Kennicutt (1983), and [NII] emission is relatively weak in this galaxy.

UGC2210 Figure 5.2 shows virtually no sign of any [NII] detection above the sky variation level. The [NII] growth curve, falls below zero and it is not possible to calculate relative $H\alpha$ to [NII] strengths for the whole galaxy.

Using the statistics option in the Image Regions utility in *GALIA*, the standard deviation per pixel was found for the area containing the entire galaxy. This value was used to calculate the weakest [NII] detection that would give a 3σ result in the investigated region. From this, an upper limit of 0.020 can be placed on [NII]/ $H\alpha$, and a lower limit of 0.980 on $H\alpha/(H\alpha + [NII])$.

UGC2855 Figure 5.3 shows that there is a high ratio of [NII] to $H\alpha$ in the nucleus. This is expected (Kennicutt & Kent, 1983) due to the higher metallicities of the old stars found in nuclear regions. The ratio then drops off along the disk. There is an arc of [NII] emission, however, located at the eastern end of one of the spiral arms.

The asymptotic value of [NII]/ $H\alpha$ is 0.18. $H\alpha/(H\alpha + [NII])$ is, therefore, 0.84.

UGC3580 Figure 5.4 shows that the separation method has not worked very well for UGC3580. The h6594 image suffers from the creased background problem, and there is also a difference in the seeing conditions (1.9" for the h6594 image and 1.0" in the n6584 image). The [NII] detection is below the sky variation. Using the Image Regions statistics option in *GALIA*, a lower limit of 0.034 is found for [NII]/ $H\alpha$ and an upper limit of 0.967 for $H\alpha/(H\alpha + [NII])$.

UGC8403 Figure 5.5 shows a high nuclear [NII] content, peaking in the centre with an [NII]/ $H\alpha$ ratio of 0.59. This falls off rapidly and there is very little sign of [NII] in the disk. The average ratio for the whole galaxy is just 0.07, which corresponds to $H\alpha/(H\alpha + [NII]) = 0.93$. This is much higher than suggested by Kennicutt (1983).

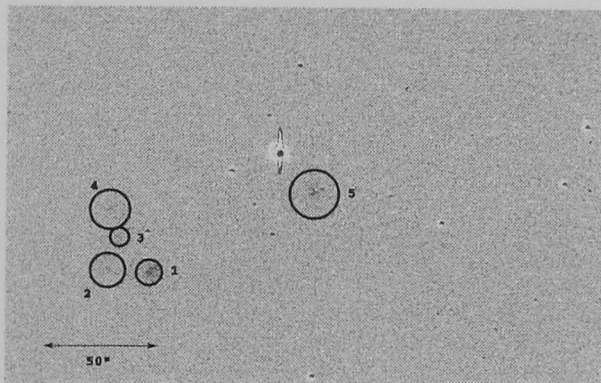
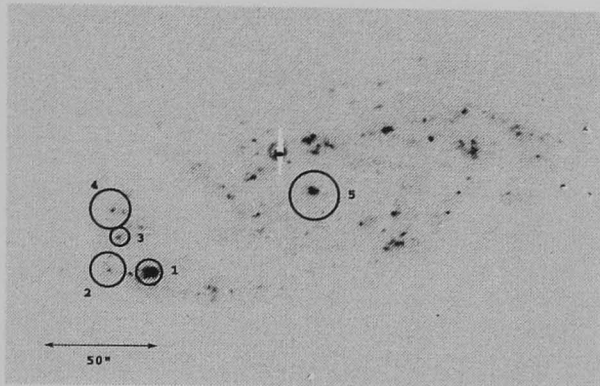
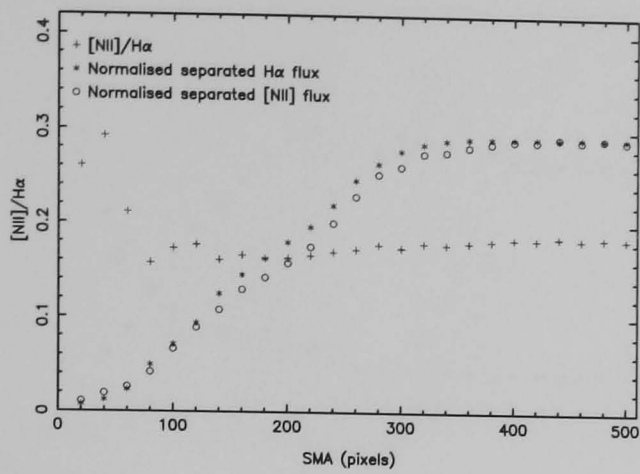


Figure 5.3: UGC2855

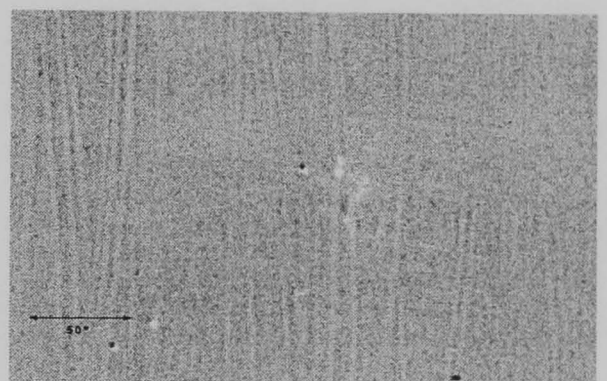
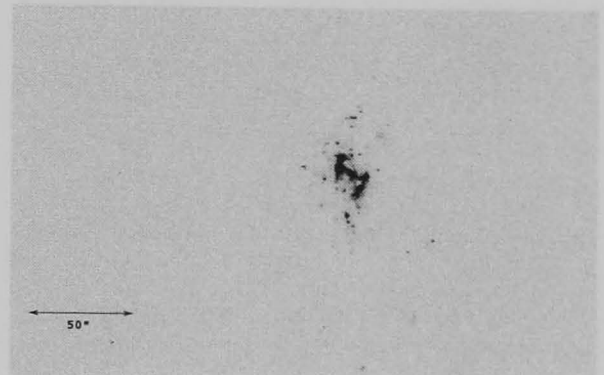
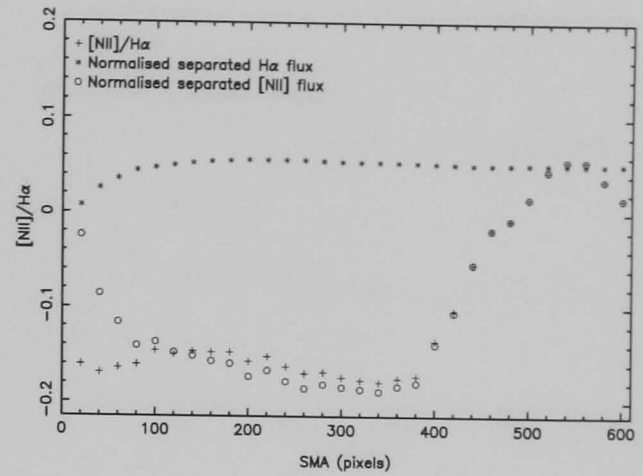


Figure 5.4: UGC3580

UGC11872 Figure 5.6 shows a very strong source of [NII] in the galaxy nucleus. UGC11872 is listed on NED as containing a low-ionisation nuclear emission region (LINER). The ratio of [NII] to $H\alpha$ is 1.33 in the centre, indicating more [NII] emission than $H\alpha$. The [NII] emission is much less in the outer regions of the disk, and the total [NII]/ $H\alpha$ ratio for the galaxy is 0.54. The fraction of $H\alpha$ to the total $H\alpha + [NII]$ flux is low at 0.65.

The above results are summarised in Table 5.1. The quoted errors represent the standard deviation in the asymptotic values calculated from the final 5 points in the [NII]/ $H\alpha$ growth curve.

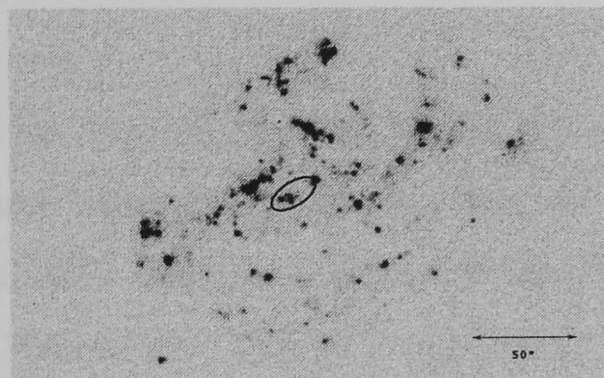
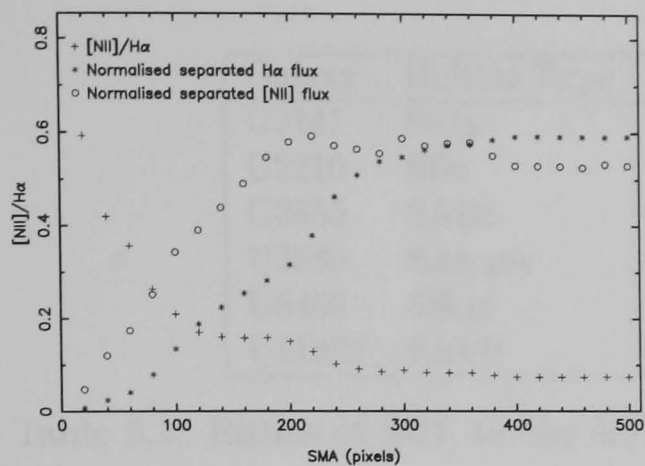


Figure 5.5: UGC8403

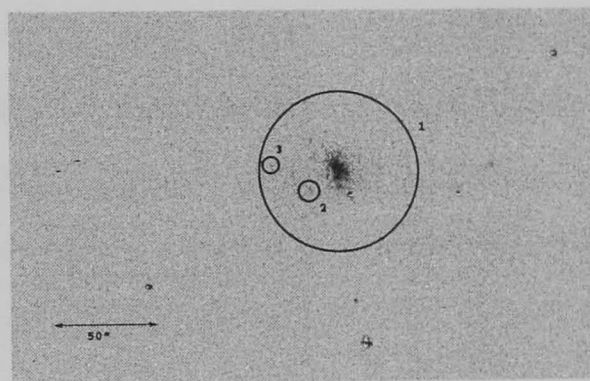
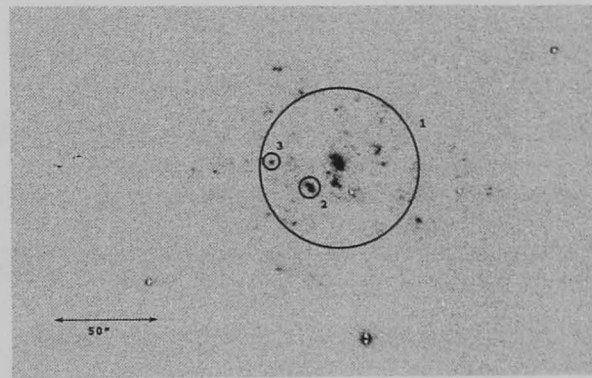
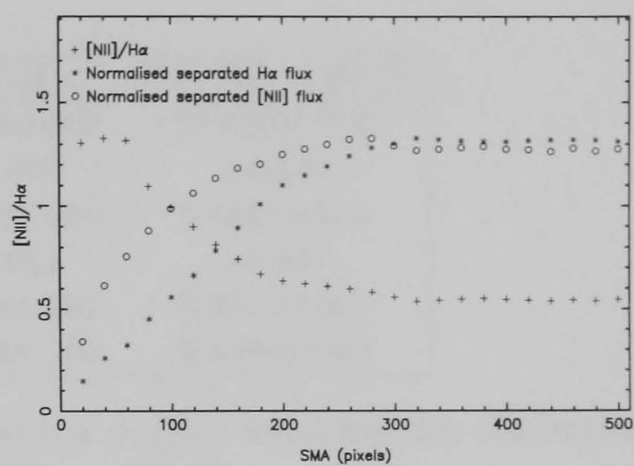


Figure 5.6: UGC11872

For the three galaxies where individual [NII]-emitting regions were visible, the ratio of [NII] to $H\alpha$ was investigated separately in each region. Circular or elliptical apertures were placed around the regions in the positions indicated in Figures 5.3, 5.5 and 5.6. The images had already had a surface fit removed, but further background subtraction was performed using a sky aperture placed over a blank piece of sky away from the galaxy. The errors caused by fluctuations in the sky level were measured by moving the sky aperture to ~ 10 different positions around the frame and calculating the standard deviation in the mean measured fluxes.

The fluxes (in counts/s) were recorded in identical apertures in both the $H\alpha$ -only image and the [NII]-only image. The results are combined in Table 5.2.

Galaxy	Hubble Type	[NII]/H α	H α /(H α + [NII])
U2141	S0/a	0.133 \pm 0.002	0.883 \pm 0.002
U2210	SBc	<0.020	>0.980
U2855	SABc	0.185 \pm 0.001	0.844 \pm 0.001
U3580	SAa pec	<0.034	>0.967
U8403	SBcd	0.074 \pm 0.001	0.931 \pm 0.001
U11872	SABb	0.541 \pm 0.003	0.649 \pm 0.002

Table 5.1: Ratios of [NII] to H α and H α to H α + [NII] measured for the entire galaxy

If we were to assume that all HII regions in a galaxy have approximately the same ratio of [NII] to H α , then the mean value of H α /(H α + [NII]) for spiral galaxies, calculated from the individual regions listed in Table 5.2, would be 0.706 \pm 0.078. This is in agreement with the value quoted in Kennicutt (1983) of 0.75 \pm 0.12. However, the majority of the above regions were selected on their [NII] observations. The process was repeated for some of the most luminous regions in the H α only image. The [NII] fluxes for these regions were predicted assuming H α /(H α + [NII]) = 0.75 and should have all been well within the range of detectability. With the exception of regions 2 and 3 in UGC11872, no corresponding [NII] flux could be measured in any of these areas.

Using the Image Region statistics in *GAIA*, a 3 σ [NII] detection would give an upper limit [NII] to H α ratio of between 0.034 and 0.117 for each of the regions investigated. Since these limits are well below the average ratio found from Table 5.2, it seems fair to say that the above assumption, regarding equal ratios of [NII] to H α in all HII regions, does not appear to be valid.

A further test of this is to remove the regions in which [NII] was detected and use a single large aperture to measure the ratio of the remaining [NII] to H α in each galaxy. The results are presented in Table 5.3.

These data confirm that, whilst the results of Kennicutt (1983) can be reproduced for the regions with the strongest [NII] detections, the overall amount of [NII] in the remainder of each of the 3 galaxies is lower than the commonly assumed value.

Region		[NII]/H α	H α /(H α + [NII])
U2855	1	0.228 \pm 0.010	0.814 \pm 0.006
	2	0.520 \pm 0.067	0.658 \pm 0.028
	3	0.407 \pm 0.028	0.711 \pm 0.014
	4	0.529 \pm 0.073	0.654 \pm 0.033
	5N	0.289 \pm 0.029	0.776 \pm 0.017
U8403	N	0.536 \pm 0.024	0.651 \pm 0.010
U11872	1N	0.800 \pm 0.032	0.556 \pm 0.010
	2	0.337 \pm 0.013	0.748 \pm 0.007
	3	0.277 \pm 0.018	0.783 \pm 0.011

Table 5.2: Ratios of [NII] to H α and H α to H α + [NII] for individual regions. An N next to a region name indicates a nuclear region.

5.1.2 [NII] contamination - summary and conclusions

The new method proposed here of photometric separation of the [NII] and H α introduces the possibility of challenging the general use of the Kennicutt (1983) [NII] corrections in H α studies.

The current sample size of this investigation is very small, but even so, we see a wide variation in the amount of [NII] in each galaxy. UGC2210 and UGC2855 are both Sc galaxies, and yet their [NII] profiles are very different.

The Kennicutt (1983) correction agrees well with this work for individual regions selected by their high [NII] fluxes. For the remaining galaxy, and the galaxy as a whole, however, Kennicutt appears to be overestimating the [NII] contamination effects.

Clearly, further observations through the n6584 filter are required, particularly of irregular galaxies, before a new set of [NII] corrections can be derived. For the work in this thesis, the current standard corrections will continue to be used for comparability with other work. If a value of H α /(H α + [NII]) of 0.83, suggested by the mean of the values for the four entire galaxies in Table 5.1, is taken, then the derived SFRs will be 8% higher.

The photometric separation method is also a good way of investigating the distri-

Galaxy	[NII]/H α	H α /(H α + [NII])	Total H α /(H α + [NII])
U2855	0.147	0.871	0.85
U8403	0.068	0.936	0.93
U11872	0.241	0.806	0.65

Table 5.3: Ratios of [NII] to H α and H α to H α + [NII] for the remainder of the galaxy after the regions in Table 5.2 have been removed. Column 4 presents a reminder of the total H α to H α + [NII] ratio for the whole galaxy, before the individual regions are removed.

bution of [NII] within each galaxy. Three out of the 4 galaxies for which positive [NII] measurements could be made showed higher [NII]/H α fractions in the metal rich nuclear regions than in their younger disks.

For more detailed investigations of individual HII regions, this method will be very useful in deriving accurate corrections for the [NII] contamination in the H α + [NII] flux measurements.

5.2 Atmospheric extinction

It is a straightforward matter to correct for scattering and absorption in the Earth's atmosphere. For a given night, both standard stars and sources with unknown fluxes will suffer the same amount of atmospheric extinction (Zeilik et al., 1992). The airmass of an object relates the amount of extinction suffered by an object to the amount of atmosphere its light passes through to reach the telescope (i.e. its position in the sky at the time of observation).

Combining the zeropoint and the airmass, as described in Sections 3.4 and 3.6, will therefore correct the observed fluxes for atmospheric extinction.

5.3 Galactic extinction

Galactic extinction is due to dust grains in the ISM within our own Galaxy. Thus, extinction along lines of sight out of the Galaxy will generally diminish with increasing Galactic latitude.

Schlegel et al. (1998) have created a full-sky 100 μm map from observations by IRAS and the Diffuse Infrared Background Experiment (DIRBE) on board the Cosmic Background Explorer (COBE) satellite. They have removed the zodiacal foreground and confirmed point sources to leave just the diffuse emission from the inter-stellar medium. The diffuse infrared emission is a direct measurement of the column density of the inter-stellar dust, and thus the map can be used as a measure of extinction for extragalactic objects.

Schlegel et al. (1998) and Burstein & Heiles (1982) confirm the dependence of extinction on Galactic latitude, but also find a large, irregular variation over the sky.

The reddening in B-V quoted by Schlegel et al. (1998) can be converted to an R-band extinction using the extinction law of Cardelli et al. (1989). The resulting value for the position of each galaxy in the H α GS sample can be found on NED.

Corrections for Galactic extinction are applied during the conversion of H α flux to SFR in Section 3.7.

5.4 Internal extinction

The major source of systematic error in the conversion of H α fluxes to SFRs is due to the effects of extinction within the galaxy being observed. There is a great deal of uncertainty as to the exact magnitude of this extinction and how it varies with galaxy luminosity and type. Studies using radio data (which are not affected by extinction) of large samples of individual HII regions in nearby galaxies yield mean extinction values ranging from $A(\text{H}\alpha) = 0.5$ mag to $A(\text{H}\alpha)$

= 1.8 mag (e.g. Caplan & Deharveng 1986; Kaufman et al. 1987; van der Hulst et al. 1988; Caplan et al. 1996). Kennicutt (1998) adopts a single correction of 1.1 mag for the effective $H\alpha$ extinction of entire galaxies for all Hubble types. These samples, however, mainly contain bright galaxies, whereas the $H\alpha$ Galaxy Survey also includes many faint and irregular galaxies. For very small irregular galaxies, extinction may be systematically lower due to the smaller quantity of inter-stellar medium through which the $H\alpha$ flux must traverse. Alternatively, most of the extinction could be associated with the star forming-region itself, in which case galaxy type and size will be of lesser importance.

The same recombination process that produces $H\alpha$ emission, also generates other recombination photons, including $Br\gamma$ emission at a rest wavelength of $2.166\mu\text{m}$. Compared to $H\alpha$, the effective extinction of the $Br\gamma$ line at $2.166\mu\text{m}$ is reduced by a factor of 7.1 (calculated using the extinction curve of Cardelli et al. 1989). If we assume case B recombination (the assumption that every Lyman line photon is scattered many times in an optically thick nebula, and is converted into lower series photons plus either $Ly\alpha$ or two continuum photons - see Osterbrock 1989), we can predict the intrinsic $Br\gamma/H\alpha$ line ratio. Comparing the measured and predicted ratios, we can calculate the excess extinction at $H\alpha$ compared to $Br\gamma$, and hence the total extinction at $H\alpha$, by the assumption of a standard extinction law.

The $H\alpha$ Galaxy Survey utilised the 1 m JKT telescope on La Palma. However, the $Br\gamma$ line is 104 times weaker than $H\alpha$ (Osterbrock 1989 for $T=10,000$ K and an electron density $N_e = 10^4 \text{ cm}^{-3}$), thus a larger telescope, with an IR detector, is required for extinction measurements. The UFTI (UKIRT Fast Track Imager) camera at UKIRT (United Kingdom InfraRed Telescope) with the $Br\gamma$ and $Br\gamma z$ filters (centred on $2.166\mu\text{m}$ and $2.173\mu\text{m}$ respectively) was ideal for this work as the filters could be used for galaxies with recession velocities up to 4500 kms^{-1} , whereas the galaxies in the $H\alpha$ study have velocities up to 3000 kms^{-1} .

Three nights of observing time (17-19 January 2001) on UKIRT were awarded for $Br\gamma$ observations of a subset of the $H\alpha$ sample.

5.4.1 UKIRT observations and data reduction

Thirty-nine galaxies were selected from the $H\alpha$ survey sample. Twenty-one of these were spirals ranging between Hubble types S0/a to Sd inclusive. The other 18 were irregulars with a range of absolute magnitudes. Only galaxies with D_{25} major axes less than or equal to 2.0 arcmin were selected. This was to ensure that all galaxies would fit on the UFTI field. During the 3-night run, 22 of the galaxies were observed through one of the 2 $Br\gamma$ filters and the K' continuum filter.

Exposure times varied from 600 s to 3600 s through the $Br\gamma$ filters, depending on the magnitude of the galaxy. The $Br\gamma$ filter was used for galaxies with velocities less than 1000 km s^{-1} , and the $Br\gamma z$ filter for those with higher redshifts. A 300 s exposure was taken for each galaxy through the K' filter (centred on $2.1123 \mu\text{m}$) to be used for continuum subtraction. A dark image was taken for each observation, and sky flats and standard stars were observed throughout the night. All observations were taken as 5-point jitters to enable bad pixel replacement.

The observations and data reduction were performed using the *ORAC-DR* pipeline package. This package is able to reduce data in near real time whilst still at the telescope, however, due to two problems encountered with a number of the images, all the data were re-reduced back at the Astrophysics Research Institute at a later date. The two problems encountered were a pattern of rings and streaks on many of the images taken through the $Br\gamma$ filter, probably due to interference effects, and a band of increased noise, thought to be filter vignetting, at the bottom of all $Br\gamma z$ images.

The solution to the first problem was to collect all the affected raw $Br\gamma$ images (making sure that they had the same size and integration times) and combine them using the *FIGARO* command *medsky*. This took the median of the images, thus removing any stars and galaxies from the final image, leaving only the pattern of rings and streaks superimposed on the dark image which had not yet been subtracted. This resultant image was then subtracted from the affected $Br\gamma$

images instead of the dark frame, thus removing both the dark counts and the superimposed pattern.

The strip of noise at the bottom of the $\text{Br}\gamma\text{z}$ images was removed by editing the bad-pixel mask to blank out the area where the band appeared. When the mask was added to the images, the pixels in the affected region were set to BLANK. This improved the registration and visual quality of the mosaiced images.

Two different *ORAC-DR* recipes were used to reduce the galaxy images. *JITTER_SELF_FLAT* was found to produce the smoothest background for the faint galaxies. This recipe creates a flatfield frame by combining normalised object frames, using the median at each pixel. Detected sources are masked out. For large, bright galaxies this recipe is inappropriate as a large percentage of the field will be masked out once the galaxy is removed. In these cases the *BRIGHT_POINT_SOURCE* recipe was applied. This uses a pre-determined flatfield frame generated from one of the observations of a blank region of sky taken throughout the night.

Standard stars were all reduced using the *BRIGHT_POINT_SOURCE* recipe. Zeropoints for each night were calculated from these stars and confirmed that all three nights were photometric. The standard stars were also used to calculate the scaling factors between the two $\text{Br}\gamma$ filters and the K' filter. For the 10 stars observed through both the K' and the $\text{Br}\gamma$ filters, the mean ratio of detected counts, $\text{K}'/\text{Br}\gamma$, was found to be 10.74 ± 0.10 . A value for $\text{K}'/\text{Br}\gamma\text{z}$ of 7.13 ± 0.09 was derived from the 8 standard stars observed through these filters.

All images were normalised to one second integration time. The K' images were divided by the above scaling constants and registered to match the appropriate $\text{Br}\gamma$ observation before being subtracted to remove the continuum emission.

5.4.2 Br γ detections

Out of the 22 galaxies observed, only 8 showed any sign of Br γ detections after continuum subtraction. In the cases of 6 of these, there were 1-3 detections of small, isolated regions. The Br γ image of UGC5786, however, contained a detection of nearly the whole galaxy, with 8 strong regions that particularly stood out (Figure 5.7). UGC5786 is the brightest galaxy observed in H α as part of the H α Galaxy Survey (Figure 5.8).

The Br γ detections measured in counts per second were converted into fluxes with units Wm^{-2} taking into account filter profiles, transmission values through the filter for the appropriate redshift of the Br γ line, the zeropoint for the night and the airmass of the observations.

In order to correlate the Br γ regions with their H α counterparts, the Br γ data were rebinned to match the pixel scale of H α images. This was done using the *magnify* command in the *IRAF* package. The pixel size of the JKT images is $0.33''/\text{pixel}$, whereas the images from UKIRT have a pixel size of $0.09''/\text{pixel}$. The Br γ images were therefore binned up by a factor of 3.66.

To measure the coordinate offset between the two sets of data, the centroid was found for the galaxy nucleus in both the JKT R-band image and the UKIRT K'-band image. In the cases where there was no bright nucleus, a bright, non-saturated star was used. An investigation using centroids of several stars around one galaxy showed no significant rotation effects between the two data sets.

Br γ fluxes were calculated by placing an aperture around each region. An annular sky region was taken in cases where there were no other sources nearby. In the case of UGC5786, in particular, it was more suitable to take a separate sky region situated well away from the galaxy. Random measurement errors were investigated in several ways. The centroiding option was turned off and the aperture was moved by small amounts, whilst still maintaining full coverage of the source. Photometry measurements were taken and the different results noted.

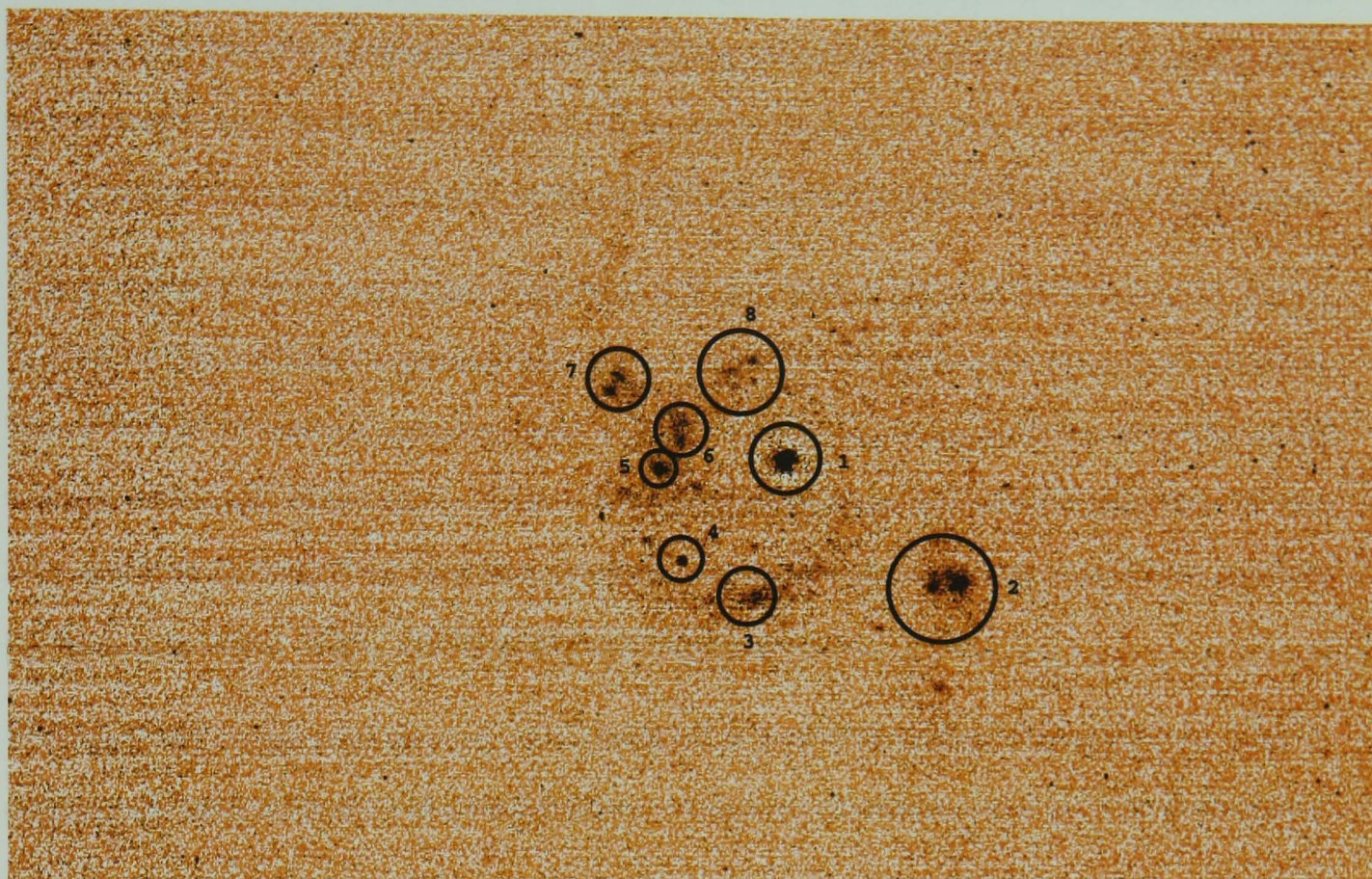


Figure 5.7: Br γ image of UGC5786. Regions investigated in Table 5.4 are labeled.

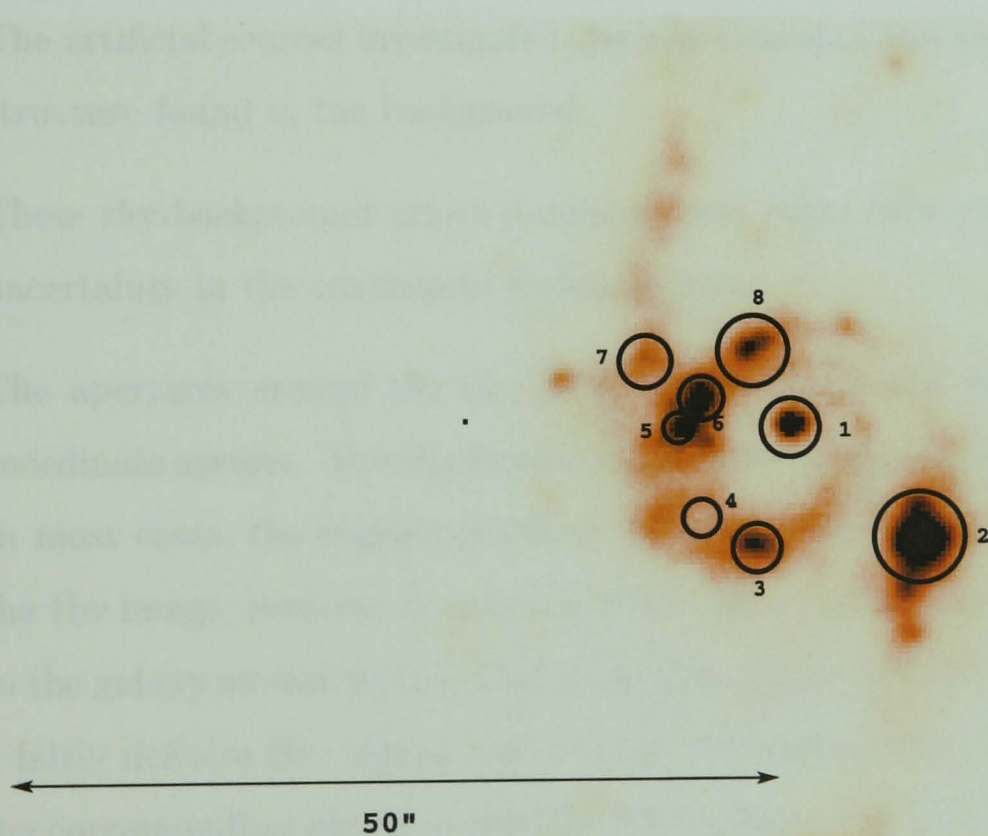


Figure 5.8: H α image of UGC5786. Regions investigated in Table 5.4 are labeled.

The sky regions were varied, either by changing the inner and outer radii of the sky annulus, or by changing the size and position of the separate sky region. The variation in results obtained was combined with those from the first investigation to calculate the mean value for the number of detected source counts, with the error conservatively estimated as the standard deviation of the different estimates.

Using the *KAPPA* command *creframe*, a frame was created with a random distribution of 25 artificially-generated sources with two-dimensional Gaussian profiles. The FWHM of these objects was set to be 10 pixels superimposed on a background with a constant value of 0. This size was comparable to the average size of the real sources detected in the Br γ frames. Aperture photometry was then applied to find the mean ‘flux’ value of the artificial sources.

For each detected real source, the artificial frame was scaled to match the source count rate and added to the real frame. Aperture photometry was then performed on the embedded fake sources and the standard deviation in values was used as a measure of the error in the determination of the flux of the real source. The artificial sources investigated the non-Gaussian and systematic effects of the structure found in the background.

These sky-background errors dominate over other sources of error, such as the uncertainty in the continuum scaling factors.

The apertures around the Br γ regions were saved and transformed to the H α coordinate system. The H α flux for the corresponding region was then calculated. In most cases, the regions detected in Br γ matched up with obvious regions in the H α image, however in some cases the Br γ region seemed to bear no relation to the galaxy as seen in H α . One particular example of this was UGC4115, where a fairly definite Br γ signal was around 10 times stronger than anything seen in the corresponding region in the H α . This galaxy was actually observed twice, on both the first and third nights. Close comparison of the two images revealed that the Br γ region appeared in a slightly, but significantly, different position in each image. This would imply that, whatever the detection was, it was not related

to the galaxy. This also raised into doubt the reality of several of the other Br γ detections with no H α counterpart, such as the region in UGC3734 and one of the regions in UGC2455.

An error on the H α measurement was calculated by moving around and varying the size of the sky regions. This was found to be much less than the errors introduced by the Br γ measurements. The dominant source of error when calculating H α fluxes was shown in Chapter 3 to be the uncertainty in the continuum scaling factors ($\sim 10\%$ for a typical galaxy observed through the h6570 or h6594 narrow-band filters). The total uncertainty was shown to be around 15%.

Table 5.4 shows the Br γ fluxes and their corresponding H α fluxes for all the detected regions, with the exception of those dubious detections with no H α counterpart. The 1σ errors given are those derived from the slight movement of the Br γ aperture and changing the sky region (1), the variation in counts measured from fake sources with the same flux as the object (2), and the error analysis for H α fluxes in Chapter 3 (3).

UGC3711 was observed on two nights: 17/01/01 (N1) and 19/01/01 (N3). The Br γ fluxes for both galaxies are in agreement within the quoted errors.

In column 9, the ratio of the detected fluxes is presented. Given that the intrinsic flux of the Br γ line is 104 times less than that of H α but that the effective extinction is a factor of 7.1 times lower, we find that the H α extinction coefficient, $A(H\alpha)$ can be calculated from the detected flux ratio using the following relation:

$$A(H\alpha) = 2.910 \log \left(\frac{104}{0.75 \times \frac{F_{H\alpha}}{F_{Br\gamma}}} \right) - A_G(H\alpha). \quad (5.3)$$

$A_G(H\alpha)$ is the correction for Galactic extinction, as discussed in Section 5.3. The factor of 0.75 comes in to correct for [NII] contamination in the H α flux (see Section 5.1). This is the correction recommended by Kennicutt (1983), however,

UGC	type	region	$F_{Br\gamma}$ (Wm^{-2})	$1\sigma(1)$	$1\sigma(2)$	$F_{H\alpha}$ (Wm^{-2})	$1\sigma(3)$	$\frac{F_{H\alpha}}{F_{Br\gamma}}$	$A(H\alpha)$
2455	IBm	1	6.662×10^{-18}	10.5%	8.8%	2.501×10^{-16}	15%	37.5	1.05 ± 0.13
		2	1.543×10^{-18}	36.0%	35.0%	2.629×10^{-18}	15%	1.7	4.96 ± 0.39
3711 (N1)	IBm	1	4.460×10^{-18}	10.3%	17.0%	2.304×10^{-16}	15%	51.7	1.01 ± 0.20
		2	1.376×10^{-18}	15.7%	28.0%	5.278×10^{-17}	15%	38.4	1.39 ± 0.31
3711 (N3)		1	4.154×10^{-18}	6.2%	15.2%	2.304×10^{-16}	15%	55.5	0.92 ± 0.18
		2	1.017×10^{-18}	11.2%	48.0%	5.278×10^{-17}	15%	51.9	1.01 ± 0.49
5731	SAab		3.878×10^{-17}	11.4%	3.6%	1.190×10^{-16}	15%	3.1	4.73 ± 0.15
5786	SABbc (pec)	1	2.306×10^{-17}	2.3%	2.9%	3.881×10^{-16}	15%	16.8	2.61 ± 0.03
		2	2.175×10^{-17}	4.3%	2.9%	1.587×10^{-15}	15%	72.9	0.75 ± 0.05
		3	7.864×10^{-18}	4.2%	7.6%	3.228×10^{-16}	15%	41.1	1.48 ± 0.09
		4	3.307×10^{-18}	8.3%	14.1%	1.066×10^{-16}	15%	32.2	1.79 ± 0.04
		5	6.305×10^{-18}	2.0%	9.8%	1.841×10^{-16}	15%	29.2	1.91 ± 0.06
		6	8.373×10^{-18}	4.5%	7.6%	3.909×10^{-16}	15%	46.7	1.32 ± 0.09
		7	9.488×10^{-18}	3.2%	7.6%	2.396×10^{-16}	15%	25.3	2.09 ± 0.09
		8	8.399×10^{-18}	16.6%	7.6%	5.144×10^{-16}	15%	61.2	0.97 ± 0.20
6123	SBb		8.291×10^{-18}	9.1%	11.1%	4.983×10^{-17}	15%	6.0	3.90 ± 0.13
7985	SABd		1.229×10^{-18}	10.8%	32.6%	9.410×10^{-17}	15%	76.6	0.68 ± 0.35

Table 5.4: Results from the investigation of Br γ regions. Column (1) gives the UGC number of the galaxy. Column (2) gives the Hubble type. Column (3) identifies the region investigated. Column (4) gives the Br γ flux measured for that region and column (7) gives the corresponding H α flux. Columns (5),(6) and (8) give 1σ errors on these measurements, as described in the text. Column (9) gives the ratio of the fluxes and column (10) gives the H α extinction coefficient calculated from these values.

if we substitute the value 0.83, suggested by the mean H α /(H α + [NII]) ratio for the four entire galaxies in Table 5.1, the values of A(H α) will be slightly lower. As an example, the extinction found for region 3 of UGC5786 will fall from 1.48 to 1.35 if this change is made.

The values of A(H α) for each region are recorded in column 10. In most cases the extinction values lie between 0.5 and 1.8 mag, in agreement with the findings of previous studies. Four regions have significantly higher values (>2.5 mag), indicating large amounts of extinguishing dust. The three high extinction regions in UGC5731, UGC6123 and UGC5786 are all situated in the nucleus of the galaxy. The high region in UGC2455 coincides with a region that is bright in the R-band image, but appears faint and diffuse when viewed in H α .

Unfortunately there are not enough data to investigate a correlation between extinction and Hubble type. The results do show, however, that extinction values vary within a single galaxy and so seem to be associated with the star-forming regions themselves. Particularly high levels of extinction are found in and around nuclear regions.

5.4.3 Putting limits on Br γ detections

Due to the low number of Br γ detections in our observations, an investigation was performed to find the minimum flux that a region would need in order to give a 3σ detection in each image. This was done by creating a frame with randomly-placed artificial sources as discussed in Section 5.4.2. The generated frame was then re-normalised and added to each of the observed Br γ galaxy images. Photometry was performed on the artificial sources and the mean value, along with the 1σ error was calculated. The re-normalisation factor was adjusted until the mean value fell below 3σ . The mean count rate was then converted into a flux in the same way as if a real Br γ source was being investigated - taking into account the zeropoint, airmass and redshift of the galaxy image frame. This calculated flux corresponds to the minimum Br γ source flux that we could reliably detect (to a 3σ certainty) in each frame.

The results varied from frame to frame, but were all between 1.2 and 5.7×10^{-18} Wm $^{-2}$. This range is around the same as the values detected for the fainter Br γ regions. Thus we are detecting Br γ at the very limits of that which is possible with the UKIRT images. Lower fluxes will not be reliably detected above the background.

This work was followed up by an investigation into whether there were any Br γ regions that should have been detected, but were not. For each galaxy observed by UKIRT, the H α image was examined and the fluxes of the brightest H α regions were measured. If an extinction of $A(\text{H}\alpha) = 1.1$ mag is assumed, there should be corresponding Br γ fluxes approximately 44 times fainter than these H α fluxes. In all cases where the predicted Br γ flux for a region was greater than or close to the calculated minimum Br γ flux that would give a 3σ detection, aperture photometry was carried out on the region in the Br γ image.

Fourteen regions were investigated in 9 different galaxies. In the majority of cases any Br γ flux found was below the 3σ certainty level. Two new regions were identified however, one in UGC2455 and a further one in UGC5786 (below region

UGC	type	region	$F_{Br\gamma}$ (Wm^{-2})	$1\sigma(1)$	$1\sigma(2)$	$F_{H\alpha}$ (Wm^{-2})	$1\sigma(3)$	$\frac{F_{H\alpha}}{F_{Br\gamma}}$	$A(H\alpha)$
2455	IBm		2.994×10^{-18}	25.3%	17.7%	9.650×10^{-17}	15%	32.2	1.24 ± 0.29
5786	SABbc pec		2.820×10^{-18}	24.0%	16.4%	1.080×10^{-16}	15%	38.3	1.57 ± 0.28

Table 5.5: Results from the investigation of Br γ regions identified from the H α . The layout is the same as in Table 5.4.

2 in Figure 5.7). Details of these are presented in Table 5.5.

The extinction values obtained here are consistent with those found previously. For the remaining regions, the upper limits for detectable-Br γ fluxes found using the randomly-placed artificial sources were used to place upper limits on the extinction coefficient for these regions. These are shown in Table 5.6. The limits show that the extinction values in these H α selected HII regions do not lie above the range of mean extinctions found by other authors (i.e. 1.8 mag). The region investigated in UGC2392 has $A(H\alpha) < 0.20$ mag and, thus, appears to contain much less extinguishing dust than normal.

Using the artificial-sources investigation, no 3σ limits for Br γ detections were found with fluxes less than $F_{H\alpha}/104$. This value is the minimum limit in the case where there are no extinction effects and our temperature and density assumptions about the HII regions apply.

5.4.4 Br γ fluxes in the literature

Br γ fluxes for a further two galaxies in our H α sample have been measured previously during spectroscopic studies of extinction in starburst galaxies. These values have been published in Kawara et al. (1989), Ho et al. (1990), and Calzetti et al. (1996).

The H α fluxes for the corresponding areas were found from our data and used to calculate the values for the H α extinction coefficient in these regions. In the case of UGC12699, the region investigated was the bright starburst nucleus. For UGC8098, Calzetti et al. (1996) observed the main star-forming region, which is

UGC	region	$F_{H\alpha}(\text{Wm}^{-2})$	$F_{Br\gamma}(\text{Wm}^{-2})$	$\frac{F_{H\alpha}}{F_{Br\gamma}}$	$A(H\alpha)$
2392		1.240×10^{-16}	$<1.299 \times 10^{-18}$	>95.46	<0.20
2455	a	6.540×10^{-17}	$<1.759 \times 10^{-18}$	>37.18	<1.06
	b	7.260×10^{-17}	$<1.759 \times 10^{-18}$	>41.27	<0.93
3711		1.300×10^{-16}	$<1.802 \times 10^{-18}$	>72.14	<0.59
5731		1.600×10^{-16}	$<2.693 \times 10^{-18}$	>59.41	<1.00
5786		1.070×10^{-16}	$<1.742 \times 10^{-18}$	>61.42	<0.97
6797		1.530×10^{-16}	$<2.162 \times 10^{-18}$	>75.39	<0.70
7232		1.130×10^{-16}	$<2.611 \times 10^{-18}$	>43.28	<1.39
7690		1.980×10^{-16}	$<3.092 \times 10^{-18}$	>64.04	<0.89
7985	a	1.380×10^{-16}	$<2.727 \times 10^{-18}$	>50.61	<1.20
	b	1.190×10^{-16}	$<2.727 \times 10^{-18}$	>43.64	<1.39
	c	1.820×10^{-16}	$<2.727 \times 10^{-18}$	>66.74	<0.85

Table 5.6: Extinction limits for the regions with the brightest $H\alpha$ fluxes, but with no $Br\gamma$ detections above the 3σ limits calculated using randomly placed artificial sources.

located a long way south of the nucleus.

The quoted $Br\gamma$ fluxes, the measured corresponding $H\alpha$ fluxes and the calculated values for the $H\alpha$ extinction coefficient are presented in Table 5.7.

The three values for UGC12699 are all in very good agreement within the quoted uncertainties. The extinction value in UGC8098 is low, but within the range quoted in the literature for individual HII regions.

5.4.5 The dependence of internal extinction on inclination and morphology

Inclination

It is of interest to the $H\alpha$ GS study to find whether internal extinction corrections are dependent on the observed inclination of a galaxy. The $Br\gamma$ investigation was not able to provide effective $H\alpha$ extinction values for entire galaxies, only individual regions. In addition, detections of $Br\gamma$ were only made in 8 galaxies. The UCM collaboration (see Section 1.3.2), however, have published data tables containing galaxy ellipticities (Pérez-González et al., 2001), morphologies (Vitores et al., 1996a) and $E(B-V)$ colour excesses (Gallego et al., 1996) for a large number of galaxies in their survey.

Reference	UGC	$F_{Br\gamma}$ (Wm^{-2})	$F_{H\alpha}$ (Wm^{-2})	$F_{H\alpha}/F_{Br\gamma}$	$A(H\alpha)$
Kawara et al. (1989)	12699	$(5.1 \pm 1.2) \times 10^{-17}$	$(2.23 \pm 0.33) \times 10^{-15}$	43.7	1.32 ± 0.26
Ho et al. (1990)	12699	$(4.7) \times 10^{-17}$	$(1.95 \pm 0.29) \times 10^{-15}$	41.5	1.38 ± 0.17
Calzetti et al. (1996)	12699	$(4.99 \pm 0.20) \times 10^{-17}$	$(2.23 \pm 0.33) \times 10^{-15}$	44.7	1.29 ± 0.05
Calzetti et al. (1996)	8098	$(3.05 \pm 0.18) \times 10^{-17}$	$(2.72 \pm 0.41) \times 10^{-15}$	89.2	0.53 ± 0.07

Table 5.7: Results using Br γ fluxes quoted in the literature.

The standard conversion of ellipticity to inclination, i , for spiral galaxies is given by:

$$\cos^2 i = \frac{q^2 - q_0^2}{1 - q_0^2} \quad (5.4)$$

where q is the axial ratio (equal to $1 -$ the ellipticity), and q_0 is the intrinsic axial ratio (Hubble, 1926). q_0 is assumed here to be 0.2 (Holmberg, 1958).

The colour excess values in Gallego et al. (1996) are computed using either $H\gamma/H\beta$ or $H\alpha/H\beta$ observed intensity ratios. Corrections for Galactic extinction can be found in Vitores et al. (1996a). These have been determined from the Burstein & Heiles (1982) maps at the Galactic coordinates of each UCM object. The corrected values of $E(B-V)$ can be converted to $A(H\alpha)$ using the extinction law of Cardelli et al. (1989), which gives:

$$A(H\alpha) = 0.828 \times R_v \times E(B - V) \quad (5.5)$$

where

$$R_v \equiv \frac{A(V)}{A(B) - A(V)} = \frac{A(V)}{E(B - V)} = 3.1. \quad (5.6)$$

Figure 5.9 shows the calculated $H\alpha$ extinction in magnitudes plotted against the cosine of the inclination for 109 UCM spiral galaxies. The solid line is the best-fit straight line through the points calculated using the least-squares regression method. The equation of the line is

$$A(H\alpha) = 1.712 - 0.440 \times \cos(i). \quad (5.7)$$

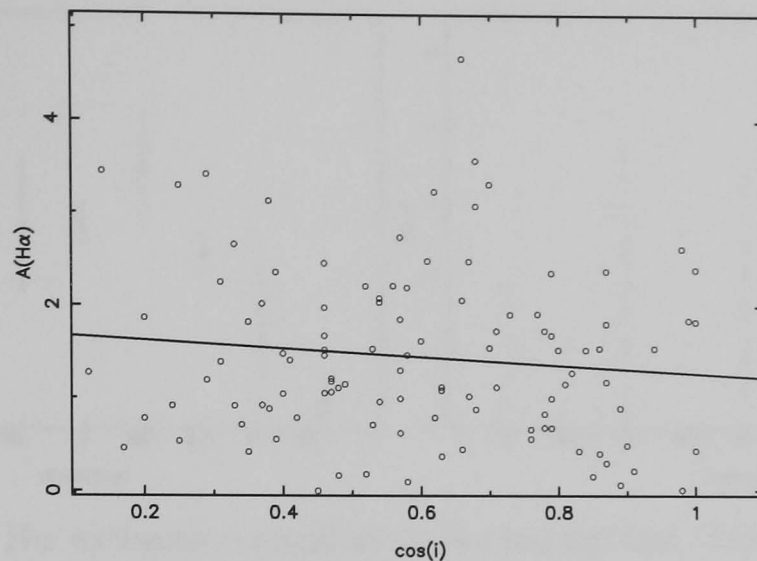


Figure 5.9: The $H\alpha$ extinction coefficient plotted against the cosine of the inclination for 109 UCM galaxies.

However, the linear correlation coefficient for this fit is 0.106, indicating the significance for the relationship to be just 72%. On this evidence, it is fair to say that there is no significant correlation between extinction and galaxy inclination.

Morphology

We can also use the UCM data to investigate whether there is significant type-dependence of extinction values. Vitores et al. (1996a) classify each of the UCM galaxies according to the classical Hubble types, as well as including the BCD (Blue Compact Dwarf) type. They define BCDs as galaxies possessing all of the following properties: compact appearance in the direct image, linear size (D_{24}) lower than 10 kpc, luminosity $M_r > -19$, and photometric parameters typical of later Hubble types. Spectral information from Gallego et al. (1996) was also used for confirmation.

The extinctions calculated from the colour-excess values in Gallego et al. (1996) are plotted against the assigned morphologies in Figure 5.10. The plot featuring the individual galaxy values shows a large amount of scatter within each galaxy type. Vitores et al. (1996a) estimate the typical uncertainty in their adopted morphologies is about one Hubble type. However, this is unlikely to be the primary cause of the scatter, as inspection of the mean extinctions for each galaxy

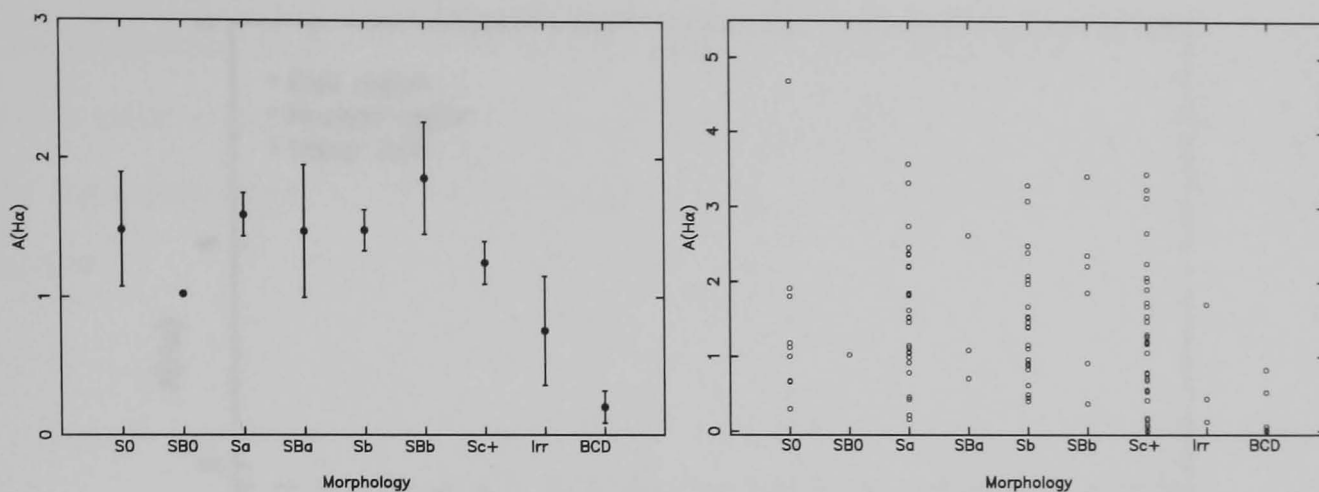


Figure 5.10: The $H\alpha$ extinction coefficient plotted against Hubble type. The plot on the left shows the mean values for each type, with the error bars representing the standard deviation divided by the square root of the number of galaxies of that type. The plot on the right shows each of the 120 UCM galaxies for which both extinction and morphology data are available.

type reveals that $A(H\alpha)$ varies very little between S0 and Sb type galaxies. The mean extinction is slightly lower for late-type spirals and drops dramatically for irregulars and BCD galaxies.

Kennicutt (1998) recommends an $H\alpha$ extinction value of 1.1 mag for all galaxy types. Figure 5.10 would suggest higher corrections of around 1.5 mag for early-type spiral galaxies, 1.2 mag for late-type spirals, and a lower value of around 0.4 mag for Magellanic irregulars and dwarf galaxies.

5.4.6 Internal extinction - summary and conclusions

Twenty-two galaxies were observed through $Br\gamma$ filters at UKIRT in order to investigate the effects of extinction internal to the galaxies observed in the $H\alpha$ GS sample. Only 8 of the galaxies provided any detections of $Br\gamma$ however, with most of these containing just 1-3 isolated regions of measurable flux. UGC5786 was the only object where nearly the whole galaxy could be detected in $Br\gamma$. These data cannot be used, therefore, to investigate the overall effective extinction for entire galaxies.

$H\alpha$ extinction coefficients were calculated for each of these individual regions and have been plotted in Figure 5.11, along with the upper limits derived from

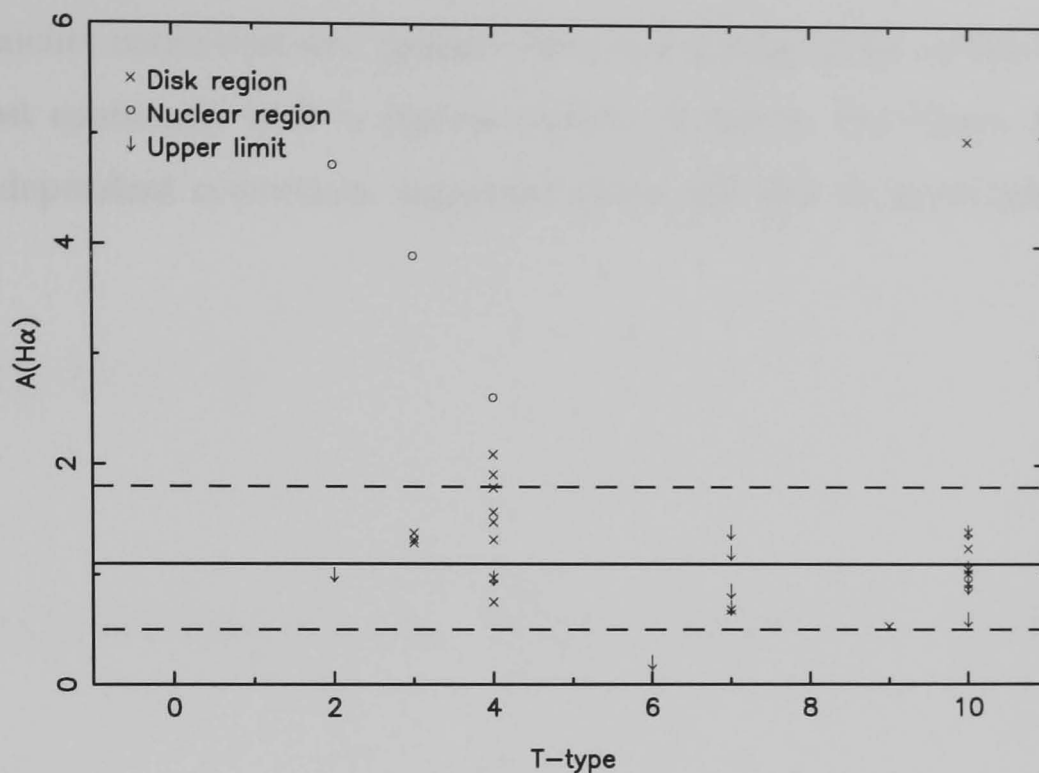


Figure 5.11: The $H\alpha$ extinction coefficients and upper limits calculated using $Br\gamma$ fluxes, plotted against Hubble T-type. Error bars have been omitted for clarity, but uncertainties can be found in Tables 5.4, 5.5 and 5.7. The solid line is positioned at $A(H\alpha)=1.1$ mag, and the dashed lines at 0.5 and 1.8 mag.

investigating the regions with the highest $H\alpha$ fluxes. In most cases, $A(H\alpha)$ values are found to be in the 0.5-1.8 mag range quoted in the literature and bounded by the dashed lines in the plot. Errors bars have been omitted here for clarity, but one third of the plotted values are consistent with the Kennicutt (1998) value of 1.1 mag, represented by the solid line. Higher extinction values were found in nuclear regions, indicating the presence of large amounts of extinguishing dust.

Not enough data were available here to investigate any relationship with galaxy morphology. It is clear, however, that $A(H\alpha)$ varies even within single galaxies.

The UCM $H\alpha$ survey has provided extinction, inclination and morphology data for over 100 galaxies. Investigating the relationship between inclination and extinction shows no evidence of a correlation. Thus, no correction for inclination will be applied to the $H\alpha$ GS data when extinction is accounted for. Kennicutt (1998) adopts a single correction for all Hubble types of 1.1 mag. The UCM data, however, suggest a correction of 1.5 mag for early-spiral types (S0-Sbc), 1.2 mag for late-spiral types (Sc+), and 0.4 mag for irregular and dwarf galaxies.

The Kennicutt correction was applied when calculating SFRs in this work as it is the most commonly used in similar studies. However, the effects of applying the type-dependent corrections suggested above will also be investigated in this thesis.

Chapter 6

Comparison of $H\alpha$ and IR SFRs

The IRAS satellite has measured FIR fluxes for over 30,000 galaxies (Moshir et al., 1992). As mentioned in Section 1.4.3, the far-infrared continuum can be used as an indirect tracer of star formation. Thus, the data from IRAS contain huge potential for the study of star formation in galaxies if they can be accurately calibrated.

Complications arise from the uncertainties in the processes responsible for the heating of the IR-emitting dust. Devereux & Young (1990) and Devereux & Hameed (1997) argue that high-mass ionising stars dominate the dust heating. If this is the case, then the FIR luminosity of a galaxy should correlate well with the $H\alpha$ luminosity, since this is also the result of the UV radiation field from OB stars. Others (e.g. Lonsdale Persson & Helou 1987; Buat & Deharveng 1988; Sauvage & Thuan 1992) have argued that cirrus emission from dust heated by the general stellar radiation field, including old, low-mass stars, is also an important factor. In this case, we would expect early-type galaxies, with older overall stellar populations, to produce higher FIR luminosities than predicted by $H\alpha$ -calculated SFRs.

The large size of the $H\alpha$ GS sample, combined with the excellent coverage of galaxy morphologies and surface brightnesses, makes it a good test bed for investigating the reliability of using FIR luminosities to trace high-mass star formation.

6.1 IRAS flux densities, FIR luminosities and converting to SFR

The H α GS sample was cross-correlated with the IRAS Faint Source Catalogue v2.0 (FSC) using a search radius of 60.0'' around the galaxy positions quoted in NED. 178 galaxies were found in common.

A convenient representation of the FIR flux measured by IRAS is that defined by Helou et al. (1988):

$$F_{FIR} = 1.26 \times 10^{-14} (2.58 f_{60} + f_{100}). \quad (6.1)$$

f_{60} and f_{100} are the nominal flux densities (in Jy) within the 60 and 100 μm bands measured by IRAS. F_{FIR} is the flux that would be measured (in Wm^{-2}) from a source within a 'square-wave' bandpass, 80 μm wide, centred at 82.5 μm . The photometric uncertainties of the flux densities are $\sim 10\text{-}15\%$ (Beichman et al., 1985).

The FIR luminosity, in Solar units, is given by:

$$L_{FIR} = 3.13 \times 10^{19} D^2 F_{FIR}, \quad (6.2)$$

where D is the galaxy's distance in Mpc, calculated as described in Section 3.11.

The calibration of L_{FIR} to SFR varies within the literature and depends on assumptions about the star formation timescale. Kennicutt (1998) gives a calibration calculated for starbursts with ages less than 10^8 years. In more quiescent, normal star-forming galaxies, the empirical relation found by Buat & Xu (1996) is the most appropriate, and hence is used here:

$$\text{SFR} (M_{\odot}\text{yr}^{-1}) = 3(2 - 6) \times 10^{-10} L_{FIR} (L_{\odot}). \quad (6.3)$$

This correlation is based on IRAS and UV flux measurements of 152 disk galaxies.

The values given in brackets indicate the 1σ interval found for the FIR to UV luminosity ratio. The IMF assumed here has a high-mass power-law index equal to -2.5 (Scalo, 1986) and an upper-mass cutoff of $100 M_{\odot}$. It should be remembered that the $H\alpha$ SFRs are determined assuming a Salpeter IMF (Salpeter, 1955).

6.2 Comparing $H\alpha$ GS and IRAS star formation rates

The 178 galaxies with both $H\alpha$ GS and IRAS SFRs are plotted in Figure 6.1. The galaxies are coded by galaxy type. The dashed line in the figure represents a one-to-one correlation. The solid line is the best-fit line calculated from a least-squares regression fit to the data. The equation of this line is:

$$\log(IRAS\ SFR) = 1.18 \log(H\alpha\ SFR) - 0.34. \quad (6.4)$$

The plot shows a good correlation between the two measures of SFR, although there is a significant deviation from the one-to-one line. The linear correlation coefficient is 0.91 (where a value of 1 is a perfect correlation and a value of 0 indicates no correlation), with a significance of >99.99%. For the most rapidly star-forming galaxies, predominantly Sb-Sc types, the two measures of SFR agree very well. For the galaxies with lower SFRs, comprised mainly of the later types, the FIR tracer seems significantly to underestimate the star formation, compared to the $H\alpha$.

Figure 6.1 can be compared with the middle plot of Figure 1.1, where $H\alpha$ SFRs are plotted against SFRs from radio-power measurements. The latter can be replaced by $60\ \mu\text{m}$ IR emission, since the top plot shows a strong one-to-one correlation between the two. The increased scatter in Figure 1.1 can largely be accounted for by the large number of different data sets the points are extracted from. The trend for IR measurements to predict lower SFRs at the low end of

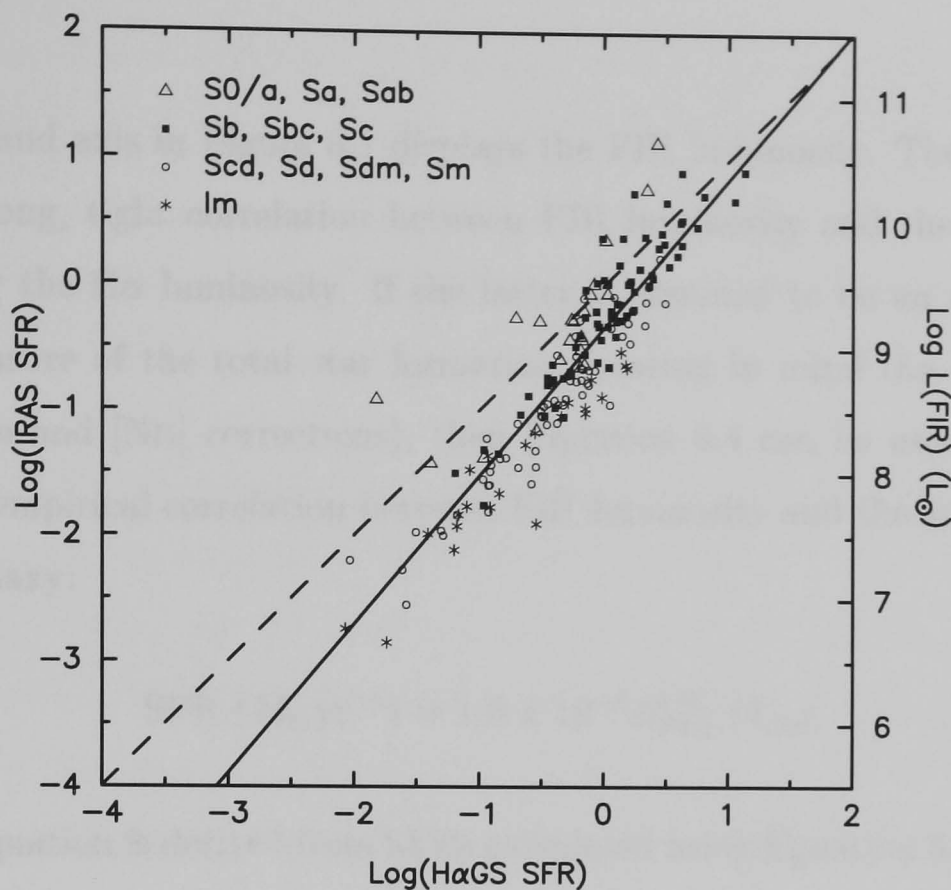


Figure 6.1: The SFRs derived using infrared compared to those found from the $H\alpha$ data. The dashed line is the one-to-one relation and the solid line is the best-fit line to the data. The axis on the right displays the FIR luminosity of the galaxies in Solar units.

the scale than the $H\alpha$ measurements is visible here. One possible reason for this is that galaxies with low SFRs may have lower dust opacities, and thus be less efficient at absorbing the stellar-UV radiation field from new stars and re-emitting it at infrared wavelengths. Other possible causes of this trend are mentioned in Section 1.4.6.

The slope of a best fit-line to the points in the middle plot of Figure 1.1 would clearly fall some way from 1, and an attempt to measure this gradient by hand results in a value of approximately 0.7. The corresponding gradient for the $H\alpha$ GS-IRAS relation is 0.85. Both investigations show that the assumption of a linear correlation between FIR luminosity and SFR in Equation 6.3 does not appear to be valid. This is further supported by Sauvage & Thuan (1992), who find a slope of 0.69 when examining the same relationship for a sample of 135 galaxies. They argue that this supports the two-component model where the FIR luminosity comes from both star-forming regions and quiescent cirrus-like regions of the

ISM.

The right-hand axis in Figure 6.1 displays the FIR luminosity. The plot clearly shows a strong, tight correlation between FIR luminosity and the SFR as determined by the $H\alpha$ luminosity. If the latter is assumed to be an accurate and reliable measure of the total star formation (bearing in mind the uncertainties in extinction and [NII] corrections), then Equation 6.4 can be used to derive a non-linear, empirical correlation between FIR luminosity and the star formation rate of a galaxy:

$$\text{SFR} (M_{\odot}\text{yr}^{-1}) = 1.6 \times 10^{-8} L_{FIR}^{0.85} (L_{\odot}). \quad (6.5)$$

Since this equation is derived from SFRs calculated using Equation 3.12, the same Salpeter IMF assumption will apply (see Section 3.7).

6.3 The dependence of the FIR luminosity on galaxy morphology

The galaxies in Figure 6.1 are coded by morphological type. It can clearly be seen that the early-type galaxies (S0/a-Sab) tend to lie above the best-fit line, indicating an excess of FIR flux compared to the predictions of the new calibration. This is in agreement with the findings of Buat & Xu (1996) and supports the theories of old, low-mass stars contributing significantly to the dust-heating stellar-radiation field. Young et al. (1996), for their sample of 120 disk galaxies, and Devereux & Young (1990), for 124 spiral galaxies from the survey of Kennicutt & Kent (1983), on the other hand, find no significant difference in the regions where the early- and late-type spiral galaxies are located on their equivalent plots.

Figure 6.2 contains histograms of the ratio of the FIR SFR (as calculated using Equation 6.5) to the $H\alpha$ SFR for different galaxy morphologies. The difference between early and late types is immediately clear. The 22 early-type spirals

	S0/a-Sab	Sb-Sc	Scd-Sm	Im	S0/a-Im
mean $\frac{SFR(FIR)}{SFR(H\alpha)}$, $A(H\alpha) = 1.1$	3.17 ± 0.91	1.29 ± 0.09	0.86 ± 0.05	0.62 ± 0.06	1.28 ± 0.13
mean $\frac{SFR(FIR)}{SFR(H\alpha)}$, variable $A(H\alpha)$	2.18 ± 0.66	0.89 ± 0.06	0.78 ± 0.05	1.18 ± 0.11	1.05 ± 0.09
N	22	70	62	24	178

Table 6.1: The mean ratios of the SFRs calculated from FIR and H α data for different Hubble types.

(S0/a-Sab) display the largest scatter, but clearly show the highest IRAS/H α GS SFR ratios. As we go along the Hubble sequence to later types, we see this ratio systematically decreasing. The mean ratios and their standard errors are given in the top row of Table 6.1. The trend is the same as that seen by Sauvage & Thuan (1992), but much stronger than the findings of Devereux & Young (1990) and Young et al. (1996).

As well as contributions from the old stellar populations, there are several other possible causes of the observed decrease in SFR(IRAS)/SFR(H α GS) along the Hubble sequence. In Figure 5.10, we saw that the H α extinction is higher in early-type spiral galaxies and falls off towards the latest types. The H α luminosities used to calculate the SFRs here have all been corrected by the same extinction factor ($A(H\alpha)=1.1$ mag), irrespective of galaxy type. If we have underestimated the extinction in early-type galaxies, then the H α luminosities will also be underestimated and the observed SFR(IRAS)/SFR(H α GS) will be too high. The converse is true for the late types. Kewley et al. (2002) compare IR and H α SFRs for a sample of 93 galaxies before and after correcting each galaxy individually for extinction. Before corrections they find the same trend as above, but after the corrections are applied they find that the SFR(IR)/SFR(H α) ratios for early and late types are approximately equal.

The results of replacing the standard 1.1 mag correction in the H α GS sample with the corrections suggested by the UCM data in Section 5.4.5, i.e. 1.5 mag for S0/a-Sc, 1.2 mag for Scd-Sm and 0.4 mag for Im galaxies, can be seen in Figure 6.3 and in the second row of Table 6.1. From these results, it appears that extinction effects are at least partly responsible for the morphological dependence.

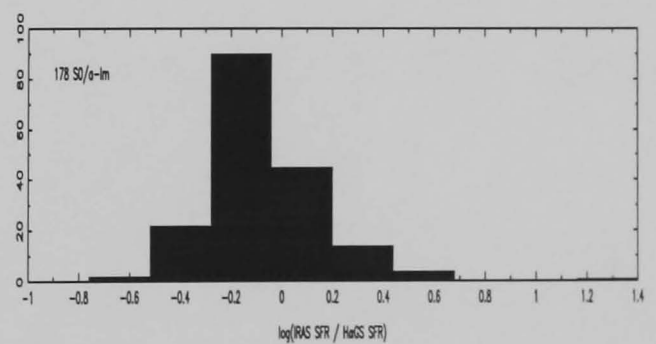
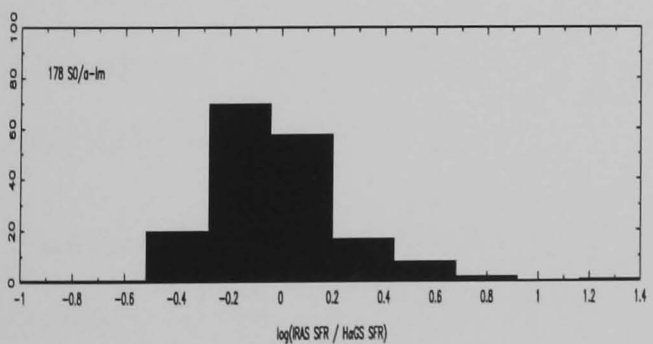
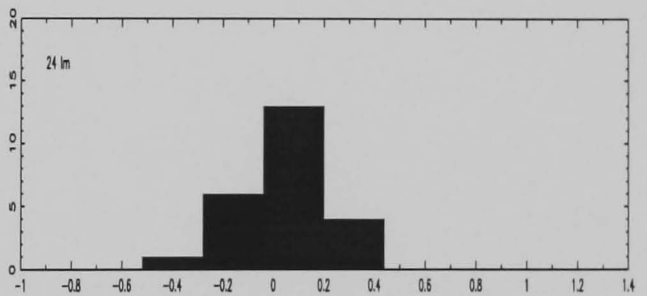
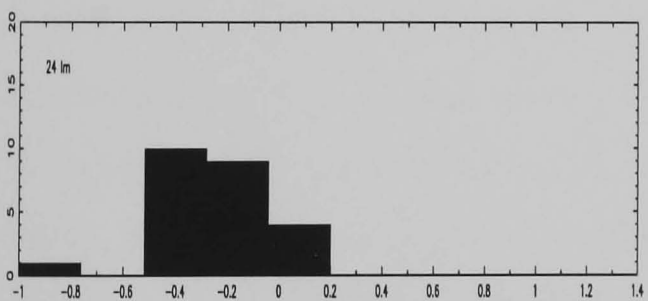
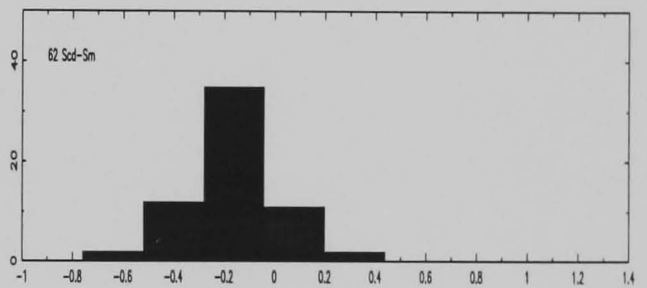
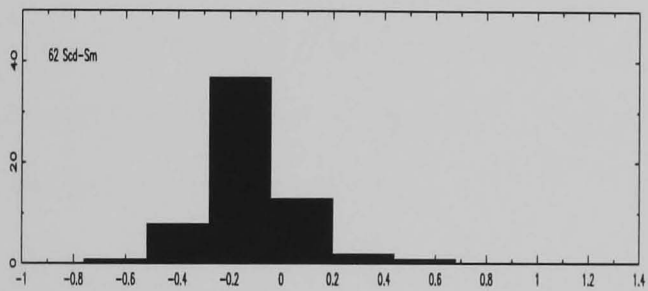
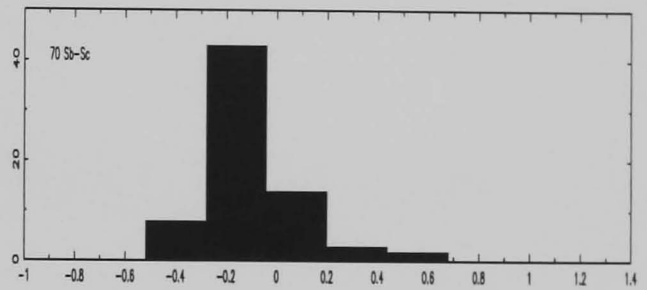
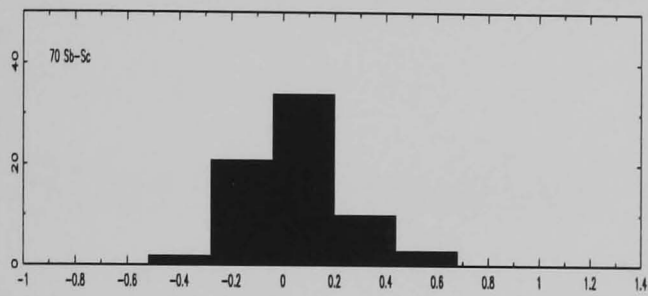
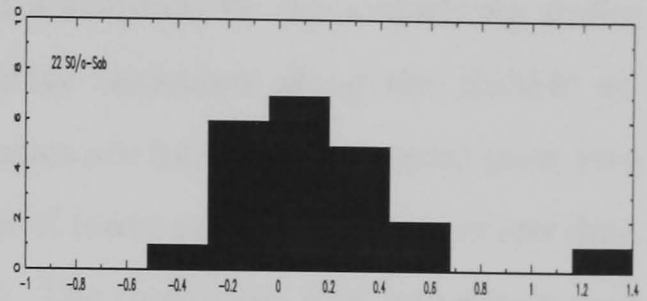
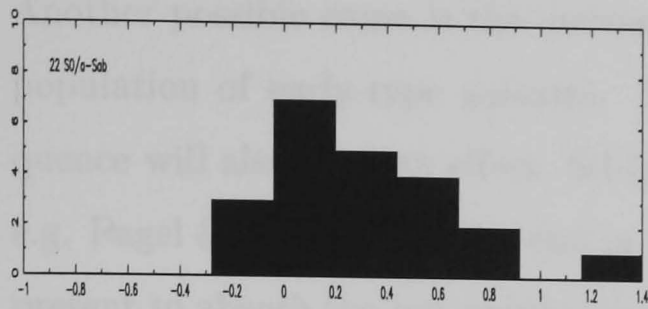


Figure 6.2: Histograms of the ratio of IRAS SFRs to H α GS SFRs as a function of morphological type. H α fluxes have been corrected using a uniform extinction correction of 1.1 mag.

Figure 6.3: As in figure 6.2, but with the morphologically-dependent extinction corrections derived from the UCM data (see text) applied to the H α fluxes.

Another possible cause is the increased $H\alpha$ absorption by the underlying stellar population of early-type galaxies. Metallicity variations along the Hubble sequence will also have an effect. Sd-Im galaxies are known to be metal poor (see e.g. Pagel & Edmunds 1981), and in regions of lower metallicity there is less dust present to absorb the bolometric luminosity. The re-emitted FIR luminosity may thus be low in these galaxies, compared to the $H\alpha$ emission.

Chapter 7

Star formation within galaxies

There are many problems with the current understanding of the formation and evolution of disks in galaxies. The impacts of spiral arms (see e.g. Roberts 1969; Seiden & Gerola 1982; Seigar & James 2002), bars (see e.g. Sérsic & Pastoriza 1967; Martinet & Friedli 1997; Ho et al. 1997), and the infall of new gas (see e.g. Stephens & Velusamy 1989; Phookun et al. 1993) on the distribution of the stellar and gaseous content of disks are still not fully understood. Environmental effects, such as interactions with intra-group or intra-cluster media (see e.g. Gunn & Gott 1972; Dressler & Gunn 1983; Mulchaey et al. 1993; Koopmann & Kenney 2002), or tidal interactions with a close neighbour (see e.g. Kennicutt et al. 1987; Bushouse et al. 1988; Byrd & Valtonen 1990; Moore et al. 1996) can also affect the distribution of stars and gas within a galaxy. It is also interesting to look at evolutionary changes in disks, implied by the relative distribution of young and old stars.

Probably the major advantage of a photometric imaging survey over a spectrophotometric survey is the ability to map star formation over the entire galaxy. One of the principal aims of the H α Galaxy Survey is to investigate the star formation distribution within galaxies. These galaxy maps also allow individual regions of star formation to be identified and investigated. Galaxies with unusual star formation distributions, such as those involved in interactions, can also be easily

recognised.

7.1 Calculating concentration indices

A straightforward approach to investigating star formation distribution, which enables easy comparisons between different galaxies, is to examine the concentration of H α light within a galaxy. It is also of interest to compare this to the concentration of the continuum emission from the galaxy to see how the star forming regions are distributed with respect to the older stars.

7.1.1 Effective radii

A first attempt to compare the relative concentrations of old and new stars is to take the ratio of the effective radii r_e in each band. The effective radius is the semi-major axis of the ellipse that contains half of the total light of the galaxy. The total H α -flux value was taken to be the value found in Section 3.6 and the total R flux was similarly taken as the value when three consecutive points in the growth curve varied by less than 0.5%. The data measured using elliptical apertures were utilised for inclined spiral galaxies, and that from circular apertures for face-on spirals and irregular galaxies.

Galaxies with higher central concentrations will have lower effective radii. If the H α light is more centrally concentrated than the R light, then the ratio $r_e(\text{H}\alpha)/r_e(\text{R})$ will be less than 1.

7.1.2 The $\log C_{31}$ index

A more sophisticated method to investigate the internal distribution of light in a galaxy is the use of concentration indices. A concentration index is an objective tracer of the radial light distribution of a galaxy and will be correlated with the

bulge-to-disk ratio and Hubble type of the galaxy (Morgan, 1958; de Vaucouleurs, 1977; Kent, 1985; Abraham et al., 1994).

de Vaucouleurs (1977) introduced the commonly used C_{31} index. This is defined as the ratio of radii that contain 75% (r_{75}) and 25% (r_{25}) of the total (asymptotic) galaxy luminosity. These radii are chosen so that the inner radius is not so small as to be affected by seeing corrections, whilst the outer radius is not so large as to be affected by errors arising from uncertainties in the sky background (Kent, 1985).

The measured R and H α growth curves for the galaxies in the H α sample were used to find values of r_{75} and r_{25} . The total H α and R flux values were defined in the same way as for the effective-radii calculations. The concentration index for each galaxy was taken as:

$$CI = \log[r_{75}/r_{25}] \quad (7.1)$$

A centrally concentrated galaxy will have a smaller r_{25} , and thus a larger value for the concentration index than a galaxy where the light is more evenly distributed. For a constant-surface-brightness, ‘top hat’, light profile, Equation 7.1 gives $CI = 0.239$. An exponential profile (such as would be expected from a galaxy’s disk) will have a concentration index of 0.447, whereas an $r^{1/4}$ law profile (similar to many galaxy bulges) will have a concentration index of 0.845.

The relative distributions of R and H α light can be compared by subtracting the H α index from the R index. A positive value indicates that the continuum light is more concentrated, whereas a negative value shows that the H α light is more centrally concentrated.

7.1.3 The Petrosian index

A second definition of the (inverse) concentration index is that used by Shimasaku et al. (2001) to investigate the light distribution of galaxies observed as part of

the Sloan Digital Sky Survey (SDSS):

$$CI_p = r_{p50}/r_{p90} \quad (7.2)$$

where r_{p50} and r_{p90} are the radii which contain 50% and 90% of the Petrosian flux, respectively. The Petrosian flux is the flux within the Petrosian radius, r_p , which itself is defined as the parameter that satisfies

$$\eta = \frac{I(r_p)}{2\pi \int_0^{r_p} I(r)rdr / (\pi r_p^2 \times (b/a))}. \quad (7.3)$$

$I(r)$ is the surface-brightness profile of the galaxy, so η is the ratio of the surface brightness at r_p to the average surface brightness within that radius (Petrosian, 1976). For values calculated using elliptical apertures, the radius is replaced by the semi-major axis of the ellipse. The factor (b/a) is the ratio of the semi-minor to semi-major axes and will equal 1 when circular apertures are used. Shimasaku et al. (2001) adopt $\eta = 0.2$. Centrally concentrated galaxies will have a lower CI_p .

The advantage of this definition of a concentration index is that using surface-brightness ratios is more objective and less susceptible to fluctuations in sky background than approximating the total flux of the galaxy. The Petrosian quantities are also physically well defined, independent of the distance of the galaxy or extinction. A further reason for calculating these indices for the low-redshift H α GS galaxies is to enable a comparison with higher-redshift Universe as sampled by the SDSS.

The Petrosian concentration index works well when investigating the smooth, continuous surface-brightness profiles of the R-band and H α Cont images. The H α emission from galaxies, however, often does not form such a continuous profile, but will consist of discrete individual regions of flux. The ratio of the surface brightness at a point to the average surface brightness up to that point will not fall off in the same, steady way as for the continuum images, but will fluctuate depending on the number of HII regions at that radius. This makes the defini-

tion of the Petrosian radius a less suitable reference point by which to define a concentration index. An example of this problem can be seen in Figures 7.1-7.3.

The relative distributions of R and H α light can be compared by dividing the R index by the H α index. A value less than 1 indicates that the continuum light is more concentrated, whereas a value greater than 1 shows that the H α light is more centrally concentrated.

7.1.4 Comparing concentration indices

The three different methods of investigating the concentration of light within a galaxy were plotted against each other and their correlations were calculated. Effective radii are dependent on galaxy size, and so only the ratio of the half-light radii of the continuum and H α images can be correlated with the relative concentration indices from the other two methods.

Figure 7.4 shows that there is a very tight correlation between the two forms of the concentration index used when examining the continuum light. The linear correlation coefficient for the relationship is 0.877 (where a value of 1 is a perfect correlation and a value of 0 indicates no correlation). The significance of this result was tested by randomly re-assigning the values of one set of concentration indices to the galaxies. The new linear correlation coefficient was then found. This was repeated 10,000 times and the number of times the new correlation coefficient was found to be greater than that of the original, observed correlation was counted. In this case, no correlation coefficients were found in the randomly re-assigned trials that were greater than 0.877, giving the correlation a significance of greater than 99.99%.

Figure 7.5 shows a correlation between the H α indices with much more scatter. At large part of this scatter will be due to the problems in calculating CI_p for H α referred to in Section 7.1.3. The linear correlation coefficient here is 0.683, again with a significance of greater than 99.99%.

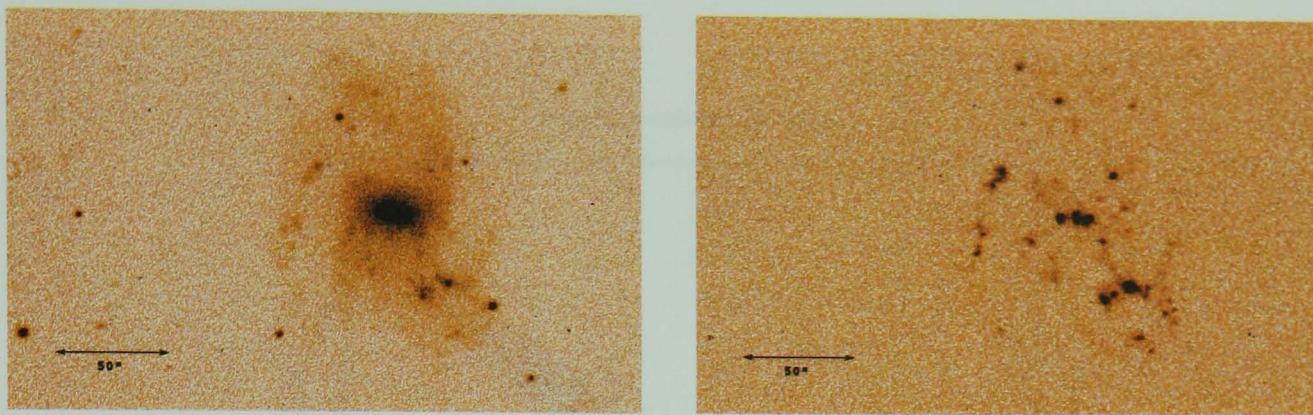


Figure 7.1: The galaxy UGC5589 in R-band light (left) and in H α (right)

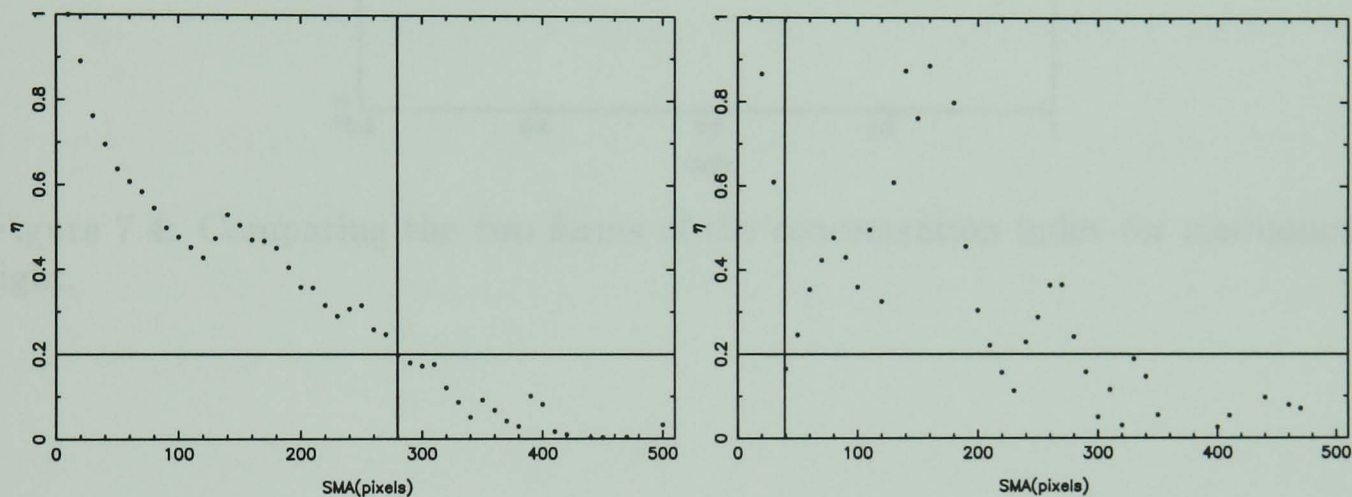


Figure 7.2: The variation of η with semi-major axis in the R-band image (left) and in H α (right). The vertical line indicates the first value where $\eta = 0.2$ for the galaxy image, and hence is located at a Petrosian radius. The H α profile crosses the $\eta = 0.2$ line several times, and hence there is clearly some ambiguity as to the location of the Petrosian radius to be used.

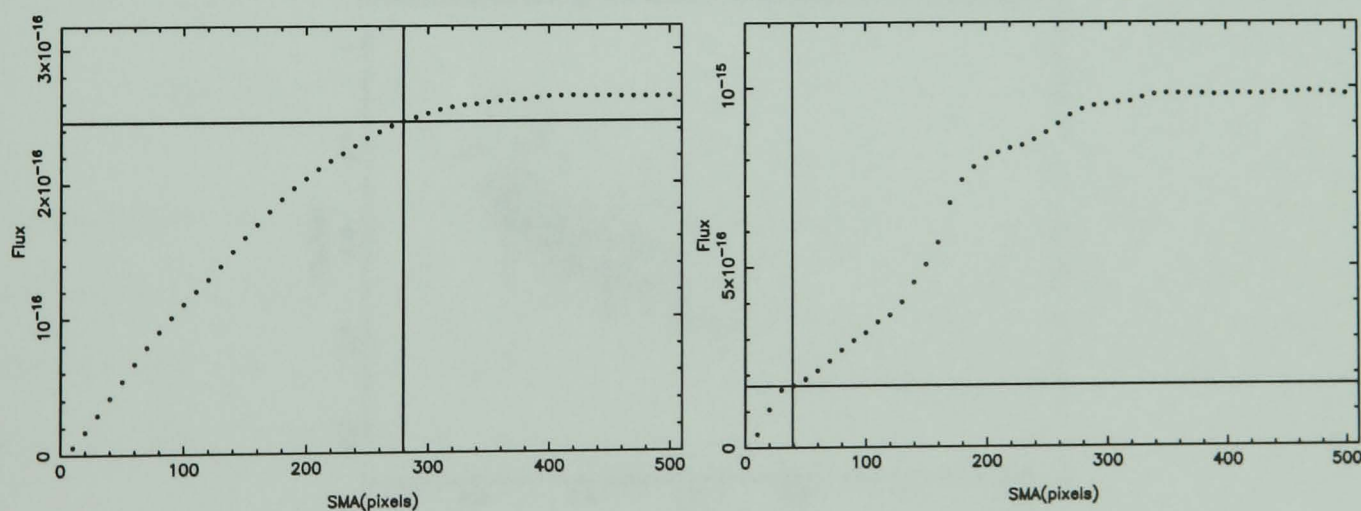


Figure 7.3: The horizontal line indicates the Petrosian flux (in $\text{Wm}^{-2}\text{nm}^{-1}$ for the continuum image (left) and in Wm^{-2} for the H α (right)) and the vertical line shows the Petrosian radius. From this example, it is clear that this method is not the most suitable for use with H α images.

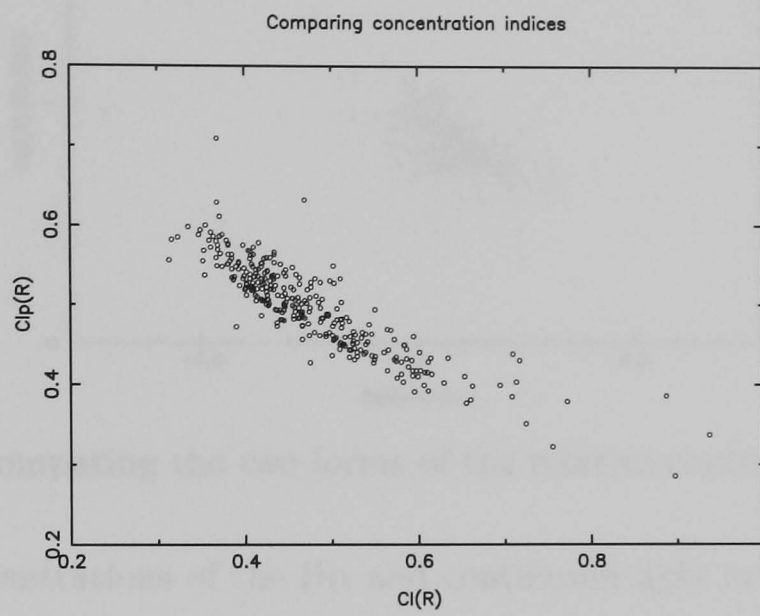


Figure 7.4: Comparing the two forms of the concentration index for continuum light.

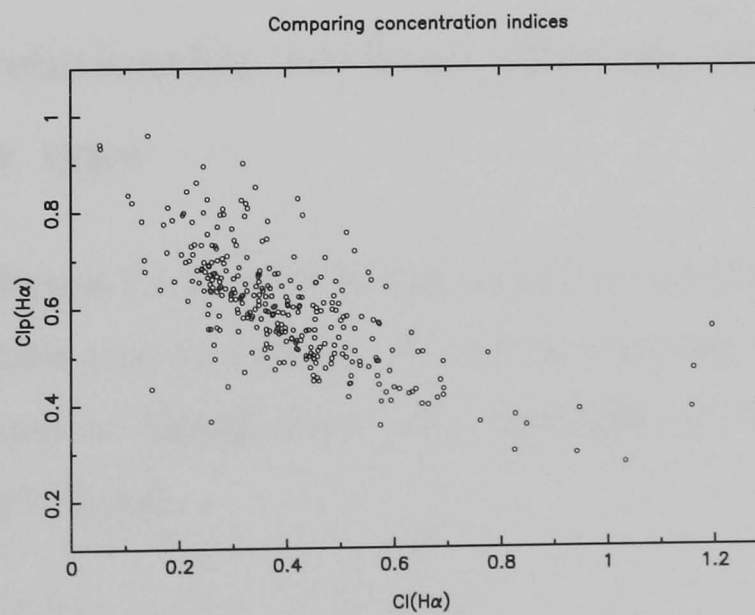


Figure 7.5: Comparing the two forms of the concentration index for $H\alpha$ light.

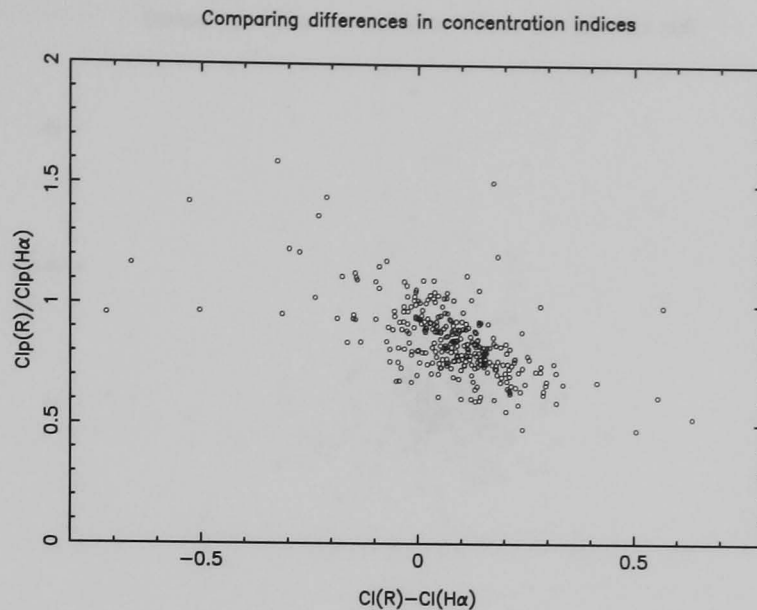


Figure 7.6: Comparing the two forms of the relative concentration index.

The relative concentrations of the $H\alpha$ and continuum light are given by $CI(R) - CI(H\alpha)$ and $CI_p(R)/CI_p(H\alpha)$. The correlation between the two is plotted in Figure 7.6. The linear correlation coefficient has a value of 0.600 with a significance of greater than 99.99%.

Comparing the values of $CI(R) - CI(H\alpha)$ with the ratio $r_e(H\alpha)/r_e(R)$ gives a correlation coefficient of 0.290 (Figure 7.7). Even though this is much lower than the other correlations, it still has a significance of greater than 99.99%.

7.1.5 The relationship between concentration index and galaxy type

As mentioned in Section 7.1.2, concentration indices are usually found to correlate well with the Hubble type of a galaxy. To test this was the case for the $H\alpha$ GS sample and the indices defined above, the concentration indices were plotted against the galaxy's T-type.

The $\log C_{31}$ index *v.* type

Figure 7.8 shows the mean and the individual values of CI binned by galaxy type. As mentioned in Section 7.1.2, an exponential profile (such as would be

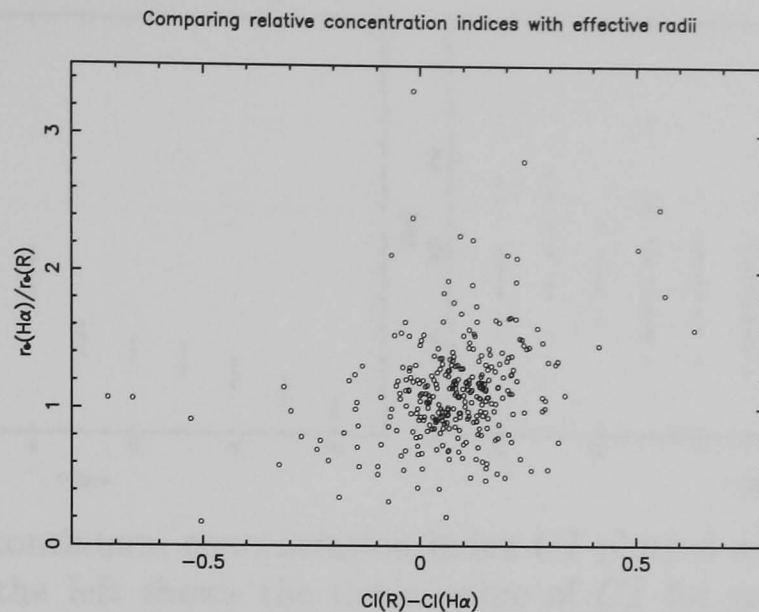


Figure 7.7: Comparing the relative concentration index to the ratio of effective radii.

expected for a galaxy's disk) will have a concentration index of 0.447, whereas an $r^{1/4}$ law profile (similar to that of a galaxy's bulge) would have a concentration index of 0.845. The plot of the mean concentration index for each type shows a clear relationship, with the bulge-dominated S0/a and Sa galaxies having the highest values as expected. The later type, disk-dominated, spiral galaxies and the irregulars have indices that approximate to those expected for exponential profiles, in accordance with the findings of Kent (1985).

The plot showing the individual values demonstrates that there is a very large dispersion within each galaxy type. This agrees with the findings of Shimasaku et al. (2001) and Gavazzi et al. (1990), and reflects the wide range of bulge-to-disk ratios within a given Hubble type (e.g. Kent 1985). The linear correlation coefficient for this relationship is 0.597, with a significance of >99.99%.

Figure 7.9 shows similar plots for the $H\alpha$ concentration index. Again, there is a clear relationship between CI and the galaxy classification, with the late-type spirals and irregulars possessing values lower than the early types. The results for the S0/a galaxies are less reliable due to the problems involved in calculating growth curves when there is extremely high continuum emission and very little $H\alpha$ line emission. Over-subtraction of the continuum and $H\alpha$ absorption can result in growth curves with negative fluxes in the centre. These effects can also

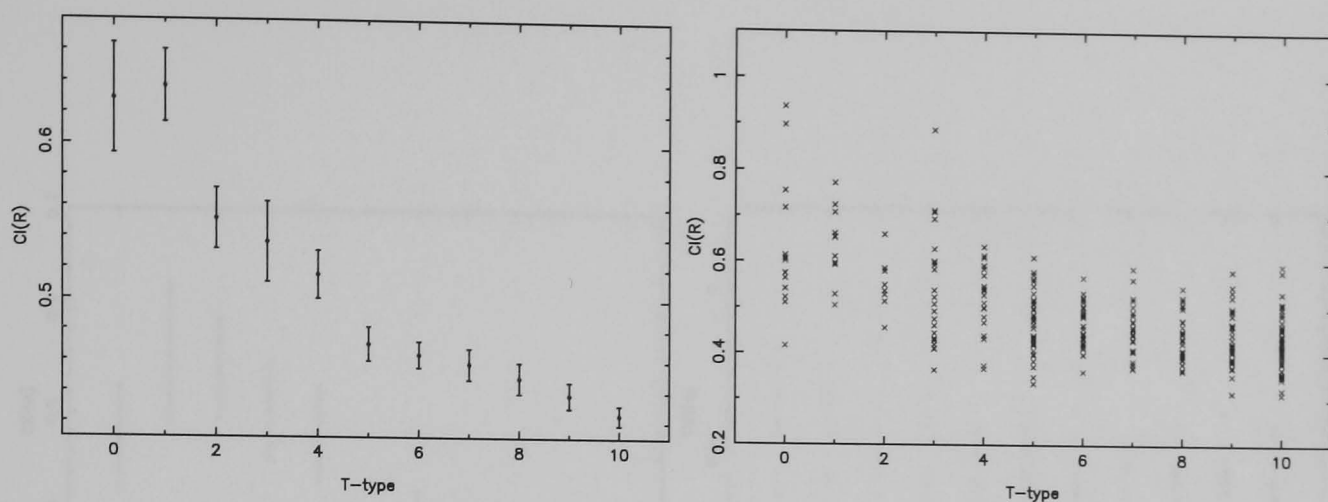


Figure 7.8: The continuum concentration index CI plotted against Hubble type T . The plot on the left shows the mean value of CI for each type, with the error bars representing the standard deviation divided by the square root of the number of galaxies of that type. The plot on the right shows each of the galaxies for which CI has been calculated.

be a problem for some of the bright Sa galaxies.

As with the continuum indices, there is a large scatter of values within each type. The linear correlation coefficient calculated here is 0.348, with a $>99.99\%$ significance.

Figure 7.10 investigates the relative concentrations of the continuum light and the $H\alpha$ line emission. If the distribution of light for the two galaxy images was identical, the value of $CI(R) - CI(H\alpha)$ would be 0. The figure clearly shows that in most cases the relative concentration is positive, implying that the continuum light is more centrally concentrated than the $H\alpha$. This is consistent with the theory that most massive-star formation takes place in the disks of galaxies, whereas the circumnuclear regions contain predominantly old stars.

Figure 7.10 shows that there is no apparent correlation with Hubble type. The correlation coefficient is just 0.0159, with a significance of 23%.

The Petrosian index *v.* type

The Petrosian index is an inverse concentration index, so a more centrally-concentrated galaxy will have a lower value of CI_p . An exponential surface brightness profile will have an index of 0.501 and an $r^{1/4}$ law profile will re-

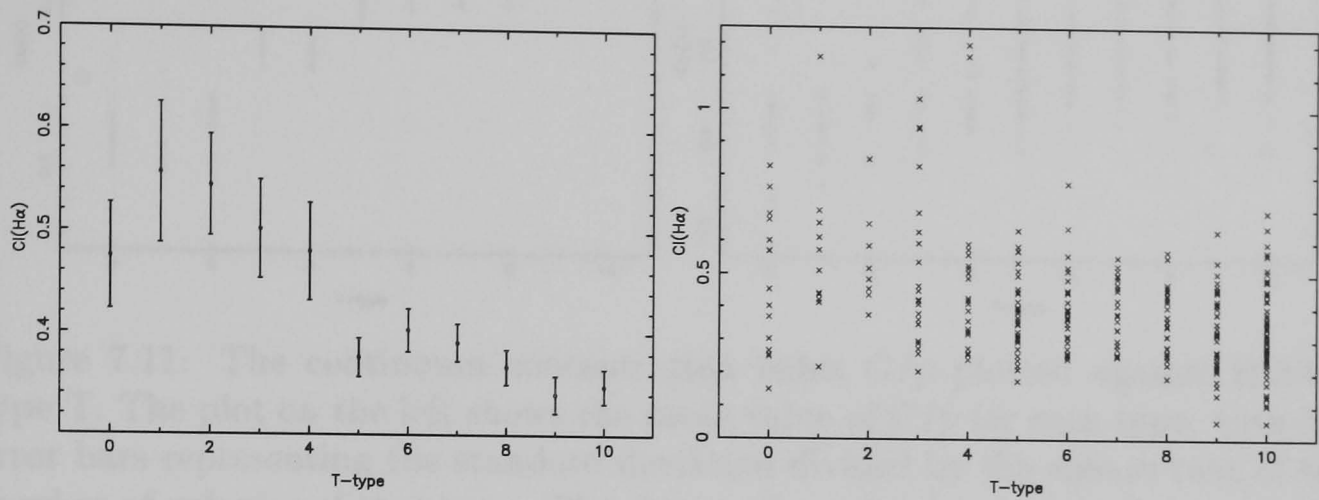


Figure 7.9: The $H\alpha$ concentration index CI plotted against Hubble type T . The plot on the left shows the mean value of CI for each type, with the error bars representing the standard deviation divided by the square root of the number of galaxies of that type. The plot on the right shows each of the galaxies for which CI has been calculated.

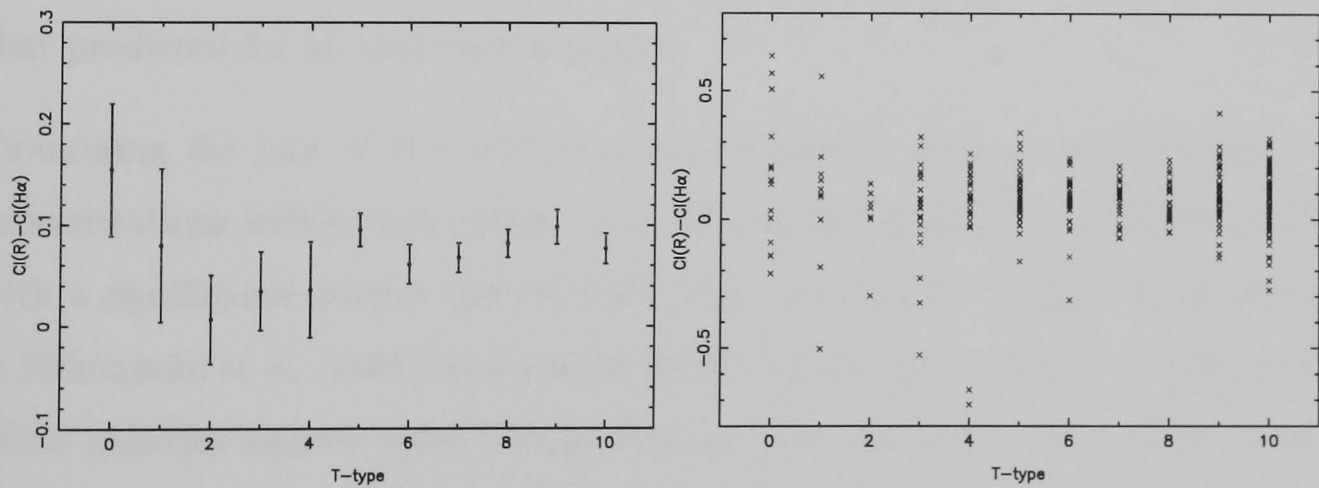


Figure 7.10: The relative concentrations $CI(R) - CI(H\alpha)$ plotted against Hubble type T . The plot on the left shows the mean values for each type, with the error bars representing the standard deviation divided by the square root of the number of galaxies of that type. The plot on the right shows each of the galaxies for which concentration indices have been calculated.

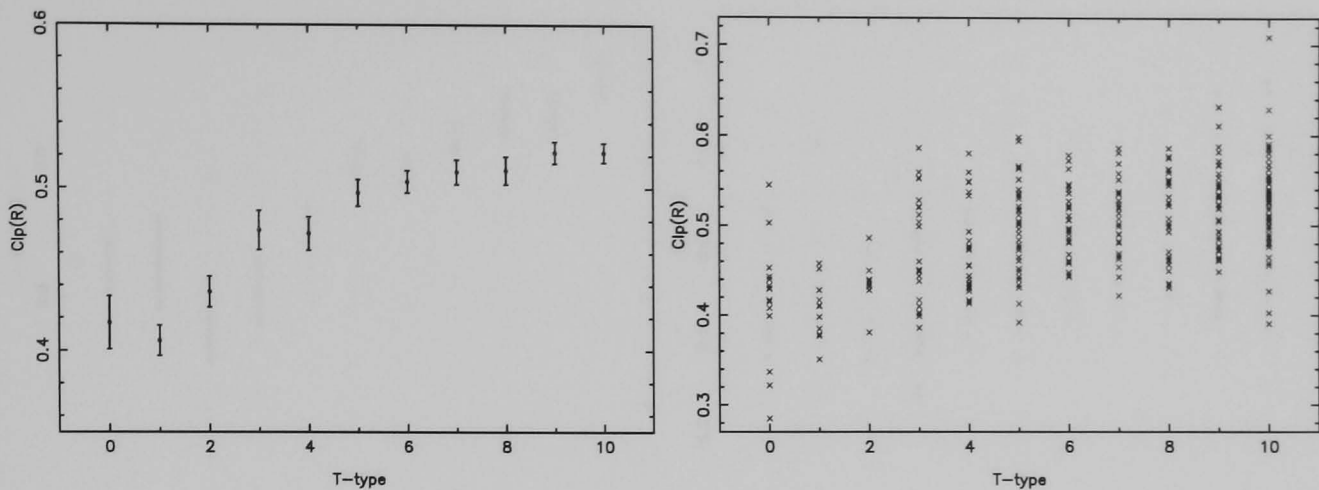


Figure 7.11: The continuum concentration index CI_p plotted against Hubble type T . The plot on the left shows the mean value of CI_p for each type, with the error bars representing the standard deviation divided by the square root of the number of galaxies of that type. The plot on the right shows each of the galaxies for which CI_p has been calculated. This plot can be compared to Figure 10 in Shimasaku et al. (2001).

sult in $CI_p = 0.371$. It is not possible for a constant ‘top hat’ surface-brightness profile to satisfy the definition of the Petrosian radius in Equation 7.3.

In Figure 7.11 the relationship between CI_p and galaxy classification is shown for the continuum light. As with the $\log C_{31}$ index, we see that the bulge-dominated S0/a and Sa galaxies have light profiles that are close to the $r^{1/4}$ law, whereas the irregulars and disk-dominated spirals have concentrations that are similar to that predicted for an exponential profile.

Examining the plot of the individual points again reveals a large dispersion of concentrations within each galaxy type. The linear correlation coefficient is 0.523 with a significance greater than 99.99%. This plot can be compared to Figure 10 in Shimasaku et al. (2001) which plots the Petrosian concentration indices for 426 SDSS galaxies against their T -classification. The values for the H α GS galaxies appear to be systematically higher in general than those of the SDSS galaxies. The majority of SDSS Sa-Im galaxies have indices between 0.35 and 0.50, whereas the H α GS galaxies mostly lie between 0.44 and 0.57 on the plot. One cause of the discrepancy could be that the higher-redshift SDSS survey is biased towards more centrally concentrated galaxies. These would be easier to detect at large distances than the galaxies with more diffuse emission, thus lower values of the

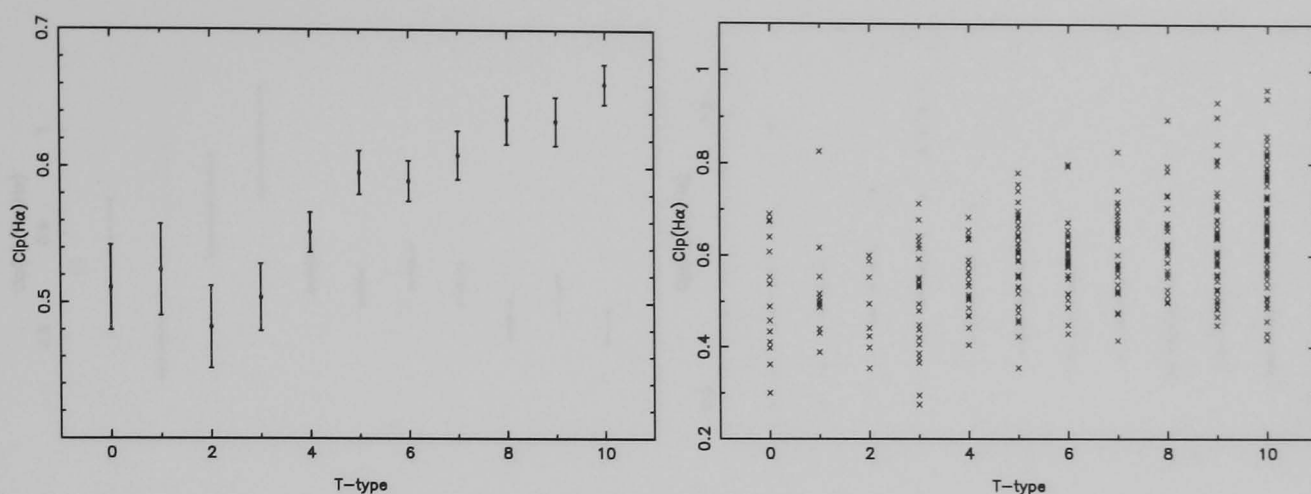


Figure 7.12: The $H\alpha$ concentration index CI_p plotted against Hubble type T. The plot on the left shows the mean value of CI_p for each type, with the error bars representing the standard deviation divided by the square root of the number of galaxies of that type. The plot on the right shows each of the galaxies for which CI_p has been calculated.

Petrosian index are more likely to be detected.

In Figure 7.12 it can be seen that, whilst the $H\alpha$ Petrosian concentration index is not always reliable for individual galaxies (see Section 7.1.3), when examining the sample on a large scale, there is a very strong dependence on Hubble type. The linear correlation coefficient is very high at 0.938.

The Petrosian indices in the two wavebands can be compared by dividing the two values. Values less than 1 imply that the continuum image is more centrally concentrated than the $H\alpha$ emission from the star-forming regions.

Figure 7.13 shows how the relative concentration varies with galaxy type. Sab and Sb galaxies appear to have statistically similar light distributions in both the continuum and the $H\alpha$, whereas all other galaxy types tend to be more centrally concentrated in the continuum. As with the $\log C_{31}$ results, this supports the idea of disk star formation being predominant.

The correlation with type is stronger than in Figure 7.10, with a linear correlation coefficient of 0.176. The significance of this result is 99.88%.

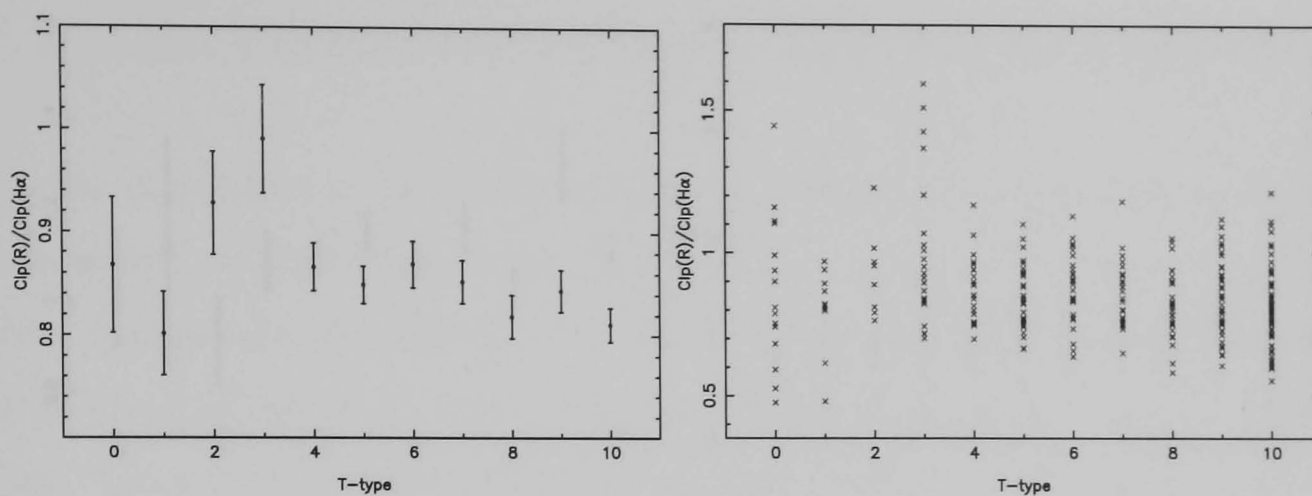


Figure 7.13: The relative concentrations $CI_p(R)/CI_p(H\alpha)$ plotted against Hubble type T. The plot on the left shows the mean values for each type, with the error bars representing the standard deviation divided by the square root of the number of galaxies of that type. The plot on the right shows each of the galaxies for which Petrosian concentration indices have been calculated.

The ratio of the effective radii *v.* type

The ratio of the effective radii of a galaxy as viewed in $H\alpha$ and in continuum emission can also be used to examine the relative concentrations of light. The value of $r_e(H\alpha)/r_e(R)$ will be greater than 1 for galaxies which have a higher central concentration in the continuum than in $H\alpha$.

Figure 7.14 examines the relationship between this ratio and Hubble type. The dispersion of values within each type is huge, particularly for the Sa, Sm and Im classes. As found with the two different concentration indices, most galaxies are more centrally concentrated in the continuum than the $H\alpha$. The correlation with type is poor. The linear correlation coefficient is just 0.0926 with a significance of 89%.

7.1.6 Concentration indices - summary

Three different methods of investigating the distribution of galaxy flux have been investigated. The most basic is the use of effective radii, which can only really be used to examine relative distributions of the old stars as seen in the continuum light, and the new-born stars as detected by the $H\alpha$ light. The two forms of the

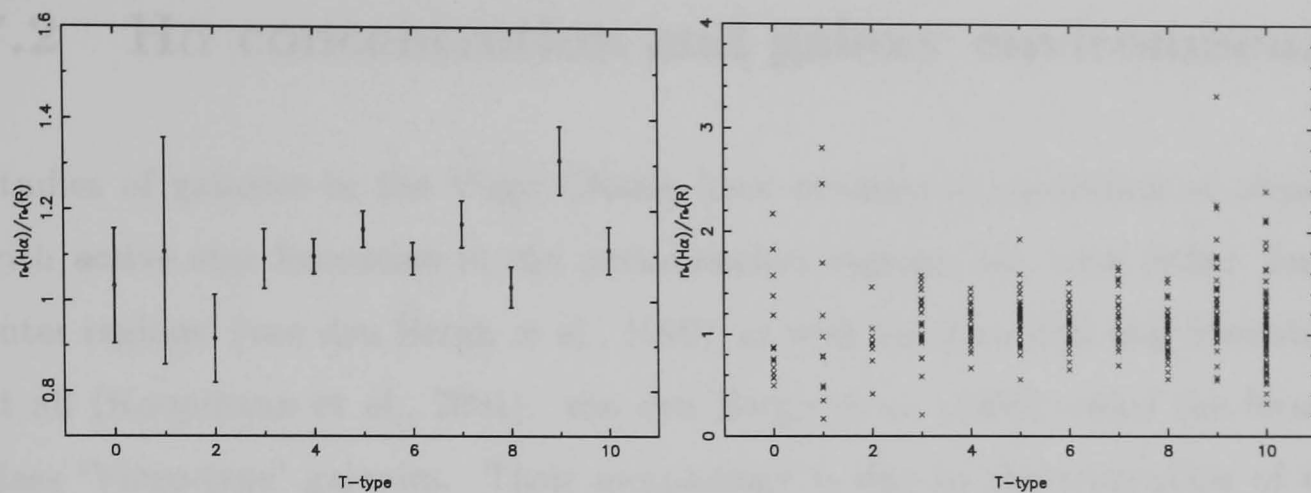


Figure 7.14: The relative effective radii $r_e(\text{H}\alpha)/r_e(\text{R})$ plotted against Hubble type T. The plot on the left shows the mean values for each type, with the error bars representing the standard deviation divided by the square root of the number of galaxies of that type. The plot on the right shows each of the galaxies for which effective radii have been calculated.

concentration index are more sophisticated, with the Petrosian index being the least subjective to the choice of total flux. The $\log C_{31}$ index is more reliable when it comes to calculating the concentration of the $\text{H}\alpha$ emission.

All three methods show a strong correlation with Hubble type, with the early-type, bulge-dominated galaxies having concentration indices close to those expected for an $r^{1/4}$ profile and the late types approximating to exponential profiles. Investigation of the relative concentrations finds that most galaxies are more centrally concentrated in the continuum light than in the $\text{H}\alpha$. This implies that the majority of the massive-star formation is occurring in the outer regions of the galaxies, whereas the majority of circumnuclear regions are dominated by old-stellar populations.

A preliminary comparison of the Petrosian concentration indices calculated for the low-redshift $\text{H}\alpha$ GS galaxies with the more distant SDSS sample reveals that the higher-redshift galaxies appear to be more centrally concentrated. This may well be due to selection effects.

7.2 $H\alpha$ concentration and galaxy environment

Studies of galaxies in the Virgo Cluster have revealed a population of objects with active star formation in the circumnuclear regions, but with either ‘fuzzy outer regions’ (van den Bergh et al., 1990), or with no other disk star formation at all (Koopmann et al., 2001). van den Bergh et al. (1990) called the former class ‘Virgo-type’ galaxies. Their morphology is due to the truncation of the star forming disk in cluster galaxies. The latter, more extreme, class have been named St galaxies (spirals with severely truncated star forming disks) by Koopmann & Kenney (1998). Koopmann & Kenney (2002) suggest that these are the products of interactions between the intra-cluster medium (ICM) and the ISM of the galaxies, stripping gas from their outer disks. The removal of gas in the outer regions inhibits the process of star formation there. Since the SFRs in the inner disks of galaxies are found by Koopmann & Kenney (2002) to be normal or enhanced, it appears that the ICM-ISM interactions do not have a strong effect on the circumnuclear regions of most Virgo galaxies. Strong tidal interactions between two galaxies can also redistribute the gas, in many cases making it more susceptible to stripping by the ICM.

Koopmann & Kenney (2002) find that 52% of their sample of 55 Virgo Cluster galaxies can be defined as having truncated star formation. The $H\alpha$ GS observed sample contains only 15 Virgo galaxies, but 53 galaxies listed as members of groups by Huchra & Geller (1982). In addition, there are also 22 galaxies in close pairs. In Figure 7.15, the $\log C_{31}$ $H\alpha$ concentration index is plotted against T-type, with galaxies in different environments coded by different colours and symbols. Whilst there is no overall trend for field or group galaxies to have more centrally-concentrated star formation for any given Hubble type, it can be seen here that 8 out of the 12 galaxies with $H\alpha$ concentration indices greater than 0.7 are found in either group or pair environments. This equates to 10% of the non-isolated sample. Only 2% of the isolated, field galaxies have concentrations this high. Whilst this cutoff is arbitrary, it does seem to separate effectively the

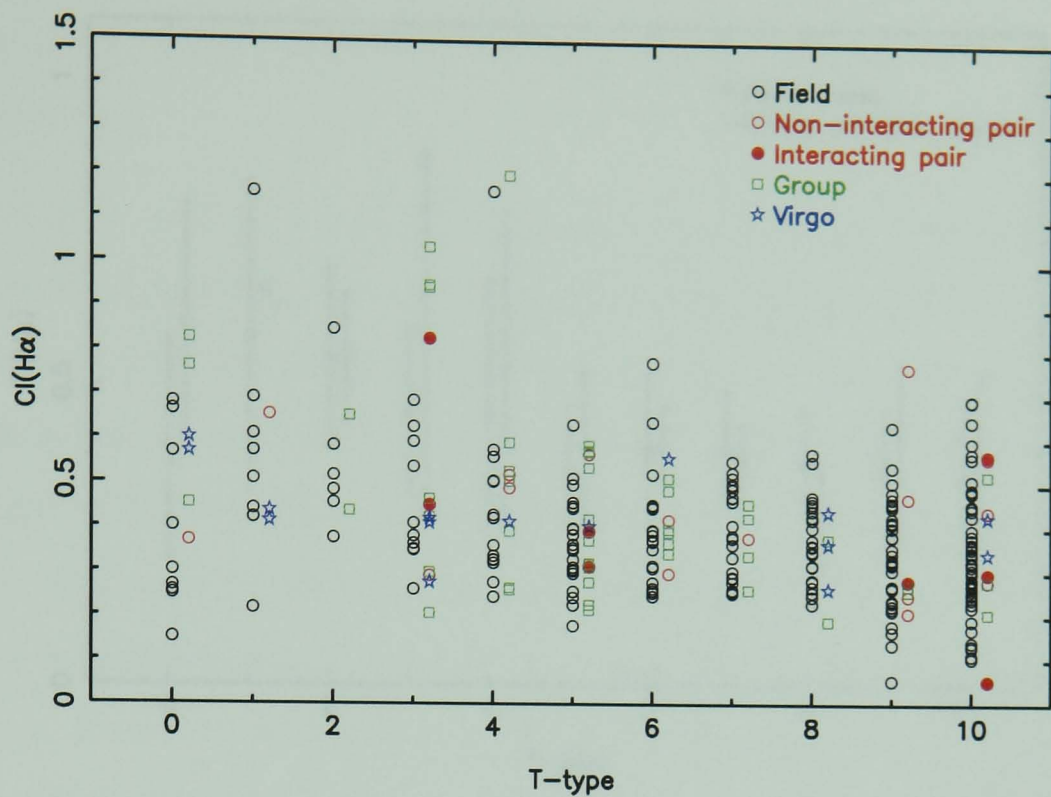


Figure 7.15: The distribution of $H\alpha$ concentration indices as a function of Hubble T-type. Different galaxy environments are coded with different colours and symbols.

highest concentrations from the main body of the distribution.

In Figure 7.16, the mean $H\alpha$ concentration indices for the field sample, and for the combined group and pair galaxies, are plotted. Virgo galaxies are excluded from this plot. Within the error bars, group and pair environments cannot be said to affect the average distribution of star formation within galaxies. The same conclusion can be reached by examining the median values, rather than the mean. If St galaxies are primarily caused by ICM-ISM interactions, as suggested by Koopmann & Kenney (2002), then this is not a surprising result. Groups dominated by spiral galaxies are not known to have a strong intra-group equivalent to the ICM, thus stripping of the ISM by this method will not occur. The group and pair galaxies seen in Figure 7.15 with the high central $H\alpha$ concentrations can still be explained as the product of tidal disruption by gravitational interactions with nearby companions.

Inspection of each of the 12 galaxies with the highest $H\alpha$ concentrations reveals peculiar and disturbed morphologies in one 'field' galaxy (UGC11269) and in the obviously interacting galaxy UGC12699. 5 of the galaxies have been classified as

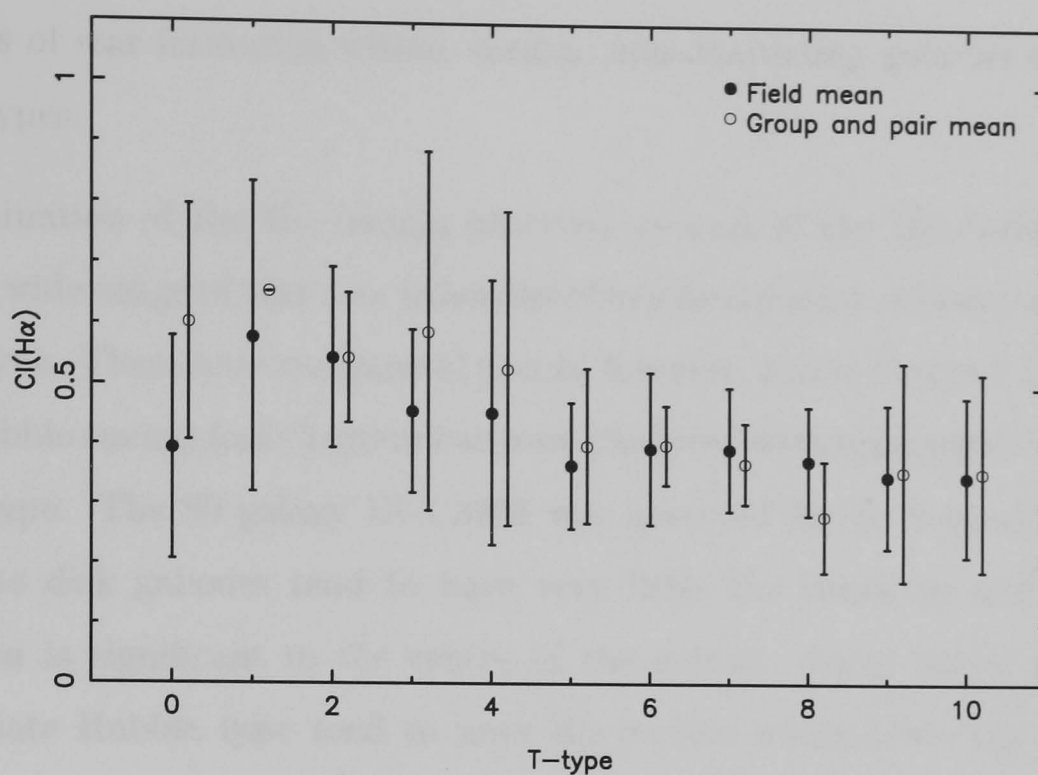


Figure 7.16: Mean H α concentration indices for field and group+pair galaxies as a function of Hubble T-type.

containing AGN. UGC3546 and UGC10470 are both field galaxies with Seyfert 2 nuclei. UGC7030 is a group galaxy with a Seyfert 1.5 nucleus, and UGC7096 (a group galaxy) and UGC12699 (the aforementioned interacting galaxy) both contain HII LINERS. The presence of AGN confuses matters slightly, as strong nuclear emission from a galaxy is obviously going to increase the continuum-light concentration index, and is quite likely to affect the H α index in a similar way. The exact relation between the presence of an AGN and galaxy environment is unknown, but it does appear that at least some types of Seyfert activity are correlated with galaxy-galaxy interactions (Adams, 1977; Dahari, 1984; Keel et al., 1985).

7.3 The distribution of star formation in normal galaxies

The morphology of a galaxy is most commonly defined by its Hubble type (Hubble, 1926). The Hubble sequence itself is partly based on the stellar content and star formation activity of galaxies. This section will very briefly discuss the dis-

tributions of star formation within normal, non-interacting galaxies of different Hubble types.

An examination of the $H\alpha$ images observed as part of the $H\alpha$ Galaxy Survey reveals a wide range of star formation distributions amongst galaxies of the same Hubble type. There are some general trends, however, and in Figure 7.17 a version of the Hubble tuning-fork diagram has been produced with representative galaxies of each type. The S0 galaxy UGC3798 was observed in the field of UGC3740. Early-type disk galaxies tend to have very little $H\alpha$ emission, and often $H\alpha$ absorption is significant in the centre of the galaxy. Large spiral galaxies of intermediate Hubble type tend to have HII regions which trace the pattern of the spiral arms. The more chaotic late-type galaxies have a wider range of star formation rates, and the HII regions have more scattered distributions.

7.4 The distribution of star formation in interacting and highly disturbed galaxies

Large-scale tidal effects between two galaxies with small separation can cause an enormous variety of extended structures. The most common are bridges and tails. Bridges are often found linking large galaxies to smaller companions, whilst tails stretch away from the perturbing galaxy. Other morphological effects include ring-like shapes caused by the passage of one galaxy through the other, and shells, generally produced by accretion of debris or smaller companion objects. A good review of the topic can be found in Barnes & Hernquist (1992).

The effects of interactions and galaxy mergers on the distribution of star formation within the galaxies involved can be quite striking. A more complete study will be the subject of future work and will include the JKT $H\alpha$ observations of interacting systems taken by P. James and S. Percival. In this section, a small selection of interacting and gravitationally-disturbed galaxies will be presented from the observed $H\alpha$ GS sample.

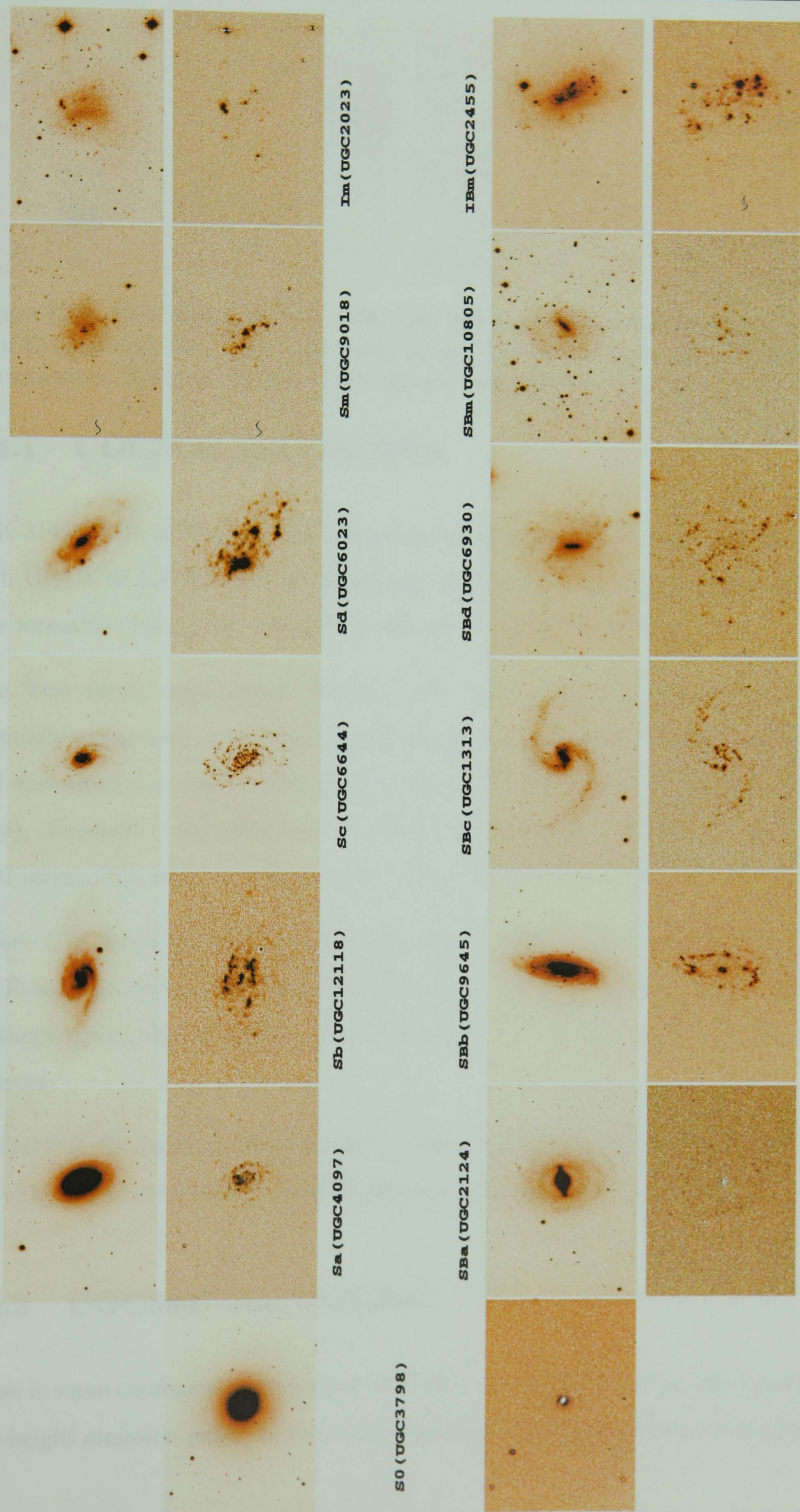


Figure 7.17: A Hubble tuning fork diagram composed of R-band (upper image of each pair) and H α (lower image) observed galaxies.

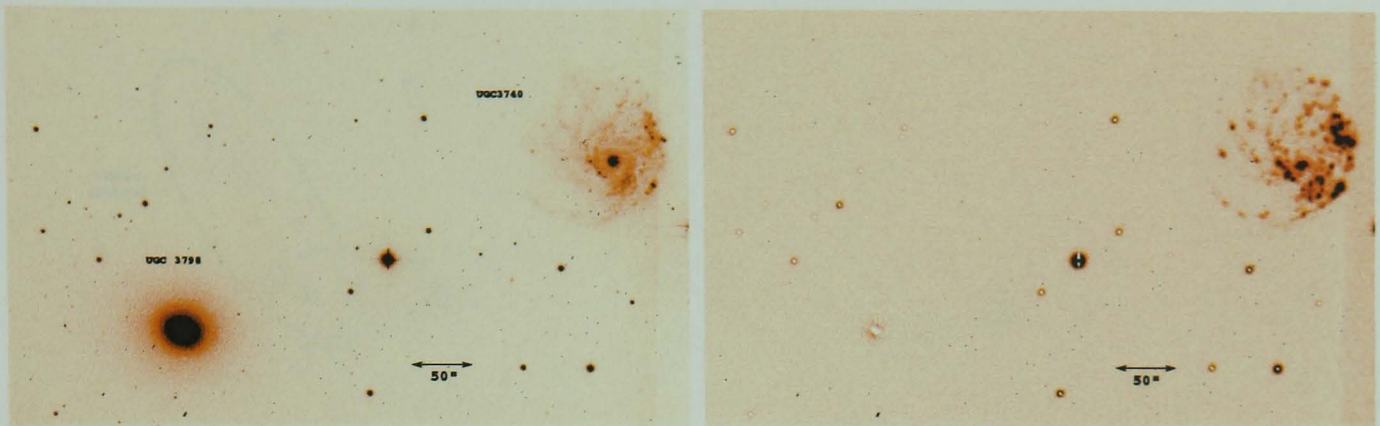


Figure 7.18: UGC3740 and UGC3798. The left-hand image contains the continuum R-band emission. The right-hand image displays the continuum-subtracted H α emission. North is the top of the images and east is to the left.

7.4.1 UGC3740 and UGC3798

UGC3740 (NGC2276) is a highly-asymmetrical, lopsided Sc galaxy interacting with UGC3798 (NGC2300), an S0 galaxy. It is also the galaxy with the highest star formation rate ($13.5 M_{\odot}\text{yr}^{-1}$) in the observed H α GS sample.

The ‘bow shock’ appearance (Figure 7.18) and enhanced star formation were originally suggested to be due to ram-pressure interaction between the galaxy and the unusually dense intra-group medium (Condon, 1983; Mulchaey et al., 1993). Gruendl et al. (1993) and Hummel & Beck (1995), however, found that tidal interaction with UGC3798 was a more likely explanation.

Figure 7.18 shows that the sharply defined curve defined by the western limb in the R-band image is even more abruptly truncated in the H α emission. The large southern spiral arm resembles the tidal tails often associated with interacting systems.

The lack of H α emission, and evidence of H α absorption seen in UGC3798, justifies the decision to exclude S0 and elliptical galaxies from the survey.

7.4.2 UGC3847 and UGC3851

There is some confusion surrounding UGC3851 (NGC2366) and its surroundings. The bright emission patch at the south-west end of the galaxy has its own NGC

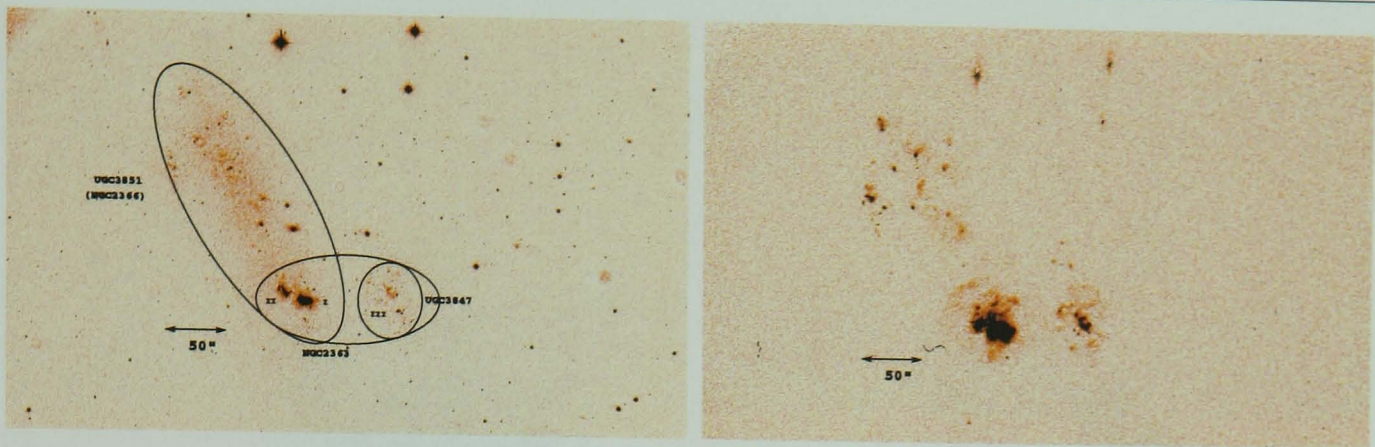


Figure 7.19: UGC3847 and UGC3851. The left-hand image contains the continuum R-band emission. The regions identified by different labels, as used in this study, are marked. The three parts of NGC2363 are as labeled in Drissen et al. (2000). The right-hand image displays the continuum-subtracted $H\alpha$ emission. North is the top of the images and east is to the left.

number (NGC2363), but is believed to be a supergiant HII complex (Youngblood & Hunter, 1999). The satellite object to the west is often included as a region of NGC2363. Drissen et al. (2000) label it as NGC2366-III. This object, in turn, has its own UGC number (UGC3847), although it is often mistakenly equated to NGC2363. For the purposes of this study, UGC3851 (including the regions defined by Drissen et al. 2000 as NGC2366-I and -II, but not the NGC2366-III region) and UGC3847 will be considered as two separate, but interacting, galaxies (see Figure 7.19).

UGC3847 and UGC3851 have the two highest $H\alpha$ equivalent widths (33 and 23 nm respectively) of all the 334 galaxies observed in the study. As can be seen from Figure 7.19, the star formation activity is dominated by the HII regions in NGC2363. The equivalent width for the region containing just NGC2363-I and -II is 85 nm. Drissen et al. (2000) and Hunter et al. (2001) note that NGC2363 competes with the 30 Doradus nebula in the Large Magellanic Cloud in terms of its star formation rate. 30 Doradus is a supergiant HII region that is often taken as defining the class of supergiant HII complexes.

Figure 7.20 gives a magnified view of the southern region of the system. There is clearly a great deal of tidal interaction going on with a complex network of filaments and shells present. There is a partial arc to the north-east of NGC2366. Hunter & Gallagher (1997) suggest that this could be part of a shell type struc-

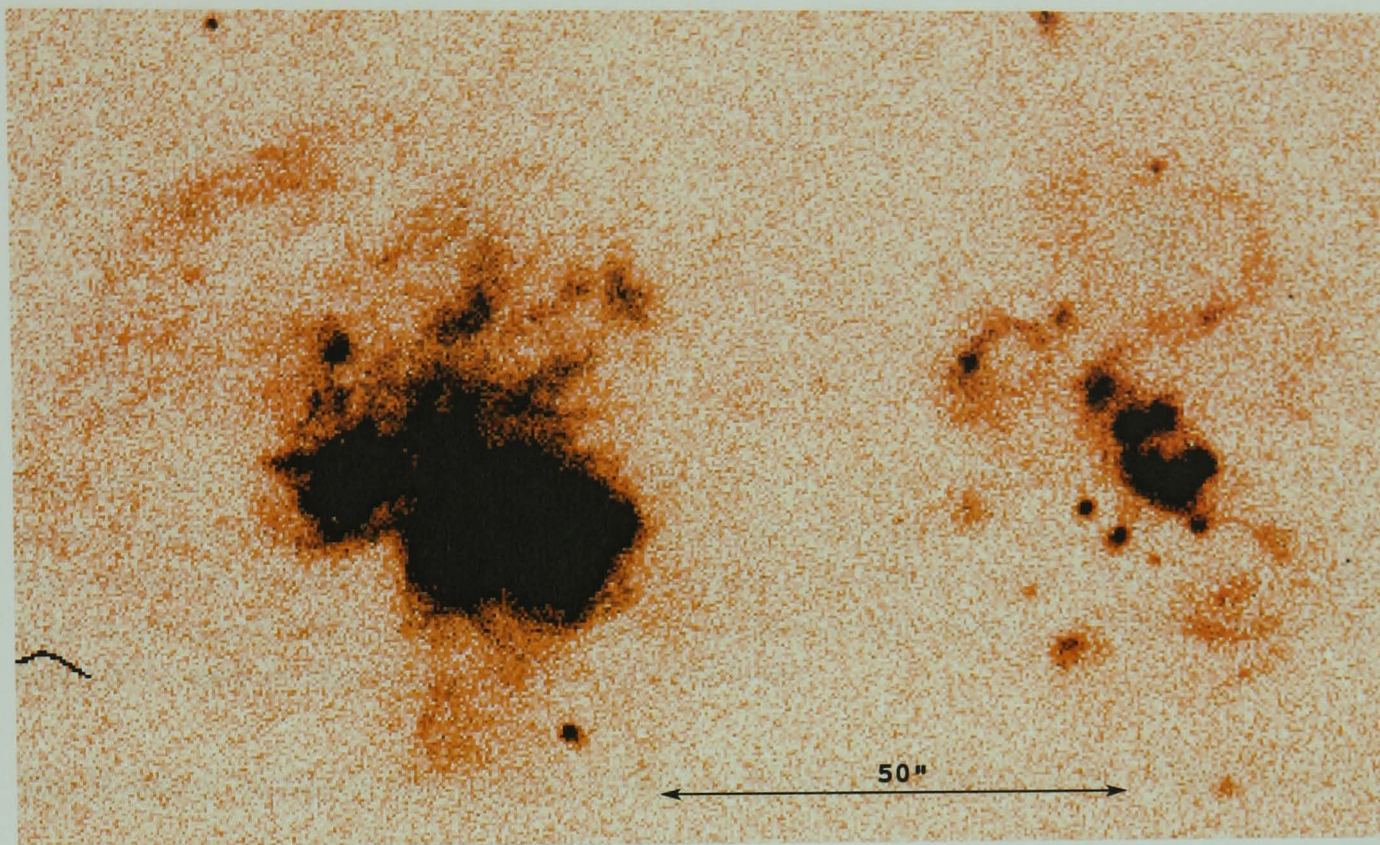


Figure 7.20: The main star forming regions of UGC3847 and UGC3851 in $H\alpha$ light. North is to the top of the image, and east is to the left

ture. There are three bubble-type structures visible in UGC3847, in the north, north-east and south-west regions of the object. There are also three knots of line emission that appear to have been ejected off to the north (out of view in Figure 7.20).

This system has been very well studied, and more in-depth descriptions of the morphology, kinematics and derived star formation history can be found in Hunter & Gallagher (1997); Martin (1998); Drissen et al. (2000); Hunter et al. (2001). Drissen et al. (2000) conclude that UGC3847 is kinematically disconnected from the main body of NGC2366 and that it may be responsible for the triggering of the observed star formation.

7.4.3 UGC12699 and UGC12700

The dramatically contrasting effects that interactions can have on galaxies are well illustrated in this system (Figure 7.21). UGC12699 (NGC7714) is an active starburst galaxy with a whole host of tidal features. The most distinguishing in

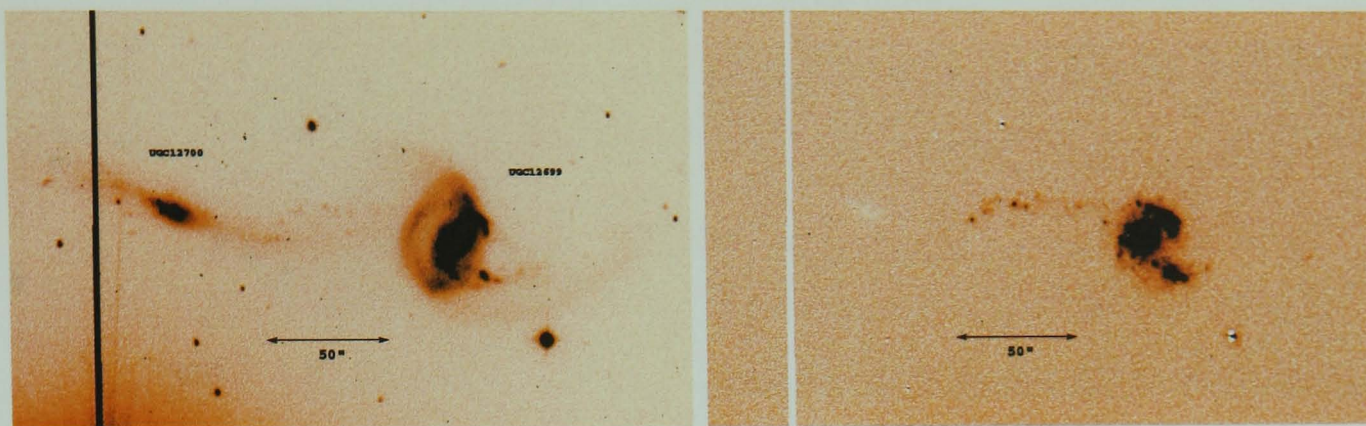


Figure 7.21: UGC12699 and UGC12700. The left-hand image contains the continuum R-band emission. The right-hand image displays the continuum-subtracted $H\alpha$ emission. North is the top of the images and east is to the left. A very bright star is situated below the south-eastern corner of the image, which has saturated the CCD and is the cause of the vertical line.

the R-band image is the partial stellar ring on the eastern side. There is also a very faint bridge linking it to UGC12700 and evidence of two tidal tails in the south-western end of the galaxy, with possibly a further one spanning out to the north-east. Smith et al. (1997) speculate that this complex morphology may have been caused by an off-centre encounter.

The $H\alpha$ image reveals that the majority of the massive-star formation is occurring in the nucleus of UGC12699. The equivalent width measured here is 21 nm, compared to the asymptotic value of 9.4 nm for the whole galaxy. The ring appears not to contain any ongoing star formation. Prominent HII regions are found in an arc at the north-western end of the galaxy and at the base of one of the south-western tails. A chain of star formation is also found crossing the bridge between the two galaxies.

The companion galaxy UGC12700 (NGC7715), on the other hand, appears to have no $H\alpha$ emission. It is believed to be in a post-starburst stage, with a large population of A and late type B stars (Bernloehr, 1993).

Further discussions of this system can be found in Bernloehr (1993); Gonzalez-Delgado et al. (1995); Smith et al. (1997); O'Halloran et al. (2000).

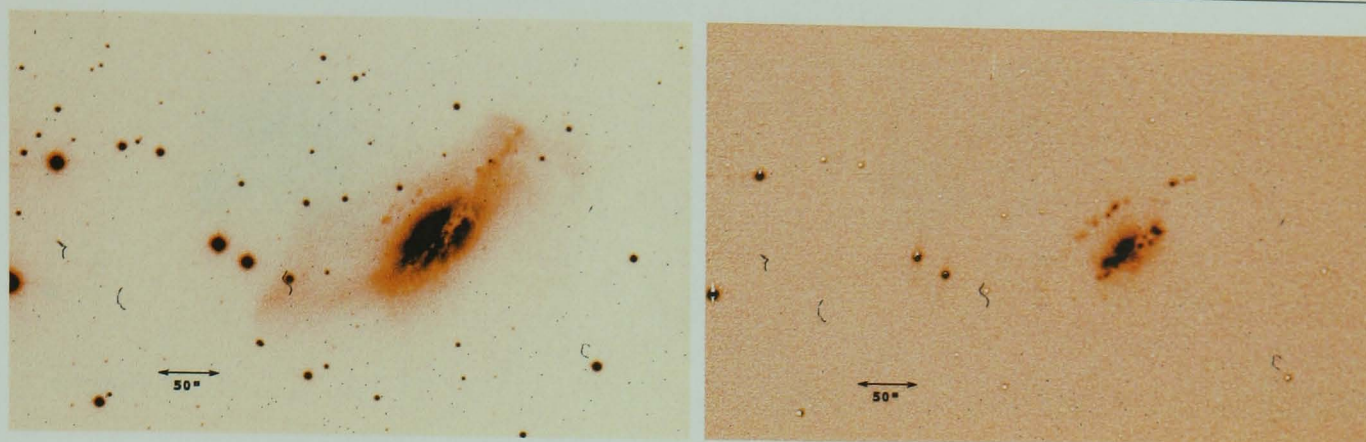


Figure 7.22: UGC3429. The left-hand image contains the continuum R-band emission. The right-hand image displays the continuum-subtracted $H\alpha$ emission. North is the top of the images and east is to the left.

7.4.4 UGC3429

UGC3429 (NGC2146) is classified as an SBab peculiar galaxy. It clearly has a disturbed morphology and the outer disk appears more like a faint, wispy and warped tail to the south-east (Figure 7.22). There are prominent dust lanes through the centre, which are often described as taking the form of a ‘dusty hand’ (Pease, 1920).

The $H\alpha$ image shows large amounts of line emission in the centre, but overall, is very different from the continuum image. The most striking feature is the string of HII regions that form an arm around the north and west sides of the galaxy. Young et al. (1988) describe the galaxy as appearing to be a ‘one armed spiral’, whilst Hutchings et al. (1990) include HI evidence to suggest that the feature is ‘the trail of a slow spiraling merging of a gas-rich companion into the presently disturbed, dominant galaxy’. Young et al. (1988) also liken the arm to the polar rings often seen in S0 galaxies, which are believed to be the result of accretion of mass from either a gas-rich dwarf, or a passing galaxy (Barnes & Hernquist, 1992).

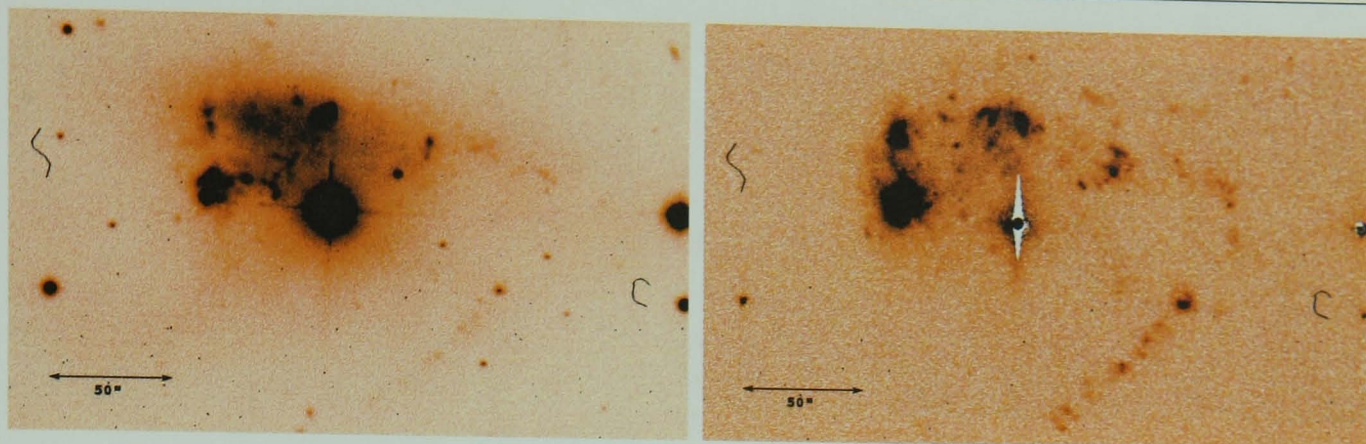


Figure 7.23: UGC5637. The left-hand image contains the continuum R-band emission. The right-hand image displays the continuum-subtracted $H\alpha$ emission. North is the top of the images and east is to the left.

7.4.5 UGC5637

UGC5637 (NGC3239) is a peculiar IBm galaxy. Figure 7.23 shows a distinct lack of symmetry and a very clumpy distribution, predominantly in the east. There is a long tail visible in the south-west of the continuum image, and a second, more diffuse tail in the south-east.

The $H\alpha$ image reveals several giant HII regions in the east. The largest of these is around 0.76 times the luminosity of 30 Doradus (Krienke & Hodge, 1991). There is a chain of star formation along the south-west tail, but none in the south-east. This morphology is well described by a merger model, where the tails are presumed to be tidal, the resultant structure is highly disturbed and star formation as been enhanced in some regions and suppressed in others.

7.4.6 UGC12048

In the R-band light, UGC12048 (NGC7292) is clearly a strongly barred irregular galaxy (Figure 7.24). The $H\alpha$ image reveals quite a different picture. There are bright regions of star formation at either end of the bar. This is a feature quite often seen in late-type disk galaxies (see Section 7.5). The eastern region has an equivalent width of 13.8 nm and the western region has an EW of 18.0 nm. The asymptotic value for the entire galaxy is 5.4 nm.

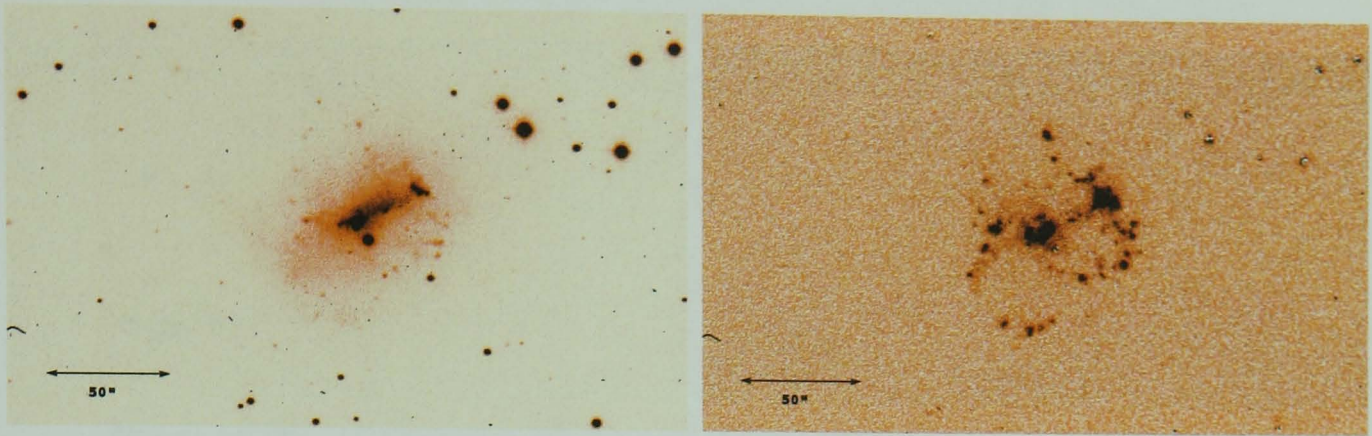


Figure 7.24: UGC12048. The left-hand image contains the continuum R-band emission. The right-hand image displays the continuum-subtracted $H\alpha$ emission. North is the top of the images and east is to the left.

Most interesting, however, are two strongly arced chains of HII regions, one in the south-east and one linking the two bar-end regions. These are very reminiscent of tidal interactions and suggest that UGC12048 could possibly be a merger remnant. This galaxy has been relatively sparsely studied, however. Measurements of the galaxy kinematics may help to resolve the origin of its structure.

7.5 The effects of bars on circumnuclear star formation

The presence and structure of bars in the centres of galaxies have been found to affect the circumnuclear star formation (see e.g. Sérsic & Pastoriza 1967; Martinet & Friedli 1997; Ho et al. 1997). Three dramatically different effects can be observed in the $H\alpha$ GS sample as the result of two different types of bar. The first type of bar has an approximately even distribution of light along its length, whereas the second is dominated by a bright central region, often, but not always, associated with an AGN of some sort.

For galaxies with the first bar type, $H\alpha$ flux is generally detected either along the length of the bar - see Figures 7.25-7.27, or, in many cases at either end of the bar, see Figures 7.28-7.30.

Galaxies with the second kind of bar are found to exhibit strong $H\alpha$ emission

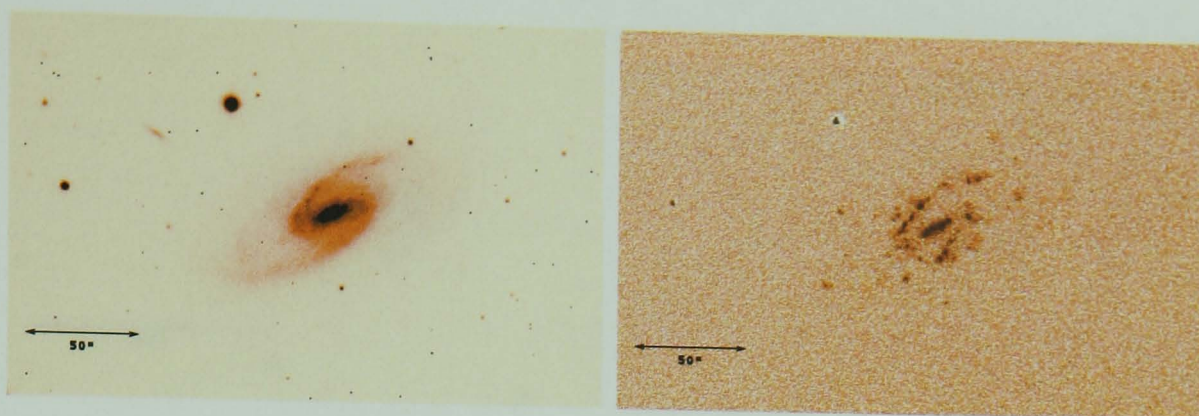
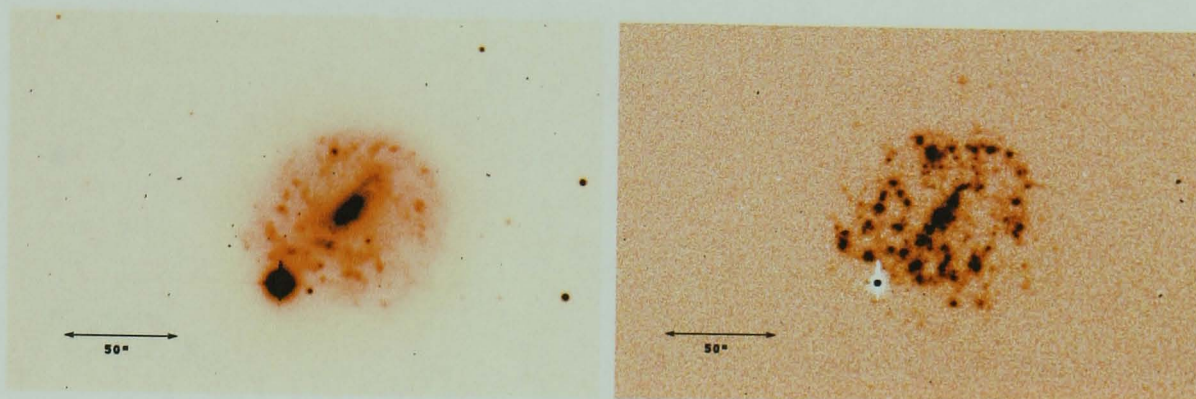
Figure 7.25: UGC4705 (SBb): R-band (left) and H α (right) images.

Figure 7.26: UGC8116 (SBc).

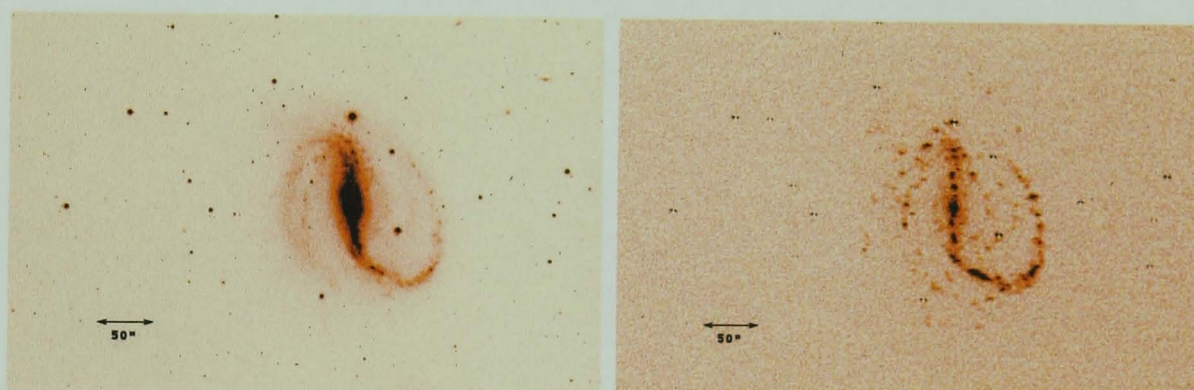


Figure 7.27: UGC12343 (SBc).

in their centres, but virtually none along the rest of the bar. Some examples of these are included in Figures 7.31-7.33.

Stellar bars in disk galaxies induce gravitational torques on the surrounding interstellar medium (see e.g. Block et al. 2001). The resulting loss in angular momentum causes a radial inflow of gas to the central regions of the galaxy. Thus the presence of a bar should help fuel nuclear star formation. The kinematics of galaxy bars are not well understood, and thus the reasons for the different distributions of H α emission observed can not easily be explained. Ho et al. (1997) speculate that inner Linblad resonances (ILRs) could prevent infalling gas

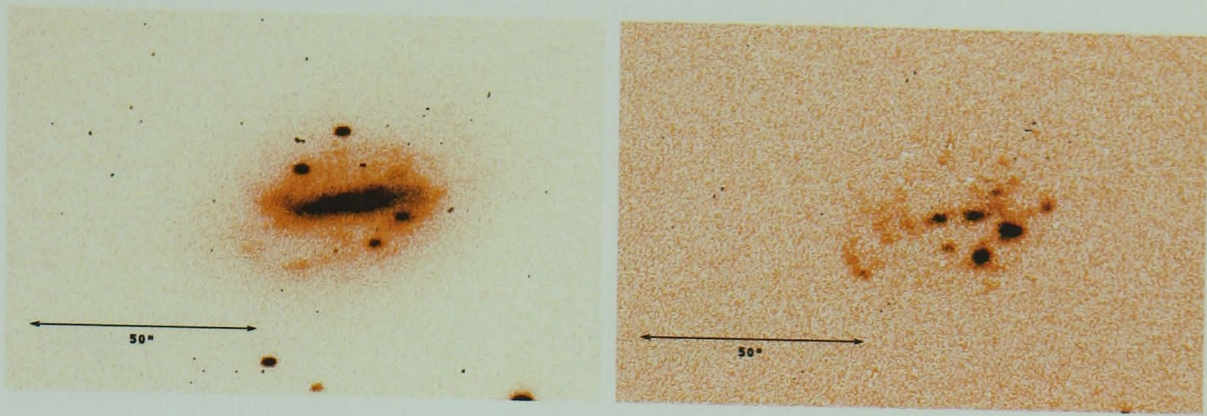
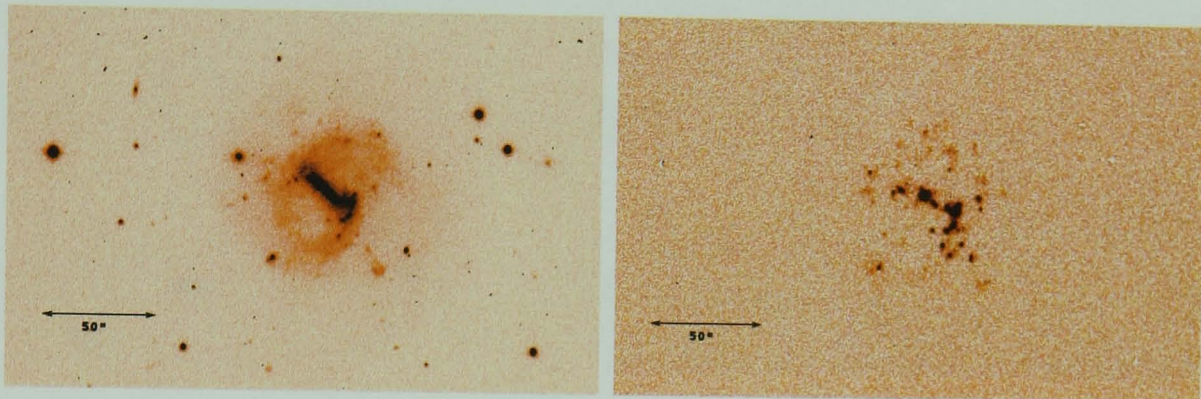
Figure 7.28: UGC4444 (SBcd): R-band (left) and $H\alpha$ (right) images.

Figure 7.29: UGC4469 (SBcd).

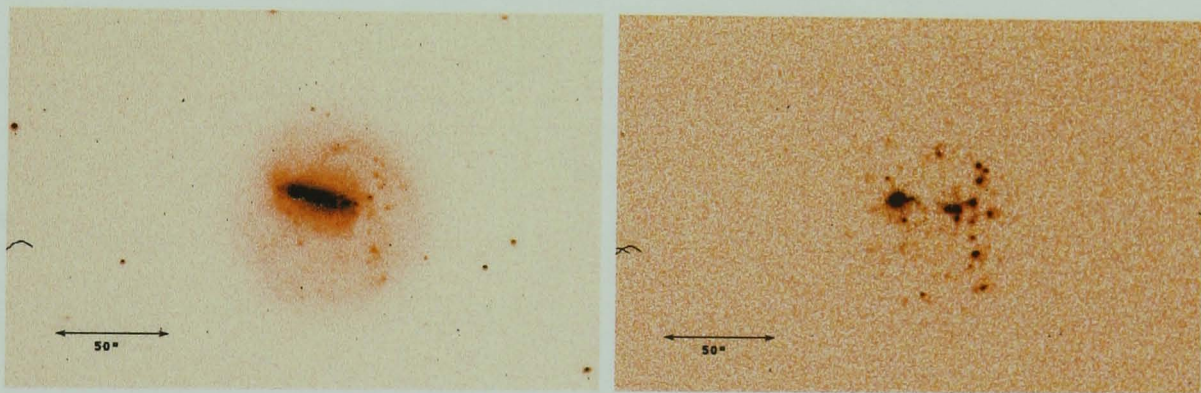


Figure 7.30: UGC6797 (SBd).

from the outer regions of the galaxy from reaching the nucleus. Gravitational instabilities in the gas accumulated at the ILR radius may lead to a burst of star formation. Early-type galaxies with large bulge-to-disk ratios have steeply-rising rotation curves. Combes & Elmegreen (1993) find that, if an ILR is present, its location roughly coincides with the turnover radius of the rotation curve. Thus, early-type galaxies with small turnover radii can have an ILR located within the bar, and close to the nucleus. An ILR in a late-type galaxy is likely to be found near the ends of the bar, away from the nucleus (Elmegreen & Elmegreen, 1985; Combes & Elmegreen, 1993). Hence, star formation regions are predicted to be found more often at the bar ends in late-type galaxies and more often within the

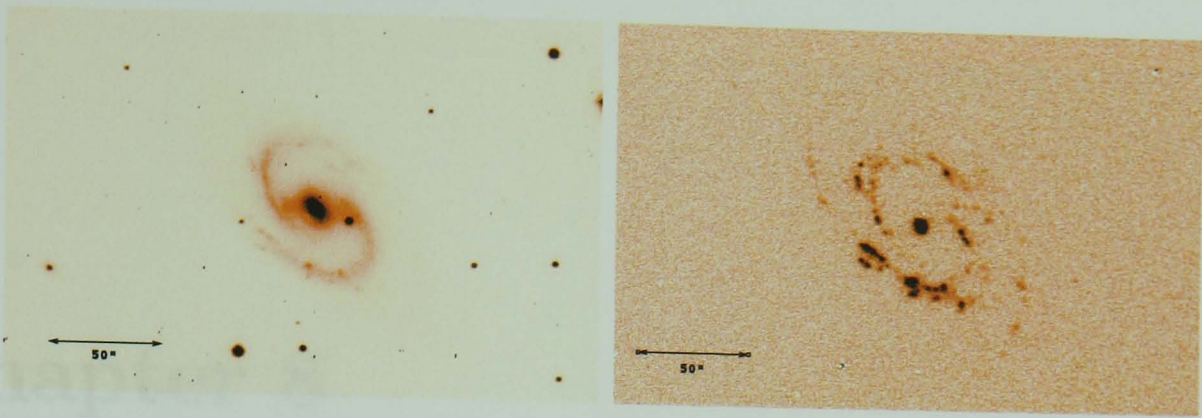


Figure 7.31: UGC4273 (SBb): R-band (left) and $H\alpha$ (right) images.

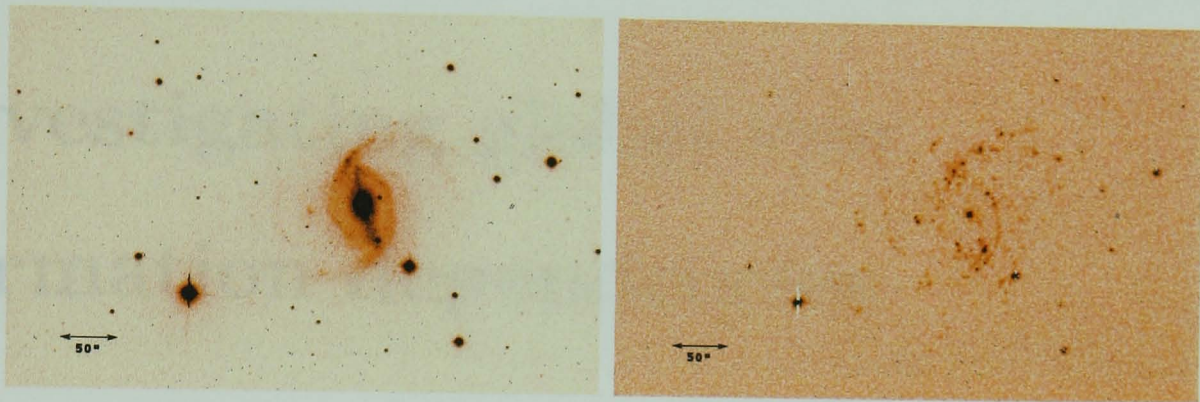


Figure 7.32: UGC9824 (SBbc).

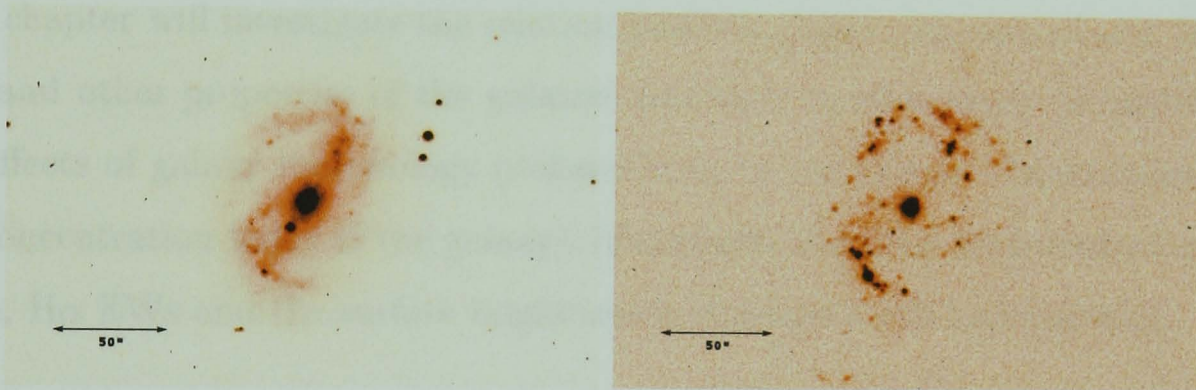


Figure 7.33: UGC10470 (SBbc).

bar in earlier types.

The observed barred galaxies with nuclear star formation in the $H\alpha$ GS sample typically have Hubble types Sb-Sbc. Galaxies with star-forming regions at the end of the bar are found to range between types Scd-Sm. Galaxies with star formation distributed more evenly along the bar cover a wide range of types, from Sb-Sdm, with the mode of the distribution being the Sc classification. Barred galaxies with the earliest spiral types are generally found to have very little circumnuclear $H\alpha$ emission, and often exhibit $H\alpha$ absorption in their centres. These observations fit in well with the theoretical model.

Chapter 8

Investigating global star formation dependencies

This chapter will investigate the relation between global measures of star formation and other properties of the galaxies and their surroundings. In particular, the effects of galaxy morphology (defined both by the Hubble classification and the concentration index of the galaxy), luminosity, and local environment on the SFRs, H α EWs and H α surface brightnesses of galaxies will be examined.

Star formation in galaxies takes place in two distinct regions: the extended disks of spiral and irregular galaxies, and the compact circumnuclear environments in the centres of spiral galaxies. Kennicutt (1998) discusses the star formation properties of the two separately and finds their attributes and dependencies are very different (see his Table 1). Decomposing the two components for the H α GS sample is beyond the scope of this thesis, and the subject for further work. The results presented here will all be for the integrated properties of the galaxies.

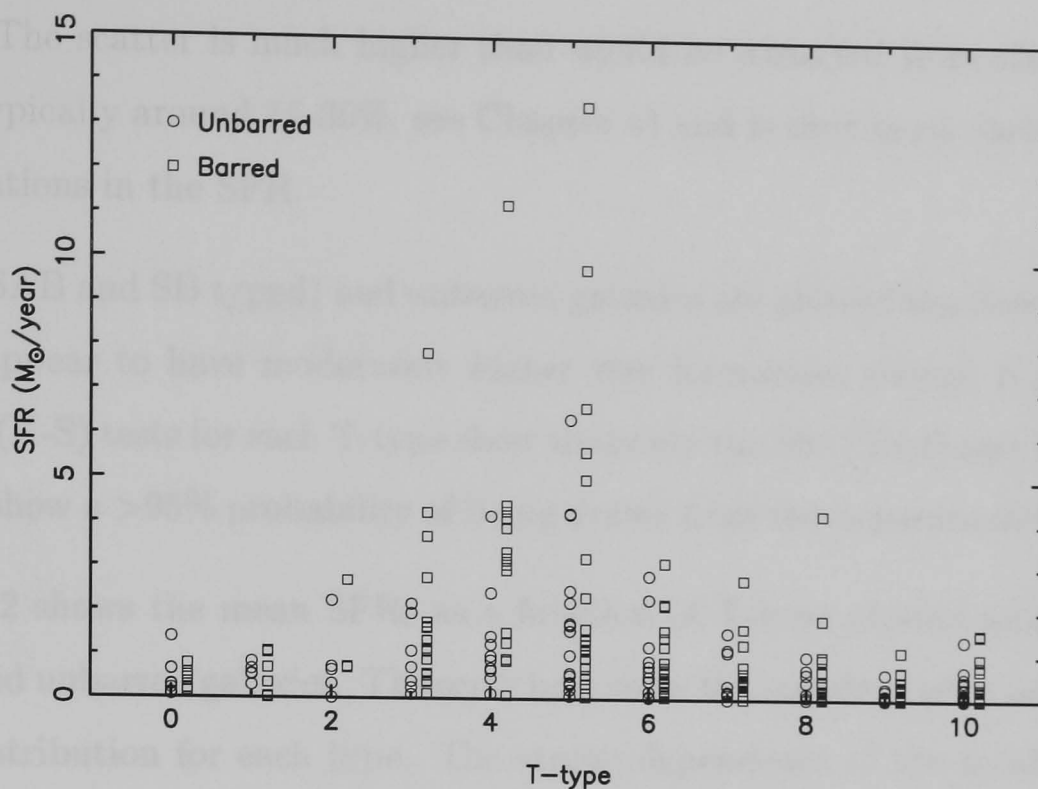


Figure 8.1: The distribution of SFRs as a function of T-type.

8.1 Morphology dependencies

8.1.1 Hubble types

As mentioned in Section 7.3, the morphology of a galaxy is most commonly defined by its Hubble type, and the Hubble sequence itself is partly based on the stellar content and star formation activity of galaxies. The proportion of young Population I stars to the older Population II objects increases from Sa to Sc. In other words, the mass-normalised formation of massive stars should increase along the sequence from early-type, Sa-Sab, spirals to the late-type, Sc-Sd, galaxies.

The relation between SFR and Hubble type

Figure 8.1 shows the distribution of star formation rates as a function of T-type for the full observed sample of 334 galaxies. We see a large scatter amongst galaxies with the same Hubble classification, but also that the highest rates of star formation occur in Sb-Sc galaxies. The modal SFR values for all Hubble types lie close to zero, thus galaxies with low SFRs are very common, independent of

T-type. The scatter is much higher than would be expected from observational errors (typically around 15-30%, see Chapter 4) and is thus most likely to reflect real variations in the SFR.

Barred (SAB and SB typed) and unbarred galaxies are plotted separately. Barred objects appear to have moderately higher star formation, though Kolmogorov-Smirnov (K-S) tests for each T-type show that only the Sbc (T=4) and Im (T=10) galaxies show a >95% probability of being drawn from two separate distributions.

Figure 8.2 shows the mean SFRs as a function of T-type plotted separately for barred and unbarred galaxies. The error bars show the standard error on the mean of the distribution for each type. The strong dependence of the total SFR in a galaxy on its morphology is very clear here. The mean SFR increases along the Hubble sequence, peaking between Sb and Sc (T-types 3-5), and then decreases towards the latest types. The presence of a bar appears to increase the mean star formation rates particularly for the Sab-Sc and Sdm-Im types. The significance of this observation follows the findings of the K-S tests.

The median SFRs for barred and unbarred spirals are plotted in Figure 8.3. Whilst it is clear that the mean values are influenced by a small number of galaxies with very high SFRs, the median values show that the overall trend is not dominated by these.

With the exception of the points at T=4 (Sbc), the difference between barred and unbarred populations is greatly reduced. Thus, the relation between star formation rates and galaxy bars is obviously more complex than that investigated here. The strength of the bar, together with the relative contributions from the bulge and disk to the integrated SFR could prove significant factors. Kennicutt (1998) and Ryder & Dopita (1994) find no significant global effects of a bar on *disk* SFR, whilst Ho et al. (1997) find a marginally significant increase in *nuclear* SFR amongst barred galaxies. Martinet & Friedli (1997) suggest a correlation between SFR and the strength and length of the bar, and in Section 7.5 we saw that different types of bars result in different distributions of H α flux in

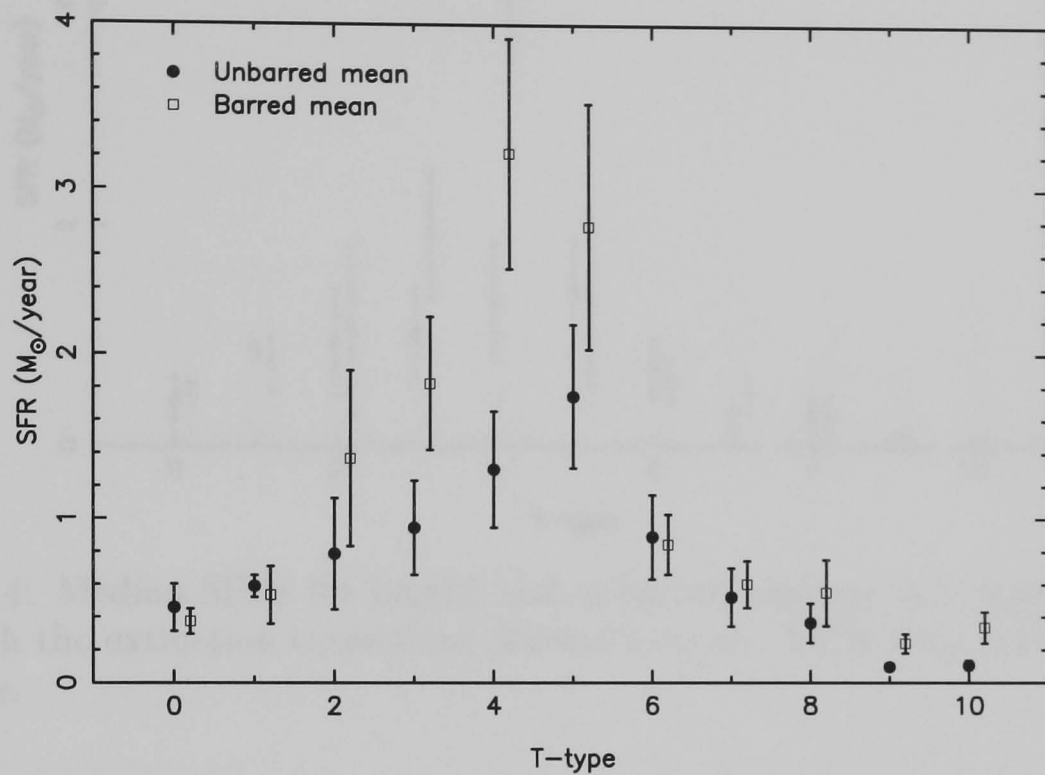


Figure 8.2: Mean SFRs for barred and unbarred galaxies as a function of T-type.

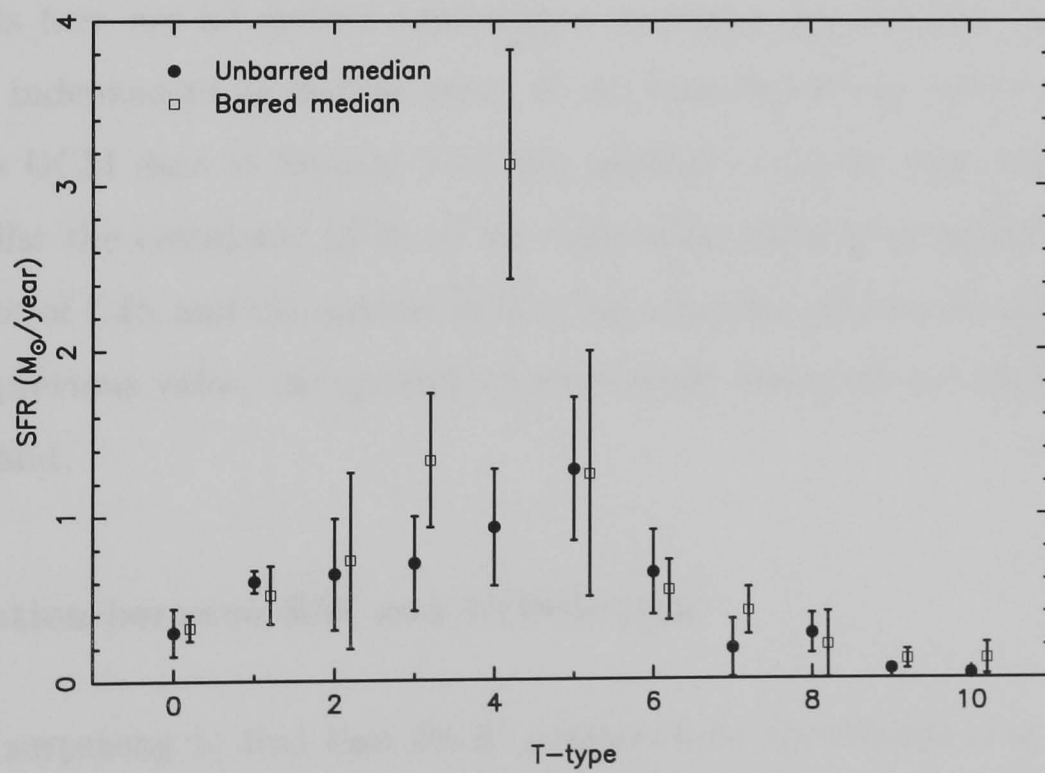


Figure 8.3: Median SFRs for barred and unbarred galaxies as a function of T-type.

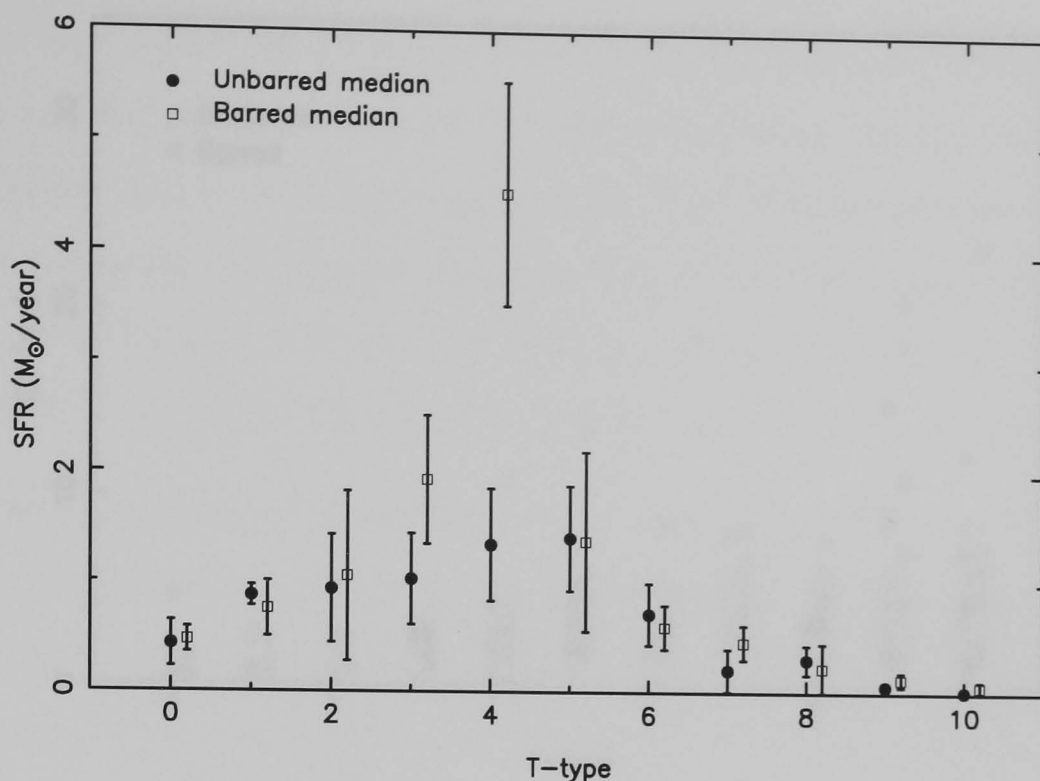


Figure 8.4: Median SFRs for barred and unbarred galaxies as a function of T-type, with the extinction corrections derived from the UCM data applied to the $H\alpha$ fluxes.

circumnuclear regions.

The SFRs here are all derived assuming a correction for internal extinction of 1.1 mag, independent of Hubble type. If the type-dependent corrections found using the UCM data in Section 5.4.5 are applied, it can be seen in Figure 8.4 that, whilst the calculated SFRs of the early-type (S0/a-Sbc) galaxies increase by a factor of 1.45, and the median SFR of the irregular galaxies is approximately half the previous value, the general trends already described in this section are all still valid.

The relation between EW and Hubble type

It is not surprising to find that Sb-Sc galaxies have the highest star formation rates. These types are, on average, physically larger than the Scd-Im galaxies, and are thus likely to contain more star-forming regions and emit greater $H\alpha$ fluxes. The early-type S0/a-Sab galaxies are gas poor, and are thus not expected to contain large amounts of star formation. Equivalent widths give a measure of the SFR per unit (red) luminosity and hence give a measure of SFR per unit

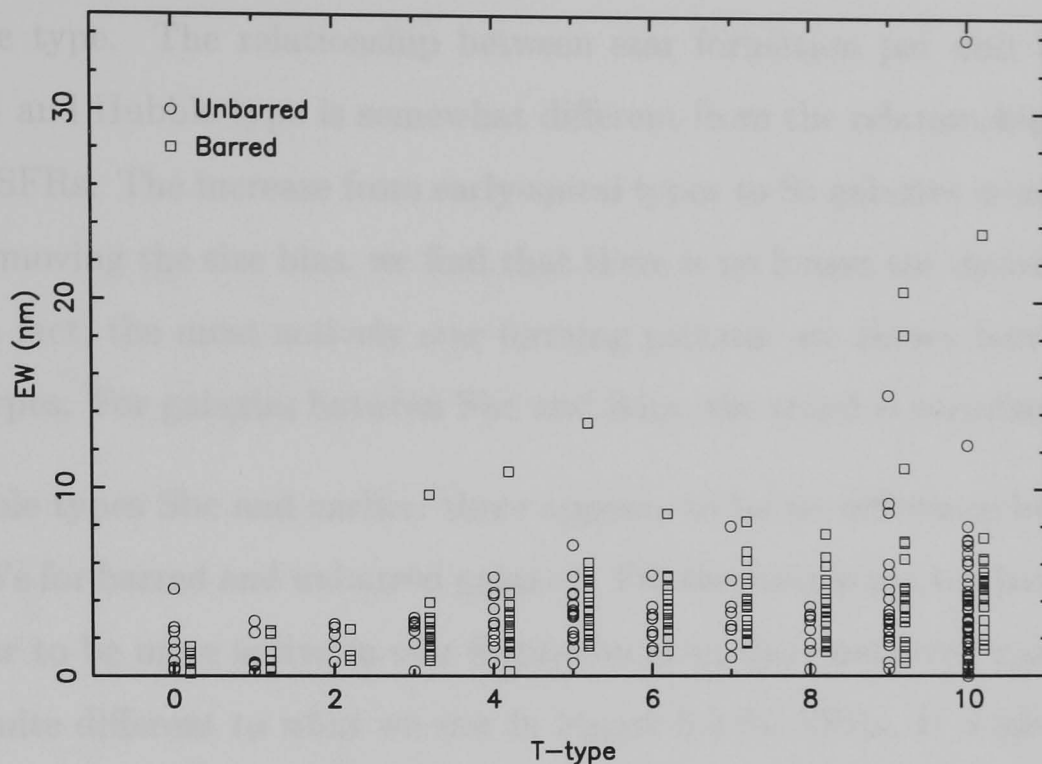


Figure 8.5: The distribution of EWs as a function of T-type.

mass, removing size biases. Another advantage of studying equivalent widths is that they are distance independent. Since the R-band luminosity emitted from a galaxy is produced predominantly by the older-stellar populations, the EW of a galaxy also provides information on the star formation history of the galaxy (see e.g. Kennicutt et al. 1994).

Figure 8.5 shows the distribution of $H\alpha$ EWs with T-type for both barred and unbarred galaxies. It should be remembered that these values include the [NII] doublet. The plot can be compared to Figure 3 in Kennicutt (1998) which is compiled from the photometric surveys of Kennicutt & Kent (1983) and Romanishin (1990). The biggest difference between the plots is the increase in the number of low-EW galaxies in the present sample, particularly for the later types.

The 5 highest EWs in Figure 8.5 belong to Sm or Im galaxies. The dependence on bar presence is less clear here, though in most cases the highest EW for each galaxy type is found in a barred galaxy. K-S tests for each Hubble type show that the probability of the barred and unbarred galaxies being drawn from different populations is only significant above 95% for the irregular galaxies.

Figure 8.6 shows the mean EWs for barred and unbarred galaxies as a function

of Hubble type. The relationship between star formation per unit luminosity (or mass) and Hubble type is somewhat different from the relationship involving absolute SFRs. The increase from early-spiral types to Sc galaxies is still present, but by removing the size bias, we find that there is no longer the decline for later types. In fact, the most actively star forming galaxies are shown here to be the Sm-Im types. For galaxies between Sbc and Sdm, the trend is surprisingly weak.

For Hubble types Sbc and earlier, there appears to be no difference between the mean EWs for barred and unbarred galaxies. For the later types the barred galaxies appear to be more active in star formation than their unbarred counterparts. This is quite different to what we saw in Figure 8.2 for SFRs. It is also contrary to the findings of Kennicutt (1998), who detects no significant difference in the EW distributions of barred and unbarred galaxies, with the possible exception of the Sa galaxies where the median EW is higher in the barred population. Note, however, that Kennicutt defines SAB galaxies to be unbarred, whereas in this study they are grouped with the SB galaxies. Kennicutt thus has fewer objects in his barred sample and comparison between the two populations is difficult due to small-number statistics.

The higher EWs for late-type barred galaxies are also seen in Figure 8.7, where the median values are plotted.

The relation between $H\alpha$ surface brightness and Hubble type

Another way to remove size effects from the total star formation rates is to normalise by the galaxy area (e.g. Ryder & Dopita 1994; Young et al. 1996). The method used here to calculate $H\alpha$ surface brightnesses (with arbitrary units), using R-band Petrosian radii and asymptotic $H\alpha$ fluxes, is described in Section 3.9. Normalising by the surface area of the galaxy, rather than by its continuum luminosity has the advantage of avoiding the effects of bulge contamination, which bias the EWs (Kennicutt, 1998).

The decimal log of the $H\alpha$ surface brightness is plotted in Figure 8.8. The range

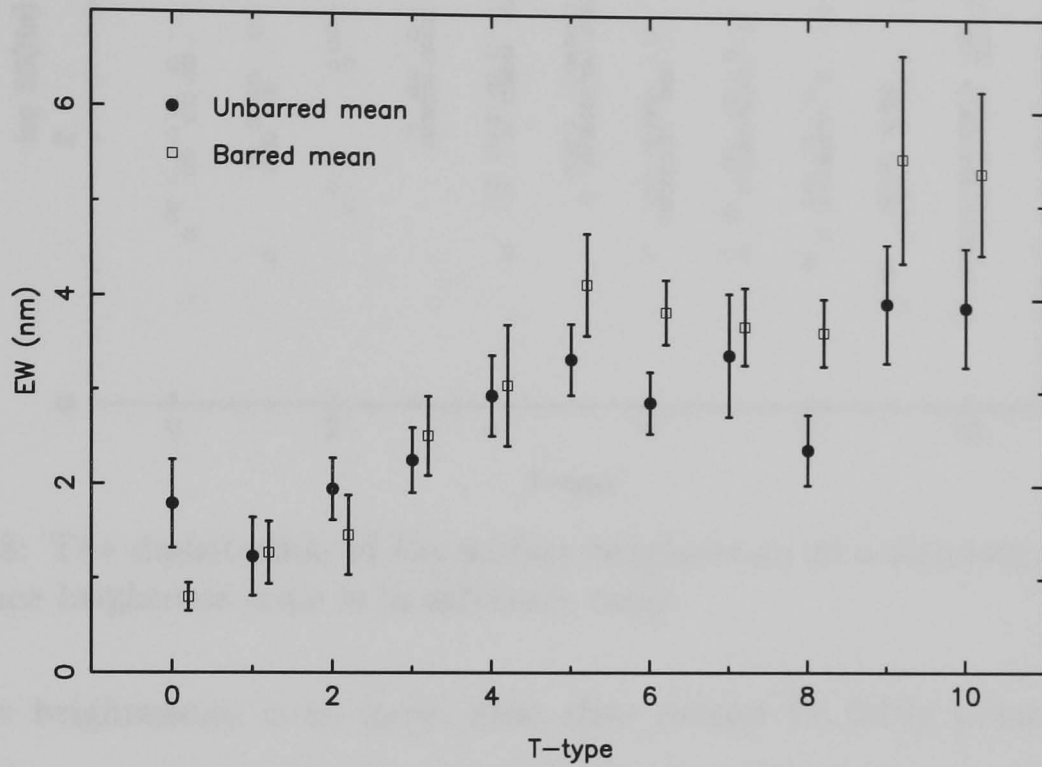


Figure 8.6: Mean EWs for barred and unbarred galaxies as a function of T-type.

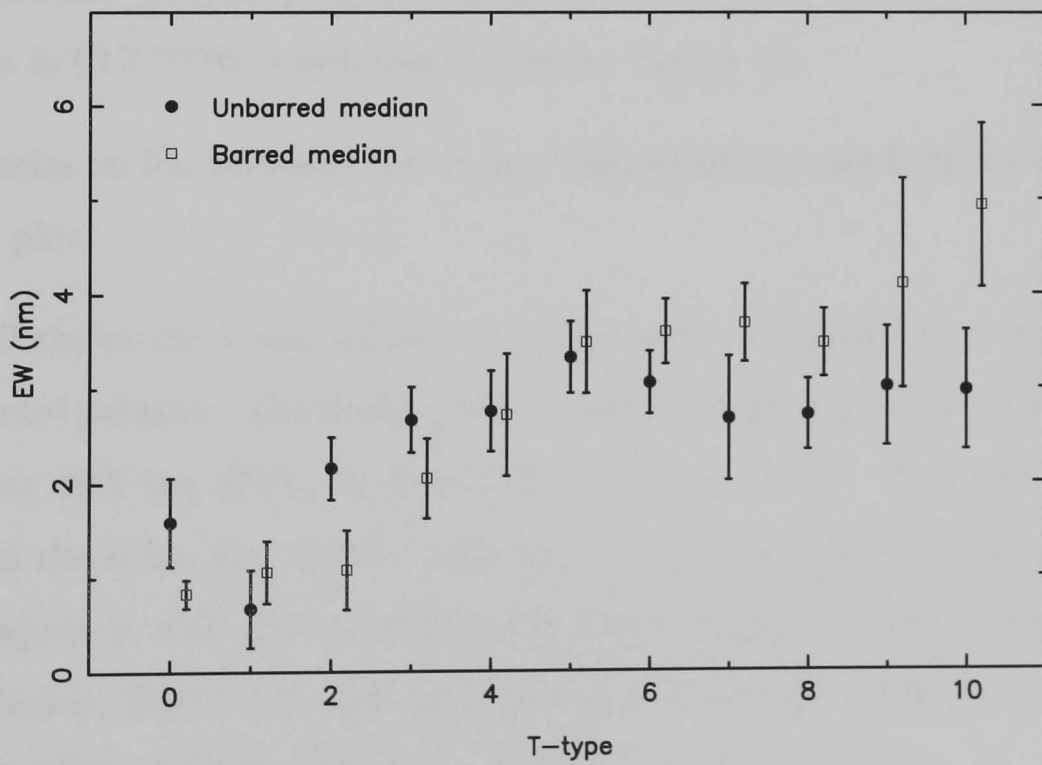


Figure 8.7: Median EWs for barred and unbarred galaxies as a function of T-type.

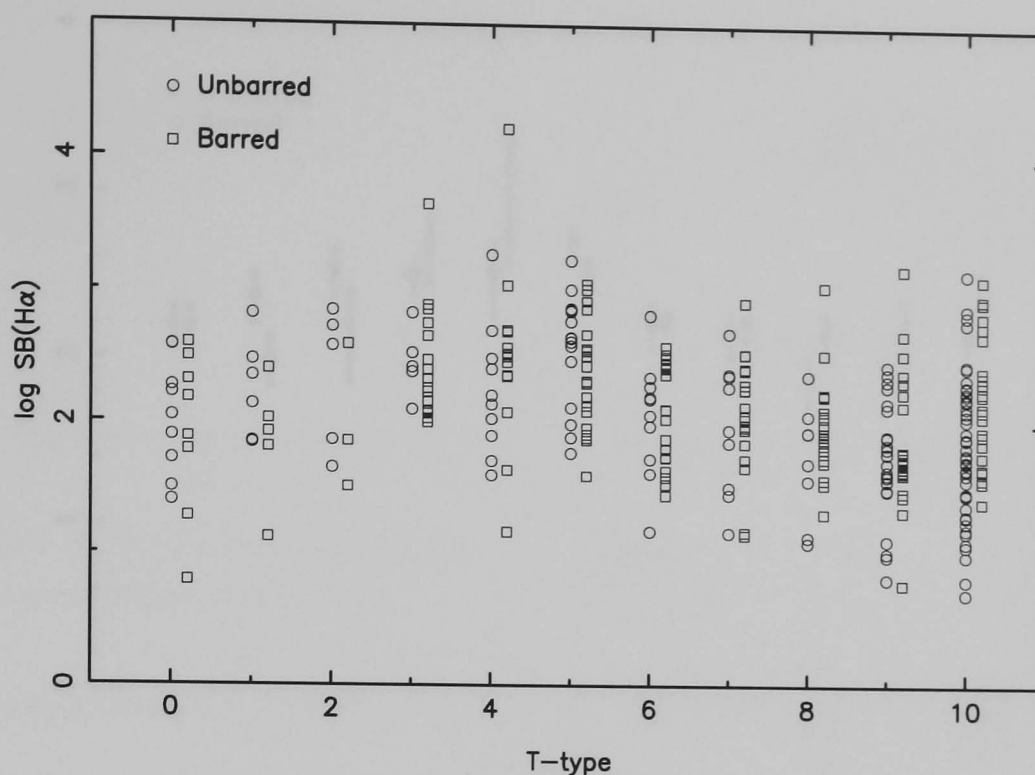


Figure 8.8: The distribution of $H\alpha$ surface brightnesses as a function of T-type. The surface brightness scale is in arbitrary units.

of surface brightnesses is so large, that they cannot be fairly presented on a linear scale. Again, the distribution within each type is large, particularly for the Sbc and Sm-Im galaxy types. The galaxy with by far the highest $H\alpha$ surface brightness is UGC5786, which can be seen in Figure 5.8.

Dependencies on bar presence and on morphological type are both hard to detect from this plot.

Figure 8.9 shows the mean values of the $H\alpha$ surface brightness for both barred and unbarred galaxies. The dependence on Hubble type is much weaker here than seen earlier with the EWs - as found by Kennicutt (1998). Young et al. (1996) found that the mean $H\alpha$ surface brightness for spiral galaxies increases along the Hubble sequence, with Sd-Im galaxies exhibiting values 2-3 times higher than the Sa-Sb galaxies. This is not seen in Figure 8.9, where the highest mean surface-brightness values are found for Sb-Sc galaxies.

The bar dependence is also weaker than seen in Figure 8.6. Plotting median values makes very little difference to the morphology trend, but reduces the bar dependence even more, in a manner similar to that which was seen in Figure 8.7. K-S tests for each type only reveal a significant (>95% probability) difference

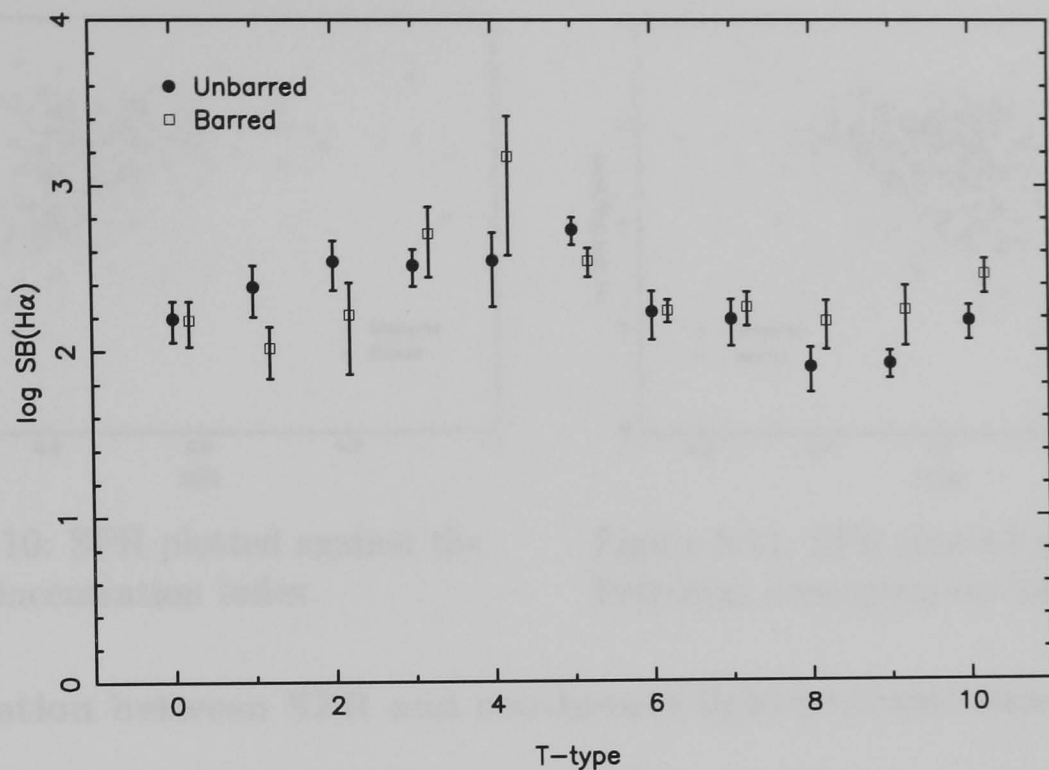


Figure 8.9: Mean H α surface brightnesses for barred and unbarred galaxies as a function of T-type.

between the barred and unbarred populations for Sc types.

In the above relations, we have seen that the amount of current star formation in a galaxy is related to its Hubble type, even if only weakly in the case of the SFR per unit area. The average star formation activity in the early-type S0/a-Sa galaxies appears to be lower than in the later types. However, we note, as did Young et al. (1996), that there are many early-type galaxies with higher SFRs than Sc galaxies of the same size.

8.1.2 Concentration Indices

Concentration indices are a more quantitative way of measuring the distribution of light, and hence the morphology of a galaxy, than assigning Hubble classifications. As shown in Section 7.1.5, there is a strong correlation between continuum concentration indices and Hubble type.

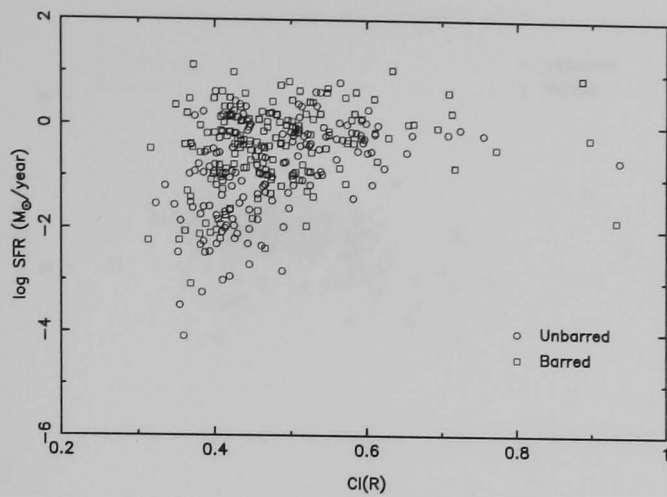


Figure 8.10: SFR plotted against the $\log C_{31}$ concentration index.

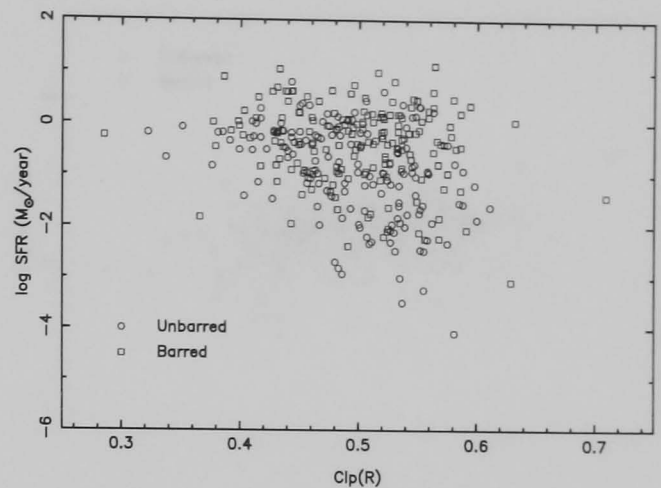


Figure 8.11: SFR plotted against the Petrosian concentration index.

The relation between SFR and continuum-light concentration

Figure 8.10 shows the star formation rates of galaxies plotted against the R-band $\log C_{31}$ concentration index. The most centrally concentrated galaxies will have high CI values, whereas the galaxies on the left side of the plot have continuum emission that is more evenly distributed. The galaxies with the lowest SFRs all appear to have diffuse concentrations of continuum light, whereas the high star forming galaxies do not seem to be constrained by R-band concentration.

The Petrosian index is a reverse concentration index, and thus low values of CI_p imply high central concentrations. Figure 8.11 supports the finding that the lowest SFRs are not detected for high central concentrations. At first, this may seem to contradict the low average SFRs observed in S0/a-Sa galaxies, since these are the most centrally concentrated galaxies. As it turns out, whilst the average SFR is low for these galaxies, the lowest individual measured SFRs are predominantly found in diffuse late-type galaxies (see Figure 8.1).

The relation between EW and continuum-light concentration

The above findings are, however, heavily influenced by the sizes of the galaxies involved, as we see when we plot EWs against R-band concentration index in Figures 8.12 and 8.13. The dependence of the luminosity-normalised star formation rate on these measures of morphology is weak, although we now see a tendency

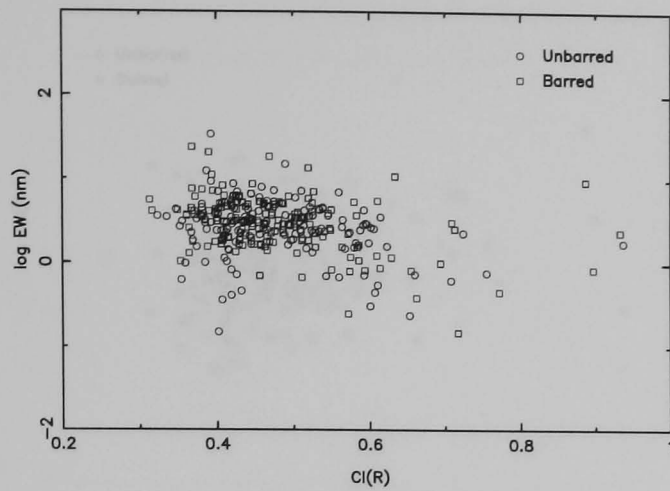


Figure 8.12: EW plotted against the $\log C_{31}$ concentration index.

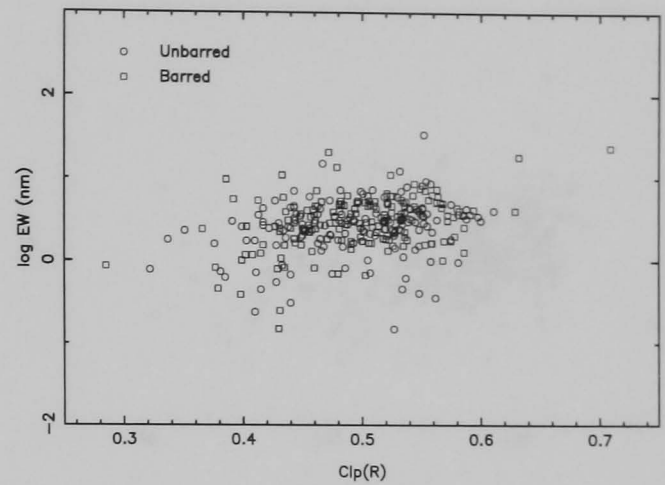


Figure 8.13: EW plotted against the Petrosian concentration index.

for highly-concentrated galaxies to have lower EWs. This is not surprising as the continuum emission from the central regions of early type spiral galaxies is generally very high, whereas the $H\alpha$ line emission is usually relatively low.

The relation between $H\alpha$ Surface Brightness and continuum-light concentration

Figures 8.14 and 8.15 show no detectable correlation between the star formation rate per unit galaxy area and either concentration index. The linear correlation coefficient for the $\log C_{31}$ index is 0.063, giving any dependence a significance of just 73%. For the Petrosian index the correlation is even less, with a coefficient of 0.016 and a significance of 23%.

8.2 Luminosity dependencies

Gavazzi et al. (1996) plotted $H\alpha$ equivalent widths against H-band luminosity, L_H , and found the star formation per unit mass to increase steeply with decreasing luminosity, for the highest values of L_H . For lower values, they found that EW was independent of L_H . They concluded that this could be interpreted as a change of stellar population with mass in the brightest galaxies, whereas systems smaller than the detected threshold are dominated by the young stellar popula-

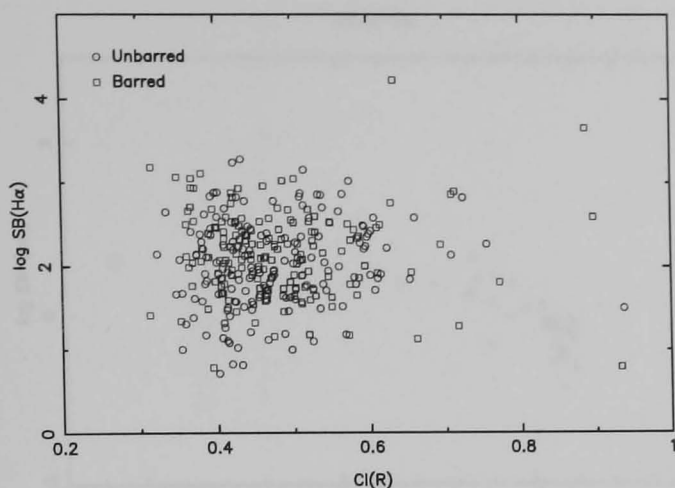


Figure 8.14: $H\alpha$ surface brightness plotted against the $\log C_{31}$ concentration index.

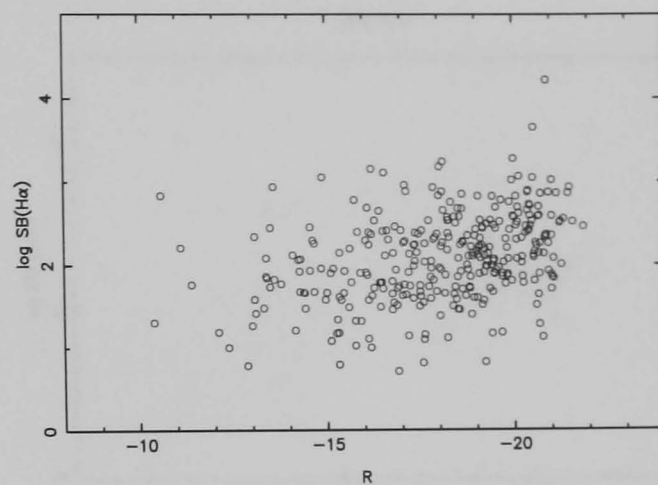


Figure 8.15: $H\alpha$ surface brightness plotted against the Petrosian concentration index.

tion, independent of their mass. They include the warning that their $H\alpha$ data is biased towards strong emission line galaxies.

In Figure 8.16, the $H\alpha$ EWs from the observed $H\alpha$ GS galaxies are plotted against R-band absolute magnitudes, as computed from the measured continuum fluxes and the galaxy distances. The galaxies are grouped into 3 bins of Hubble type so that they can be compared to Figure 4 of Gavazzi et al. (1996). The first plot, containing the S0/a-Sa galaxies is in agreement with the findings of Gavazzi et al. (1996), with the brightest galaxies having the lowest EWs. For magnitudes fainter than -18 , the EW appears to become independent of M_R , though, of course, no firm conclusion can be drawn from 3 galaxies. Any correlation between EW and magnitude disappears for the later-type bins. A least-squares regression fit to the total sample finds a best-fit line with equation:

$$\log EW = 0.03 \times M_R + 1.03. \quad (8.1)$$

Thus, $H\alpha$ EW appears to be virtually independent of galaxy luminosity, and therefore mass, for all but the brightest early-type spiral galaxies. There is, of course, a large scatter at any given magnitude, corresponding to the other influencing factors.

The galaxies in the $H\alpha$ GS sample cover a much larger range of magnitudes than those studied by Gavazzi et al. (1996). In particular, the fainter-luminosity galax-

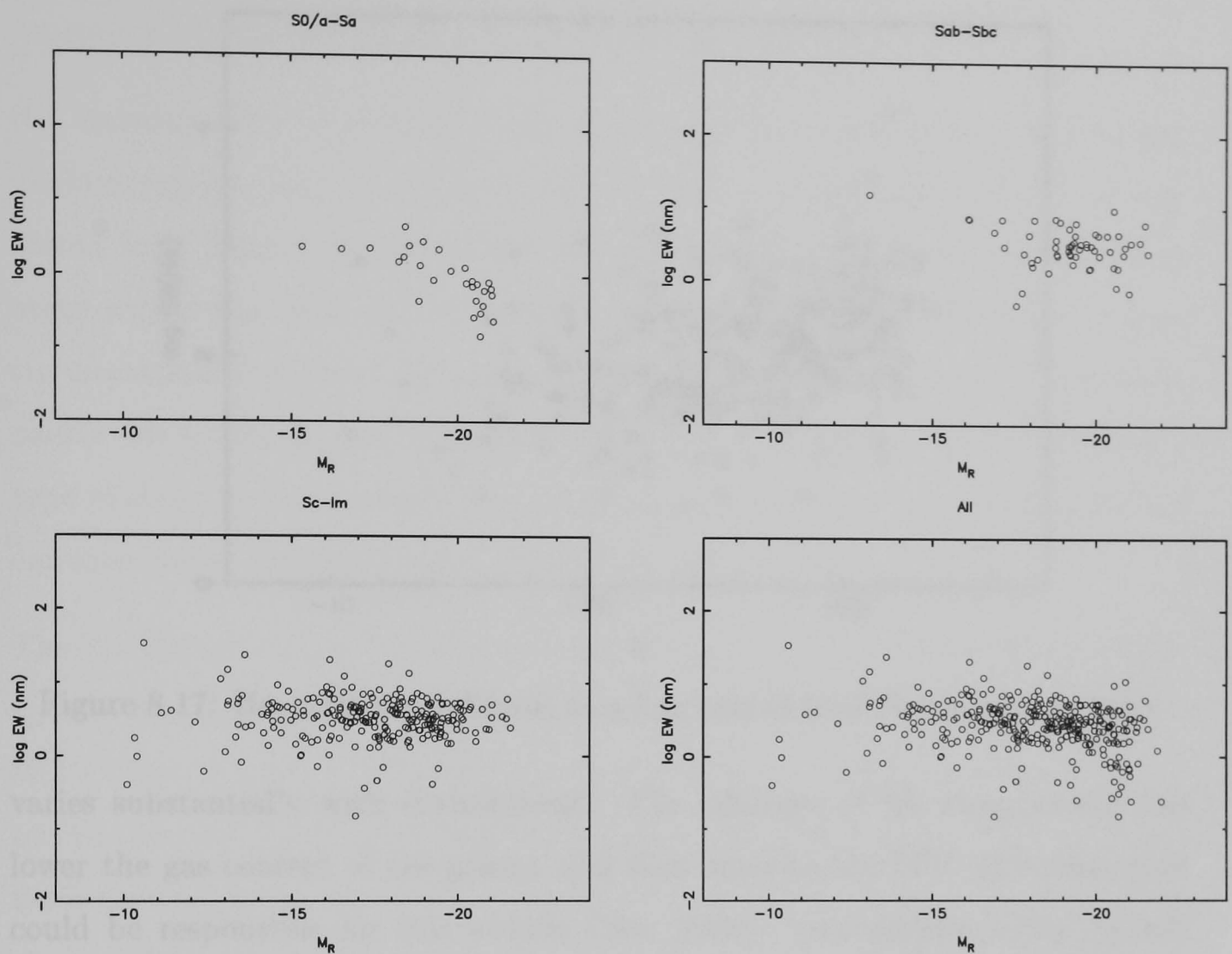


Figure 8.16: The relationship between the R band magnitude and the $H\alpha$ EW of $H\alpha$ GS galaxies, grouped into 3 bins of Hubble type, and for all types together.

ies are more thoroughly represented.

The scatter in the $H\alpha$ surface brightnesses when plotted against R-band magnitude is even greater than that seen in the EWs (Figure 8.17). Again, the size-normalised star formation rates appear to be independent of luminosity. The only obvious outliers are two bright spirals with the highest $H\alpha$ surface brightnesses, UGC5786 (see Figure 5.8) and UGC12699 (Figure 7.21).

8.3 Environmental dependencies

The effect of local environment on a galaxy's properties, including its star formation activity, is a huge topic, and the subject of much debate.

There is much evidence that the rate at which a given type of galaxy has evolved

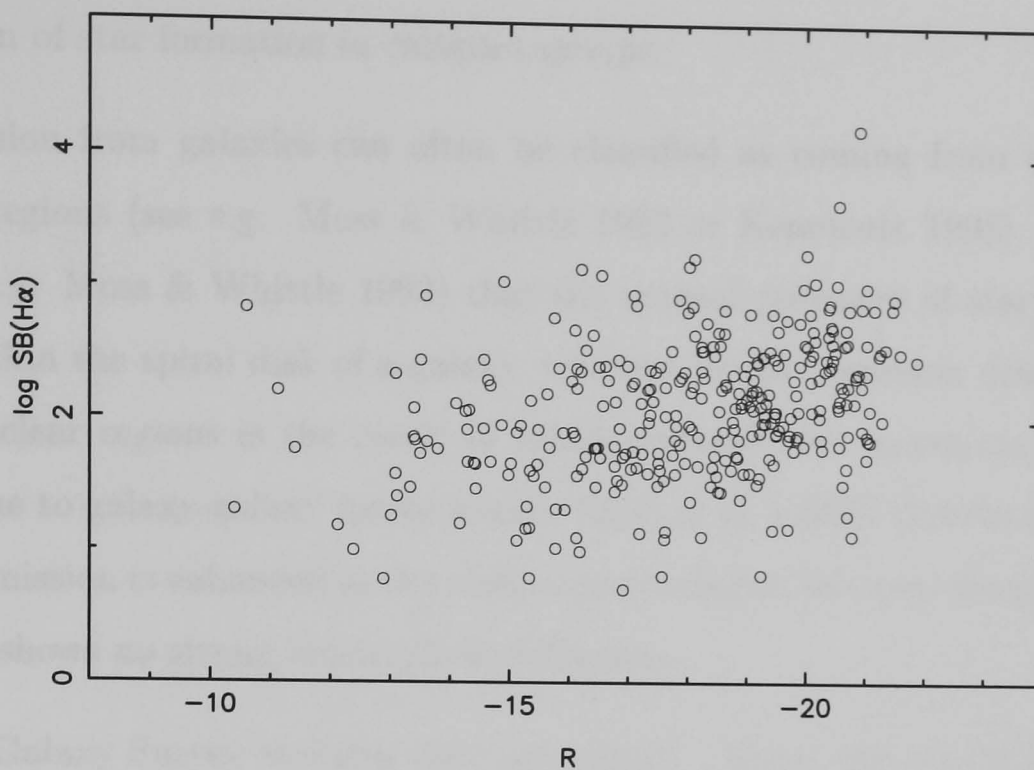


Figure 8.17: H α surface brightness as a function of total R-band magnitude.

varies substantially with environment. The influence of the environment can lower the gas content of the galaxy, and thus decrease the SFR. Processes that could be responsible for this include (Yee, 2000): ram-pressure stripping and evaporation in rich environments (e.g. Gunn & Gott 1972); tidal stripping from close encounters of galaxies (e.g. Byrd & Valtonen 1990); and the decrease of the accretion rate of new gas into a galaxy in rich environments (e.g. Gunn & Gott 1972; van den Bergh 1976; Dressler & Gunn 1983). Similar processes can also serve to *increase* the SFR in the short term: e.g. ram-pressure and tidal shocks (e.g. Moore et al. 1999), and mergers and harassment of galaxies in close encounters (e.g. Moore et al. 1996; Hashimoto & Oemler 2000).

Studies of cluster versus field galaxies have produced conflicting results. Some have suggested a reduced SFR in clusters, with respect to field galaxies of the same morphological type (e.g. Kennicutt 1983; Hashimoto et al. 1998; Koopmann & Kenney 2002) whereas others find a similar or higher SFR in cluster spirals (e.g. Kennicutt et al. 1984; Moss et al. 1998). Similar conflicting results have been found for compact groups of galaxies. Moles et al. (1994) find a slight enhancement in compact groups compared to field galaxies, Iglesias-Páramo & Vílchez (1999) find no enhancement, and Allam et al. (1999) find evidence of a

depression of star formation in compact groups.

H α emission from galaxies can often be classified as coming from one of two distinct regions (see e.g. Moss & Whittle 1993 or Kennicutt 1998). It is suggested (e.g. Moss & Whittle 1993) that the normal processes of star formation occur within the spiral disk of a galaxy, whereas the H α emission detected from circumnuclear regions is the result of tidally-induced star formation (predominantly due to galaxy-galaxy interactions). Moss et al. (1998) find that the latter type of emission is enhanced in the cluster environment, whereas the normal disk emission shows no strong cluster/field difference.

The H α Galaxy Survey includes only one cluster - Virgo, and this was partially ignored in the main study to concentrate on field and group galaxies. A total of 15 Virgo galaxies, as identified by Binggeli et al. (1985), were observed. A complementary study of the cluster, using INT H α imaging of a number of Virgo fields defined by J. Davies et al. as part of the INT Wide Field Survey (McMahon et al., 2001), is in progress, but is beyond the scope of this thesis.

Fifty-three of the galaxies in the observed sample have been designated as group members by Huchra & Geller (1982) (as were 7 of the 15 observed Virgo galaxies).

Twenty-nine galaxies form optically close pairs, in the sense that they appear in the same field of view. The odd number comes from a galaxy paired with a non-included S0 type. Seven of the paired galaxies are also classified as group galaxies, but will be treated here as pairs. Five of the pairs (9 galaxies, not including the S0) are defined as interacting in the notes published on NED (which in turn come from the UGC and RC2).

Whilst the star-forming properties of compact groups (e.g. Moles et al. 1994; Hashimoto et al. 1998; Iglesias-Páramo & Vílchez 1999; Allam et al. 1999) and of Virgo Cluster galaxies (e.g. Koopmann et al. 2001) have been well studied, and will be further studied, the effects of lower density environments have been relatively ignored (although see Allam et al. 1999). The remainder of this section will primarily concentrate on the differences between isolated field galaxies, and

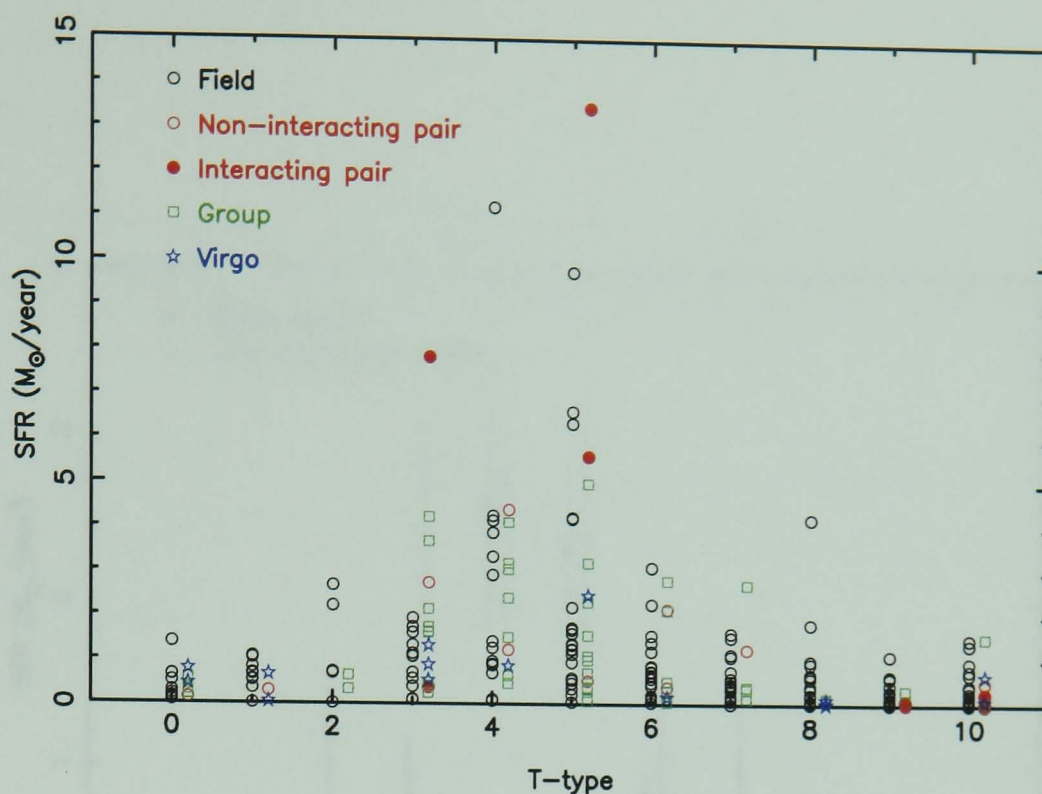


Figure 8.18: The distribution of SFRs as a function of T-type. Different galaxy environments are coded with different colours and symbols.

those in groups or pairs.

8.3.1 SFR dependence on environment

In Figure 8.18, the total star formation rates for the observed sample have been plotted against T-type, with different colours and symbols for the different environments occupied by the galaxies. The environment appears to play very little role in the distribution of SFRs amongst the different Hubble types, with the exception that 3 of the 8 galaxies with $\text{SFR} > 5 \text{ M}_{\odot} \text{yr}^{-1}$ are involved in interactions.

In Figure 8.19, the Virgo galaxies have been removed from the sample, and the galaxies in groups and pairs have been investigated as one population. The mean star formation rates are plotted for field and group+pair galaxies, separated into Hubble types. The error bars represent the standard errors on the points. No error bars are plotted for points derived from the data of only one galaxy, in this case for the T=1 group galaxy. For most Hubble types, we see no difference between the field and the group+pair samples. The exceptions are for Sab and

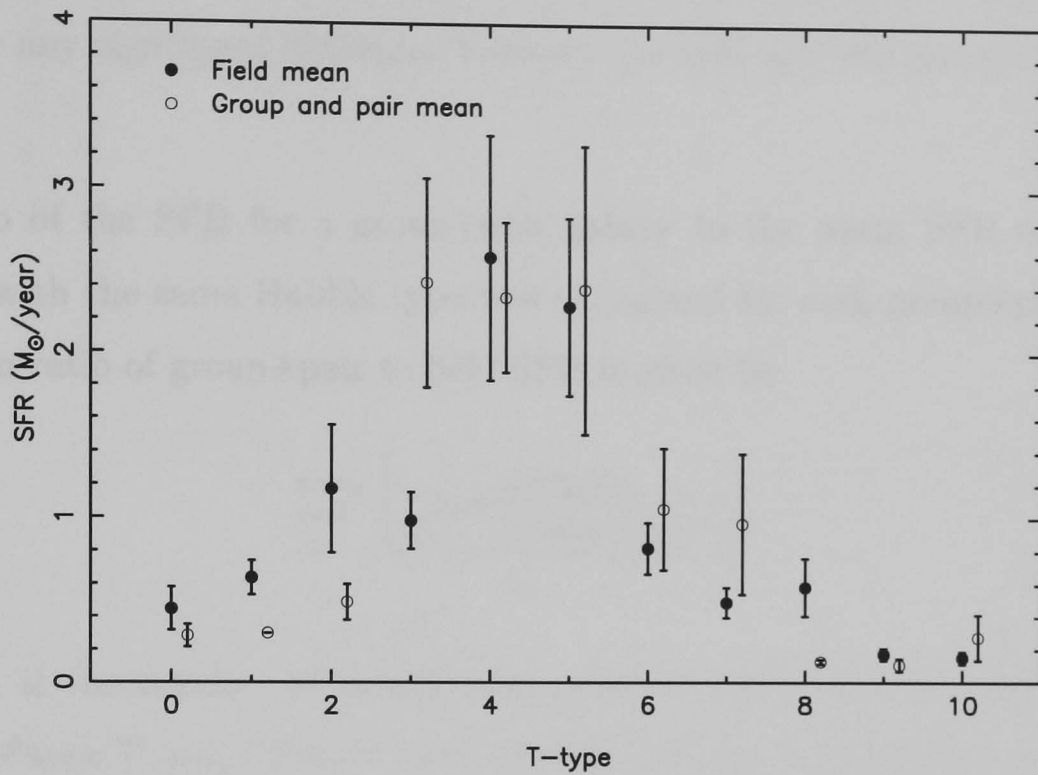


Figure 8.19: Mean SFRs for field and group+pair galaxies as a function of T-type.

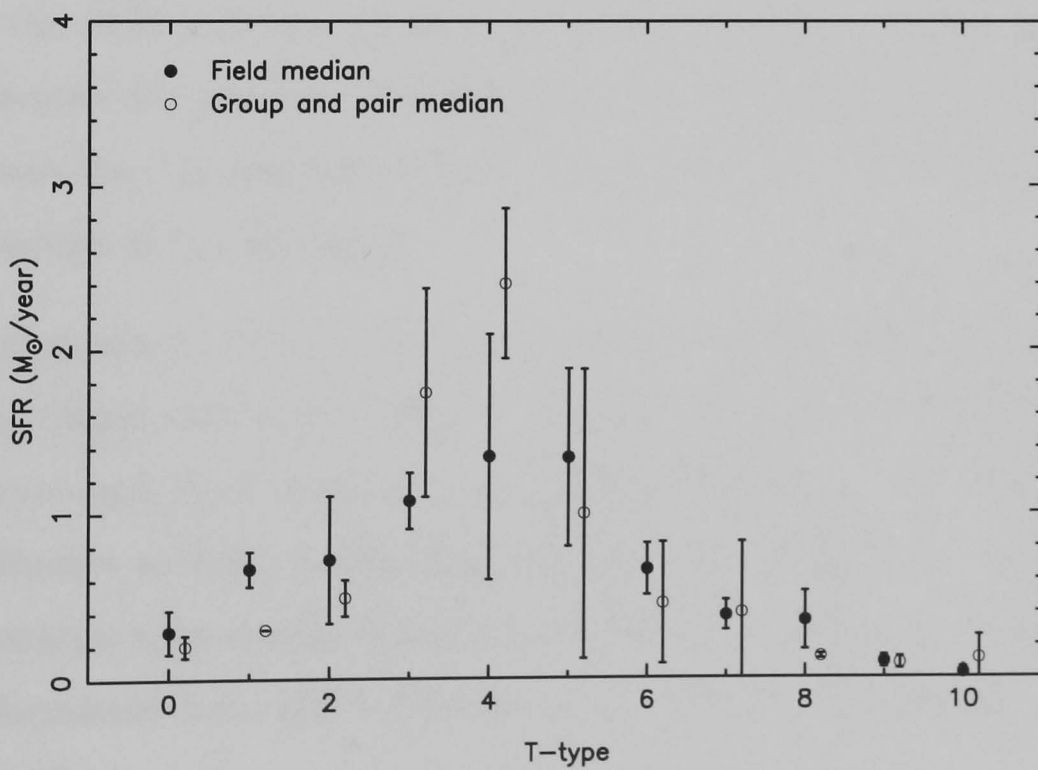


Figure 8.20: Median SFRs for field and group+pair galaxies as a function of T-type.

Sdm galaxies, where we see a reduced mean SFR for group+pair members. and for Sb galaxies, where we find a higher mean SFR for group+pair galaxies.

Figure 8.20 shows the median SFRs for each type. Within the errors, there is no longer any significant difference between the field and the group+pair populations.

The ratio of the SFR for a group+pair galaxy to the mean SFR of the field galaxies with the same Hubble type was calculated for each group+pair galaxy. The mean ratio of group+pair to field SFR is given by:

$$\frac{\sum_1^{n_g} \left[\frac{SFR_g(T)}{\sum_1^{n_f(T)} [SFR_f(T)]/n_f(T)} \right]}{n_g}, \quad (8.2)$$

where n_g is the number of group+pair galaxies, $n_f(T)$ is the number of field galaxies of type T, and $SFR_f(T)$ and $SFR_g(T)$ are the star formation rates of the field and group+pair galaxies which are of Hubble type T. For the 75 group+pair galaxies, the SFR is found, on average, to be 1.32 times higher than for the equivalent-type field galaxies. The standard error on this result is 0.21, however, which means that the difference found between the SFRs of the group+pair and the field sample is not significant.

Figure 8.21 shows the SFRs of the galaxies plotted against the $\log C_{31}$ concentration index. Objects are colour coded by their environment. In this plot, the Virgo galaxies have again been included, and the group sample has been separated back into the Huchra & Geller (1982) groups and the paired galaxies. Plotting SFR on a logarithmic scale reveals that the lowest SFRs occur mainly in field galaxies. For star formation rates above $0.01 \text{ M}_{\odot}\text{yr}^{-1}$, the environmental effects seem to be very small.

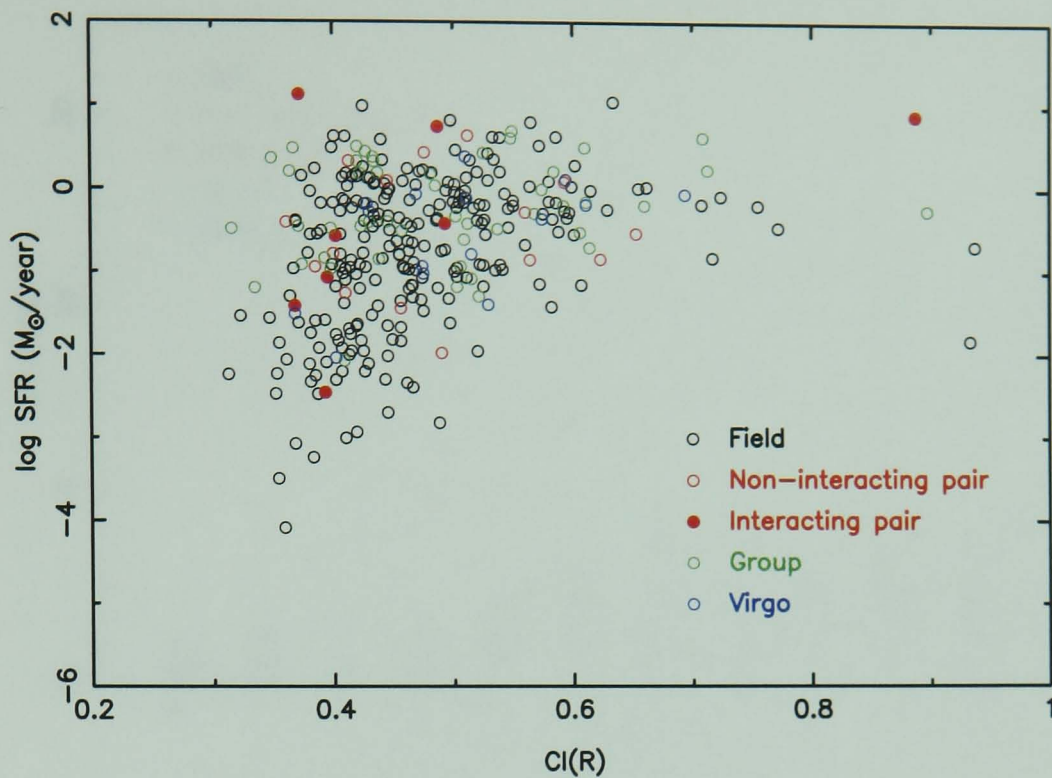


Figure 8.21: SFR plotted against the $\log C_{31}$ concentration index. Different galaxy environments are coded with different colours.

8.3.2 EW dependence on environment

The environmental dependencies of luminosity-normalised star formation activity are investigated in this section. Figure 8.22 shows the EWs of the observed galaxies binned by Hubble type, with galaxies in different environments coded with different colours and symbols. It can be seen from the two highest points in the Im (T=10) bin (the pair UGC 3847 and UGC 3851, see Figure 7.19) and the highest EW point in the Sb (T=3) bin (UGC 12699, see Figure 7.21) that galaxy interactions can significantly increase the star formation above the modal value for galaxies of those types. It can also be seen from the lowest point in the Im bin (UGC 12700 - the partner of UGC 12699) that interactions can effectively halt the production of new stars in a galaxy.

Another trend apparent from Figure 8.22 is the lack of group and Virgo Cluster galaxies with low EWs, particularly for types later than Sbc (T=4).

Plotting the mean value EWs of the field and group+pair galaxies (Figure 8.23) shows no difference within the errors between the two samples for the majority of Hubble types. The exceptions are the Sb, (T=3), Sd (T=7) and Im (T=10)

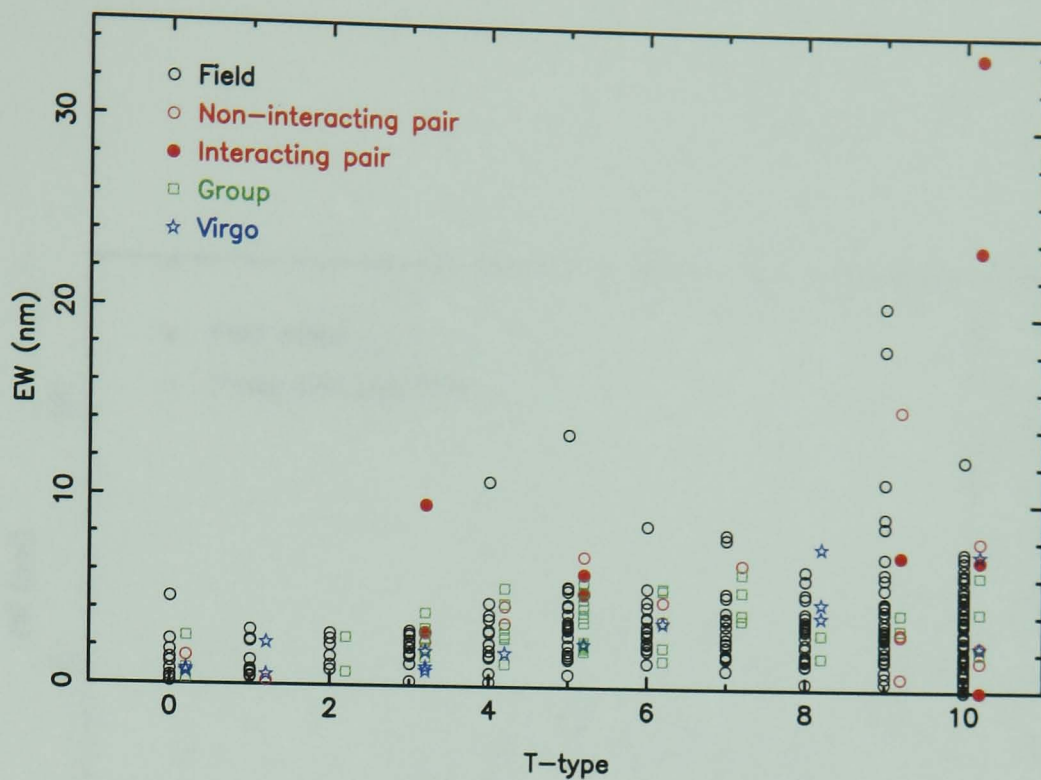


Figure 8.22: The distribution of EWs as a function of T-type. Different galaxy environments are coded with different colours and symbols.

galaxies, where the mean group+pair EW is higher than the mean field value. In the cases of the Sb and the Im galaxies, the group+pair mean EW is at least partially influenced by the increased activity in the interacting galaxies mentioned above, as can be seen when plotting the median values in Figure 8.24.

Calculating the ratios of group+pair EWs to the mean field EW for the appropriate Hubble type as before, we find that, in the mean, the equivalent widths of group+pair galaxies are 1.37 times higher than the field. The standard error is 0.15, thus this result is marginally significant. Removing the 3 high EW, interacting galaxies mentioned above causes the mean ratio to drop to 1.13, with a standard error of 0.07. The finding is therefore below 2 standard errors, and so no significant difference between the field and the group+pair populations can be said to be found.

Koopmann & Kenney (2002) plot equivalent widths against R-band continuum concentration for 29 isolated and 84 Virgo Cluster galaxies. They find that the isolated galaxies mostly fall into a narrow range on this plot. The Virgo galaxies have a much larger spread in EW, mostly due to galaxies with reduced star formation, but also partially due to large enhancements in the EWs for several galaxies.

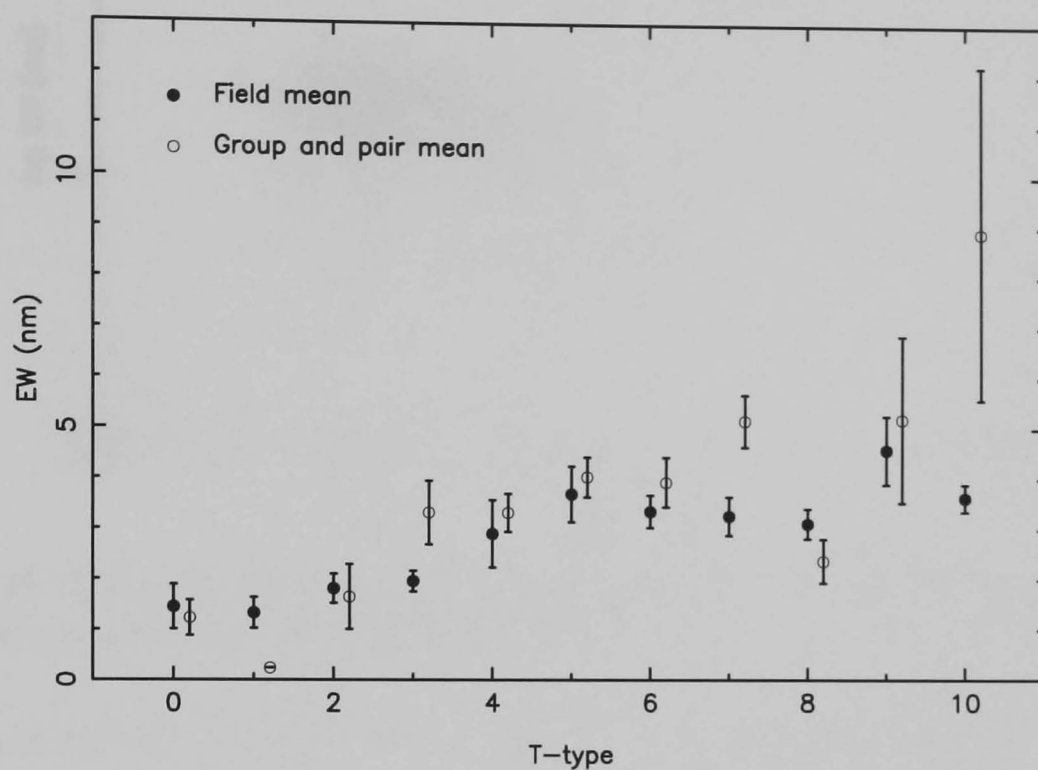


Figure 8.23: Mean EWs for field and group+pair galaxies as a function of T-type.

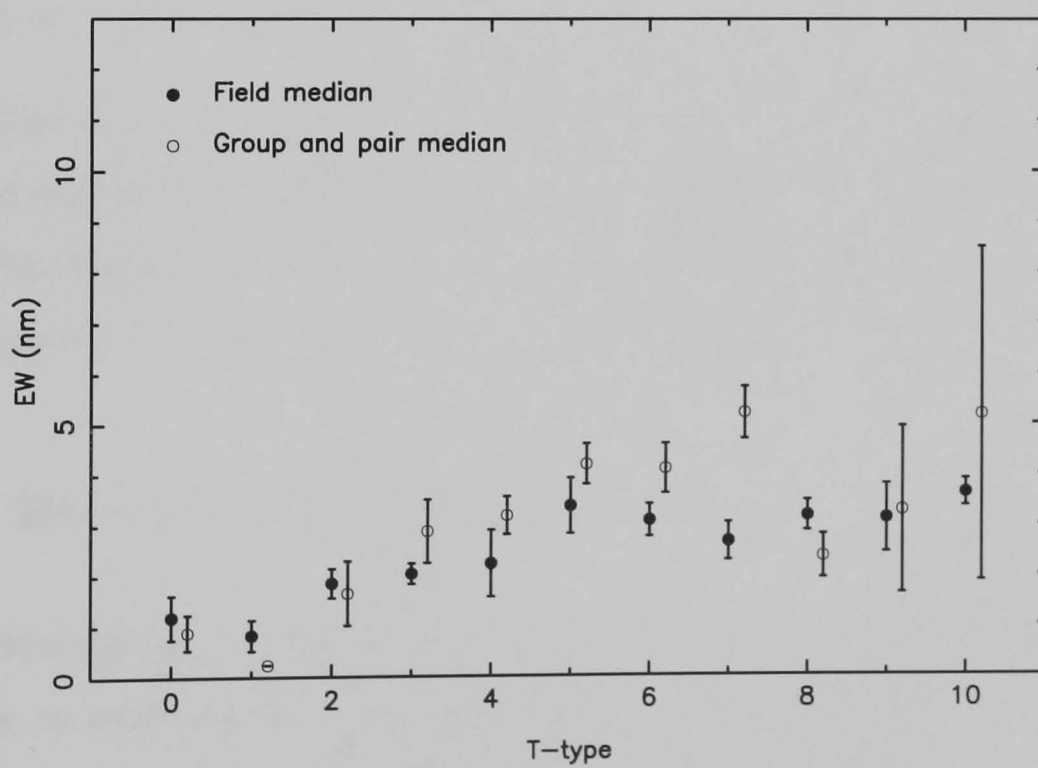


Figure 8.24: Median EWs for field and group+pair galaxies as a function of T-type.

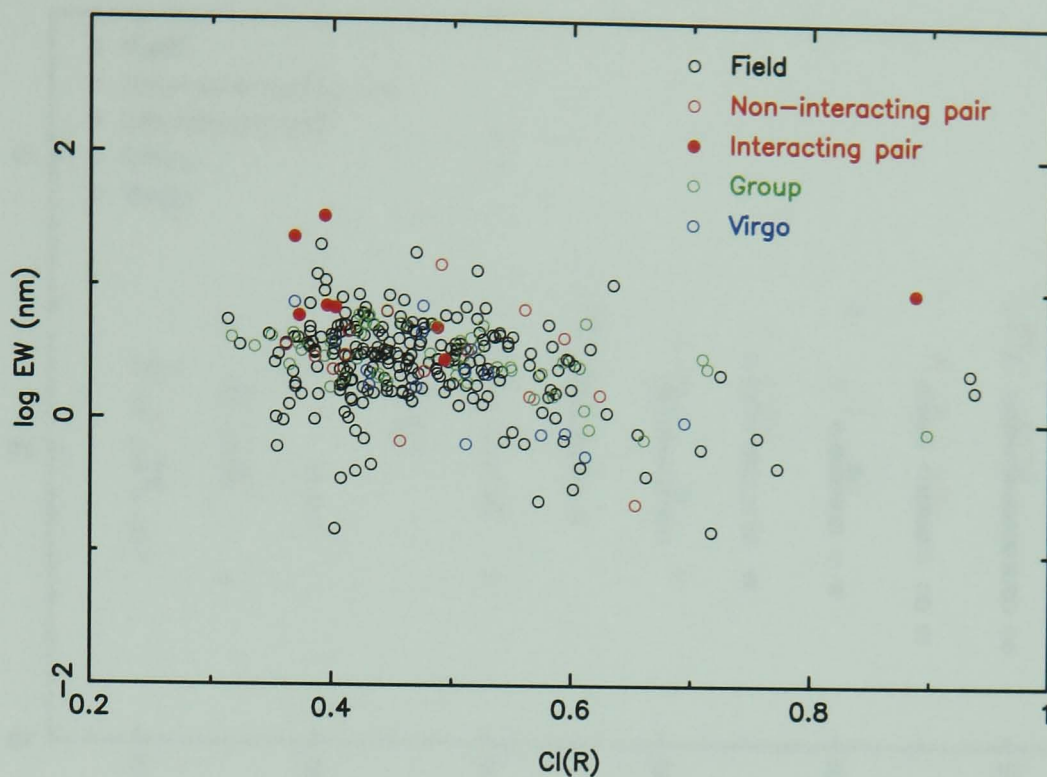


Figure 8.25: EW plotted against the $\log C_{31}$ concentration index. Different galaxy environments are coded with different colours.

In Figure 8.25, the equivalent widths are plotted against the $\log C_{31}$ R-band concentration index for the observed $H\alpha$ GS galaxies. Different local environments are coded with different colours.

The findings of Koopmann & Kenney (2002) are not reproduced here for either the group galaxies or the 15 Virgo galaxies. With the exception of the 3 high-EW, interacting galaxies, the isolated field galaxies appear to cover a marginally larger range than the galaxies in denser environments.

8.3.3 $H\alpha$ surface brightness dependence on environment

Finally, we investigate the effect of environment on the size-normalised star formation rates, as represented by the $H\alpha$ surface brightnesses of the galaxies. Figure 8.26 shows the distribution of surface brightnesses within each Hubble type, with the different galaxy environments coded by different colours and symbols. We see very few non-field galaxies with low $H\alpha$ surface-brightness values. However, 8 out of 12 galaxies with $\log SB(H\alpha) > 3.0$ are from pairs, groups or Virgo.

Plotting the mean $H\alpha$ surface brightnesses in Figure 8.27, we see that there is an

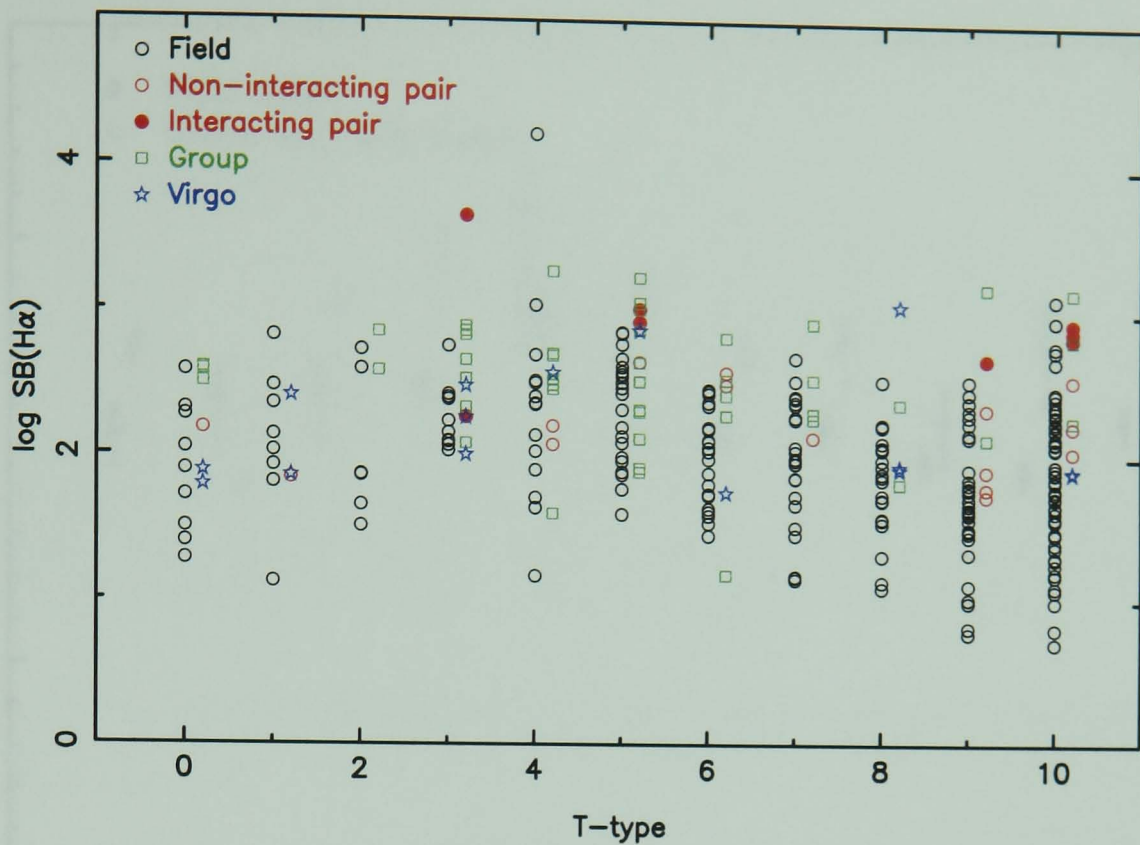


Figure 8.26: The distribution of $H\alpha$ surface brightnesses as a function of T-type. Different galaxy environments are coded with different colours and symbols.

increase in the average star formation rate per unit surface area in the group+pair galaxies compared to the isolated field objects. The situation is almost identical if the median values were to be plotted.

On average, the $H\alpha$ surface brightness for group+pair galaxies is found to be 2.67 times higher than their field counterparts. The standard error on this result is 0.44, so this is a significant result. K-S tests applied to galaxies of each Hubble type are consistent with the field and group+pair samples being drawn from different populations.

Plotting the mean R-band surface brightnesses (Figure 8.28) shows that the continuum light per unit surface area is also enhanced in group+pair galaxies compared to the field. This finding remains true if we change our method of constructing a measure of surface brightness. Figure 8.29 shows the $H\alpha$ and R-band surface brightnesses defined using the R-band effective radii of the galaxies instead of the Petrosian radii.

A plot of the size-normalised star formation rate against R-band concentration index (Figure 8.30) again shows that galaxies in pairs, groups or in the Virgo

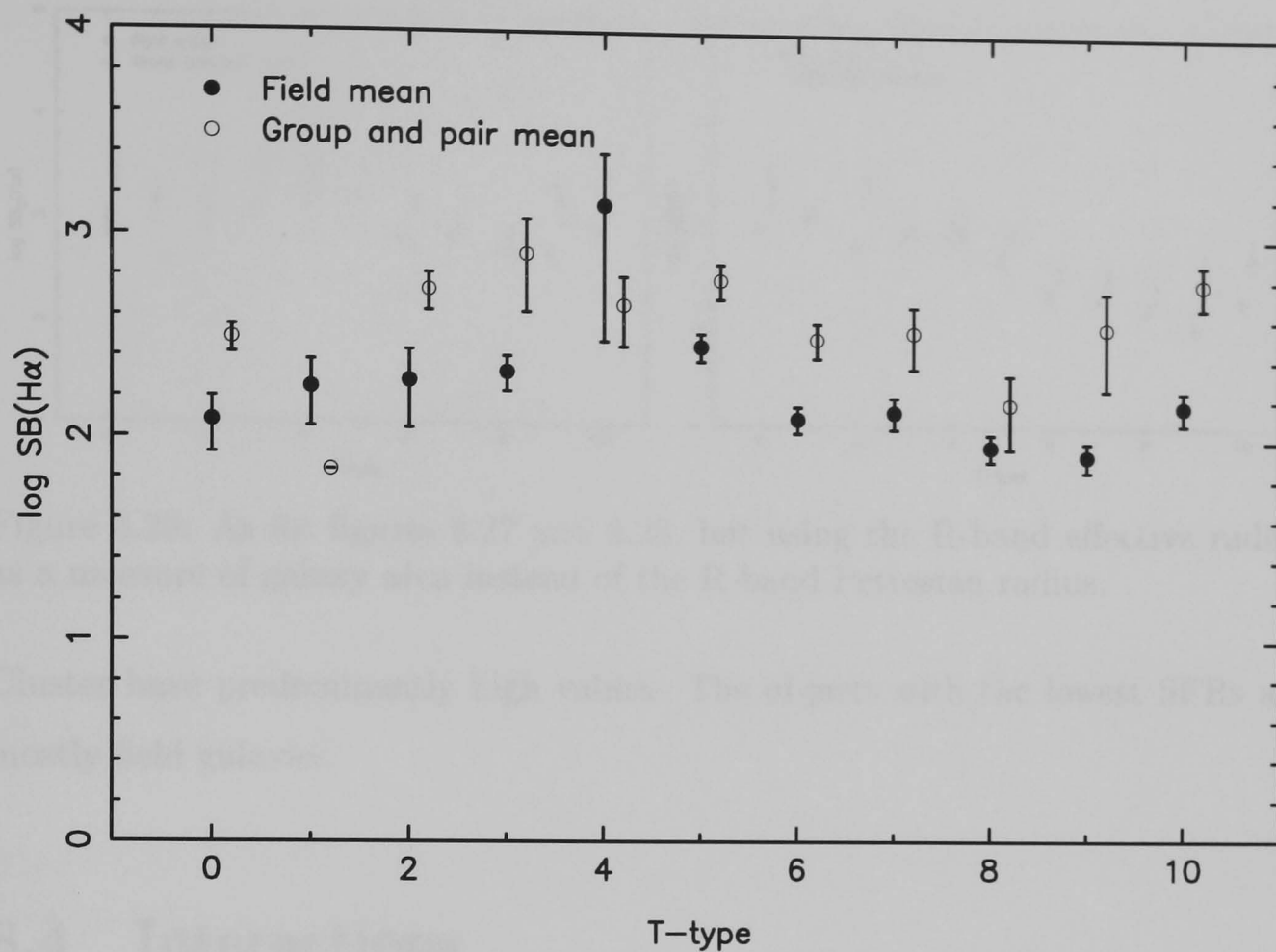


Figure 8.27: Mean H α surface brightnesses for field and group+pair galaxies as a function of T-type.

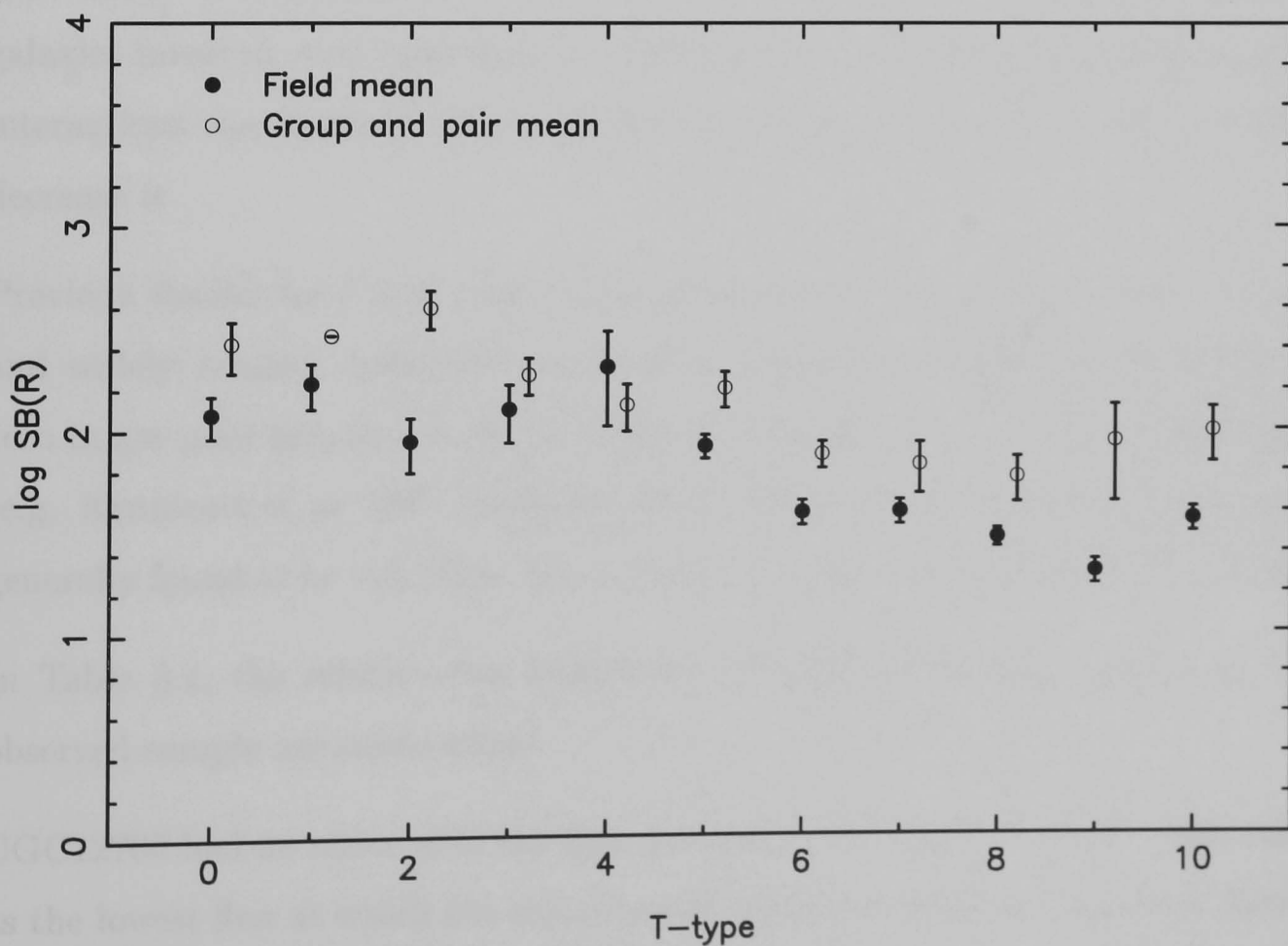


Figure 8.28: Mean R-band surface brightnesses for field and group+pair galaxies as a function of T-type.

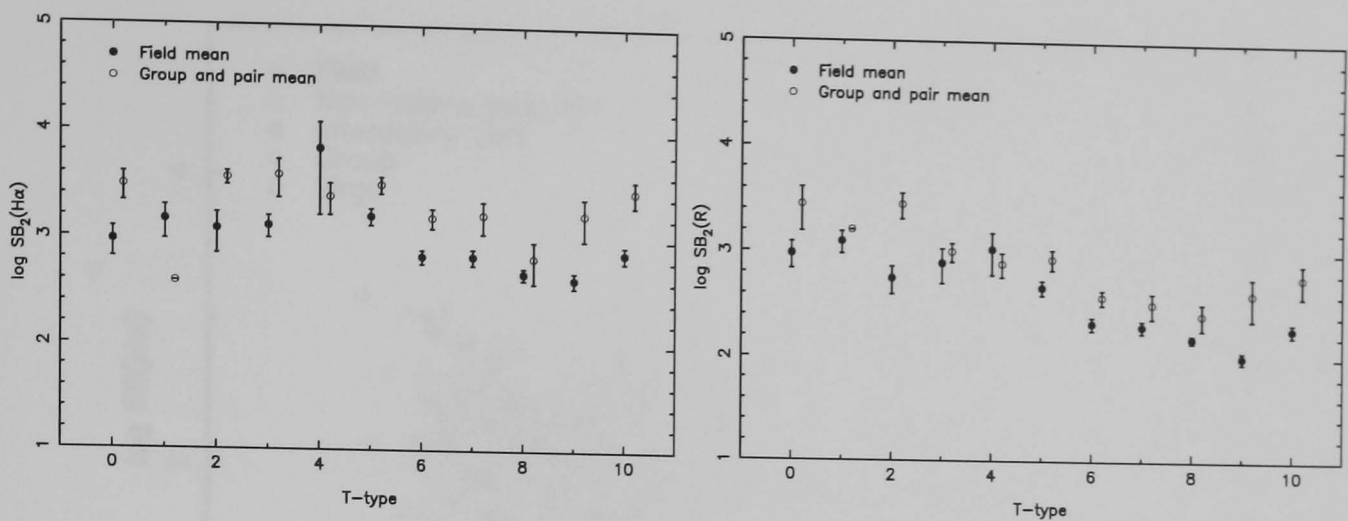


Figure 8.29: As for figures 8.27 and 8.28, but using the R-band effective radius as a measure of galaxy area instead of the R-band Petrosian radius.

Cluster have predominantly high values. The objects with the lowest SFRs are mostly field galaxies.

8.4 Interactions

The effects of interactions on the distribution of the star formation within the galaxies involved were investigated in Section 7.4. In Section 8.3.2 we saw that interactions can increase the star formation activity of a galaxy, but can also decrease it.

Previous studies have found that interacting and merging galaxies show strong and widely ranging enhancements in their star formation rates, ranging from zero in gas poor galaxies, to on the order of 100 times in the most extreme cases (e.g. Kennicutt et al. 1987; Bushouse et al. 1988). The average enhancement is generally found to be 2-3 times that found in isolated galaxies (Kennicutt, 1998).

In Table 8.1, the relative star formations of the 9 interacting galaxies in the observed sample are summarised.

UGC12700 had no observable $H\alpha$ flux, so a value of $1.0 \times 10^{-17} \text{ Wm}^{-2}$ was taken as the lowest flux at which $H\alpha$ was detected within the survey. The upper limits in the table are derived from this.

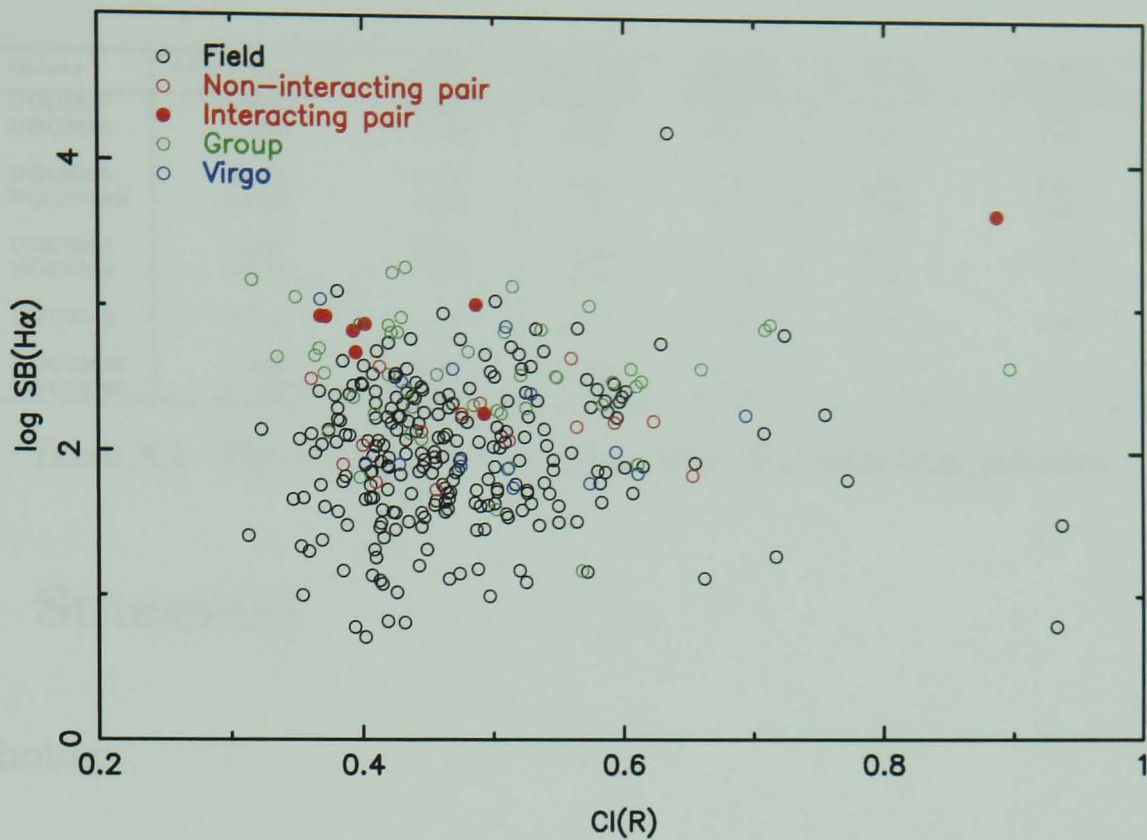


Figure 8.30: H α surface brightness plotted against the $\log C_{31}$ concentration index. Different galaxy environments are coded with different colours.

Table 8.1 shows that the SFRs found in the interacting galaxies can fall both above and below the mean found from the field galaxies for the same Hubble type. This is not surprising as the size of the galaxy will play a large part in the overall SFRs. Several of the interacting galaxies were only observed as they happened to appear in the same field of view as their companion galaxy, and thus can fall above or below the diameter limits of the parent sample.

With the exception of UGC12700, which is believed to be a post-starburst galaxy (Bernloehr, 1993), the equivalent widths of interacting galaxies are increased over those of their isolated equivalents. UGC3847 has its EW enhanced by nearly an order of magnitude.

In most cases, the star formation rate per unit area is also significantly enhanced by interactions. For this measure of activity, UGC12699 has experienced the largest increase.

Galaxy	SFR ($M_{\odot}\text{yr}^{-1}$)	$\frac{SFR}{SFR_{field}}$	EW (nm)	$\frac{EW}{EW_{field}}$	log SB(H α)	$\frac{SB(H\alpha)}{SB(H\alpha)_{field}}$
UGC3847	0.00354	0.0234	33.88	9.33	2.83	4.62
UGC3851	0.0390	0.258	23.61	6.50	2.93	5.83
UGC6595	0.385	0.392	2.88	1.47	2.27	0.87
NGC3769A	0.0859	0.498	7.20	1.57	2.88	9.08
UGC8034	0.514	3.405	8.00	2.20	2.54	2.36
NGC4810	0.271	1.792	7.00	1.93	2.88	5.15
UGC3740	13.48	5.905	6.06	1.64	2.93	2.97
UGC12699	7.849	7.981	9.65	4.92	3.66	21.1
UGC12700	< 0.028	< 0.185	< 0.7	< 0.193	-	-

Table 8.1: The star formation properties of interacting galaxies.

8.5 Summary

Morphology

For all the different measures of star formation, a large scatter amongst galaxies with the same morphology is found. When investigating the total star formation rate of a galaxy, the highest values are found for Hubble-types Sb-Sc. When normalising for galaxy mass or size, the Sm-Im galaxies are found to be the most active on average, and the early-type S0/a-Sa galaxies the least. However, there are still many early-type galaxies with higher amounts of star formation activity than many of the later types, and in fact, the lowest individual star formation rates generally belong to the Sm-Im classes. Overall, these latest types have the largest range in star-forming properties.

The modal SFR, for all types, is close to zero, indicating that galaxies with low star formation rates are much more common in the local Universe than those with high SFRs.

Bars

There appears to be some weak dependence on bar presence. The highest EWs are generally found in barred galaxies, particularly for the later types. The strength of the dependence weakens if median values are studied rather than mean star formation rates. Further investigation is required involving the length and strength

of the bars before their true contribution can be fully understood.

Luminosity

Gavazzi et al. (1996) found that EW increased steeply with decreasing galaxy luminosity for the brightest galaxies and was independent of luminosity below a certain threshold. The results from the H α Galaxy Survey are in agreement with this finding for early-type galaxies (S0/a-Sa), but for all later types, there appears to be no correlation between the star formation per unit mass and the continuum emission from the galaxy. The H α GS sample contains more faint galaxies than that studied by Gavazzi et al. (1996).

No correlation is found between H α surface brightness and R-band absolute magnitude either, although there is a very large scatter.

Environment

Allam et al. (1999) find a slight decrease in the mean [OII] λ 3727 EWs for galaxies in loose groups in the Las Campanas Redshift Survey, compared to field galaxies. The H α GS data reveal no significant difference in the mean or median SFRs and H α EWs for the Huchra & Geller (1982) group galaxies and those in close pairs compared to the field sample. However, for both measures of star formation, the lowest values are predominantly found in the field. Koopmann & Kenney (2002) find a larger spread of EWs for Virgo Cluster galaxies than for the isolated galaxies. The reverse has been found here for the group, pair and Virgo objects.

When the H α surface brightnesses of the galaxies are used as a measure of size-normalised star formation, a significant increase in activity is noted in the group and pair galaxies. Only a very few non-field galaxies are detected with the lowest surface brightnesses, whereas 8 out of 12 of the highest surface-brightness galaxies are in pairs, groups or the Virgo Cluster. Higher H α surface brightnesses are found for group+pair galaxies when the mean and median values are compared. These

galaxies are found to experience a mean enhancement in their size-normalised star formation rates by a factor of 2.67 ± 0.44 . The R-band surface brightnesses of group+pair galaxies are also enhanced over those in the field. These findings do not change if we alter our method for representing galaxy sizes.

The difference between the findings from the EW and the $H\alpha$ surface brightness investigations could imply that galaxies in groups and pairs have experienced constant star formation enhancements over large timescales. Thus, the number of old stars in these galaxies will have increased in proportion to the number of newly-formed stars and the equivalent widths (which are also a measure of star formation history) will be relatively unaffected. The detected increase in R-band surface brightnesses in group+pair galaxies supports this theory.

Interactions

In agreement with previous studies, we find a general enhancement in the star formation of galaxies involved in interactions. The magnitude of this enhancement is variable, and on average is higher when measured using $H\alpha$ surface brightness than when EWs are taken. Interactions can also effectively halt the formation of new stars, as seen in UGC12700.

Chapter 9

Star formation in the local Universe

Amongst the main aims of the H α Galaxy Survey are the calculations of the current star formation rate of the local Universe and the contribution of galaxies of different types and luminosities to this total. Madau et al. (1996) plotted the SFR density as a function of redshift. They found that the star formation rate at high redshifts was greater than the present day value, suggesting an epoch of disk formation at $z \sim 1$. Madau et al. (1998) detected a star formation peak at a redshift of $z \approx 1.5$, followed by a fall at higher redshifts. Steidel et al. (1999) find that, if corrections for dust extinction are made, the star formation as a function of redshift remains essentially constant for all $z > 1$. There is still significant evolution below $z = 1$, however. Hopkins et al. (2000) find that the density of star formation at $z \approx 1.3$ is an order of magnitude greater than that locally.

The results from this survey can be used to more fully determine the SFR density at $z = 0$ on the Madau plot. A thorough calculation, including a full treatment of the various selection biases, sample completion, extinction corrections, AGN contamination and local clustering effects, is beyond the scope of this thesis. However, initial results can still be obtained.

9.1 The local luminosity function

In order to apply the results of the H α Galaxy Survey to the local Universe, the make-up of the galaxy population must be known. One way to do this is to plot the space density of galaxies as a function of absolute magnitude.

An investigation into this luminosity function was made using the original parent sample from the UGC, described in Section 2.1. It was assumed that the UGC was complete within its selection criteria, that is, all galaxies to a limiting diameter of 1.0' and a limiting blue apparent magnitude of 14.5 at declinations greater than -2.5° . Selection biases in the UGC are beyond the scope of this work (but see de Jong & Lacey 2000 who find biases against low surface-brightness and small scale-size galaxies). One hundred and eighty spiral galaxies which had been excluded from the parent sample due to their high inclinations were reinstated for this analysis. To prevent the results being skewed by the high density of galaxies in the Virgo cluster, galaxies with right ascensions between 12^h10^m and 12^h46^m , and declinations between $3^\circ14'$ and $20^\circ13'$ were excluded.

The apparent blue magnitudes quoted by NED for each galaxy were used. These are generally taken from RC3. Magnitudes fainter than 17 are quoted to low precision - to the nearest magnitude. In the majority of these cases, more precise values were found in the literature references listed by NED, and these were used in preference. To convert the apparent magnitudes to absolute magnitudes, distances were calculated for each galaxy using the Virgo-infall correction method described in Section 3.11. Figure 9.1 shows the distribution of absolute blue magnitudes (M_B) within the parent sample (excluding Virgo region galaxies, but including highly inclined spirals). It should be noted that these magnitudes are not corrected for extinction in this preliminary investigation. Applying corrections would result in brighter magnitudes for all galaxies, with the exact change being dependent on their position in the sky and their dust content. Inclusion of the highly inclined galaxies introduces further complications as the extinguishing effects of dust depend both upon its quantity and distribution within each galaxy.

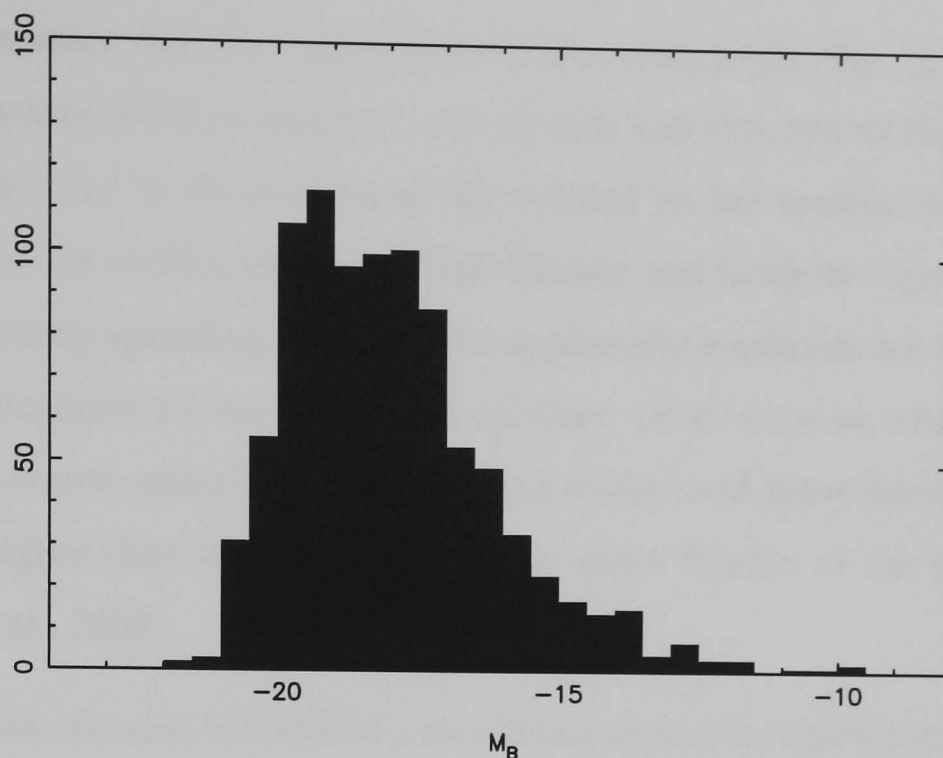


Figure 9.1: The distribution of absolute blue magnitudes within the parent sample, with galaxies in the Virgo region removed, and highly inclined galaxies included. Each bin represents 0.5 mag.

If galaxy disks are optically thick, as argued by Disney et al. (1989), and the dust is distributed in a smooth, vertically extended layer, then the galaxy will appear less luminous when seen edge on than when viewed face on. If the dust is confined to small clumps around luminous stars, the inclination dependence will be negligible.

It can be seen from Figure 9.1 that the vast majority of galaxies (915 out of 925) have magnitudes between -22 and -13 .

One way to derive a luminosity function is to group the sources in a complete sample into intervals of 1 magnitude of absolute luminosity. These are then divided by the volume over which each group is completely represented in the sample. An alternative method is to sum the separate contributions to each luminosity grouping from each source. These can be computed by dividing unity by the volume over which the source could be observed in the sample (Schmidt, 1968; Felten, 1976). This can be written as

$$\phi(M_B) = \frac{4\pi}{\Omega} \sum_i \frac{1}{V_m^i}. \quad (9.1)$$

$\phi(M_B)$ is the space density of galaxies with blue magnitude M_B , V_m^i is the visibility volume within which a galaxy, i , can be seen and included in the sample, and the quantity $\Omega/4\pi$ is the fraction of sky covered by the sample in question. In this case, $\Omega = 2\pi \times 0.695$, once the Virgo Cluster and Galactic regions have been removed. Strictly speaking, Equation 9.1 applies when galaxies are randomly distributed throughout a static Euclidean universe. However, even with the removal of the Virgo region, galaxies still cluster, and so the local space density of galaxies should be higher than the universal average space density at the present epoch (Condon et al., 2002).

Each selection criterion will define a maximum volume in which a galaxy of given properties can be observed. The visibility volume is defined as the minimum of these volumes for the galaxy in question (Disney & Phillipps, 1983; Davies et al., 1994). There are three sets of selection limits applicable to the parent sample that will define maximum volumes in which a galaxy is observable. The UGC limiting absolute magnitude, m_{lim} , is 14.5 (although many galaxies have quoted magnitudes fainter than this on NED). A galaxy with absolute magnitude M can therefore be found anywhere within a volume

$$V_{m,mag} \text{ (Mpc}^3\text{)} = \frac{4\pi}{3} 10^{0.6(m_{lim}-M-25)}. \quad (9.2)$$

This equation does not take into account extinction corrections.

The H α GS sample was selected to contain galaxies with apparent angular diameters between 1.7' and 6.0'. A galaxy with an absolute diameter D will be excluded from the sample if its distance, d , is low enough for the apparent diameter to measure greater than 6.0', or if it is so far away that the apparent diameter falls below 1.7'. Thus the volume in which it can be observed is

$$V_{m,D} \text{ (Mpc}^3\text{)} = \frac{4\pi}{3} d^3 \left[\left(\frac{D}{1.7} \right)^3 - \left(\frac{D}{6.0} \right)^3 \right]. \quad (9.3)$$

Galaxies which are intrinsically small and faint will only be detected at the smallest distances due to the apparent magnitude and the minimum apparent

diameter limits. The galaxies with the largest intrinsic sizes can only be observed at larger distances, due to the maximum angular diameter limit. To account for this uneven observable distribution, the parent sample was split into 5 redshift shells: $v \leq 1000$, $1000 < v \leq 1500$, $1500 < v \leq 2000$, $2000 < v \leq 2500$, and $2500 < v \leq 3000 \text{ kms}^{-1}$. These redshift limits were converted to distance limits using the Virgo infall model described in Section 3.11. The distances taken are the mean values computed at each redshift for 687 systematic positions around the sky, excluding regions close to the Virgo Cluster and the Galactic plane. These distance limits are: 15.6, 22.0, 27.9, 33.6 and 39.3 Mpc. Galaxies were redistributed into the correct distance shell when appropriate.

In each shell, there will, therefore, also be a maximum volume in which a galaxy can be observed due to the distance limits of that shell:

$$V_{m,shell} (\text{Mpc}^3) = \frac{2\pi}{3} \times 0.695(d_o^3(shell) - d_i^3(shell)), \quad (9.4)$$

where $d_o(shell)$ is the outer-distance limit for the shell in which the galaxy is located, and $d_i(shell)$ in the inner-distance limit. The factor of 0.695 comes from integrating the volume of sky through 2π radians of right ascension and from -2.5 - 90° in declination, with the Virgo Cluster and regions that lie within 20° of the Galactic plane removed.

For the majority of the galaxies (~ 790), $V_{m,shell}$ is the smallest of the 3 volumes, and thus corresponds to the visibility volume of the galaxy. For the faintest galaxies in each bin (~ 100 in total), the visibility generally becomes equal to $V_{m,mag}$. For a small number of galaxies (~ 30), predominantly in the lowest-distance shell, $V_{m,D}$ is the smallest volume. This shows that, by binning up the galaxies by distance, we have produced a largely volume-limited sample.

The results of applying Equation 9.1 to each shell are shown in Figure 9.2. The error bars represent $\phi(M_B)/\sqrt{n}$, where n is the number of galaxies contributing to the point. It can clearly be seen that the faintest galaxies are only to be found in the lowest-distance shells, whereas the brightest galaxies are more com-

mon at higher redshifts. These plots have been combined, assuming a Poisson error distribution, by taking the weighted mean ($\sum_{shell} n\phi(M_B)/\sum_{shell} n$) for each magnitude to produce a luminosity function for the entire parent sample out to $v=3000 \text{ kms}^{-1}$ (Figure 9.3). A total of 915 galaxies comprise the data in Figure 9.2. Three points in the plots are derived from only one galaxy (and thus have no error bars). These points were omitted when deriving the weighted mean for each magnitude grouping, and so Figure 9.3 contains data from 912 galaxies.

Luminosity functions of field galaxies are often found to be described well by a Schechter function (Schechter, 1976) (see e.g. Efstathiou et al. 1988):

$$\phi(M)dM = (0.4 \ln 10)\phi^*10^{0.4(M^*-M)(\alpha+1)} \exp(-10^{0.4(M^*-M)}). \quad (9.5)$$

This formula describes a function where the number of galaxies decreases approximately as a power law with increasing galaxy luminosity at faint magnitudes, but cuts off very sharply for galaxies brighter than some characteristic magnitude, M^* . α gives the slope of the luminosity function at the faint end and ϕ^* sets the over-all normalisation of galaxy density. The function was derived assuming that galaxies form by self-similar gravitational condensation, and thus all have the same mass-to-light ratio (Press & Schechter, 1974; Condon et al., 2002).

A Schechter fit was made to the galaxies in Figure 9.3 by scanning through ϕ^* , M^* and α parameter space and finding the values that minimise the χ^2 statistic:

$$\chi^2 = \sum_M \frac{(\log \phi_{fit} - \log \phi_{calc})^2}{(\log(1 \pm 1/\sqrt{n}))^2}, \quad (9.6)$$

where ϕ_{fit} comes from Equation 9.5 and ϕ_{calc} from Equation 9.1. If $\phi_{fit} > \phi_{calc}$, then the plus sign is used in the denominator, and if $\phi_{fit} < \phi_{calc}$, then the minus sign is used. The best-fit Schechter function to the calculated points is represented as the solid line in Figure 9.3. The parameters are given in Table 9.1. The fit is poor, particularly at the bright end where there are very few galaxies brighter than M_B to constrain χ .

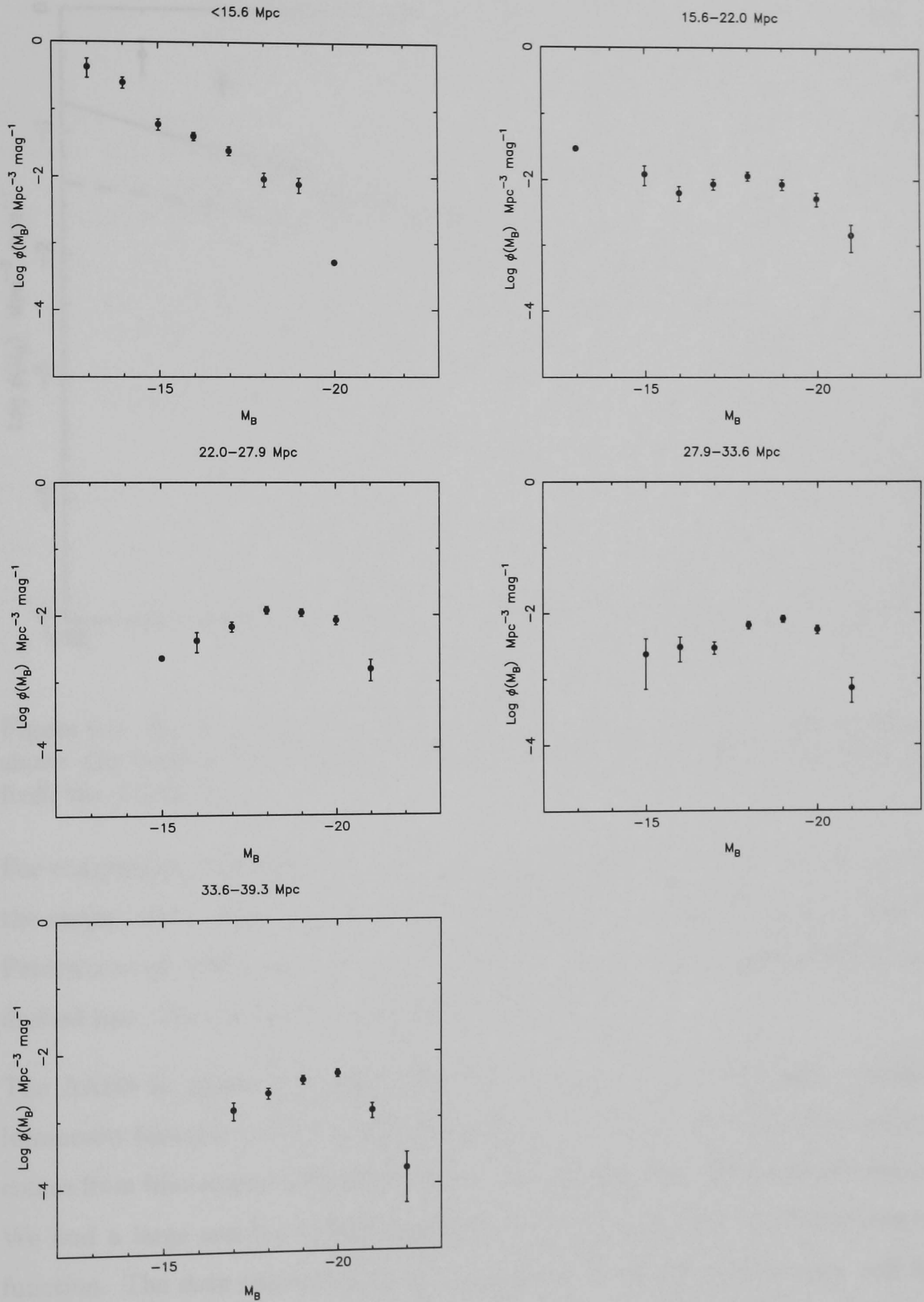


Figure 9.2: The calculated parent luminosity functions for each distance shell. The error bars represent $\phi(M_B)/\sqrt{n}$, where n is the number of galaxies contributing to the point.

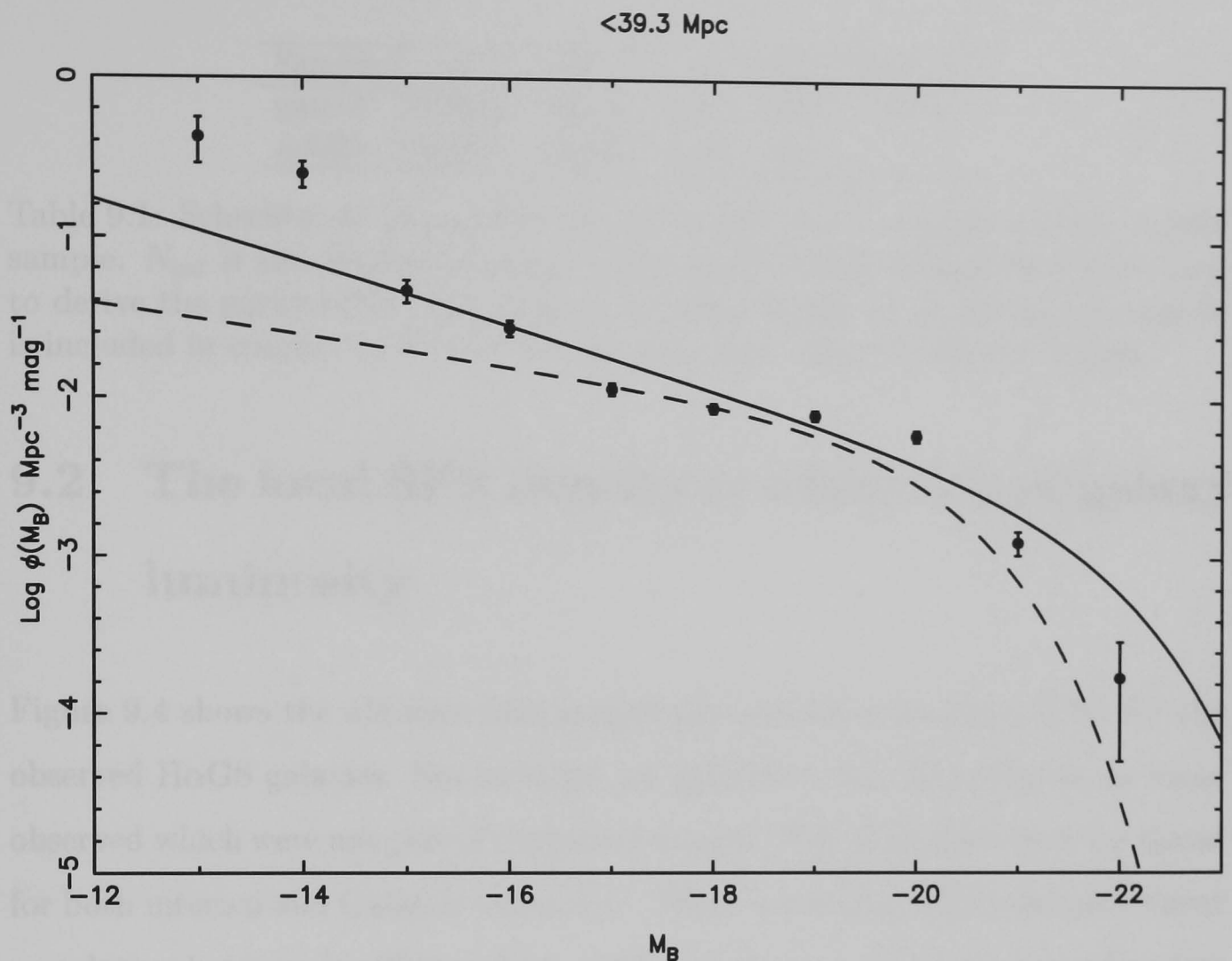


Figure 9.3: The luminosity function for the entire parent sample. The solid line shows the best-fit Schechter curve and the dashed line shows the Schechter fit from the AARS data.

For comparison, the Schechter function that best describes the spiral galaxies in the range $-22 \leq M_B \leq -17$ from the Anglo-Australian Redshift Survey (AARS; Peterson et al. 1986) as found in Efstathiou et al. (1988) is represented by the dashed line. The parameters are again given in Table 9.1.

The AARS fit agrees relatively well with the bright end of the parent sample luminosity function, and no re-normalisation was required. The main discrepancy comes from blue magnitudes fainter than -17 (below the limit of the AARS data). We find a large number of faint galaxies not predicted by the AARS-Schechter function. The data calculated for the $H\alpha$ GS parent sample are not very well fit by a Schechter function due to these low-luminosity galaxies. One of the principal advantages of the $H\alpha$ Galaxy Survey over previous star formation studies is the inclusion of this large population of faint galaxies.

Sample	ϕ^*	M^*	α	N_{gal}	Red. χ^2
parent	0.0022	-21.85	-1.49	912	13.67
AARS	0.0067	-20.26	-1.24	340	

Table 9.1: Schechter fit parameters for the H α GS parent sample and the AARS sample. N_{gal} is the number of galaxies contained in each sample that were used to derive the parameters. The reduced χ^2 value for the fit to the parent sample is included in column 6. A value for H_0 of 75 kms $^{-1}$ Mpc $^{-3}$ has been taken.

9.2 The local SFR density as a function of galaxy luminosity

Figure 9.4 shows the absolute blue magnitudes and the calculated SFRs for the observed H α GS galaxies. Not included are galaxies in the Virgo region, or those observed which were not part of the parent sample. The SFRs have been corrected for both internal and Galactic extinction. There is a strong, approximately-linear correlation between log SFR and M_B , although there is a large amount of scatter within each magnitude grouping. The highest star formation rates are found in the brightest galaxies.

In order to scale up the observed sample to more accurately represent the parent sample (and thus reduce observing biases), each galaxy was placed into a morphology-magnitude bin. Figure 9.5 shows the distribution of absolute magnitudes amongst each galaxy T-type for both the parent and the observed samples. Whilst the faintest galaxies tend to be irregulars, the range of the distribution is very large. K-S tests applied to each galaxy type show that the observed sample is consistent with being drawn randomly from the parent sample. For each T-type, the distribution was divided into high, medium and low magnitudes and the number of galaxies in each T- M_B bin was counted for both the parent and the observed samples.

The points in the luminosity function found in the previous section were used to predict the number of galaxies within each magnitude grouping that should

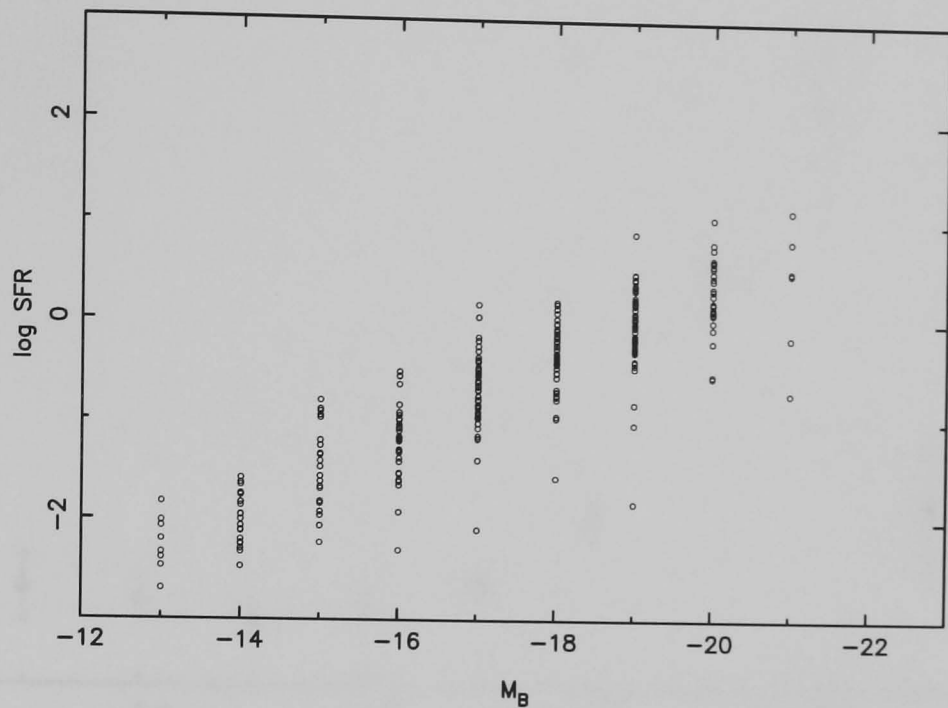


Figure 9.4: The log of the star formation rate plotted against binned absolute blue magnitudes for the observed galaxies.

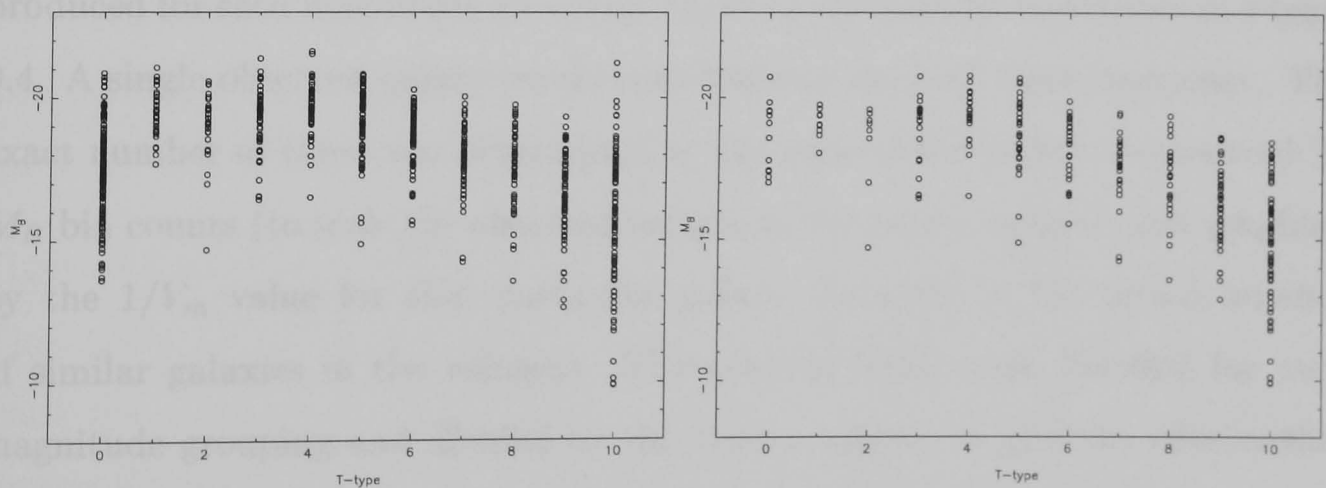


Figure 9.5: The distribution of absolute magnitudes amongst each galaxy T-type for both the parent (left) and the observed samples (right).

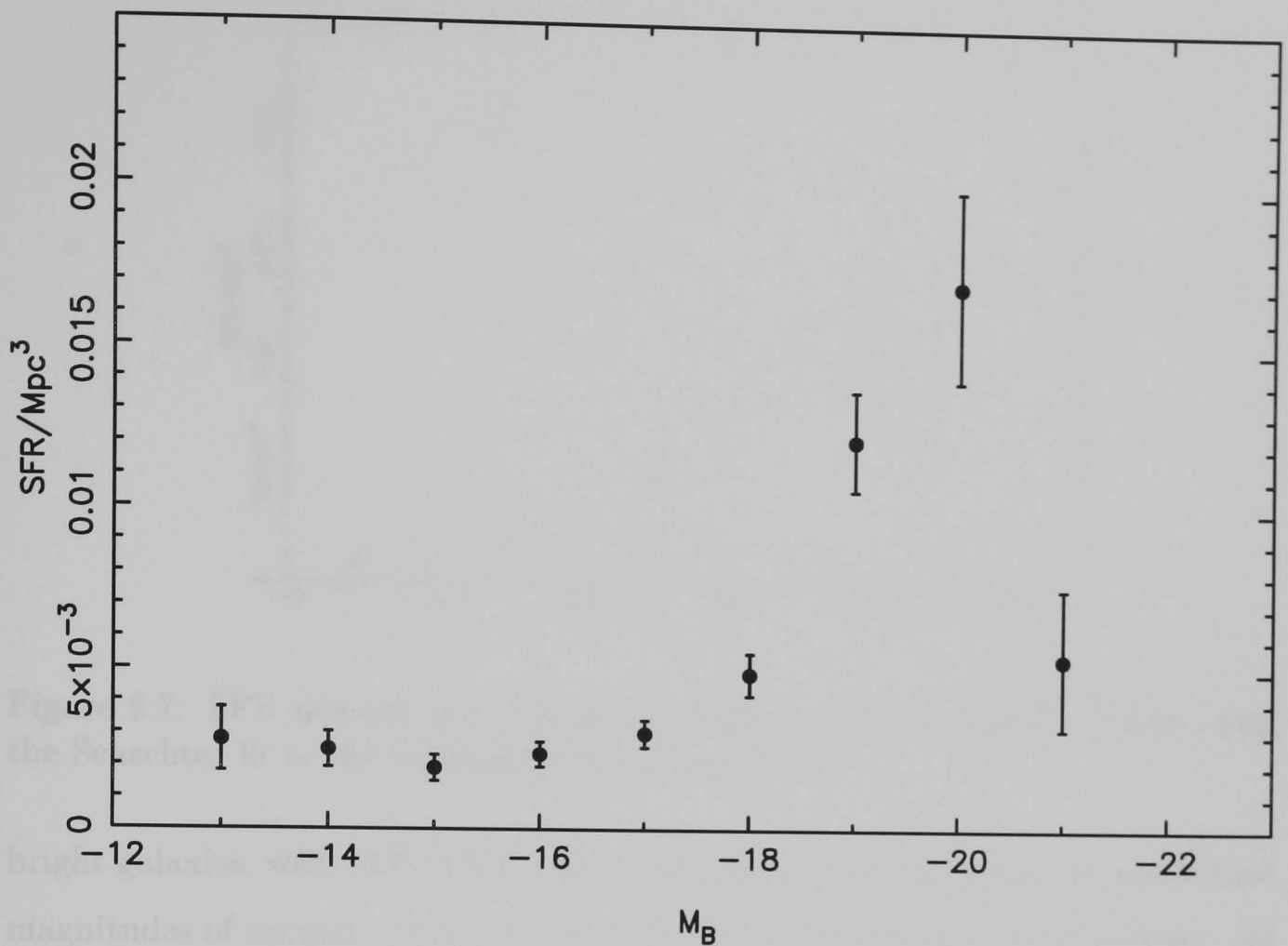


Figure 9.6: SFR density as a function of absolute blue magnitude found using the points in the luminosity function (Fig. 9.3).

be present in a volume chosen to be 1000 times larger than that covered by the Survey. For each of these predicted galaxies, an SFR value was randomly allocated from a pool of values compiled from the observed data. A separate pool was produced for each magnitude grouping, based on the distribution shown in Figure 9.4. A single observed galaxy would contribute to the pool more than once. The exact number of times was determined by the ratio of the parent to observed $T-M_B$ bin counts (to scale the observed sample to the parent sample) and weighted by the $1/V_m$ value for that particular galaxy (to scale to the actual number of similar galaxies in the volume). The selected SFRs were summed for each magnitude grouping and divided by the chosen volume to give the relationship between SFR density (in $M_{\odot} \text{yr}^{-1} \text{Mpc}^{-3}$) and absolute blue magnitude. The results are shown in Figure 9.6. The error bars represent SFR density divided by the square root of the number of observed galaxies in the magnitude grouping.

The plot shows that in the local Universe, the star formation is dominated by

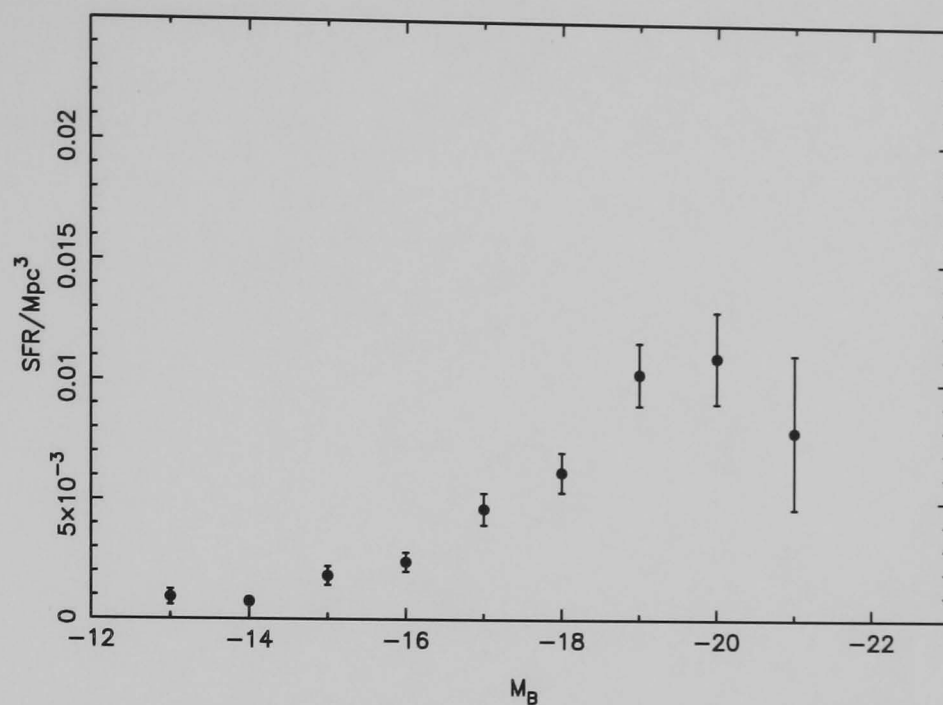


Figure 9.7: SFR density as a function of absolute blue magnitude found using the Schechter fit to the luminosity function (Fig. 9.3).

bright galaxies, with 55% of the total taking place in galaxies with absolute blue magnitudes of around -19 to -20 . Fainter galaxies with magnitudes between -13 and -17 contribute approximately-equal amounts (around 5% of the total) per magnitude.

If the Schechter fit to the luminosity function is used to predict the number of galaxies in a given volume, then we obtain a different SFR-luminosity function (Figure 9.7). Since the fit predicts a lower number of faint galaxies, we find a lower contribution to the total SFR density from galaxies with $M_B < -14$. We also find that the contribution from galaxies with $M_B = -20$ drops, whilst that from the very bright $M_B = -21$ galaxies increases.

Figure 9.8 shows the SFR-luminosity function if the AARS-Schechter fit is used. This, again, predicts a much smaller contribution from the faint end than is found using the points in the M_B luminosity function. The shape of the bright end is similar to that in Figure 9.6, but systematically lower.

All three plots show that the current SFR is dominated by bright galaxies with M_B between -19 and -20 .

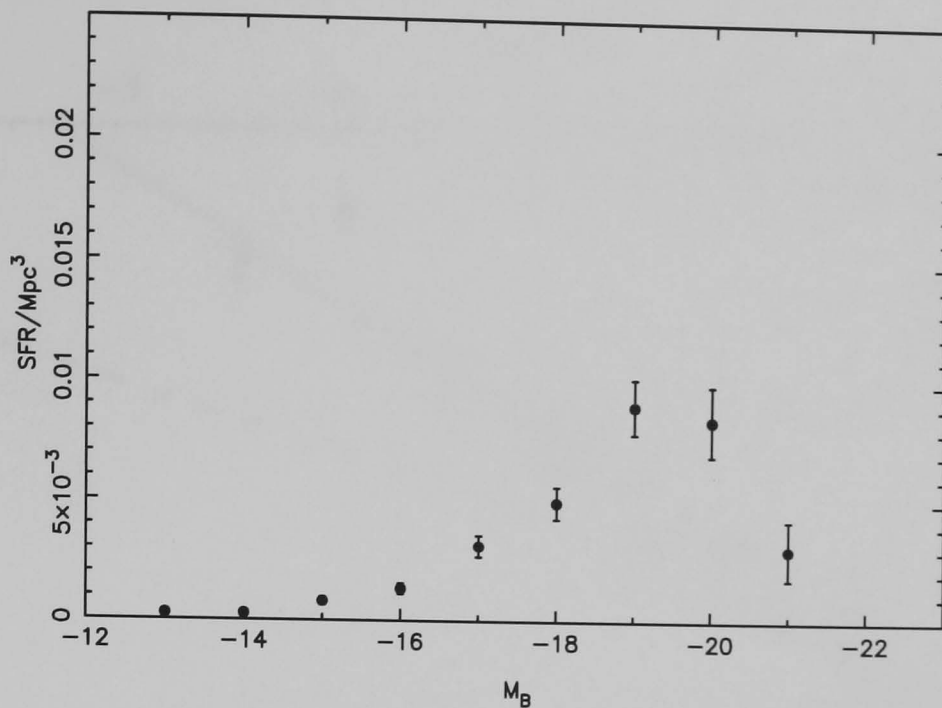


Figure 9.8: SFR density as a function of absolute blue magnitude found using the Schechter fit to the AARS luminosity function (Fig. 9.3).

9.3 The $H\alpha$ luminosity function

An $H\alpha$ luminosity function plots the number of galaxies per unit volume, grouped according to their $H\alpha$ luminosity, and hence SFR. It provides information on the relative contributions of galaxies with different amounts of star formation, and can be used to find the total star formation rate density.

The $H\alpha$ luminosity function cannot be calculated directly from the observed galaxies as this sample is not statistically complete. Instead, the same SFRs used to form the SFR-luminosity function in Figure 9.6 were distributed into bins with width 0.5 in \log SFR. Equation 3.12 was used to convert these back to (extinction corrected) $H\alpha$ luminosities. Figure 9.9 shows the $H\alpha$ luminosity function found when using the points (as opposed to the Schechter fit) from the M_B luminosity function in Figure 9.3 to predict the number of galaxies in the local Universe. This shows a decrease in the number of galaxies with increasing $H\alpha$ luminosity, with a characteristic ‘knee’ shape at high luminosities. This is in agreement with the findings of Salzer (1989); Boroson et al. (1993); Gallego et al. (1995), and Gronwall (2000).

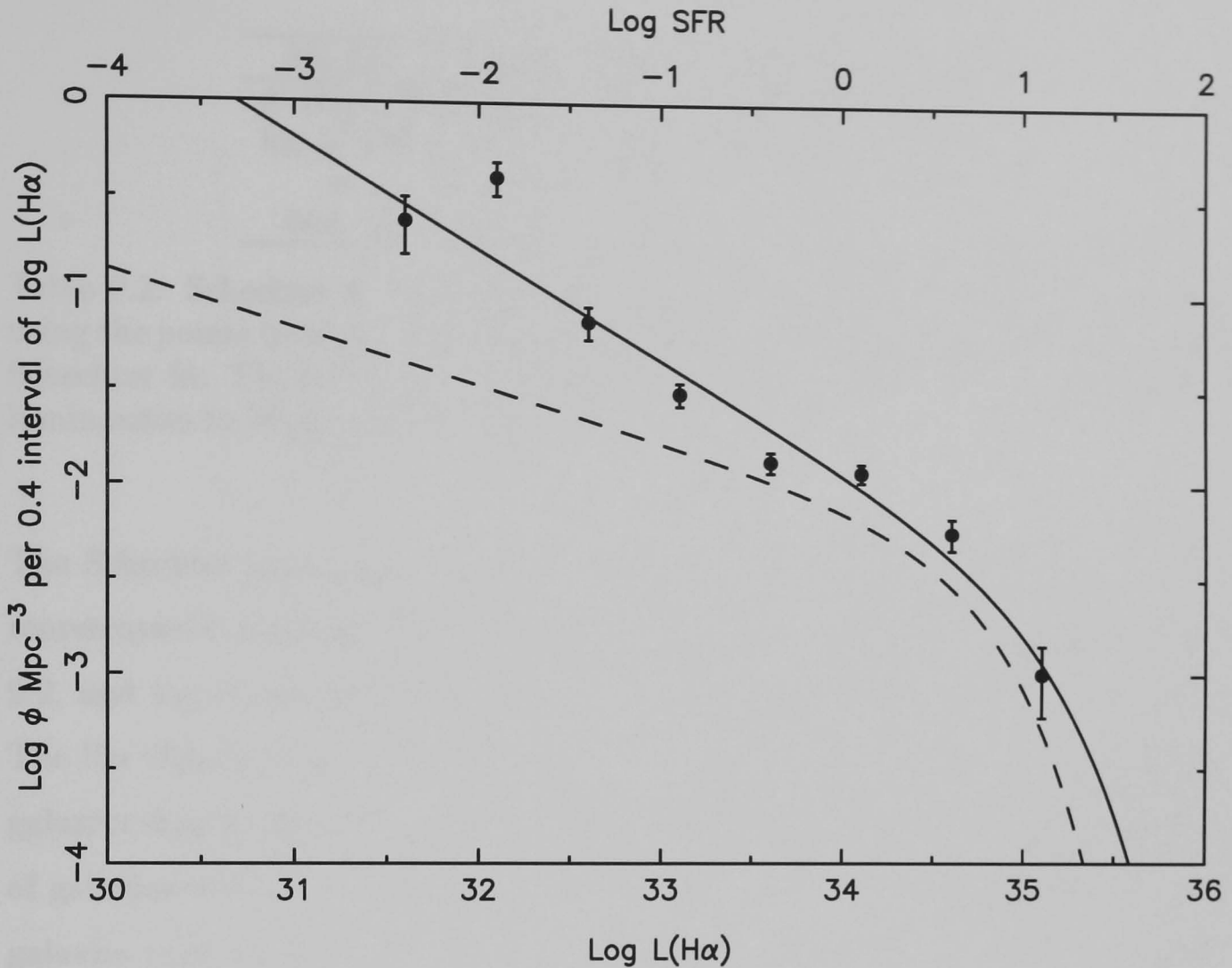


Figure 9.9: The $H\alpha$ luminosity function found using the points in the M_B luminosity function (Fig. 9.3). The solid line represents the best-fit Schechter function, and the dashed line is the fit found by Gallego et al. (1995) for the UCM data. The scale at the top of the diagram indicates the log of the SFR corresponding to the $H\alpha$ luminosity.

The luminosity version of the Schechter function is given by:

$$\phi(L)dL = \phi^*(L/L^*)^\alpha \exp(-L/L^*)d(L/L^*), \quad (9.7)$$

where $\phi(L)$ is related to $\phi(\log L)$ by the equation:

$$\phi(\log L) \frac{d \log L}{0.4} = \phi(L)dL. \quad (9.8)$$

The values of ϕ^* , L^* and α that best fit the data in Figure 9.9 were found by searching through parameter space to find the minimum χ^2 value. These are given in Table 9.2 and the Schechter function is included as the solid line in Figure 9.9.

M_B LF:	Points	Scht. fit	AARS fit	UCM
ϕ^* (Mpc^{-3})	0.0011	0.0029	0.0036	0.0021
$\log L^*$ (W)	35.16	34.86	34.69	34.79
α	-1.58	-1.37	-1.19	-1.3
Red. χ^2	4.53	1.20	1.129	

Table 9.2: Schechter fit parameters for the $H\alpha$ luminosity function, as derived using the points from the M_B luminosity function, its Schechter fit, and the AARS Schechter fit. The UCM values (converted to $H_0 = 75 \text{ kms}^{-1}\text{Mpc}^{-3}$ and to have luminosities in Watts) are included for comparison.

The Schechter parameters found by Gallego et al. (1995) for the ‘UCM survey representative complete sample’ (see Section 1.3.2) are also included in Table 9.2, and the corresponding function is plotted as the dashed line in Figure 9.9. The $H\alpha$ Galaxy Survey has consistently detected higher numbers of star forming galaxies than predicted by the Schechter fit to the UCM-survey data. The number of galaxies with low star formation rates are particularly more populous. These galaxies were not included in the UCM $H\alpha$ luminosity function, which only goes down to $\log L(H\alpha)(\text{W})=33.2$.

If the Schechter fit to the M_B luminosity function is used to derive the $H\alpha$ luminosity function, we find a shallower slope at the faint end than before, though the number of galaxies with low SFR is still higher than that predicted by Gallego et al. (1995) (Figure 9.10). The best-fit Schechter function (solid line) is fairly similar in shape to the UCM fit (dashed line), but consistently higher. The parameters for the fit are included in Table 9.2.

In Figure 9.11, the $H\alpha$ luminosity function plotted is derived from the AARS M_B Schechter fit. This produces a very flat $H\alpha$ function at the low luminosity end. The best-fit Schechter function (solid line) is in good agreement with the UCM findings (dashed line), particularly at the high-SFR end of the scale. The parameters for the Schechter fit are included in Table 9.2.

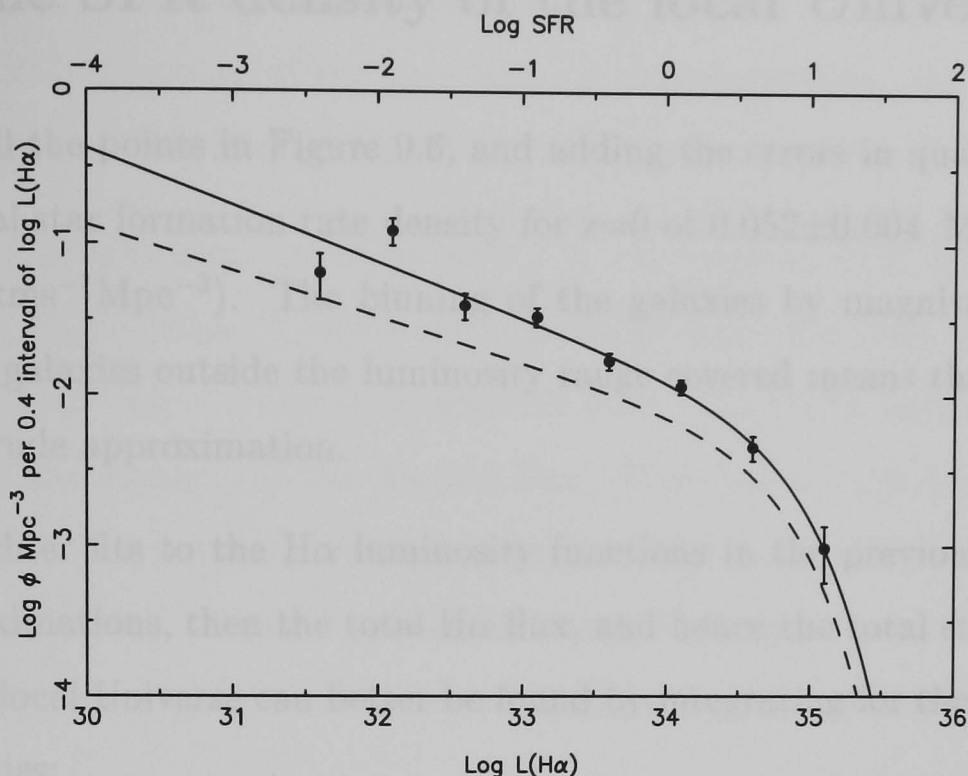


Figure 9.10: The $H\alpha$ luminosity function found using the Schechter fit to the M_B luminosity function (Fig. 9.3). The solid line represents the best-fit Schechter function, and the dashed line is the fit found by Gallego et al. (1995) for the UCM data. The scale at the top of the diagram indicates the log of the SFR corresponding to the $H\alpha$ luminosity.

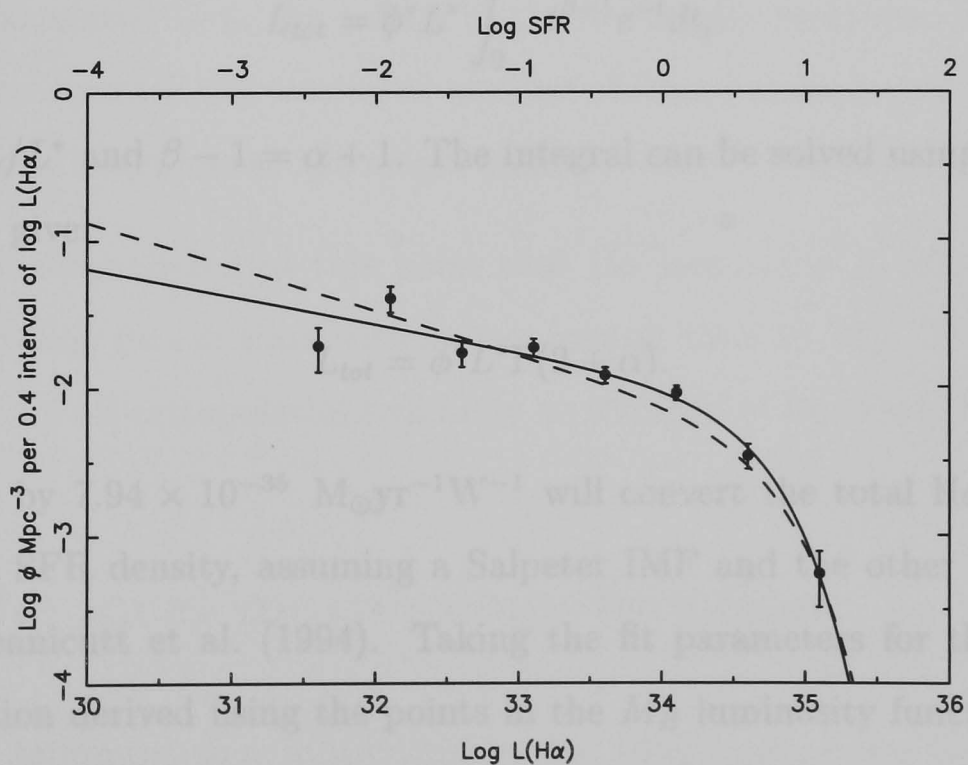


Figure 9.11: The $H\alpha$ luminosity function found using the Schechter fit to the AARS M_B luminosity function (Fig. 9.3). The solid line represents the best-fit Schechter function, and the dashed line is the fit found by Gallego et al. (1995) for the UCM data. The scale at the top of the diagram indicates the log of the SFR corresponding to the $H\alpha$ luminosity.

9.4 The SFR density of the local Universe

Summing all the points in Figure 9.6, and adding the errors in quadrature, produces a total star formation rate density for $z=0$ of $0.052 \pm 0.004 \text{ M}_\odot \text{yr}^{-1} \text{Mpc}^{-3}$ ($H_0 = 75 \text{ kms}^{-1} \text{Mpc}^{-3}$). The binning of the galaxies by magnitude, and the omission of galaxies outside the luminosity range covered means that this result is a fairly crude approximation.

If the Schechter fits to the $H\alpha$ luminosity functions in the previous section are good approximations, then the total $H\alpha$ flux, and hence the total star formation rate, of the local Universe can better be found by integrating for the whole range of luminosities:

$$L_{tot} = \int_0^\infty \phi(L) L dL. \quad (9.9)$$

Substituting in Equation 9.7, we find:

$$L_{tot} = \phi^* L^* \int_0^\infty t^{\beta-1} e^{-t} dt, \quad (9.10)$$

where $t = L/L^*$ and $\beta - 1 = \alpha + 1$. The integral can be solved using the gamma function, to give:

$$L_{tot} = \phi^* L^* \Gamma(2 + \alpha). \quad (9.11)$$

Multiplying by $7.94 \times 10^{-35} \text{ M}_\odot \text{yr}^{-1} \text{W}^{-1}$ will convert the total $H\alpha$ luminosity to the total SFR density, assuming a Salpeter IMF and the other assumptions listed in Kennicutt et al. (1994). Taking the fit parameters for the $H\alpha$ luminosity function derived using the points in the M_B luminosity function, we find that $\Gamma(2 + \alpha) = 2.11$ for $\alpha = -1.58$, and thus, the density of the total star formation rate for $z=0$ is $0.027 \pm 0.006 \text{ M}_\odot \text{yr}^{-1} \text{Mpc}^{-3}$. The error is calculated as $\sqrt{\sum_i [(\phi_i \text{SFR}_i)^2 / n_i]}$, where i represents the 8 $L(H\alpha)$ /SFR bins centered around SFR_i , and n_i is the number of observed galaxies in each bin. If the

type-dependent extinction corrections found in Section 5.4.5 are applied when calculating SFRs, instead of the standard 1.1 mag correction, the derived SFR density is $0.030 \pm 0.006 \text{ M}_{\odot} \text{ yr}^{-1} \text{ Mpc}^{-3}$.

Gallego et al. (1995) used the UCM survey to calculate an SFR density value of $0.014 \pm 0.001 \text{ M}_{\odot} \text{ yr}^{-1} \text{ Mpc}^{-3}$, where their published value has been converted here to $H_0 = 75 \text{ kms}^{-1} \text{ Mpc}^{-3}$ and to a Salpeter IMF. The UCM sample is selected according to the strength of the $\text{H}\alpha$ line flux. Their value quoted is for galaxies with $\text{EW}(\text{H}\alpha + [\text{NII}]) > 1.0 \text{ nm}$. Approximately 10% of the $\text{H}\alpha$ GS observed sample have $\text{EW}(\text{H}\alpha + [\text{NII}]) < 1.0 \text{ nm}$, but we also find more galaxies for all $\text{H}\alpha$ luminosities, as seen in Figure 9.9. These extra galaxies will contribute towards our higher result.

Integrating under the $\text{H}\alpha$ luminosity functions in Figure 9.10 (derived using the Schechter fit to the parent sample) and Figure 9.11 (derived using the Schechter fit to the AARS sample) gives total current SFR densities of 0.024 ± 0.005 and $0.016 \pm 0.003 \text{ M}_{\odot} \text{ yr}^{-1} \text{ Mpc}^{-3}$ respectively. These values are lower in both cases than that calculated from the points in the luminosity function. Both the M_B Schechter fits decrease the estimated number of faint galaxies, and the AARS fit is also systematically low at the bright end.

It should be remembered at this point that $\text{H}\alpha$ luminosity is only sensitive to the the formation rate of stars with masses greater than 10 M_{\odot} . The total SFRs quoted here are all extrapolations and rely on the IMF of the newly-formed stars.

9.5 The local morphology function

In order to determine the contribution to the total current star formation rate from different galaxy types, a similar process to that described earlier in this chapter needs to be employed. In this case, instead of investigating relationships with luminosity, we substitute in the galaxies' T-types. A morphology function is a plot of the space density of galaxies as a function of Hubble type.

The morphological make-ups of both the parent and the observed samples were shown in Figure 2.1. Using the parent sample as described in Section 9.1 and the $1/V_m$ method, morphology functions were derived for each distance shell (Figure 9.12). Using this method, the same galaxies should be predicted as with the luminosity function, but instead of being grouped by their luminosity, the galaxies are binned by their Hubble type.

A number of galaxies (27) were classified by NED simply as being S, SA, SAB or SB spirals. These were allocated a T-type of 12. The shape of the morphology function varies between each shell. The shell containing the closest galaxies is dominated by the Sd-Im galaxies (types 7-10), whereas the furthest shell contains a peak between Sb-Scd (types 3-6). The functions in the middle shells are almost flat. These observations are similar to those noted in Section 2.3. The reason for the differences in the morphology functions in each shell is related to the wide distribution of luminosities within each Hubble classification seen in Figure 9.5. The irregular galaxies found in the first shell are predominantly the low-luminosity galaxies seen in the equivalent luminosity function in Figure 9.2, whereas the high luminosity irregulars are found in the outer shells.

The functions in each shell were combined by taking a weighted average to produce a morphology function for the entire parent sample out to $v=3000 \text{ kms}^{-1}$ (Figure 9.13). A total of 915 galaxies are included. The resulting function shows an increase in galaxy density with increasing T-type. The gradient is shallow for the earlier types, but becomes steeper for the latest types.

9.6 The local SFR density as a function of galaxy morphology

The range of observed SFRs for each Hubble type was shown in Figure 8.1 in Section 8.1.1 for the entire observed sample. The relationship between SFR and galaxy morphology is more complicated than that between SFR and luminosity.

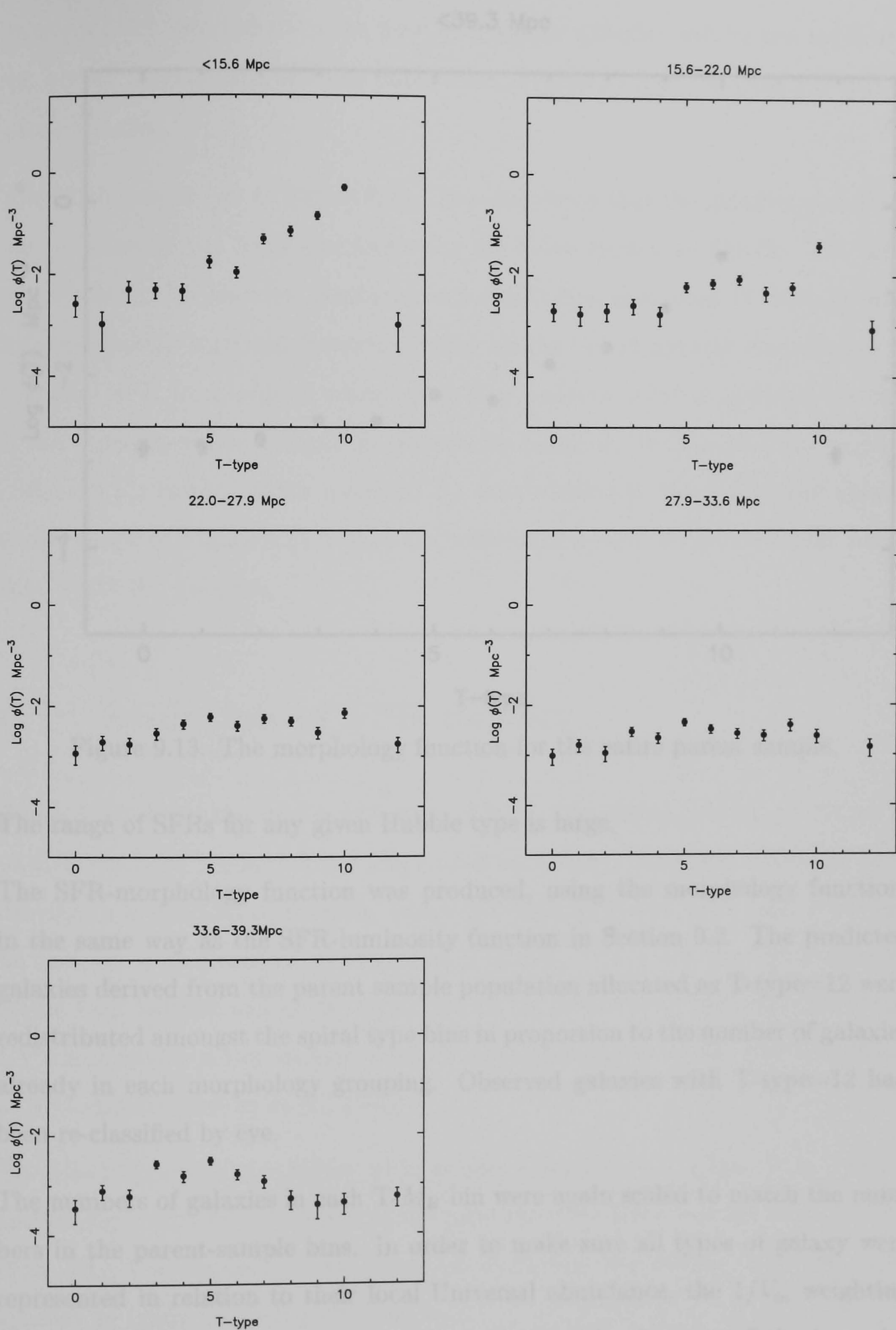


Figure 9.12: The calculated parent morphology functions for each distance shell. The error bars represent $\phi(T)/\sqrt{n}$, where n is the number of galaxies contributing to the point, and T is the T-type of the galaxy.

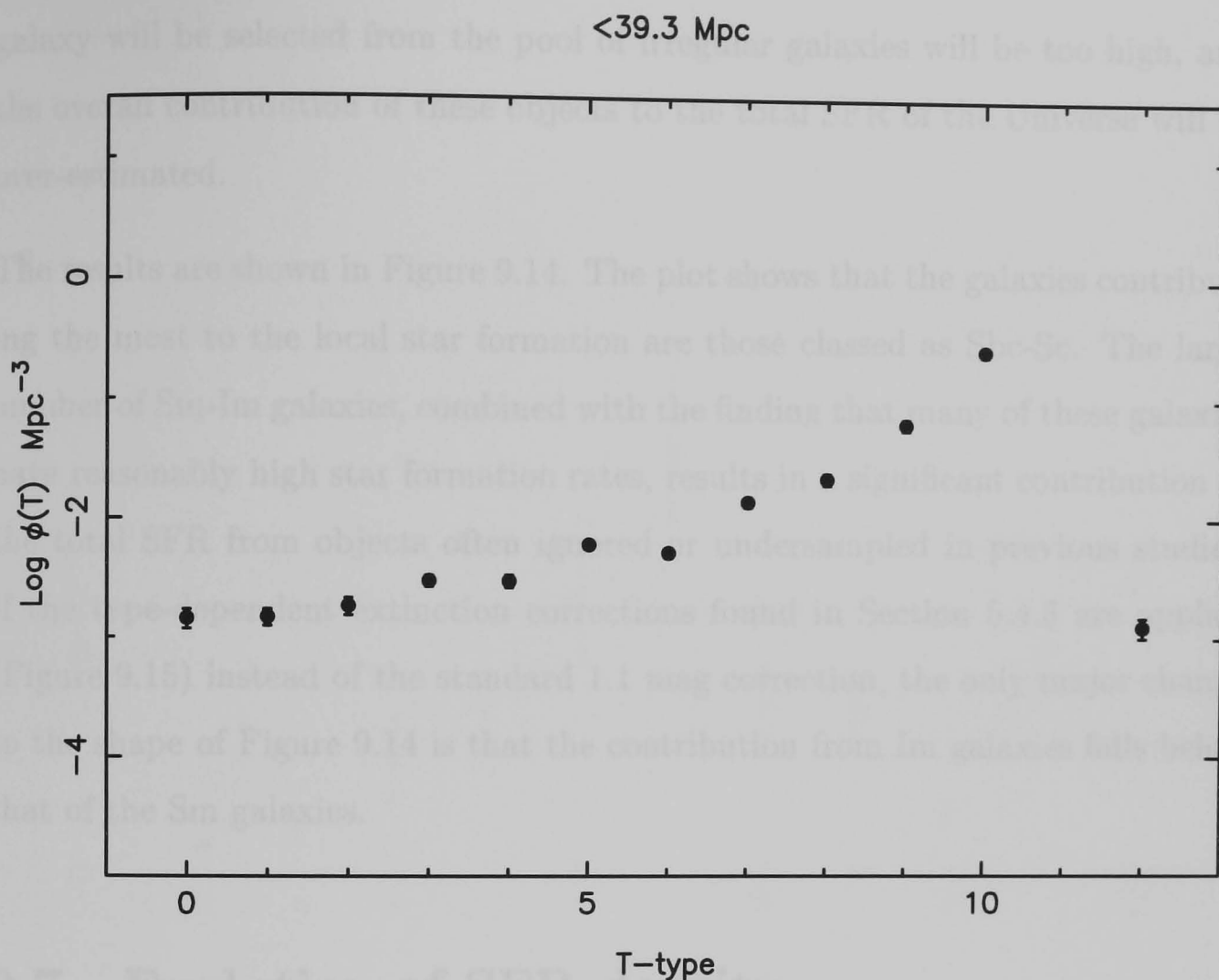


Figure 9.13: The morphology function for the entire parent sample.

The range of SFRs for any given Hubble type is large.

The SFR-morphology function was produced, using the morphology function, in the same way as the SFR-luminosity function in Section 9.2. The predicted galaxies derived from the parent sample population allocated as T-type=12 were redistributed amongst the spiral type bins in proportion to the number of galaxies already in each morphology grouping. Observed galaxies with T-type=12 had been re-classified by eye.

The numbers of galaxies in each T- M_B bin were again scaled to match the numbers in the parent-sample bins. In order to make sure all types of galaxy were represented in relation to their local Universal abundance, the $1/V_m$ weighting was again applied. This was especially important in the case of the irregular galaxies. The number of bright irregular galaxies observed over-represents the true abundance of similar objects (as can be seen when these scalings are not applied). Thus, without these weightings, the number of times a bright irregular

galaxy will be selected from the pool of irregular galaxies will be too high, and the overall contribution of these objects to the total SFR of the Universe will be over-estimated.

The results are shown in Figure 9.14. The plot shows that the galaxies contributing the most to the local star formation are those classed as Sbc-Sc. The large number of Sm-Im galaxies, combined with the finding that many of these galaxies have reasonably high star formation rates, results in a significant contribution to the total SFR from objects often ignored or undersampled in previous studies. If the type-dependent extinction corrections found in Section 5.4.5 are applied (Figure 9.15) instead of the standard 1.1 mag correction, the only major change to the shape of Figure 9.14 is that the contribution from Im galaxies falls below that of the Sm galaxies.

9.7 Evolution of SFR density

Figure 9.16 shows the H α GS SFR density for $z=0$ ($0.027 \pm 0.006 \text{ M}_{\odot} \text{ yr}^{-1} \text{ Mpc}^{-3}$) plotted onto the Madau plot of Hopkins et al. (2000). This plot shows the SFR density as a function of redshift, where UV-derived points have been corrected for extinction as described in Steidel et al. (1999). There are large uncertainties at the high redshift end of the figure due to uncertainties in the faint end of the UV luminosity function at high redshift and uncertainties in the dust extinction at all redshifts (Steidel et al., 1999).

The H α GS point is at a higher SFR density than that of Gallego et al. (1995), and implies very little evolution in the total star formation rate for redshifts less than 0.3. The majority of the observed evolution over cosmic look-back time appears to occur between $z=0.3$ and $z=1$.

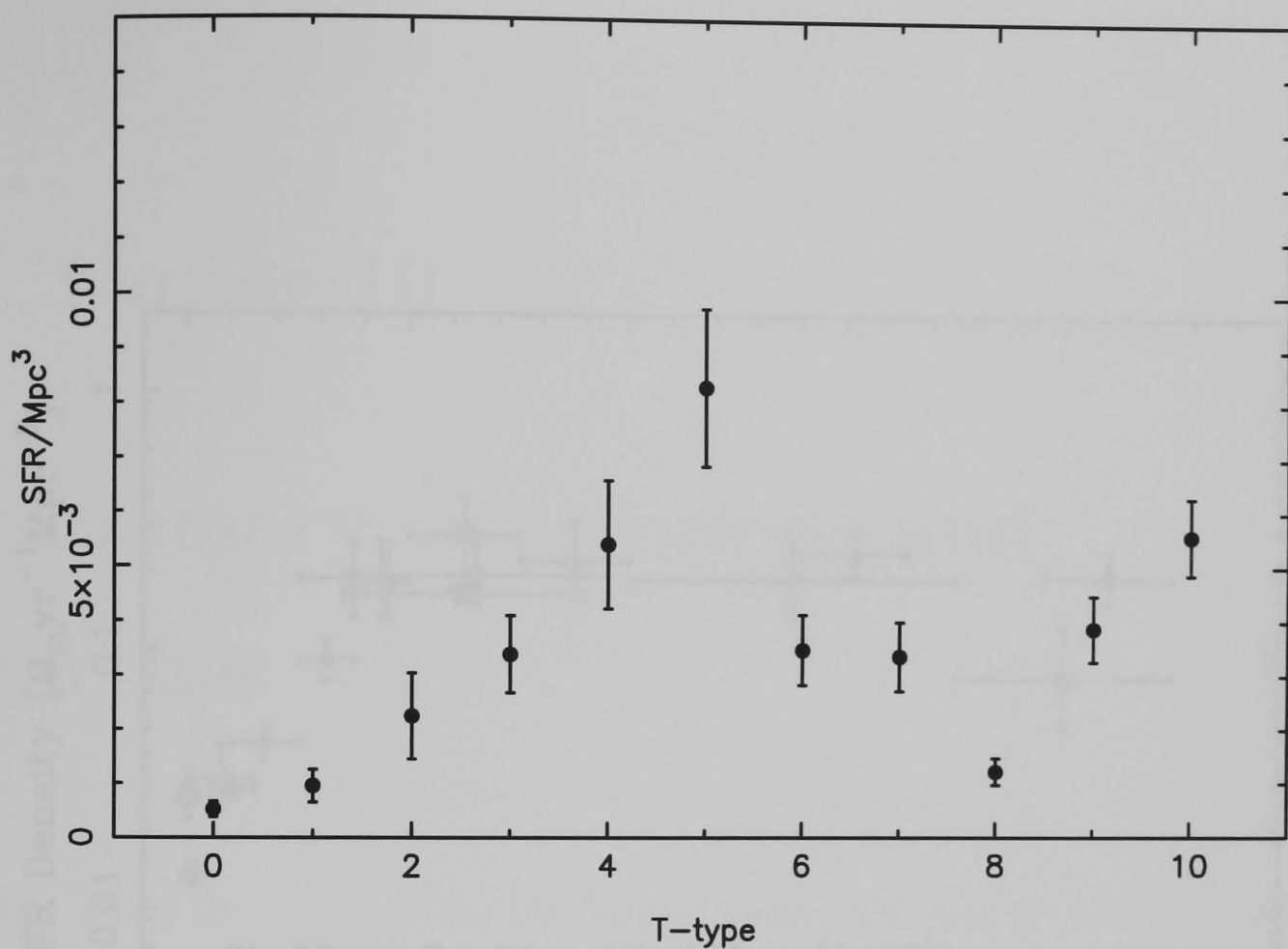


Figure 9.14: SFR density as a function of galaxy morphology with the standard 1.1 mag extinction correction applied to all galaxies.

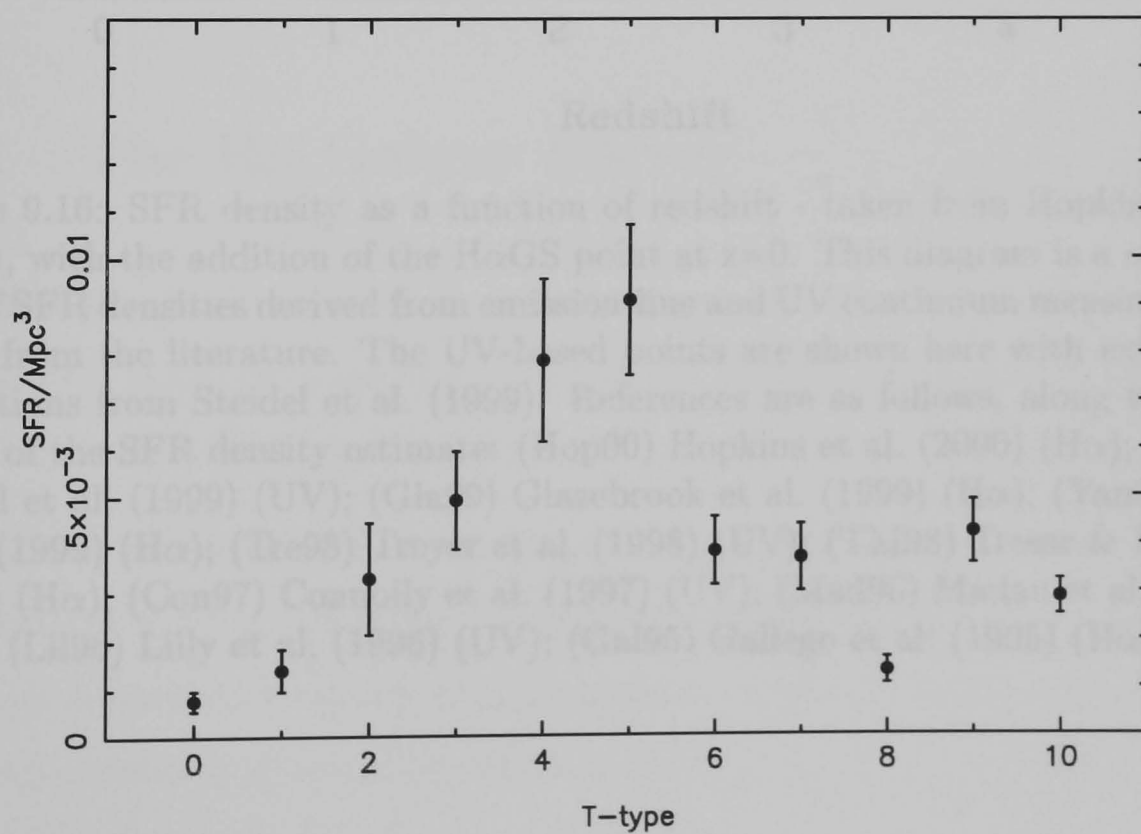


Figure 9.15: SFR density as a function of galaxy morphology with the type-dependent extinction corrections from the UCM data applied.

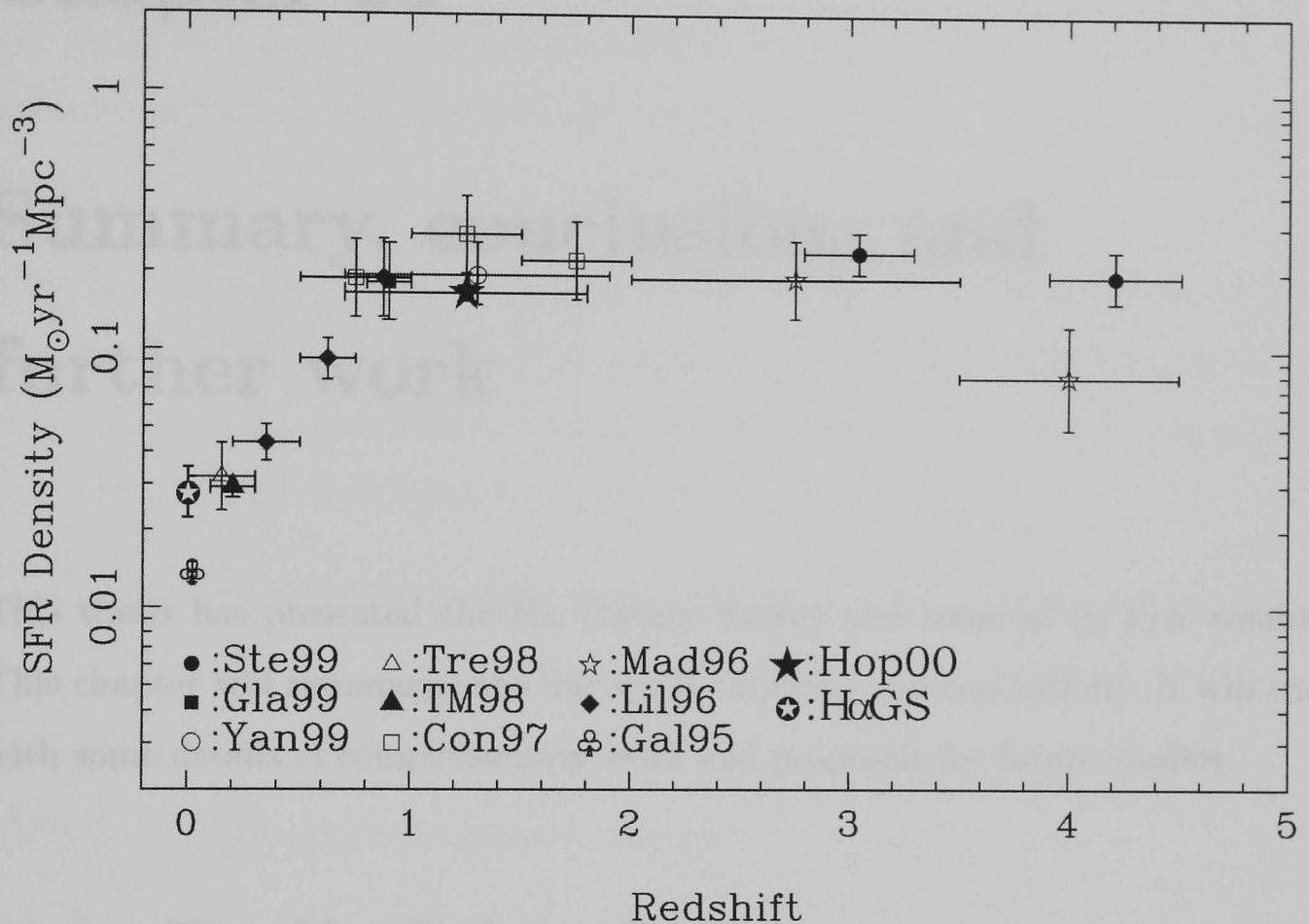


Figure 9.16: SFR density as a function of redshift - taken from Hopkins et al. (2000), with the addition of the H α GS point at $z=0$. This diagram is a compilation of SFR densities derived from emission-line and UV continuum measurements taken from the literature. The UV-based points are shown here with extinction corrections from Steidel et al. (1999). References are as follows, along with the origin of the SFR density estimate: (Hop00) Hopkins et al. (2000) (H α); (Ste99) Steidel et al. (1999) (UV); (Gla99) Glazebrook et al. (1999) (H α); (Yan99) Yan et al. (1999) (H α); (Tre98) Treyer et al. (1998) (UV); (TM98) Tresse & Maddox (1998) (H α); (Con97) Connolly et al. (1997) (UV); (Mad96) Madau et al. (1996) (UV); (Lil96) Lilly et al. (1996) (UV); (Gal95) Gallego et al. (1995) (H α).

Chapter 10

Summary, conclusions and further work

This thesis has presented the H α Galaxy Survey and some of its first results. This chapter will summarise the Survey, its findings and conclusions. It will end with some details of complementary work and proposals for future studies.

10.1 The H α Galaxy Survey

A total of 334 spiral and irregular galaxies have been imaged in the H α line using the Jacobus Kapteyn Telescope. This is the largest and most representative optical sample of nearby galaxies to date.

The sample was selected from the UGC in 5 redshift shells in order to fairly represent the different observable populations at different distances. The inner shells are dominated by small and faint galaxies, whilst the large, bright galaxies are more commonly detected in the outer shells.

Elliptical and lenticular galaxies were omitted as their spectra are shown to be dominated by absorption features, with no sign of H α emission (Kennicutt, 1992). Highly inclined galaxies were also excluded due to the uncertainties in the optical

depth of the dusty ISM.

Three hundred and thirteen of the observed galaxies obeyed the selection criteria. Eleven other galaxies were observed due to their presence in the field of view of a companion galaxy. The overall sampling of the parent sample by the observed galaxies is generally good, with a slight under-representation of Sc galaxies and those with intrinsic diameters between 15-25 kpc. K-S tests show that the observed galaxies are consistent with being drawn at random from the parent sample.

Objects in the Virgo Cluster were generally avoided in order to focus on field galaxies. A complementary study of the region will be described in Section 10.3.2. 60 of the observed galaxies were classified by Huchra & Geller (1982) as belonging to groups, and 29 were found to be in optical-pair systems.

Approximately half of the galaxies were classified as showing evidence of a nuclear bar.

10.1.1 Non-astrophysical errors

Several non-astrophysical sources of error in the calculated quantities were investigated in Chapter 4. The most significant when calculating $H\alpha$ fluxes and concentration indices is found to be the uncertainty in the continuum scaling factors. The effects of fluctuations in the sky background are not as significant as found in some previous studies, due to the subtraction of a surface fit of the background from a galaxy image during the data-reduction procedure.

Distance uncertainties contribute a further error of 24% when calculating $H\alpha$ luminosities and star formation rates. Error propagation results in a total uncertainty in the SFR of around 30% in an average galaxy, rising to $\sim 40\%$ for galaxies with low equivalent widths.

10.1.2 Astrophysical errors

In Chapter 5, the effects of extinction and [NII] contamination were addressed.

The Kennicutt (1983) [NII] corrections were applied to the $H\alpha$ GS data, but a new study, involving the photometric separation of the [NII] and $H\alpha$ light was initiated. This found that there is a wide variation in the amount of [NII] in each galaxy. It also found that, whilst the Kennicutt corrections agreed well for individual regions selected by their high [NII] fluxes, for the remainder of the galaxy, and for the galaxy as a whole, they appear to be overestimating the amount of contamination. [NII]/ $H\alpha$ fractions were generally found to be higher in the metal-rich nuclear regions of galaxies than in the disks.

A standard $H\alpha$ extinction correction of 1.1 mag was applied to galaxies of all types, as recommended by Kennicutt (1998). An investigation into this assumption was attempted using $Br\gamma$ imaging of 22 galaxies. In most cases, no emission could be detected, and, with the exception of UGC5786, only 1-3 isolated regions contained measurable flux in the remainder of the sample. Thus, it was not possible to investigate the effective extinction over the whole galaxy.

Investigation of the $Br\gamma$ emitting regions found $A(H\alpha)$ values were generally in the 0.5-1.8 mag range quoted in the literature. Higher extinction values were found in nuclear regions, indicating the presence of large amounts of dust. Not enough data were available to investigate any relationship with galaxy morphology, but it is clear that $A(H\alpha)$ varies even within single galaxies.

Data from the UCM survey showed no correlation between inclination and extinction, but suggests corrections of 1.5 mag for early-type spirals (S0-Sbc), 1.2 mag for late-type spirals (Sc+), and 0.4 mag for irregular and dwarf galaxies.

10.2 Results and conclusions

10.2.1 Comparison of $H\alpha$ and FIR as a measure of star formation

One hundred and seventy-eight $H\alpha$ GS galaxies have also been detected by IRAS. A good correlation is found between the SFRs derived from the $H\alpha$ fluxes and those from the FIR data, although there is a significant deviation from the one-to-one line, particularly for galaxies with low SFRs. The non-unity gradient of the slope of the best-fit line to the data suggests a non-linear power-law correlation. An empirical formula relating the FIR luminosity to the SFR of the galaxy is derived in Section 6.2.

Using the uniform 1.1 mag extinction correction for the $H\alpha$ data, there is a clear trend for the ratio of IRAS to $H\alpha$ GS SFRs to decrease along the Hubble sequence to later types. This supports the theories of old, low-mass stars contributing significantly to the dust-heating stellar-radiation field. However, if the type-dependent extinction corrections suggested by the UCM data are applied, then the strength of this trend is significantly reduced, in agreement with the findings of Kewley et al. (2002).

10.2.2 Star formation within galaxies

One way to investigate the distribution of star formation regions within galaxies is to generate concentration indices. Three forms of index were investigated, the Petrosian index being the least subjective to the choice of total flux, but the $\log C_{31}$ index being the most reliable when it came to calculating $H\alpha$ concentration.

A strong correlation between continuum concentration and Hubble type is confirmed. Continuum emission also appears to be more centrally concentrated than $H\alpha$ emission, implying that the majority of massive-star formation is occurring in the outer regions of the galaxies.

Petrosian indices calculated for the low-redshift H α GS galaxies appear to show less central concentration in continuum light than in the more distant SDSS sample.

The H α $\log C_{31}$ concentration index was investigated for field and group galaxies separately. Whilst there was no overall trend for either population to have more centrally-concentrated star formation, 8 out of the 12 galaxies with the highest H α central concentrations were found to be in group or pair environments. These findings support the suggestion of Koopmann & Kenney (2002) that the truncation of star formation in Virgo Cluster galaxies is due primarily to ICM-ISM interactions, but also, in some cases, due to gravitational interactions between two galaxies, possibly leading to nuclear starbursts.

The distribution of star formation in normal galaxies is found to vary by a large amount, even for galaxies with similar morphologies. In general, early-type disk galaxies have very little H α emission and are often dominated by nuclear H α absorption. Large spirals galaxies of intermediate Hubble type tend to have HII regions which trace the pattern of the spiral arms, whereas late-type galaxies have a wider range of SFRs and scattered distributions of HII.

Gravitational interactions between galaxies can cause an enormous variety of extended structures. In the observed H α GS sample, we see examples of tidal bridges, tails, rings and shells in the interacting and disturbed galaxies. The features seen in the H α are often very different from those seen in the continuum, and reveal the location of high concentrations of star-forming gas. These HII regions are often some of the brightest in the observed Universe. In some cases star formation has been enhanced in the core of a galaxy, whereas in other cases, the brightest H α fluxes are detected in the outskirts of the galaxy, or along a well-defined outer edge.

Three different effects can be seen in the distribution of nuclear star formation as the result of two different types of bar. Galaxies with bars containing an approximately even distribution of light along their length are generally found

to be emitting $H\alpha$ flux either along the length of the bar, or in many cases at either end. Galaxies with bars dominated by a bright central region are found to exhibit strong $H\alpha$ emission in their centres, but virtually none along the rest of the bar. There is a general relation between the three different distributions of $H\alpha$ light and galaxy type, with earlier-type galaxies tending to have the high central concentrations and the bar-end emission usually being found in the later types. Galaxies with intermediate Hubble types fill in the gap by having star formation along the length of the bar. These findings are in agreement with the theoretical models of bars.

10.2.3 Global star formation dependencies

There is a large amount of scatter in the quantity of star formation present in galaxies of the same Hubble type, with the latest types having the greatest range. On average, once normalisations for galaxy mass or size have been applied, Sm-Im galaxies are found to be the most active and S0/a-Sa types, with high central concentrations, appear the least active. The lowest individual star formation rates generally belong to diffuse Sm-Im objects. For all types, the modal SFRs are very low.

There appears to be a weak dependence of the amount of star formation on bar presence for some Hubble types, but a more detailed investigation, taking into account the properties of the bar, is needed.

With the exception of early-type (S0/a-Sa) galaxies, there appears to be no correlation between $H\alpha$ EW or surface brightness and the continuum emission from the galaxy. This is in contrast to some previous findings (e.g. Gavazzi et al. 1996).

No significant difference is found between field and group galaxies when examining the the mean or median SFRs and $H\alpha$ EWs, although for both measures of star formation, the lowest values are predominantly found in the field. The spread of

EWs for group, pair and Virgo galaxies is less than that found in the field. This is in contrast to the findings of Koopmann & Kenney (2002) for Virgo objects.

Probably, the most significant result from this section is that both the H α and the R-band surface brightnesses are enhanced for galaxies in groups or pairs compared to isolated galaxies. These findings do not change if we alter our method of representing galaxy sizes. It is proposed that galaxies in these environments experience star formation enhancements over large timescales, resulting in an increase in both the number of new stars, and the number of old stars. EWs will thus remain relatively unaffected.

Galaxy-galaxy interactions are found to increase the star formation rates of the galaxies involved in most cases. The magnitude of the enhancement is variable. It is also seen that, in some cases, interactions can halt the formation of new stars.

10.2.4 Star formation in the local Universe

The luminosity function derived from the parent sample (and the highly inclined galaxies excluded from the parent sample) using the $1/V_m$ method shows a very large number of galaxies at the faint end ($M_B > -14$). The slope of the Schechter fit is much steeper than found in previous studies. For $-22 \leq M_B \leq -17$ the points in the luminosity function are in good agreement with the fit to the AARS data for spiral galaxies over that range.

A plot of the SFR density of the local Universe as a function of absolute blue galaxy magnitude reveals that the present total SFR is dominated by bright galaxies, with M_B between -19 and -20 . Fainter galaxies with magnitudes between -13 and -17 contribute approximately equal amounts for each magnitude bin. Plotting the SFR density against Hubble type shows that the galaxies contributing the most to the local star formation are those classed as Sbc-Sc. A significant contribution is also found from galaxies with types Sm-Im. These objects have

often been ignored or undersampled by previous studies.

The $H\alpha$ luminosity function found by combining the $H\alpha$ luminosities of the observed sample with the points in the M_B luminosity function, reveals a much steeper increase in the number of galaxies with low star formation rates with decreasing $H\alpha$ luminosity than found by Gallego et al. (1995). Integrating under the $H\alpha$ luminosity function results in a value for the density of the total star formation rate for $z=0$ of $0.027 \pm 0.006 \text{ M}_{\odot} \text{ yr}^{-1} \text{ Mpc}^{-3}$, almost twice that found by Gallego et al. (1995). Plotting this point on a Madau plot reveals that very little evolution has occurred in the total star formation rate for redshifts less than 0.3.

10.3 Further work

The 334 galaxies observed by the $H\alpha$ Galaxy Survey form a large dataset from which much further work can be based. A number of suggestions for future study have been mentioned throughout this thesis. These will be summarised here, and several other projects will also be presented.

10.3.1 Further investigation into [NII] contamination

The method described in Section 5.1 has been shown to be a useful way of investigating the contribution of [NII] to the total $H\alpha + [\text{NII}]$ observed flux for different galaxies. It also has the advantage of allowing the distribution of [NII] within a galaxy to be studied.

The preliminary study presented in this thesis contains just 6 galaxies. Planned observations of around 14 large, bright face-on spiral galaxies of types Sa-Sd, and 16 Magellanic irregulars should allow for the dependence of [NII] contamination on galaxy type to be better investigated, and for a new set of corrections to be derived if necessary.

10.3.2 Star formation in the Virgo Cluster

Rather than observing galaxies in Virgo individually, a contiguous strip running from the centre of the cluster to a radial distance of 5° has been observed in $H\alpha$ and R using the Wide Field Camera on the INT. The star-forming properties of the detected galaxies can be compared to those in the field and in groups.

The $H\alpha$ observations will complement the Virgo Wide Field Survey of J. Davies et al., which has surveyed the same region in the UBZ bands. These observations have found typically several hundred galaxies per square degree, down to luminosities comparable to the faintest Local Group dwarf spheroidals. The fraction of these that are detected at $H\alpha$ remains to be seen.

10.3.3 Star formation in interacting galaxies

Some work into the investigation of both the global and internal effects of galaxy interactions has been presented in this thesis.

A further 31 $H\alpha$ and continuum observations have been taken with the JKT by P. James and S. Percival, covering a full range of interactions, from relatively-undisturbed near-neighbours to ongoing mergers and galaxies with strongly-distorted optical morphologies. With this larger sample, a better understanding of the processes involved in galaxy-galaxy interactions and their effects on the gas distributions of the galaxies will become available.

10.3.4 Disk and circumnuclear star formation

The SFRs, $H\alpha$ EWs and surface brightnesses presented in this thesis have all been derived from the integrated $H\alpha$ fluxes of entire galaxies. Kennicutt (1998), however, has shown that star formation takes place in two distinct regions: the extended disks of spiral and irregular galaxies, and the compact-circumnuclear environments in the centres of spirals. The attributes and dependencies of the

star formation in the two regions are believed to be very different. As a future study, it is suggested a way is found to decompose the H α GS data into these two components so that they can be investigated separately.

UKIRT time has been applied for by P. James, C. Mundell and J. Knapen on a related topic. This application concentrates on the relation between nuclear star formation and AGN presence and strength. It aims to determine whether strong nuclear H α emission in a galaxy is due to a starburst or to AGN activity, or a combination of both. It is important to fully appreciate the contribution from AGN to the total H α flux of a galaxy so that corrections can be applied for this non-star formation contribution. Pascual et al. (2001) found that correcting their calculation of the SFR density at $z \approx 0.24$ for the estimated AGN contribution reduced their value by $\sim 15\%$.

10.3.5 Arm-induced star formation in spiral galaxies

M. Seigar and P. James are investigating the location and strength of star formation in spiral galaxies with respect to perturbations in the old stellar population, as detected by K-band emission (Seigar & James, 2002).

There are two leading theories linking star formation to density waves in spiral galaxies. The *large-scale galactic shock scenario* (Roberts, 1969) predicts a shock forming near the trailing edge of the galaxy arms. This will compress the gas to densities at which stars can form and should be characterised by dust lanes seen on the trailing edges of the arms.

In the *stochastic star formation model* (see e.g. Seiden & Gerola 1982), a supernova explosion triggers self-propagating star formation. Density waves then concentrate the new HII regions along the spiral arms, but are not responsible for the triggering of star formation. Star formation efficiency (i.e. normalised to unit mass of disk material) should be unaffected by location in arm or inter-arm regions.

Images from the H α Galaxy Survey were amongst those used by Seigar & James (2002) to identify the new star-forming regions in a sample of 20 spiral galaxies. The SFRs were found to be significantly enhanced in the vicinity of the spiral arms as traced by the old stellar population through K-band light, therefore supporting the large-scale shock scenario. The face-on spirals in the complete H α GS sample can be used to further this investigation.

10.3.6 HII luminosity functions

A. Cardwell and J. Beckman are currently using a semi-automated technique to determine the positions, angular sizes, and absolute fluxes of the HII regions in individual galaxies in order to construct luminosity functions for the galaxy as a whole, and for individual components (bar, disk, etc.). An example using UGC12343 (NGC7479) is described in Rozas et al. (1999). Physical differences between, for example, the bar and the disk, can be explored through the property of their HII regions. Approximately 60 H α GS galaxies are currently being utilised as part of this project.

Bibliography

- Abraham, R. G., Valdes, F., Yee, H. K. C., & van den Bergh, S. 1994, *ApJ*, 432, 75
- Adams, T. F. 1977, *ApJS*, 33, 19
- Allam, S. S., Tucker, D. L., Lin, H., & Hashimoto, Y. 1999, *ApJ Lett.* 522, 89
- Barnes, J. E. & Hernquist, L. 1992, *ARA&A*, 30, 705
- Beichman, C. A., Neugebauer, G., Habing, H. J., Clegg, P. E., & Chester, T. J. 1985, *Infrared astronomical satellite (IRAS) catalogs and atlases. Explanatory supplement, Vol. 85* (Washington: Government Printing Office)
- Bell, E. F. & Kennicutt, R. C. 2001, *ApJ*, 548, 681
- Bernloehr, K. 1993, *A&A*, 268, 25
- Bertelli, G., Bressan, A., Chiosi, C., Fagotto, F., & Nasi, E. 1994, *A&AS*, 106, 275
- Bianchi, L. & the GALEX Team. 1999, *Memorie della Societa Astronomica Italiana*, 70, 365
- Biermann, P. 1976, *A&A*, 53, 295
- Binggeli, B., Sandage, A., & Tammann, G. A. 1985, *AJ*, 90, 1681
- Binney, J. & Merrifield, M. 1998, *Galactic Astronomy* (Princeton, NJ : Princeton University Press, 1998.)

- Block, D. L., Puerari, I., Knapen, J. H., Elmegreen, B. G., Buta, R., Stedman, S., & Elmegreen, D. M. 2001, *A&A*, 375, 761
- Boroson, T. A., Salzer, J. J., & Trotter, A. 1993, *ApJ*, 412, 524
- Bruzual, A., G. & Charlot, S. 1993, *ApJ*, 405, 538
- Buat, V. 1992, *A&A*, 264, 444
- Buat, V. & Deharveng, J. M. 1988, *A&A*, 195, 60
- Buat, V. & Xu, C. 1996, *A&A*, 306, 61
- Burstein, D. & Heiles, C. 1982, *AJ*, 87, 1165
- Bushouse, H. A., Werner, M. W., & Lamb, S. A. 1988, *ApJ*, 335, 74
- Byrd, G. & Valtonen, M. 1990, *ApJ*, 350, 89
- Calzetti, D., Kinney, A. L., & Storchi-Bergmann, T. 1996, *ApJ*, 458, 132
- Caplan, J. & Deharveng, L. 1986, *A&A*, 155, 297
- Caplan, J., Ye, T., Deharveng, L., Turtle, A. J., & Kennicutt, R. C. 1996, *A&A*, 307, 403
- Cardelli, J. A., Clayton, G. C., & Mathis, J. S. 1989, *ApJ*, 345, 245
- Colina, L., Bohlin, R., & Castelli, F. 1996, Instrument Science Report CAL/SCS-008 (Baltimore: STScI)
- Combes, F. & Elmegreen, B. G. 1993, *A&A*, 271, 391
- Condon, J. J. 1983, *ApJS*, 53, 459
- . 1992, *ARA&A*, 30, 575
- Condon, J. J., Anderson, M. L., & Helou, G. 1991, *ApJ*, 376, 95
- Condon, J. J., Cotton, W. D., & Broderick, J. J. 2002, *AJ*, 124, 675

- Connolly, A. J., Szalay, A. S., Dickinson, M., Subbarao, M. U., & Brunner, R. J. 1997, *ApJ Let.*, 486, 11
- Cowie, L. L., Songaila, A., Hu, E. M., & Cohen, J. G. 1996, *AJ*, 112, 839
- Cram, L., Hopkins, A., Mobasher, B., & Rowan-Robinson, M. 1998, *ApJ*, 507, 155
- Dahari, O. 1984, *AJ*, 89, 966
- Davies, J., Phillipps, S., Disney, M., Boyce, P., & Evans, R. 1994, *MNRAS*, 268, 984
- de Jong, R. S. & Lacey, C. 2000, *ApJ*, 545, 781
- de Vaucouleurs, G. 1977, in *The Evolution of Galaxies and Stellar Population*, eds. R. Larson and B. Tinsley (New Haven Yale University Observatory)
- de Vaucouleurs, G., de Vaucouleurs, A., & Corwin, H. G. 1976, *Second Reference Catalogue of Bright Galaxies* (University of Texas Monographs in Astronomy, Austin: University of Texas Press)
- de Vaucouleurs, G., de Vaucouleurs, A., Corwin, H. G., Buta, R. J., Paturel, G., & Fouque, P. 1991, *Third Reference Catalogue of Bright Galaxies* (Volume 1-3. Springer-Verlag Berlin Heidelberg New York)
- Devereux, N. A. & Hameed, S. 1997, *AJ*, 113, 599
- Devereux, N. A. & Young, J. S. 1990, *ApJ Let.*, 350, 25
- Disney, M., Davies, J., & Phillipps, S. 1989, *MNRAS*, 239, 939
- Disney, M. & Phillipps, S. 1983, *MNRAS*, 205, 1253
- Dressler, A. & Gunn, J. E. 1983, *ApJ*, 270, 7
- Drissen, L., Roy, J., Robert, C., Devost, D., & Doyon, R. 2000, *AJ*, 119, 688
- Efstathiou, G., Ellis, R. S., & Peterson, B. A. 1988, *MNRAS*, 232, 431

- Ellis, R. S. 1997, *ARA&A*, 35, 389
- Elmegreen, B. G. & Elmegreen, D. M. 1985, *ApJ*, 288, 438
- Felten, J. E. 1976, *ApJ*, 207, 700
- Fioc, M. & Rocca-Volmerange, B. 1997, *A&A*, 326, 950
- Gallagher, J. S., Hunter, D. A., & Tutukov, A. V. 1984, *ApJ*, 284, 544
- Gallego, J., Zamorano, J., Aragon-Salamanca, A., & Rego, M. 1995, *ApJ Lett.*, 455, 1
- Gallego, J., Zamorano, J., Rego, M., Alonso, O., & Vitores, A. G. 1996, *A&AS*, 120, 323
- Gallego, J., Zamorano, J., Rego, M., & Vitores, A. G. 1997, *ApJ*, 475, 502
- Gavazzi, G., Garilli, B., & Boselli, A. 1990, *A&AS*, 83, 399
- Gavazzi, G., Pierini, D., & Boselli, A. 1996, *A&A*, 312, 397
- Gil de Paz, A., Aragón-Salamanca, A., Gallego, J., Alonso-Herrero, A., Zamorano, J., & Kauffmann, G. 2000, *MNRAS*, 316, 357
- Glazebrook, K., Blake, C., Economou, F., Lilly, S., & Colless, M. 1999, *MNRAS*, 306, 843
- Gonzalez-Delgado, R. M., Perez, E., Diaz, A. I., Garcia-Vargas, M. L., Terlevich, E., & Vilchez, J. M. 1995, *ApJ*, 439, 604
- Gronwall, C. 2000, in *Dwarf Galaxies and Cosmology*, ed. T. Thuan, C. Balkowski, V. Cayatte, and J. Thanh Van (Editions Frontieres), p41
- Gruendl, R. A., Vogel, S. N., Davis, D. S., & Mulchaey, J. S. 1993, *ApJ Lett.*, 413, 81
- Gunn, J. E. & Gott, J. R. I. 1972, *ApJ*, 176, 1
- Hashimoto, Y. & Oemler, A. J. 2000, *ApJ*, 530, 652

- Hashimoto, Y., Oemler, A. J., Lin, H., & Tucker, D. L. 1998, *ApJ*, 499, 589
- Helou, G., Khan, I. R., Malek, L., & Boehmer, L. 1988, *ApJS*, 68, 151
- Ho, L. C., Filippenko, A. V., & Sargent, W. L. W. 1997, *ApJ*, 487, 591
- Ho, P. T. P., Beck, S. C., & Turner, J. L. 1990, *ApJ*, 349, 57
- Holmberg, E. 1958, *Meddelanden fran Lunds Astronomiska Observatorium Serie II*, 136, 1
- Hopkins, A. M., Connolly, A. J., & Szalay, A. S. 2000, *AJ*, 120, 2843
- Hubble, E. P. 1926, *ApJ*, 64, 321
- . 1929, *Proc. Nat. Acad. Sci. (Wash.)*, 15, 168
- Huchra, J. P. & Geller, M. J. 1982, *ApJ*, 257, 423
- Hummel, E. & Beck, R. 1995, *A&A*, 303, 691
- Hunter, D. A., Elmegreen, B. G., & van Woerden, H. 2001, *ApJ*, 556, 773
- Hunter, D. A. & Gallagher, J. S. 1997, *ApJ*, 475, 65
- Hutchings, J. B., Lo, E., Neff, S. G., Stanford, S. A., & Unger, S. W. 1990, *AJ*, 100, 60
- Iglesias-Páramo, J. & Vílchez, J. M. 1999, *ApJ*, 518, 94
- Kauffmann, G., White, S. D. M., & Guiderdoni, B. 1993, *MNRAS*, 264, 201
- Kaufman, M., Bash, F. N., Kennicutt, R. C., & Hodge, P. W. 1987, *ApJ*, 319, 61
- Kawara, K., Nishida, M., & Phillips, M. M. 1989, *ApJ*, 337, 230
- Keel, W. C. 1983, *ApJS*, 52, 229
- Keel, W. C., Kennicutt, R. C., Hummel, E., & van der Hulst, J. M. 1985, *AJ*, 90, 708

- Kennicutt, R., Tamblyn, P., & Congdon, C. 1994, *ApJ*, 435, 22
- Kennicutt, R. C. 1983, *ApJ*, 272, 54
- . 1989, *ApJ*, 344, 685
- . 1992, *ApJ*, 388, 310
- . 1998, *ARA&A*, 36, 189
- Kennicutt, R. C., Bothun, G. D., & Schommer, R. A. 1984, *AJ*, 89, 1279
- Kennicutt, R. C., Keel, W. C., van der Hulst, J. M., Hummel, E., & Roettiger, K. A. 1987, *AJ*, 93, 1011
- Kennicutt, R. C. & Kent, S. M. 1983, *AJ*, 88, 1094
- Kent, S. M. 1985, *ApJS*, 59, 115
- Kewley, L. J., Geller, M. J., Jansen, R. A., & Dopita, M. 2002, *AJ*, in press, astro-ph/0208508
- Kirk, J. G., Melrose, D. B., Priest, E. R., Benz, A. O., & Courvoisier, T. J., eds. 1994, *Plasma Astrophysics*
- Koopmann, R. A. & Kenney, J. D. P. 1998, *ApJ Let.*, 497, L75
- . 2002, *ApJ*, submitted, astro-ph/0209547
- Koopmann, R. A., Kenney, J. D. P., & Young, J. 2001, *ApJS*, 135, 125
- Krienke, K. & Hodge, P. 1991, *PASP*, 103, 268
- Landolt, A. 1992, *AJ*, 104, 340
- Lanzetta, K. M., Yahata, N., Pascarella, S., Chen, H., & Fernández-Soto, A. 2002, *ApJ*, 570, 492
- Larson, R. B. & Tinsley, B. M. 1978, *ApJ*, 219, 46
- Lehnert, M. D. & Heckman, T. M. 1995, *ApJS*, 97, 89

- . 1996, *ApJ*, 472, 546
- Leitherer, C. & Heckman, T. M. 1995, *ApJS*, 96, 9
- Lilly, S. J., Le Fevre, O., Hammer, F., & Crampton, D. 1996, *ApJ Lett.* 460, 1
- Lonsdale Persson, C. J. & Helou, G. 1987, *ApJ*, 314, 513
- Madau, P., Ferguson, H. C., Dickinson, M. E., Giavalisco, M., Steidel, C. C., & Fruchter, A. 1996, *MNRAS*, 283, 1388
- Madau, P., Pozzetti, L., & Dickinson, M. 1998, *ApJ*, 498, 106
- Martin, C. L. 1998, *ApJ*, 506, 222
- Martinet, L. & Friedli, D. 1997, *A&A*, 323, 363
- McMahon, R. G., Walton, N. A., Irwin, M. J., Lewis, J. R., Bunclark, P. S., & Jones, D. H. 2001, *New Astronomy Review*, 45, 97
- Moles, M., del Olmo, A., Perea, J., Masegosa, J., Marquez, I., & Costa, V. 1994, *A&A*, 285, 404
- Moore, B., Katz, N., Lake, G., Dressler, A., & Oemler, A. 1996, *Nature*, 379, 613
- Moore, B., Lake, G., Quinn, T., & Stadel, J. 1999, *MNRAS*, 304, 465
- Morgan, W. W. 1958, *PASP*, 70, 364
- Moshir, M., Kopman, G., & Conrow, T. A. O. 1992, *IRAS Faint Source Survey, Explanatory supplement version 2* (Pasadena: Infrared Processing and Analysis Center, California Institute of Technology)
- Moss, C. & Whittle, M. 1993, *ApJ*, 407, L17
- Moss, C., Whittle, M., & Pesce, J. E. 1998, *MNRAS*, 300, 205
- Mulchaey, J. S., Davis, D. S., Mushotzky, R. F., & Burstein, D. 1993, *ApJ Lett.* 404, L9

- Nilson, P. 1973, Uppsala general catalogue of galaxies (Acta Universitatis Upsaliensis. Nova Acta Regiae Societatis Scientiarum Upsaliensis - Uppsala Astronomiska Observatoriums Annaler, Uppsala: Astronomiska Observatorium. 1973)
- O'Halloran, B., Metcalfe, L., Delaney, M., McBreen, B., Laureijs, R., Leech, K., Watson, D., & Hanlon, L. 2000, *A&A*, 360, 871
- Osterbrock, D. E. 1989, *Astrophysics of gaseous nebulae and active galactic nuclei* (University Science Books)
- Pérez-González, P. G., Gallego, J., Zamorano, J., & Gil de Paz, A. 2001, *A&A*, 365, 370
- Pagel, B. E. J. & Edmunds, M. G. 1981, *ARA&A*, 19, 77
- Pascual, S., Gallego, J., Aragón-Salamanca, A., & Zamorano, J. 2001, *A&A*, 379, 798
- Pease, F. G. 1920, *ApJ*, 51, 276
- Peterson, B. A., Ellis, R. S., Efstathiou, G., Shanks, T., Bean, A. J., Fong, R., & Zen-Long, Z. 1986, *MNRAS*, 221, 233
- Petrosian, V. 1976, *ApJ Let.*, 209, 1
- Phookun, B., Vogel, S. N., & Mundy, L. G. 1993, *ApJ*, 418, 113
- Press, W. H. & Schechter, P. 1974, *ApJ*, 187, 425
- Puxley, P. J., Brand, P. W. J. L., Moore, T. J. T., Mountain, C. M., Nakai, N., & Yamashita, T. 1989, *ApJ*, 345, 163
- Puxley, P. J., Hawarden, T. G., & Mountain, C. M. 1990, *ApJ*, 364, 77
- Roberts, W. W. 1969, *ApJ*, 158, 123
- Romanishin, W. 1990, *AJ*, 100, 373

- Rozas, M., Zurita, A., Heller, C. H., & Beckman, J. E. 1999, *A&AS*, 135, 145
- Rubin, V. C. & Ford, K. W. 1986, *ApJ Let.*, 305, 35
- Ryder, S. D. & Dopita, M. A. 1994, *ApJ*, 430, 142
- Sérsic, J. L. & Pastoriza, M. 1967, *PASP*, 79, 152
- Salpeter, E. E. 1955, *ApJ*, 121, 161
- Salzer, J. J. 1989, *ApJ*, 347, 152
- Sandage, A. & Tammann, G. A. 1981, *A revised Shapley-Ames Catalog of bright galaxies* (Washington: Carnegie Institution, 1981)
- Sauvage, M. & Thuan, T. X. 1992, *ApJ Let.*, 396, 69
- Scalo, J. M. 1986, *Fundam. Cosm. Phys.*, 11, 1
- Schechter, P. 1976, *ApJ*, 203, 297
- Schechter, P. L. 1980, *AJ*, 85, 801
- Schlegel, D. J., Finkbeiner, D. P., & Davis, M. 1998, *ApJ*, 500, 525
- Schmidt, M. 1959, *ApJ*, 129, 243
- . 1968, *ApJ*, 151, 393
- Seiden, P. E. & Gerola, H. 1982, *Fundam. Cosm. Phys.*, 7, 241
- Seigar, M. S. & James, P. A. 2002, *MNRAS*, in press, astro-ph/0208401
- Shimasaku, K., Fukugita, M., Doi, M., Hamabe, M., Ichikawa, T., Okamura, S., Sekiguchi, M., Yasuda, N., Brinkmann, J., Csabai, I., Ichikawa, S., Ivezić, Z., Kunszt, P. Z., Schneider, D. P., Szokoly, G. P., Watanabe, M., & York, D. G. 2001, *AJ*, 122, 1238
- Silk, J. 1974, *ApJ*, 193, 525
- . 1977, *A&A*, 59, 53

- Smith, B. J., Struck, C., & Pogge, R. W. 1997, *ApJ*, 483, 754
- Steidel, C. C., Adelberger, K. L., Giavalisco, M., Dickinson, M., & Pettini, M. 1999, *ApJ*, 519, 1
- Stephens, A. S. & Velusamy, T. 1989, Proceedings of the 21st International Cosmic Ray Conference. Volume 3 (OG Sessions), p.221, 3. 221
- Tresse, L. & Maddox, S. J. 1998, *ApJ*, 495, 691
- Treyer, M. A., Ellis, R. S., Milliard, B., Donas, J., & Bridges, T. J. 1998, *MNRAS*, 300, 303
- Tully, R. B. 1988, Nearby galaxies catalog (Cambridge and New York, Cambridge University Press, 1988)
- Tully, R. B. & Shaya, E. J. 1984, *ApJ*, 281, 31
- van den Bergh, S. 1976, *ApJ*, 206, 883
- van den Bergh, S., Pierce, M. J., & Tully, R. B. 1990, *ApJ*, 359, 4
- van der Hulst, J. M., Kennicutt, R. C., Crane, P. C., & Rots, A. H. 1988, *A&A*, 195, 38
- Vitores, A. G., Zamorano, J., Rego, M., Alonso, O., & Gallego, J. 1996a, *A&AS*, 118, 7
- Vitores, A. G., Zamorano, J., Rego, M., Gallego, J., & Alonso, O. 1996b, *A&AS*, 120, 385
- Weinberg, S. 1972, Gravitation and cosmology: Principles and applications of the general theory of relativity (New York: Wiley)
- Yahil, A., Sandage, A., & Tammann, G. A. 1980, in *Physical Cosmology*, 127 -159
- Yan, L., McCarthy, P. J., Freudling, W., Teplitz, H. I., Malumuth, E. M., Weymann, R. J., & Malkan, M. A. 1999, *ApJ Let.*, 519, 47

- Yee, H. K. C. 2000, in ASP Conference Series. Cosmic Evolution and Galaxy Formation: Structure, Interactions, and Feedback
- Young, J. S., Allen, L., Kenney, J. D. P., Lesser, A., & Rownd, B. 1996. AJ. 112. 1903
- Young, J. S., Claussen, M. J., Kleinmann, S. G., Rubin, V. C., & Scoville, N. 1988, ApJ Let., 331, 81
- Young, J. S., Xie, S., Tacconi, L., Knezek, P., Viscuso, P., Tacconi-Garman, L., Scoville, N., Schneider, S., Schloerb, F. P., Lord, S., Lesser, A., Kenney, J., Huang, Y., Devereux, N., Claussen, M., Case, J., Carpenter, J., Berry, M., & Allen, L. 1995, ApJS, 98, 219
- Youngblood, A. J. & Hunter, D. A. 1999, ApJ, 519, 55
- Zamorano, J., Gallego, J., Rego, M., Vitores, A. G., & Alonso, O. 1996, ApJS, 105, 343
- Zamorano, J., Rego, M., Gallego, J. G., Vitores, A. G., Gonzalez-Riestra, R., & Rodriguez-Caderot, G. 1994, ApJS, 95, 387
- Zeilik, M., Gregory, S. A., & Smith, E. V. P. 1992, Introductory astronomy and astrophysics (Fort Worth : Saunders College Pub. 3rd ed.)

Appendix A

The H α Galaxy Survey observed galaxies

The photometric, distance and star formation data for the 334 observed galaxies are presented here. Column 1 contains the number of each galaxy in the Uppsala Galaxy Catalogue; column 2 the Hubble type, taken from NED; column 3 the heliocentric recession velocity from NED; column 4 the distance in Mpc of the galaxy, assuming a Hubble constant of $75 \text{ kms}^{-1}\text{Mpc}^{-1}$ and after corrections from a Virgo infall model; column 5 the galaxy major axis in minutes of arc; column 6 the major-to-minor axis ratio; column 7 the total, apparent, R magnitude derived from this study; column 8 the total H α flux, with a decimal exponent given in brackets such that 1.2(-15) should be read as $1.2 \times 10^{-15} \text{ Wm}^{-2}$; column 9 the equivalent width in nm of the H α line; and column 10 contains the total star formation rate, based on the total measured H α line flux, with the conversion factor as described in the Section 3.7. The galaxies are listed in Right Ascension order, within each of the five recession velocity shells, starting with the lowest velocity shell (up to 1000 kms^{-1}). Serendipitously discovered galaxies, without UGC numbers, are listed at the end of the table. Data for the different recession velocity shells are separated by a horizontal line in the table.

Photometric, distance and star formation data for 334 galaxies

UGC	Class.	v	Dist	Diam	a/b	m_R	H α flux	EW	SFR
		kms^{-1}	Mpc	a_{min}		mag	Wm^{-2}	nm	$\text{M}_{\odot}\text{yr}^{-1}$
17	Sm	878	9.9	2.5	1.5	14.49	2.074(-16)	5.99	0.04476
75	IBm pec	865	9.7	2.8	1.3	12.33	4.204(-16)	1.65	0.11672
655	Sm	836	10.6	2.5	1.0	14.05	8.625(-17)	1.65	0.02239
891	SABm	643	7.2	2.3	2.3	14.05	5.389(-17)	1.03	0.00588
1176	Im	633	7.3	4.6	1.3	14.29	1.810(-16)	4.32	0.02747
1195	Im	774	8.8	3.4	3.1	13.35	1.739(-16)	1.75	0.03855
1200	IBm	808	9.2	2.0	1.4	13.19	3.442(-16)	2.99	0.07951
1865	Sm:	580	7.5	2.8	1.3	14.42	1.141(-16)	3.08	0.01487
1983	SAB:?	609	8.0	2.4	1.8	11.49	1.707(-15)	3.09	0.24712
2002	Sdm:	597	7.8	2.3	1.6	12.00	1.028(-15)	2.98	0.14666
2017	Im	985	12.1	2.3	1.4	15.27	2.446(-17)	1.44	0.01110
2014	Im:	565	7.5	2.0	3.3	14.69	8.942(-17)	3.08	0.01377
2023	Im:	603	7.8	1.7	1.0	13.42	3.538(-16)	3.81	0.06622
2141	S0/a?	987	12.2	2.5	2.3	12.02	1.562(-15)	4.63	0.65391
2193	SAC	518	6.9	3.0	1.1	11.08	3.063(-15)	3.80	0.33302
2455	IBm	375	4.9	3.3	1.3	11.91	2.763(-15)	7.40	0.28004
2684	Im?	350	4.6	1.8	2.0	16.19	2.095(-17)	2.88	0.00152
2947	SBm pec	863	10.8	3.6	4.0	11.99	1.288(-15)	3.71	0.44129
3174	IABm:	670	9.2	1.7	1.5	15.36	8.27(-17)	5.30	0.02144
3371	Im:	816	13.3	4.6	1.3	14.73	6.770(-17)	2.42	0.04179
3429	SBab pec	893	14.5	6.0	1.8	10.06	5.118(-15)	2.48	2.67733
3711	IBm	436	7.6	2.2	1.3	12.29	1.340(-15)	5.10	0.23388
3734	SAC:	974	15.9	1.7	1.0	11.60	3.392(-16)	0.68	0.21435
3817	Im:	438	8.3	1.8	2.0	15.16	8.127(-17)	4.32	0.01747
3847	IRR	70	1.2	1.7	1.5	14.75	9.239(-16)	33.88	0.00354
3851	IBm	100	1.2	8.1	2.5	11.76	1.017(-14)	23.61	0.03898
3876	SAd	860	14.5	2.2	1.7	12.97	3.540(-16)	2.50	0.16304
3966	Im	361	6.2	1.7	1.0	14.51	8.230(-17)	2.40	0.00872
4115	IAM	338	5.8	1.8	1.8	13.70	2.517(-16)	3.49	0.02206

Photometric, distance and star formation data for 334 galaxies

UGC	Class.	v	Dist	Diam	a/b	m_R	H α flux	EW	SFR
		kms $^{-1}$	Mpc	amin		mag	Wm $^{-2}$	nm	M $_{\odot}$ yr $^{-1}$
4165	SBd	514	9.0	2.9	1.1	11.51	2.004(-15)	3.70	0.35182
4173	Im:	860	14.3	1.9	3.2	14.48	2.102(-16)	5.98	0.11221
4274	SBm pec	447	7.7	1.7	1.1	11.40	2.466(-15)	4.11	0.32804
4325	SAm?	524	9.2	3.5	1.5	12.59	6.568(-16)	3.29	0.12216
4426	Im:	397	6.7	2.0	2.0	14.72	8.361(-17)	2.98	0.00998
4499	SABdm	691	12.2	2.6	1.4	13.06	6.422(-16)	4.94	0.20470
4514	SBcd?	691	12.2	2.1	2.3	13.18	3.365(-16)	2.88	0.10718
4645	SAB0/a	692	12.3	3.6	1.1	10.04	1.811(-15)	0.86	0.56751
4879	IAm	600	10.5	1.7	1.3	13.18	1.790(-17)	0.15	0.00498
5139	IABm	143	2.3	3.6	1.2	13.71	3.973(-16)	5.54	0.00576
5221	SAC pec	3	2.1	5.9	2.2	10.21	6.241(-15)	3.49	0.06412
5272	Im	520	7.7	2.1	2.6	13.78	4.122(-16)	6.17	0.06289
5340	Im/BCD	503	7.2	2.7	2.7	14.14	2.570(-16)	5.34	0.03392
5336	Im	46	0.7	2.5	1.3	13.88	1.070(-16)	1.75	0.00015
5364	IBm	20	1.0	5.1	1.6	13.58	3.305(-16)	4.11	0.00084
5373	Im	301	3.9	5.1	1.5	12.58	7.260(-16)	3.59	0.02907
5398	I0 pec	14	2.1	5.4	1.2	10.35	6.621(-15)	4.21	0.08377
5414	IABm	603	9.5	3.2	1.5	13.07	6.366(-16)	4.94	0.14429
5637	IBm pec	753	10.8	5.0	1.5	11.07	4.991(-15)	6.17	1.53147
5672	Sab?	531	6.8	1.8	3.6	13.72	1.531(-16)	2.16	0.01467
5692	Sm:	180	2.9	3.2	1.8	13.67	1.828(-16)	2.46	0.00336
5721	SABd?	537	6.9	2.1	2.1	12.16	1.223(-15)	4.11	0.12129
5719	SBdm:	941	17.1	2.9	2.4	13.14	7.089(-16)	5.88	0.41786
5740	SABm	649	10.9	1.7	1.4	13.67	2.283(-16)	3.09	0.05583
5761	SABdm	641	8.1	2.2	1.3	12.20	3.692(-16)	1.29	0.05056
5764	IBm:	586	7.8	2.0	1.8	14.57	1.501(-16)	4.63	0.02335
5786	SABbc pec	993	18.2	3.1	1.3	10.40	1.634(-14)	10.90	11.23121
5829	Im	629	8.6	4.7	1.1	13.13	1.502(-15)	12.34	0.28592
5848	Sm:	822	14.9	2.1	2.1	14.09	1.410(-16)	2.80	0.06239

Photometric, distance and star formation data for 334 galaxies

UGC	Class.	v kms ⁻¹	Dist Mpc	Diam amin	a/b	m _R mag	H α flux Wm ⁻²	EW nm	SFR M _⊙ yr ⁻¹
5889	SABm	572	6.9	2.2	1.0	13.63	1.182(-16)	1.54	0.01203
5918	Im:	340	5.4	2.4	1.0	14.52	6.923(-17)	2.05	0.00505
6123	SBb	979	20.9	3.4	1.2	10.80	4.050(-15)	3.91	3.68377
6161	SBdm	756	12.3	2.6	2.2	13.52	2.880(-16)	3.40	0.08806
6251	SABm:	927	17.1	1.8	1.1	14.39	1.775(-16)	4.64	0.10501
6272	SA0/a:	628	7.1	5.2	2.7	10.70	2.941(-15)	2.57	0.30517
6399	Sm:	805	14.4	2.8	3.5	13.27	2.648(-16)	2.47	0.11222
6439	SAb	770	12.2	5.9	1.9	10.08	3.520(-15)	1.75	1.07886
6446	SAd	645	10.5	3.5	1.5	13.88	4.870(-16)	8.00	0.10949
6565	Irr	229	3.1	2.5	1.3	11.68	1.612(-15)	3.49	0.03877
6572	Im	229	2.9	2.0	1.8	13.77	4.436(-16)	6.57	0.00966
6595	SBb:	732	11.8	3.1	3.1	11.69	1.328(-15)	2.88	0.38551
6618	SABcd:	739	11.7	1.7	1.5	12.55	1.111(-15)	5.35	0.31199
6628	SAm	850	15.2	2.9	1.0	12.38	5.781(-16)	2.37	0.28113
6644	SAc	993	16.9	4.3	1.4	10.39	6.733(-15)	4.42	4.20560
6670	IBm	922	17.6	3.0	3.3	12.63	1.197(-15)	6.19	0.95954
6778	SABc:	977	18.5	4.5	1.6	10.35	7.945(-15)	5.04	5.62477
6781	SB0/a: pec	905	18.5	1.4	1.4	13.05	2.023(-16)	1.55	0.14320
6782	ImV	525	5.7	2.0	1.0	15.71	5.561(-17)	4.93	0.00471
6797	SBd	961	18.2	1.9	1.1	12.33	6.774(-16)	2.67	0.46879
6813	SAd:	954	17.7	2.6	1.0	12.60	4.891(-16)	2.47	0.31047
6815	SAcd:	968	18.1	5.1	3.9	11.58	7.555(-16)	1.49	0.51236
6818	SBb?	819	14.0	2.0	2.0	13.58	2.246(-16)	2.78	0.09133
6817	Im	243	2.9	4.1	2.7	13.90	3.574(-16)	5.96	0.00780
6824	S0/a	906	16.9	1.7	2.1	12.28	1.200(-16)	0.45	0.07100
6833	SABc	919	17.6	3.2	1.3	12.67	2.500(-15)	13.50	1.60286
6869	SABc:	807	13.9	2.9	1.7	10.70	6.018(-15)	5.26	2.40535
6900	Sd	590	6.8	2.1	1.6	13.93	5.840(-17)	1.00	0.00558
6904	SABc	842	15.4	3.9	3.5	11.94	9.769(-16)	2.68	0.47018

Photometric, distance and star formation data for 334 galaxies

UGC	Class.	v	Dist	Diam	a/b	m_R	H α flux	EW	SFR
		kms $^{-1}$	Mpc	amin		mag	Wm $^{-2}$	nm	M $_{\odot}$ yr $^{-1}$
6917	SBm	910	17.0	3.5	1.8	13.20	1.888(-16)	1.65	0.11435
6930	SABd	778	13.2	4.4	1.6	12.46	8.635(-16)	3.81	0.31725
6956	SBm	917	17.1	2.2	1.0	14.43	1.063(-16)	2.89	0.06420
6955	IBm:	905	16.5	5.0	1.9	13.32	2.002(-16)	1.96	0.13716
6962	SABcd	784	11.8	2.3	1.2	11.89	1.381(-15)	3.61	0.39687
6973	Sab:	701	9.7	2.6	2.2	11.28	1.719(-15)	2.57	0.33395
7002	SBb:	932	17.5	2.5	1.3	12.09	6.243(-16)	1.96	0.40288
7007	Sm:	774	9.4	1.7	1.1	14.14	3.458(-17)	0.72	0.00629
7030	SABbc	725	10.6	5.2	1.3	10.05	6.628(-15)	3.19	1.50931
7047	IAm	210	2.8	3.3	1.9	12.59	9.035(-16)	4.52	0.01818
7045	SAc	769	9.1	4.1	2.4	10.70	2.230(-15)	1.95	0.38500
7054	SBa: pec	913	17.6	4.4	2.6	11.04	1.080(-15)	1.30	0.69171
7075	SABc:?	752	12.6	2.8	3.5	11.86	2.171(-15)	5.56	0.70757
7081	SABbc	760	12.9	5.8	2.6	10.08	8.912(-15)	4.43	3.05664
7096	SABb?	837	15.2	3.0	1.8	10.47	3.648(-15)	2.58	1.73880
7134	SABc	609	6.8	4.0	1.1	11.27	1.502(-15)	2.22	0.14227
7151	SABcd?	265	3.3	6.0	4.6	11.32	2.321(-15)	3.59	0.05139
7199	IAm	165	1.9	1.8	1.1	12.87	1.273(-16)	0.82	0.00117
7215	SBdm	378	3.9	5.1	2.8	11.09	3.698(-15)	4.62	0.11806
7216	SBcd pec:	-183	17.4	1.9	2.4	13.69	2.546(-16)	3.49	0.16574
7232	Im pec	228	2.6	1.7	1.1	12.42	4.815(-16)	2.05	0.00850
7261	SBdm	861	9.0	3.6	1.2	12.43	1.640(-15)	7.10	0.28348
7267	Sdm:	472	6.6	2.1	2.6	13.73	1.223(-16)	1.75	0.01111
7271	SBd:	546	7.0	2.0	3.3	13.89	1.120(-16)	1.85	0.01118
7315	SABbc	867	17.6	2.1	1.6	11.18	1.319(-15)	1.80	0.86490
7323	SABdm	517	6.8	5.0	1.3	11.29	1.161(-15)	1.75	0.10880
7326	Im:	-164	17.4	1.9	3.2	15.29	1.211(-16)	7.29	0.09633
7328	SB0/a:	890	10.4	2.9	1.3	10.82	8.957(-16)	0.88	0.20008
7405	SB0/a	893	17.6	5.6	2.2	10.25	1.156(-15)	0.67	0.77647

Photometric, distance and star formation data for 334 galaxies

UGC	Class.	v	Dist	Diam	a/b	m_R	H α flux	EW	SFR
		kms^{-1}	Mpc	a_{min}		mag	Wm^{-2}	nm	$M_{\odot}\text{yr}^{-1}$
7414	SABdm:	232	2.4	1.7	1.1	12.03	2.547(-15)	7.60	0.03123
7523	SBb	922	17.5	3.6	1.1	10.52	1.362(-15)	1.01	0.88517
7539	SAC?	716	8.2	3.6	1.8	9.61	7.214(-15)	2.32	0.99766
7559	IBm	218	2.5	3.2	1.6	13.62	3.994(-16)	5.13	0.00628
7561	SBa:	439	4.6	3.6	2.0	11.80	9.380(-16)	2.26	0.04101
7622	SB0/a?	508	18.8	3.8	2.9	11.14	6.110(-16)	0.80	0.44393
7690	Im:	537	6.8	1.7	1.1	12.45	5.612(-16)	2.47	0.06810
7753	SBb	486	18.1	5.4	1.3	9.95	1.870(-15)	0.82	1.32046
7826	SABb?	631	18.0	1.7	1.5	11.80	7.683(-16)	1.85	0.53519
7866	IABm	359	4.2	3.4	1.1	13.80	3.270(-16)	5.00	0.01477
7874	SABdm:	291	3.0	2.1	2.3	13.10	4.878(-16)	3.90	0.00924
7901	SAC	805	17.8	4.0	1.5	10.33	3.710(-15)	2.32	2.46318
7971	Sm:	467	6.5	2.2	1.0	13.45	2.990(-16)	3.29	0.02548
7985	SABd	652	6.8	2.7	1.6	11.29	4.104(-15)	6.17	0.39849
8024	IBm	376	4.1	3.0	1.4	13.46	4.240(-16)	4.70	0.01772
8034	Im pec	915	17.6	1.7	1.9	13.61	6.270(-16)	8.00	0.51418
8054	SACd:	778	20.7	2.8	2.5	11.46	3.050(-15)	5.36	2.80638
8098	SBm:	847	11.0	4.0	2.7	12.35	4.565(-15)	18.24	1.11300
8116	SBc	969	17.1	2.2	1.0	10.96	3.803(-15)	4.21	2.31398
8188	SAm	321	3.7	6.0	1.1	12.53	8.710(-16)	4.11	0.02420
8201	Im	37	0.5	3.5	1.8	13.06	1.263(-16)	0.98	0.00008
8256	SABbc	946	18.9	5.8	2.1	9.46	4.406(-15)	1.23	3.19880
8303	IABm	944	18.9	2.2	1.2	13.11	7.832(-16)	6.29	0.70730
8313	SBc?	625	8.3	1.7	4.3	13.52	3.312(-16)	3.91	0.04632
8320	IBm	195	2.4	3.6	2.6	12.82	5.965(-16)	3.70	0.00866
8331	IAm	260	3.3	2.7	3.0	13.79	1.694(-16)	2.57	0.00460
8396	SBd?	946	18.6	1.7	3.4	13.06	1.073(-15)	8.26	0.75172
8403	SBcd	965	19.1	4.0	1.4	11.49	2.899(-15)	5.24	2.13149
8490	SAm	201	2.8	5.0	1.7	11.44	3.132(-15)	5.44	0.04962

Photometric, distance and star formation data for 334 galaxies

UGC	Class.	v	Dist	Diam	a/b	m_R	H α flux	EW	SFR
		kms^{-1}	Mpc	a_{min}		mag	Wm^{-2}	nm	$M_{\odot}\text{yr}^{-1}$
8508	IAm	62	0.8	1.7	1.7	13.41	3.583(-16)	3.80	0.00057
8565	SABdm	232	3.1	1.7	1.2	13.24	3.964(-16)	3.59	0.00767
8760	Im	193	2.3	2.2	3.1	13.80	7.434(-17)	1.13	0.00099
8837	IBm	144	1.9	4.3	3.3	12.07	4.487(-16)	1.39	0.00408
8839	Im	957	20.5	4.0	1.5	14.01	2.490(-17)	0.46	0.02706
9013	SAcd pec	273	3.8	4.8	1.1	10.80	2.280(-15)	2.20	0.06639
9018	SAM	304	4.3	1.7	1.3	13.64	7.003(-16)	9.24	0.02608
9128	Im	154	1.8	1.7	1.3	13.86	3.840(-17)	0.62	0.00032
9179	SABd	305	4.5	5.8	1.6	11.21	2.855(-15)	4.00	0.11793
9211	Im:	686	11.2	1.7	1.2	15.00	3.620(-16)	0.00	0.11287
9219	Im:	663	10.2	2.6	2.0	13.17	4.710(-16)	4.00	0.12198
9240	IAM	150	1.9	1.8	1.0	12.98	3.737(-16)	2.67	0.00337
9405	Im	222	3.2	1.7	2.8	14.24	7.885(-17)	1.80	0.00202
9649	SBb?	447	7.7	3.7	1.7	11.77	8.682(-16)	2.03	0.10832
9753	SAbc:?	772	13.8	4.2	3.2	11.42	1.667(-15)	2.84	0.64133
9769	SABdm:	841	15.1	2.7	1.4	13.34	1.855(-16)	1.85	0.08615
9866	SAbc?	435	7.4	2.2	2.2	11.78	9.565(-16)	2.26	0.10895
9906	Sc pec	656	11.6	3.3	1.3	12.18	1.296(-15)	4.42	0.35149
10075	SAcd	835	14.7	5.4	2.6	10.96	2.741(-15)	3.06	1.19927
10310	SBm	716	12.7	2.8	1.3	13.08	8.007(-16)	6.28	0.26100
10445	SBc	963	16.9	2.8	1.6	12.89	7.801(-16)	5.14	0.47324
10521	SAC	852	15.0	3.0	2.3	11.24	3.670(-15)	5.30	1.68468
10606	SBcd:	919	15.9	3.6	2.4	14.21	3.911(-16)	8.67	0.20168
10736	SABdm	490	8.6	3.1	3.4	13.92	9.678(-17)	1.64	0.01529
10806	SBdm	932	15.7	2.1	2.3	12.76	6.718(-16)	3.92	0.34693
11300	SBcd	490	8.4	3.8	2.9	12.29	7.562(-16)	2.88	0.12409
12048	IBm	986	12.2	2.1	1.2	12.15	1.665(-15)	5.55	0.70427
12082	Sm	802	10.1	2.6	1.2	13.47	2.741(-16)	3.09	0.06938
12101	SAd	786	9.9	2.2	2.0	12.63	7.151(-16)	3.71	0.16714

Photometric, distance and star formation data for 334 galaxies

UGC	Class.	v	Dist	Diam	a/b	m_R	H α flux	EW	SFR
		kms^{-1}	Mpc	a_{min}		mag	Wm^{-2}	nm	$M_{\odot} \text{yr}^{-1}$
12613	Im	-183	1.0	5.0	1.9	14.89	9.610(-18)	0.40	0.00002
12732	Sm:	749	8.9	3.0	1.1	13.70	6.309(-16)	8.75	0.12203
12754	SBcd	751	8.9	4.4	1.5	11.45	2.645(-15)	4.63	0.49357
12893	SAdm	1108	12.5	1.7	1.0	13.33	3.624(-17)	0.36	0.01205
763	SABm	1162	12.7	5.1	1.4	11.38	1.938(-15)	3.18	0.65674
2053	Im	1029	12.7	2.0	2.0	14.40	3.875(-17)	1.03	0.02053
2210	SBc	1211	13.9	4.9	1.1	11.57	2.625(-15)	5.13	1.09533
2275	Sm:	1025	11.9	7.5	1.4	17.52	2.364(-17)	11.10	0.00810
2302	SBm:	1104	12.8	4.8	1.3	14.37	7.955(-16)	20.53	0.31187
2855	SABc	1202	17.5	4.4	2.2	11.11	2.646(-15)	3.38	9.78296
3384	Sm:	1089	17.0	1.7	1.0	14.68	1.345(-16)	4.62	0.12291
3403	SBcd?	1264	19.2	2.7	3.4	13.02	3.300(-16)	2.46	0.41793
3439	SABc:	1494	22.3	3.3	2.7	12.81	2.837(-16)	1.74	0.35026
3574	SACd	1441	21.8	4.2	1.2	12.21	6.113(-16)	2.15	0.64872
3580	SAa pec:	1201	18.8	3.6	2.3	12.44	6.727(-16)	2.92	0.53003
4097	SAa	1442	22.5	1.9	1.3	11.33	4.598(-16)	0.72	0.54614
4121	Sm:	1092	18.0	2.0	2.5	15.14	3.521(-17)	1.85	0.02434
4637	SAB0/a	1404	21.8	4.9	1.2	11.20	1.950(-16)	0.27	0.19613
4781	Scd:	1443	24.3	1.7	2.8	14.40	1.393(-16)	3.69	0.17936
4779	SAC:	1289	21.3	3.2	1.9	11.15	1.590(-15)	2.10	1.55850
5349	Sdm:	1381	24.4	2.5	2.8	13.30	3.319(-16)	3.18	0.40205
5393	SBdm:	1448	25.5	1.9	1.7	13.54	2.652(-16)	3.17	0.34984
5589	SBcd	1154	20.3	3.0	1.6	12.28	1.009(-15)	3.79	0.84386
5731	SAab	1408	25.9	1.9	1.1	11.36	4.599(-16)	0.74	0.64573
6023	Sd	1334	25.5	1.9	2.4	12.49	1.127(-15)	5.12	1.52035
6077	SBb:	1434	27.4	2.3	1.1	11.82	1.045(-15)	2.56	1.61345
6112	Sd?	1036	22.0	2.2	2.8	13.21	1.860(-16)	1.64	0.18542
6923	Im:	1066	19.8	2.0	2.5	12.91	4.434(-16)	2.98	0.45318
9036	SAm:	1390	24.0	1.5	1.7	12.94	5.039(-16)	3.48	0.59840

Photometric, distance and star formation data for 334 galaxies

UGC	Class.	v kms ⁻¹	Dist Mpc	Diam amin	a/b	m _R mag	H α flux Wm ⁻²	EW nm	SFR M _⊙ yr ⁻¹
9465	SABdm	1491	26.4	2.3	1.9	13.19	4.700(-16)	4.10	0.66772
9645	SABb	1359	24.5	3.5	1.8	11.10	1.229(-15)	1.56	1.64062
9824	SBbc	1480	25.6	4.5	1.1	10.79	2.355(-15)	2.23	3.34193
9935	SBd	1447	24.8	4.5	1.3	12.10	1.157(-15)	3.69	1.61630
9987	SBd:	1108	20.0	2.9	3.6	12.24	6.837(-16)	2.46	0.59626
10470	SBbc	1362	21.2	3.0	1.2	11.10	2.981(-15)	3.79	2.92524
10546	SABcd	1280	20.4	2.8	1.6	12.51	8.168(-16)	3.79	0.72963
10564	SBd	1129	18.4	2.6	2.2	13.27	5.266(-16)	4.93	0.38020
10762	SA0/a	1198	19.1	3.7	1.1	10.69	3.548(-16)	0.31	0.28695
10792	Im	1233	19.4	1.8	1.0	14.37	1.590(-16)	4.10	0.15916
10876	Scd:	1164	18.6	2.7	3.4	12.87	5.702(-16)	3.69	0.42708
10897	SAC	1324	20.5	2.5	1.1	11.40	1.906(-15)	3.18	1.73154
11218	SAC	1484	22.2	3.6	2.1	10.72	3.779(-15)	3.38	4.23486
11557	SABdm	1390	19.7	2.2	1.3	12.62	6.781(-16)	3.48	0.92418
11604	SABbc	1424	20.2	3.9	1.2	10.54	2.171(-15)	1.64	4.26980
11782	SBm	1112	13.4	2.3	1.6	13.53	2.597(-16)	3.08	0.10196
11820	Sm	1104	13.3	2.0	1.1	14.43	1.018(-16)	2.77	0.04795
11861	SABdm	1481	20.9	3.5	1.3	12.51	1.106(-15)	5.12	4.21805
11868	SBm	1093	13.2	1.9	1.2	13.10	2.269(-16)	1.82	0.09558
11872	SABb	1150	13.2	2.7	1.4	10.68	1.354(-15)	1.17	0.57387
12043	S0/a	1008	12.4	1.6	2.7	13.06	3.063(-16)	2.36	0.10844
806	SABcd:	1761	19.3	3.5	1.2	11.94	1.936(-15)	5.33	1.56428
1356	SABa	1733	19.3	2.3	1.1	16.11	1.870(-17)	2.40	0.01500
1670	Sm:	1601	18.1	2.2	1.0	14.43	1.096(-16)	2.97	0.07924
1736	SABc	1562	17.6	5.2	1.4	11.00	1.956(-15)	2.25	1.34047
1888	SABc:	1507	17.5	3.8	1.7	11.56	9.779(-16)	1.89	1.37066
1954	SABc	1608	18.1	3.3	1.3	12.20	7.793(-16)	2.71	0.54643
2045	Sab	1543	18.5	4.0	2.0	10.94	2.539(-15)	2.76	2.21816
2183	Sa:	1545	18.6	1.9	1.3	11.93	8.489(-16)	2.31	0.83042

Photometric, distance and star formation data for 334 galaxies

UGC	Class.	v	Dist	Diam	a/b	m_R	H α flux	EW	SFR
		kms^{-1}	Mpc	a_{min}		mag	Wm^{-2}	nm	$\text{M}_{\odot} \text{yr}^{-1}$
2245	SABc	1519	17.3	3.8	1.4	10.78	5.018(-15)	4.71	3.20738
2345	SBm:	1506	17.2	3.5	1.2	14.06	2.325(-16)	4.51	0.16152
2392	Scd?	1548	19.0	1.9	3.8	14.53	4.465(-17)	1.33	0.04042
2729	S0/a	1940	26.1	3.5	1.4	13.24	1.529(-16)	1.39	1.38826
3546	SBa:	1871	26.9	2.6	1.9	11.16	6.120(-16)	0.82	1.03444
3496	Im:	1581	23.4	2.1	1.4	15.42	6.328(-17)	4.30	0.10617
3598	IBm	1991	28.4	2.0	1.7	13.07	6.362(-16)	4.93	1.49245
3685	SBb	1797	26.3	3.3	1.2	11.69	7.299(-16)	1.59	1.14407
3826	SABd	1733	25.7	3.5	1.2	12.63	3.483(-16)	1.81	0.53552
4238	SBd	1544	23.5	2.6	1.7	12.97	3.164(-16)	2.25	0.37832
4533	Sdm pec	1939	29.8	1.9	2.7	12.93	3.602(-16)	2.46	0.68754
4659	SAdm:	1756	27.6	1.7	3.4	14.59	4.231(-17)	1.33	0.06748
4680	Sbc?	1631	26.2	1.7	3.4	12.63	6.943(-16)	3.58	0.97183
4708	SBb:	1815	28.5	3.0	2.0	11.66	9.637(-16)	2.05	1.61467
4922	SAm	1991	30.7	3.5	1.8	13.18	4.789(-17)	0.41	0.09352
5015	SABdm	1650	27.3	1.7	1.1	13.74	1.065(-16)	1.54	0.17894
5688	SBm:	1920	29.2	3.5	1.8	13.57	3.510(-16)	4.31	0.63397
5717	SABbc:	1686	26.8	2.0	2.0	12.50	6.227(-16)	2.87	0.90993
6506	SBd	1580	29.1	1.7	3.0	14.74	4.823(-17)	1.74	0.08520
7656	SAa?	1774	32.3	1.7	1.1	11.50	3.022(-16)	0.55	0.65949
9576	SABd	1567	27.4	3.0	1.2	12.09	1.659(-15)	5.22	2.71474
9579	Sbc?	1681	28.8	4.2	4.2	10.71	2.775(-15)	2.45	5.00329
9926	SAc	1958	31.2	2.8	1.4	10.97	2.915(-15)	3.28	6.36373
10805	SBm	1554	23.8	1.7	1.1	14.10	1.587(-16)	3.17	0.23307
11124	SBcd	1613	23.7	2.5	1.1	12.38	4.844(-16)	2.00	0.58788
11238	SB0/a	1821	26.2	2.9	1.3	11.36	9.555(-17)	0.15	0.15092
11283	SBdm?	1959	27.5	1.8	1.2	12.79	1.057(-15)	6.36	1.82058
11331	Sm:	1554	22.9	1.5	1.3	14.58	9.482(-17)	2.97	0.11563
11332	SBd pec?	1558	23.0	2.5	2.8	12.88	1.018(-15)	6.66	1.25210

Photometric, distance and star formation data for 334 galaxies

UGC	Class.	v	Dist	Diam	a/b	m_R	H α flux	EW	SFR
		kms^{-1}	Mpc	a_{min}		mag	Wm^{-2}	nm	$M_{\odot} \text{yr}^{-1}$
11921	IBm	1678	19.6	1.7	2.4	13.49	3.758(-16)	4.30	0.40917
11944	Im:	1734	20.3	2.4	3.0	15.44	1.011(-16)	6.97	0.11384
12178	SABdm	1931	21.8	3.1	1.9	12.19	8.313(-16)	2.87	0.98869
19	SABc:	2309	26.1	3.6	3.6	11.40	9.217(-16)	1.54	1.42064
858	SAB	2374	26.3	3.1	1.6	11.59	1.449(-15)	2.88	2.14830
859	SAB0/a:	2134	24.0	2.4	1.6	12.14	3.604(-16)	1.18	0.50818
895	Sdm	2247	25.0	2.0	2.9	13.23	4.115(-16)	3.70	0.58689
907	SAB	2272	24.0	5.6	1.3	9.87	5.812(-16)	0.24	0.70854
914	SABcd:	2338	25.8	4.3	2.9	12.13	8.499(-16)	2.77	1.20321
1211	Im:	2408	27.1	2.3	1.2	14.62	1.428(-17)	0.46	0.02996
1554	SAC:	2101	23.9	2.8	2.3	12.11	4.655(-16)	1.49	0.59341
3504	SABcd	2100	29.5	2.8	1.1	12.00	1.493(-15)	4.33	3.10491
3530	SBcd:	2101	29.6	2.5	1.9	12.49	6.786(-16)	3.09	1.39950
3522	S0/a	2132	30.0	1.8	1.6	13.99	9.969(-17)	1.80	0.20929
3653	SABbc	2222	31.1	3.7	1.5	11.20	1.854(-15)	2.58	4.12245
3740	SABc	2410	33.2	2.8	1.0	11.08	4.871(-15)	6.06	13.48202
3834	SABc:	2042	29.1	3.5	2.5	12.56	6.362(-16)	3.08	1.13738
3994	SABab:	2080	29.5	2.7	1.9	12.11	3.368(-16)	1.08	0.69507
4066	Scd:	2296	32.2	1.7	1.0	13.26	3.333(-16)	3.09	0.75162
4260	Im:	2254	32.8	1.6	1.1	13.81	4.670(-16)	7.20	1.36703
4273	SBb	2471	35.4	2.7	2.3	11.84	9.439(-16)	2.36	2.74807
4270	SABbc	2479	35.1	1.6	1.5	13.28	2.619(-17)	0.25	0.07259
4375	SABc:	2061	30.9	2.5	1.5	11.92	5.901(-16)	1.60	1.23455
4362	SA0/a	2344	33.1	1.9	1.4	11.96	2.806(-16)	0.78	0.64463
4393	SBc?	2124	31.5	2.2	1.5	13.26	5.788(-16)	5.36	1.24953
4390	SBd	2169	31.1	1.9	1.2	13.69	2.174(-16)	2.99	0.44543
4444	SBcd?	2081	31.3	1.5	1.7	13.31	3.192(-16)	3.09	0.67236
4469	SBcd	2094	31.5	2.1	1.0	12.50	1.006(-15)	4.63	2.16769
4484	SBb:	2135	32.1	2.0	1.5	11.94	5.994(-16)	1.65	1.33397

Photometric, distance and star formation data for 334 galaxies

UGC	Class.	v kms ⁻¹	Dist Mpc	Diam amin	a/b	m _R mag	H α flux Wm ⁻²	EW nm	SFR M _⊙ yr ⁻¹
4541	Sa	2060	31.4	3.6	3.0	11.37	1.452(-16)	0.24	0.29922
4574	SBb	2160	31.1	2.7	1.7	11.26	2.112(-15)	3.09	4.23323
5056	Sa	2146	33.4	2.2	2.0	11.80	2.605(-16)	0.63	0.66460
5102	SABb:	2432	36.9	1.7	2.8	12.55	6.070(-16)	2.93	1.74133
6517	Sbc	2491	38.8	1.7	1.8	13.19	2.198(-16)	1.90	0.69819
7563	Im	2350	38.4	2.1	2.1	13.69	1.716(-16)	2.36	0.66618
11113	SABd	2331	32.0	1.9	1.1	13.68	1.655(-16)	2.26	0.44115
12221	SAd	2057	28.4	2.2	2.8	13.09	3.378(-16)	2.68	1.08629
12270	SABd	2116	24.0	1.8	1.0	12.65	3.326(-16)	1.75	0.41406
12294	SABc	2194	25.0	2.3	2.3	11.29	2.946(-15)	4.43	4.16117
12343	SBc	2381	26.9	4.0	1.2	10.83	3.545(-15)	3.49	6.63491
12350	Sm	2140	24.3	2.8	3.1	13.72	1.462(-16)	2.06	0.22359
550	Sb	2674	30.3	1.8	2.2	13.58	1.940(-16)	2.41	0.39244
1192	Sb	2988	33.6	3.3	1.9	12.17	7.847(-16)	2.67	1.94081
1276	SBdm	2749	31.3	1.9	2.1	13.15	2.711(-16)	2.26	0.64107
1305	SABc	2665	30.5	3.7	1.4	11.43	4.055(-16)	0.70	0.88097
1313	SABc	2931	33.5	3.0	1.9	13.30	3.628(-16)	3.49	0.94720
1378	SBa:	2935	37.6	3.5	2.5	12.15	1.172(-16)	0.39	1.07001
1547	IBm	2640	30.3	2.2	1.0	13.25	2.690(-16)	2.46	0.78947
2081	SABcd	2616	29.6	2.5	1.4	13.76	9.137(-17)	1.33	0.16731
2124	SBa:	2631	29.7	2.6	1.0	11.83	1.868(-16)	0.46	0.34924
2247	SBbc	2758	31.3	4.5	2.3	11.85	6.109(-16)	1.54	1.27298
2603	Im	2516	33.7	1.7	1.2	14.59	5.882(-17)	1.85	0.39701
3463	SABbc	2692	36.2	2.7	1.4	11.85	1.181(-15)	2.98	3.88576
3701	SACd:	2915	39.2	1.8	1.0	13.65	2.477(-16)	3.29	0.87252
3804	Scd:	2887	39.0	1.9	1.5	12.15	7.112(-16)	2.36	2.26945
4705	SBb	2526	36.4	2.2	2.0	12.75	3.911(-16)	2.26	1.07418
6157	SAdm	2958	44.4	1.9	1.1	13.67	2.436(-16)	3.29	0.99364
7308	Sd	2762	39.9	1.7	3.4	13.33	3.429(-16)	3.39	1.14205

Photometric, distance and star formation data for 334 galaxies

UGC	Class.	v kms ⁻¹	Dist Mpc	Diam amin	a/b	m _R mag	H α flux Wm ⁻²	EW nm	SFR M _⊙ yr ⁻¹
11269	SABab? pec	2582	35.0	2.5	1.9	12.10	2.618(-16)	0.83	0.72654
12118	Sab	2825	32.1	2.0	2.9	12.66	2.886(-16)	1.54	0.71412
12442	SABc:	2674	29.8	2.1	3.7	12.98	6.026(-16)	4.31	1.23834
12447	SBbc: pec	2678	29.9	3.3	3.0	11.35	2.125(-15)	3.39	4.41212
12690	SBm:	2605	28.9	2.0	1.1	15.41	7.043(-17)	4.72	0.12922
12699	SBb: pec	2798	31.0	1.9	1.4	11.90	3.656(-15)	9.65	7.84897
12700	Im pec	2770	30.7	2.6	5.2	13.00	0.000(+00)	0.00	0.00000
12788	SAC	2956	32.8	2.2	1.2	12.51	9.332(-16)	4.32	2.19752
N2604B	Im	2104	31.7	0.7	1.8	14.71	6.820(-17)	2.40	0.16670
060-036	Sc	2115	32.0	0.9	4.5	14.39	2.660(-16)	7.00	0.53539
+74.0041	Im	2160	31.1	0.5	1.7	14.37	6.240(-17)	1.60	0.14673
0809+363	SBm	2471	35.4	0.4	2.0	15.02	1.500(-17)	0.70	0.03687
Shane1	Sm?	649	10.9	0.6	3.0	17.13	4.590(-17)	15.00	0.01071
N3769A	SBm pec:	761	12.6	1.1	2.8	14.38	2.760(-16)	7.20	0.08587
N4810	Im pec:	912	17.7	1.9	2.4	14.08	3.550(-16)	7.00	0.27064